Structural and biochemical characterization of Malaria parasites

Andrea Johana Lopez Moreno

Thesis for the degree of Philosophiae Doctor (PhD)
University of Bergen, Norway
2021

UNIVERSITY OF BERGEN

Structural and biochemical characterization of Malaria parasites

Andrea Johana Lopez Moreno

Thesis for the degree of Philosophiae Doctor (PhD)
at the University of Bergen

Date of defense: 17.09.2021

Year: 2021

Title: Structural and biochemical characterization of Malaria parasites

Name: Andrea Johana Lopez Moreno

Print: Skipnes Kommunikasjon / University of Bergen

To my mom, family and friends

Scientific environment

This project was performed in the Biorecognition Group at the Department of Biomedicine, University of Bergen, Norway, during the years 2017-2021 under the supervision of Professor Inari Kursula (University of Bergen, Norway, and University of Oulu, Finland) and co-supervised by Dr. Juha Vahokoski (University of Bergen, Norway). The project was financed by the Research Council of Norway (NFR) and the Sigrid Jusélius Foundation, Finland.

The grid preparation and cryo-EM data collection were performed at the Structural Biology of Cells and Viruses Laboratory, Francis Crick Institute, London, UK. Mass spectrometry measurements were carried out at the Biocenter Oulu Proteomics and Protein Analysis Core Facility, Faculty of Biochemistry and Molecular Medicine, University of Oulu, Finland.

Additional financial support for courses and conferences was provided by the National Graduate School in Biocatalysis in Norway (BioCat), Norwegian Biochemical Society (NBS), The Federation of European Biochemical Societies (FEBS), and The International School of Crystallography (ISC_oC).

Acknowledgements

First, I would like to express my gratitude to Prof. Inari Kursula for allowing me to be part of this challenging and exciting project, for her support in my career and personal life, and for her patience and guidance during the last 3.5 years. Thanks for believing in my capabilities and changing my life, giving me this opportunity to continue my career studying Apicomplexan parasites and introduce me to this exciting side of structural biology. I also extend my gratitude to Juha Vahokoski for co-supervising my project, giving me ideas and suggestions and the training to carry out my project.

Also, I want to thank Ju Xu for her technical assistance, for helping me with part of the long experiments, searching for reagents, and remind me about holiday days and the closing time of the supermarkets. Furthermore, I would like to thank the IK group Oulu for their online help and the people in Bergen who are no longer part of the group. Thanks for answering my questions, sending me samples, giving me suggestions and protocols. Mainly, I would like to thank the former member of the group, Dr. Esa-Pekka, for his guidance at the beginning of this journey. I also wish to express my gratitude to Juha K, and Leila for helping me in the lab. Likewise, I would like to thank Isa for helping me with the MS samples and the discussions and sometimes just talking about our failed experiments and our lives. I am very grateful for the suggestions and discussions in the lab meetings with Dr. Petri Kursula and all the members of his group. Many thanks to my colleagues on the 5th floor for assisting me with some of the instruments and the meetings and social events.

I would like to thank my friends in Bergen for making me feel welcome in this country, to listen to me talking about my research even if sometimes you do not understand what I am talking about, for the friendly trips, bord games, food, hikes, etc. Kelly, thanks for being a very good friend, teaching me norwegian and reading my thesis, I consider you as part of my family. Jessica and Kelly, many thanks for helping me with the chemical compounds and instruments in

the lab and for the lovely lunchtimes. Sometimes it is good to practice Spanish and Castellano, not to forget it.

I am very grateful of Matthijs for supporting and tolerating all long working hours and weekend absences during the lab work. I have to travel to the other side of the world to find somebody like you, and I love you so much. Thanks for encouraging me to continue even when things do not look good at all. Also, for all your assistance with the software installations and programming issues, I learned a lot. Also, I wish to thank Teun, Jetty, Wouter, and Ella for supporting me.

Last but not least, my family in Colombia, my dad, brothers, my lovely nephews, cousins, aunts, uncles, my grandma, friends etc., which I have not met for almost two years. Thanks for their support, sharing pictures, calls, and messages even when we can only understand half of the conversation because of the lousy internet connection. Also, Diana, Laura, Lili, Juan, and Erik, it is nice to have some people in Europe to share Christmas time or call in the same time zone. Mom, I want to express my deepest gratitude to you for all your efforts to educate me, for your unconditional support and love. We survived to many things in life, and it is because of you. I miss you so much, but you are always present in my heart.

Summary

The Apicomplexa phylum includes more than 6000 species, and some of them are pathogens of humans and animals of socio-economic importance. The most representative parasites are *Plasmodium* spp. and *Toxoplasma gondii*. *Plasmodium* spp. cause malaria, a parasitic infection with a wide distribution in tropical and subtropical areas. These parasites display a unique mode of cell motility called gliding motility. A macromolecular motor complex, the glideosome, is indispensable for parasite locomotion and host cell infection. The core of the glideosome is formed by an actomyosin motor comprised of actin as well as myosin (Myo) A and its two light chains, essential light chain (ELC) and MyoA tail interacting protein (MTIP). *Plasmodium* spp. have six myosins classified into three classes (VI, XII, and XIV). MyoA from class XIV is the most studied of these. The force for parasite gliding motility is produced by the hydrolysis of ATP, which promotes the movement of MyoA along actin filaments. *Plasmodium* spp. have two actin isoforms, of which the major isoform, ActI, is the most studied.

In this work, a biochemical and structural characterization was performed on *Plasmodium falciparum* actins, focusing on the minor isoform, ActII. *In vitro* experiments were performed to understand the polymerization properties of these unconventional actins. The critical concentration, the kinetics of the elongation phase, and spontaneous depolymerization were studied. This thesis work showed that the filament stability of *Plasmodium* actins is different between the isoforms and from canonical actins. Especially for ActI, which forms shorter filaments than ActII. Atomic structures were determined by cryogenic electron microscopy (cryo-EM) of *Pf*ActII in the ADP-Mg^{2+} form in the absence and presence of the stabilizing agent jasplakinolide (JAS) at resolutions of 3.5 and 3.2 Å, respectively. The structures reveal monomer interactions along the filament, the effect of JAS on the filaments, and conformational changes in the actin protomers upon polymerization, including the D-loop conformation.

In addition, this work contributed to obtaining the first high-resolution structure of the *Plasmodium* actomyosin motor complex at an average resolution of 3.1 Å, and the structure of filamentous *Pf*ActI with a resolution of 2.6 Å showing details of the nucleotide and JAS binding sites. Besides, a preliminary characterization of class VI myosins was performed. A molecular tool was generated, which can be used to study protein-protein interactions in order to find the interacting light chains for other *Plasmodium* myosins.

Understanding the structure and biochemical properties of the glideosome components and other actomyosin complexes provides a basis for developing new treatments against these devasting pathogens.

Keywords: actin, Apicomplexa, cryo-EM, filament, glideosome, jasplakinolide, malaria, myosin

List of Publications

Paper I

Kumpula EP, **Lopez AJ**, Tajedin L, Han H & Kursula I. (2019) Atomic view into *Plasmodium* actin polymerization, ATP hydrolysis, and fragmentation. *PLoS Biol* 17(6): e3000315. doi: 10.1371/journal.pbio.3000315.

Paper II

Lopez AJ, Vahokoski J, Calder LJ, Rosenthal PB & Kursula I. (2021) Polymerization properties and near-atomic structure of filamentous *Plasmodium falciparum* actin II. *Manuscript to be submitted.*

Paper III

Vahokoski J, Calder LJ, **Lopez AJ**, Molloy JE, Rosenthal PB & Kursula I. (2020) High-resolution structures of malaria parasite actomyosin and actin filaments. *bioRxiv* doi: https://doi.org/10.1101/2020.07.02.183871

Contents

Abbreviations

Act	Actin
ACTs	Artemisinin-based combination therapy
ADF	Filament- severing actin-depolymerizing factors
ADP	Adenosine-5'-diphosphate
AMA1	Apical membrane antigen 1
Arp2/3	Actin Related Protein 2/3 complex
ATP	Adenosine-5'-triphosphate
b2	Phosphate clamp distance
BAC	Bacterial artificial chromosome
c	Cleft mouth
CaM	Calmodulin database and Meta-analysis predictor
CAP	Cyclase associate protein
C_c	Critical concentration
COR	Coronin
CP	Capping protein
CRT	Chloroquine resistance transporter protein
Cryo-EM	Cryogenic electron microscopy
DAD	Photodiode arrays
DLS	Dynamic light scattering
DPA	Proliferation arrest
DTT	1,4-dithiothreitol
EBAs	Erythrocyte-binding antigens
EDTA	Ethylenediaminetetraacetic acid
ELC	Essential light chain
EM	Electron microscopy
ER	Endoplasmic reticulum
ESI	Electrospray ionization
FRM	Formin
G-actin	Globular actin
GAP	Gliding-associated proteins
GFP	Green fluorescent protein
Hsp90	Heat shock protein 90
ID	Inner domain
IMC	Inner membrane complex
JAS	Jasplakinolide
k_-	Dissociation rate constant
k_+	Association rate constant
K13	Kelch13
LC	Liquid chromatography
loxP	Locus of X-over P1
MALDI-TOF	Matrix-assisted laser desorption/ionization protein
MJ	Moving junction
MS	Mass spectrometry

MTIP	MyoA tail interacting protein
MW	Molecular weight
Myo	Myosin
NAA80	N-alpha-acetyltransferase 80
NatA	N-terminal acetyltransferase A complex
NatB	N-terminal acetyltransferase B complex
NatH	N-terminal acetyltransferase H complex
OD	Outer domain
p10	Polyhedrin promoter
Pb	*Plasmodium berghei*
PCS	photon correlation spectroscopy
PDB	Protein Data Bank
Pf	*Plasmodium falciparum*
PM	Plasma membrane
PMF	Peptide mass fingerprinting
PRF	Profilin
PTM	Post-translational modification
PV	Parasitophorous vacuole
Pyrene	N-(1-pyrene)iodoacetamide
RBC	Red blood cells
RH	Reticulocyte binding-like homolog
r_H	Hydrodynamic radius
RH5	Reticulocyte binding-like protein 5
ROM	Rhomboid protease
SD	Subdomain
SDS-PAGE	SDS-polyacrylamide gel electrophoresis
SEC	Size exclusion chromatography
SEC-MALS	Size exclusion chromatography- a multi-angle light scattering
Sf	*Spodoptera frugiperda*
TCEP	Tris(2-carboxyethyl)phosphine hydrochloride
tcs	TEV NIa protease cleavage site
TEM	Transmission electron microscopy
TEV	Tobacco etch virus
Tg	*Toxoplasma gondii*
TIRF	Internal reflection fluorescence microscopy
TRAP	Thrombospondin-related anonymous protein
Unc45	Uncoordinated mutant number 45
UPLC	Ultra-performance liquid chromatography
WH2	Wiskott–Aldrich syndrome homology region 2
WHO	World Health Organization
θ	Twist angle

1. Introduction

1.1. Apicomplexan parasites

Apicomplexan parasites include some of the most successful deadly pathogens in humans and animals (Plattner & Soldati-Favre, 2008). They are obligate intracellular parasites with a wide distribution in the subtropical and tropical areas (Dondorp & Von Seidlein, 2017). The first apicomplexan parasite identified was an oocyst of *Eimeria* in a rabbit in 1674. Nowadays, the phylum comprises around 6000 species, and some are opportunistic pathogens, which affect vertebrate and invertebrate animals **(Table 1)**.

Subclass	Pathogen	Dissease	Intermediate host	Definitive host
Haemosporidia	*Plasmodium spp.*	Malaria	Vertebrates: humans, monkeys, reptiles and birds.	Mosquitoes
Coccidians	*Toxoplasma gondii*	Toxoplasmosis	Vertebrates: mammals, fish, reptiles, amphibians.	Felines
	Eimeria spp.	Coccidiosis	-	Vertebrates: chickens and cattles
Gregarines	*Cryptosporidium ssp.*	Cryptosporidiosis	-	Mammals, birds, reptiles, fishes
	Gregarina spp.		-	Invertebrates: cockroaches and shrimps
Piroplasmida	*Babesia spp.*	Babesiosis	Vertebrates: Humans and domestic animals	Arthropods: ticks
	Theileria spp.	Theuleriosis	Vertebrates: cattles	

Table 1. Representative opportunistic pathogens from the Apicomplexa phylum (Becker, 2011; Morrissette & Sibley, 2002; Rueckert et al., 2019).

Apicomplexa are single-celled organisms and possess unique structures, such as the apical complex, the conoid, the apicoplast, the pellicle, and the apical polar ring (Morrissette & Sibley, 2002). *Toxoplasma gondii* is the most common model organism because it is relatively easy to cultivate, the complete genome is available, it is fairly easy to manipulate genetically, and the parasite can be studied using microscopy techniques. As *Plasmodium* is a public health problem worldwide, many studies have also been carried out on this organism, placing it as the second most common study model of the phylum (Kooij et al., 2006; Roos et al., 1995; Weiss & Kim, 2007).

1.2. Worldwide distribution of *Plasmodium* spp.

Malaria is caused by *Plasmodium* spp., which are the most clinically relevant representatives of this phylum. Four species infect humans, *P. falciparum*, *P. vivax*, *P. malariae*, and *P. ovale*. Occasionally, species that generally infect other animals, can infect humans, an example being *P. knowlesi* (Antinori et al., 2012). In 2019, approximately 409000 people died of the over 229 million malaria cases registered worldwide, and the population living in the tropical regions has the highest risk of infection **(Fig. 1)**. *P. falciparum* is the most prevalent species worldwide, especially in Africa (99.7%), South-east Asia (50%), East of the Mediterranean (71%), and the pacific region (65%). This species causes the most severe clinical symptoms. On the other hand, *P. vivax* is predominant in central and south America (75%) and India (75%). This species develops faster than *P. falciparum* and can stay latent and cause recurrent infections (White, 2016; World Health Organization, 2019, 2020).

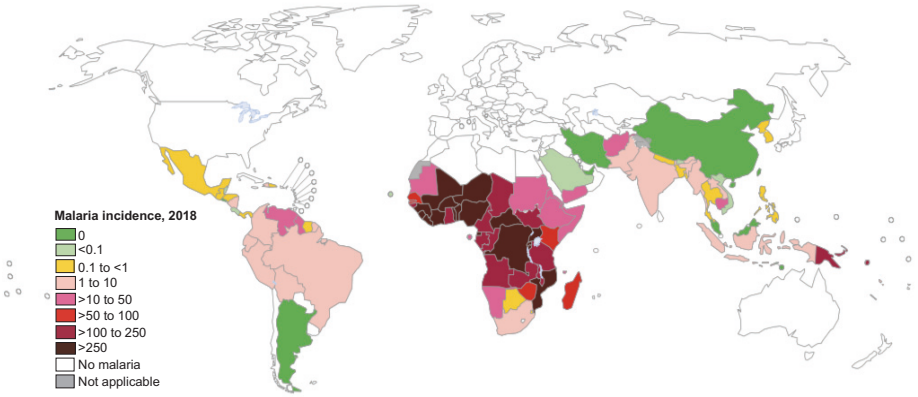

Figure 1. Worldwide distribution of malaria. The map shows the incidence rate (number of cases per 1000 people) by country in 2018. Reproduced from World malaria report 2019. Geneva: World Health Organization; 2019. License: CC BY-NC-SA 3.0 IGO.

1.3. *Plasmodium* ssp.: Overview

Plasmodium spp. transform into different cellular stages through their life cycle that involves two hosts. In the intermediate host, cellular stages such as merozoites, trophozoites, and schizonts develop, whereas ookinetes, oocysts, and sporozoites develop in the definitive host. There are many morphological and metabolic differences between those stages **(Fig. 2)**.

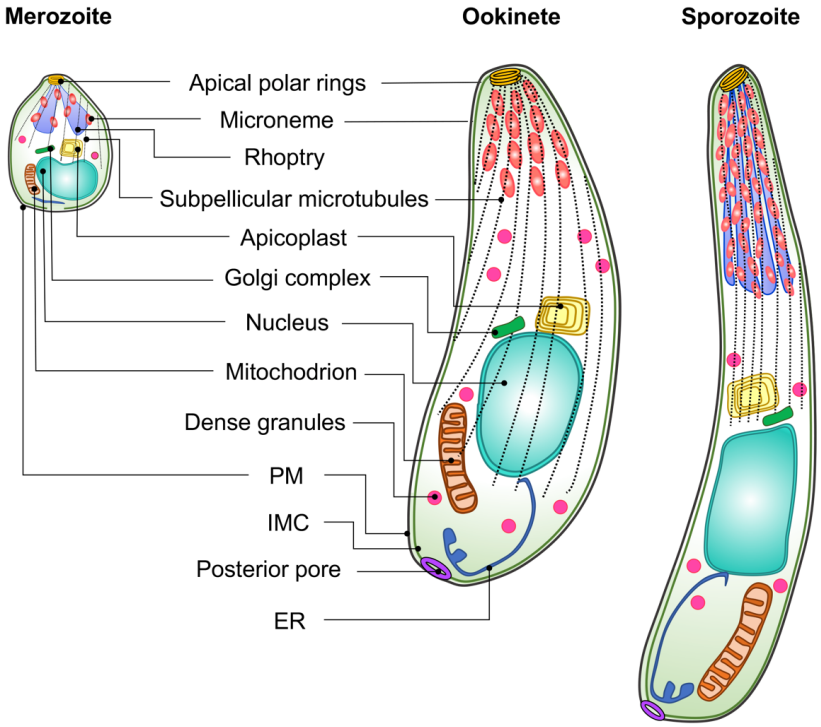

Figure 2. Schematic model of the ultrastructure of the *Plasmodium* spp. Depicted are the merozoite, the ookinete, and the sporozoite. Redrawn and adapted from Frénal et al., 2017. PM: plasma membrane, IMC: inner membrane complex, ER: endoplasmic reticulum.

Merozoites are the stage responsible for expanding the infection because they multiply very fast in the red blood cells (RBC) of the host. Merozoites with a diameter of ~1-2 µm are among the smallest eukaryotic cells (Bannister et al., 1986). They contain two rhoptries and only few micronemes. Micronemes are secretory organelles localized in the apical pole. Because of the low microneme

content, merozoites are virtually nonmotile (Carruthers & Tomley, 2008). In contrast to the globular merozoites, sporozoites and ookinetes are slightly curved, with an elongated form. For example, the sporozoite is 10 µm long and 1µm in diameter. Both forms move by gliding; sporozoites are faster (~2 µm s^{-1}) than ookinetes (~ 5 µm min^{-1}). Both of these motile forms have an abundance of micronemes. One of the significant differences is that ookinetes do not contain rhoptries (Frénal, Dubremetz, et al., 2017). This organelle is correlated with the moving junction (MJ), which is necessary for the parasite during the penetration in the host cell (Besteiro et al., 2011). Ookinetes are only able to migrate through the epithelium of the mosquito midgut but not to invade host cells like the sporozoites.

1.3.1. Life cycle

The life cycle of *Plasmodium* spp. involves a sexual and asexual phase **(Fig. 3)**. *Plasmodium* parasites infect female *Anopheles* mosquitoes. The mosquito, where the sexual cycle takes place, is the definitive host of the parasite. The parasites develop motile but non-invasive ookinetes that migrate to the epithelium through the mosquito midgut and develop into oocysts. Finally, parasites differentiate into sporozoites that migrate to the salivary glands. Mosquitos can transmit the parasite to the intermediate mammalian host, *e.g.,* human, by a bite. After a bite of an infected mosquito, the sporozoites travel through the skin epithelium and blood vessels to the liver. They migrate through the sinusoidal cells, cross the Kupffer cells and invade hepatocytes, where asexual replication occurs. After a time that can vary from a week to even years, the parasites differentiate into asexual blood-stage parasites called merozoites. The life cycle's liver stages do not display clinical manifestations (Crompton et al., 2014; De Niz et al., 2016). In the following steps, merosomes (vesicles containing merozoites) are released into the bloodstream. Free merozoites invade RBCs to replicate and develop in three consecutive forms: ring forms, trophozoites, and schizonts. Approximately 36 merozoites are

released for each infected RBC into the bloodstream to invade new cells (Grüring et al., 2011). Every cycle of invasion of RBCs takes approximately 48 h (LH Miller et al., 2002). This stage is responsible for the clinical manifestations of the disease (Crompton et al., 2014). Some parasites can develop into sexual forms called gametocytes, circulating in the bloodstream. These are subsequently transmitted to the mosquito when it bites an infected intermediate host (Frénal, Dubremetz, et al., 2017).

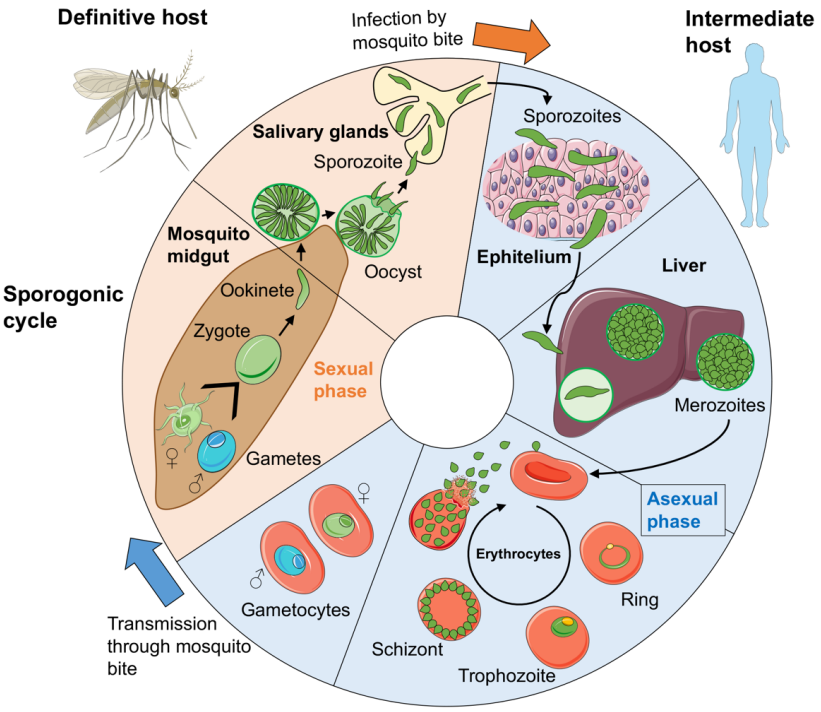

Figure 3. The life cycle of *Plasmodium* spp. Redrawn and adapted from (Aly et al., 2009; Bourgard et al., 2018; Frénal, Dubremetz, et al., 2017).

1.3.2. Invasion

Host cell invasion is completed within 20-30 s. The first contact of the merozoite with the RBC is mediated by the interaction of the merozoite surface proteins (MSPs) and the surface of the RBC. Afterwards, Ca^{2+} is released into the host

cell, triggered by the interaction of reticulocyte binding-like protein 5 (RH5) and basigin (Volz et al., 2016). The parasite is then reoriented with its apical end perpendicular to the host cell by the interactions of erythrocyte-binding antigens (EBAs) and reticulocyte binding-like homologs (RH) with host cell receptors. The interaction of EBA-175 with glycophorin A causes the deformation of the RBC, which is essential for invasion. Secreted components of micronemes and rhoptry proteins are discharged at the apical end of the parasite (Plattner & Soldati-Favre, 2008). Some of these components participate in the formation of the moving junction (MJ). The MJ is a tight ring-shaped structure formed by AMA1 and RON proteins (RON2-RON4-RON5). The MJ mediates the contact between the parasite and the host cell plasma membrane. This structure moves from the apical pole to the posterior end of the parasite as it enters the cell. The force that drives invasion is produced by a macromolecular complex named glideosome (Opitz & Soldati, 2002) **(Fig. 5)**. Once the parasite invades the host cell, it induces the formation of a parasitophorous vacuole (PV), formed by the secretion of rhoptries. A small pore in the parasitophorous vacuole membrane allows the parasite to uptake small nutrients from the host cell. Thereafter, the parasite replicates and eventually egresses (Besteiro et al., 2011) **(Fig. 4).**

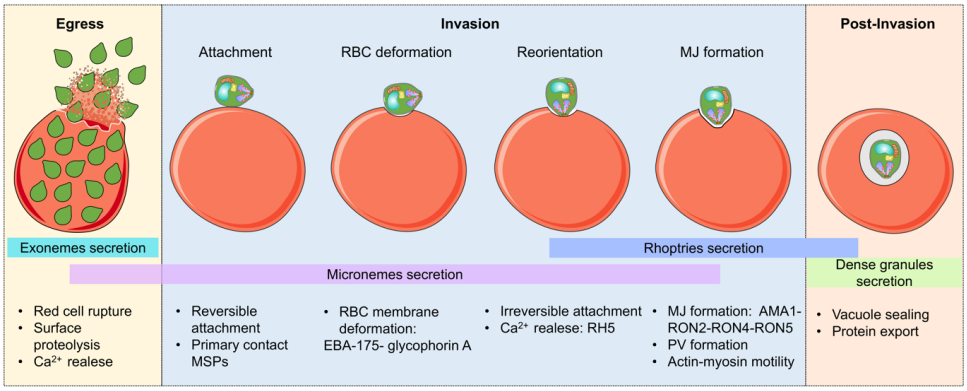

Figure 4. Scheme of merozoite invasion of the RBC. Redrawn and adapted from (Cowman et al., 2012; Frénal, Dubremetz, et al., 2017).

1.4. Glideosome

Most unicellular organisms have a locomotion system mainly formed by pseudopods, cilia, or flagella. Apicomplexan parasites lack these traditional locomotory structures. Instead, the motile and invasive stages of the *Plasmodium* life cycle (sporozoites, ookinetes, and merozoites) display a unique, rapid mode of substrate-dependent locomotion called gliding motility. The glideosome is responsible for generating and transmitting the gliding force (Opitz & Soldati, 2002). Gliding motility allows the parasite to cross non-permissive biological barriers (migration), penetrate different cell types (invasion) (Håkansson et al., 1999), and release from infected cells (egress) (Blackman & Carruthers, 2013).

The core of the glideosome is formed by an actomyosin system: actin, myosin (Myo) A, its two light chains, the MyoA tail interacting protein (MTIP; Bergman, 2003), and the essential light chain (ELC; Green *et al.*, 2017). This motor is linked to the IMC of the parasite by the gliding-associated proteins (GAP) 45, 50 (Baum et al., 2006), and 40 (Frénal et al., 2014). On the other side, the actin filaments are linked to the plasma membrane *via* the glideosome-associated connector (GAC; (Jacot *et al.*, 2016; Graindorge *et al.*, 2016) and transmembrane adhesins (invasins) of the thrombospondin-related anonymous protein (TRAP) family (Sultan et al., 1997). Thus, the motor complex is localized between the plasma membrane and the IMC and is translocated from the apical to the posterior end of the parasite during motility and invasion (Frénal, Dubremetz, et al., 2017; Keeley & Soldati, 2004) **(Fig. 5a).**

MyoA, the motor protein of the complex, is a type XIV myosin and has only a very short tail. The chemical energy released by ATP hydrolysis by the head (or motor) domain is transformed into directed movement along filamentous (F) actin. The neck region contains so-called IQ motifs (calmodulin-binding motifs), to which the light chains (MTIP and ELC) bind (Jones et al., 2012). *P. falciparum* MTIP is localized in the periphery of merozoites during the late

schizont stage (Green et al., 2006). When merozoites are released, the protein is localized at the anterior half of the parasite, which is related to the directionality, by which parasites invade RBCs (Pinder et al., 1998).

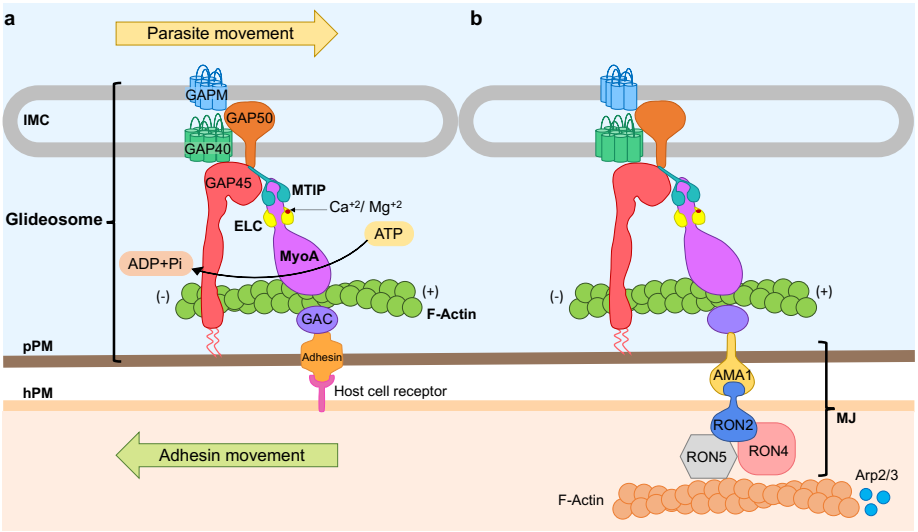

Figure 5. The glideosome. **a.** Components of the glideosome. Different adhesins have been identified for specific stages of the life cycle; EBAs and RHs proteins in merozoites (Wright & Rayner, 2014) and TRAP proteins in sporozoites (Sultan et al., 1997). **b.** The glideosome in contact with the MJ during invasion. Redrawn and adapted from (Besteiro et al., 2011; Boucher & Bosch, 2015; Frénal et al., 2017).

MyoA is a fast motor that shares similar kinetic and mechanical properties with skeletal muscle myosins. *In vitro* motility assays have shown that MyoA can reach high speeds of ~4 μm s^{-1} when S19 is phosphorylated (Robert-Paganin et al., 2019). The speed increases ~2-fold when MyoA is in complex with the light chains MTIP and ELC (Bookwalter et al., 2017; Green et al., 2006). *In vivo,* the speed of the motor varies according to the life cycle stage. While at the liver stage, sporozoites can move at speeds up to ~2 μm s^{-1}, in the mosquito stage, the sporozoites move slower through the salivary duct <2 μm s^{-1} (Münter et al., 2009).

In contrast, the blood-stage forms have limited motility. Merozoites require a force of ~40pN against the RBC for invasion (Crick et al., 2014). Additionally, in conditional knockouts of *Pf*MyoA and *Pf*ELC, merozoites were not successful in invading, RBCs did not deform, and no internalization into the RBC took place (Blake et al., 2020). Recent studies have suggested that gliding motility is not only restricted to host cell invasion. Merozoites can translocate with a speed of 0.59 μm s^{-1} for not more than 43 s in *in vitro* motility assays (Yahata et al., 2020). The authors suggested that parasites use gliding to move across the surface of the RBCs until they are able to invade the cell (McGhee, 1953).

1.4.1. Other myosins in *Plasmodium* spp.

Among Apicomplexa, *T. gondii* has the largest number of myosins (11 isoforms). The second place is occupied by *Haemosporidia* members, which include *Plasmodium* spp. These encode 6 myosin isoforms. MyoA is by far the most studied myosin because of its critical function in the glideosome complex. However, the other myosins also have interesting and crucial functions **(Table. 2)**.

Myosins in class XIVc (MyoB and MyoE) are unique for *Plasmodium* spp. MyoB binds to a large and unusual light chain and is located at the extreme apical end of motile and invasive parasites (Yusuf *et al.*, 2015). On the other hand, MyoE appears to be necessary for the motility of the sporozoites to the salivary glands, and it is dispensable for any life cycle stage (Wall et al., 2019).

MyoF belongs to class XXII; this myosin is present in all of the Apicomplexa members. *Pb*MyoF is transcribed abundantly after *Pb*MyoA in all of the stages of the life cycle. However, the expression is higher in insect stages; *Pb*MyoF is located in the apical end in mature ookinetes, while in oocysts, it is uniformly distributed. In *T. gondii,* MyoF is associate with the apicoplast, whereas, in *Plasmodium* spp., its function is unknown. The primary function of MyoF might be the positioning of the centrosomes during cell division or ookinete

development (Frénal et al., 2020; Wall et al., 2019). However, these hypotheses have to be investigated.

Myosin class VI includes MyoK and MyoJ. A recent study using GFP-tagging in parasites showed that *Pb*MyoJ is localized at the intersection between the mature oocyst and the sporozoite body structure. Evidence from *T. gondii* and *Plasmodium* spp. suggests that MyoJ could be involved in cell division and basal constriction (Frénal, Jacot, et al., 2017; Wall et al., 2019). Interestingly, MyoK appears to be essential in *T. gondii* but not in *Plasmodium* spp. *Pb*MyoK is localized in the centrocones, and its function is still unknown. It could be associated with the organization of the nucleus and with genome integrity during cell division (Wall et al., 2019). Additional studies need to be done to understand the role of these motors in apicomplexan parasites.

In *Plasmodium* spp., the binding site of the light chains or Ca^{+2} that correspond to the IQ motifs is unclear for many of the myosins. Apparently, MyoJ lacks the IQ motifs, in contrast to MyoK, which likely has three (Foth et al., 2006). In addition, this class of myosins in higher organisms like mammals, *Morone saxatilis*, *Drosophila* spp., and *Caenorhabditis elegans* commonly have an insertion between the motor domain and the IQ motifs. This region is responsible for an unusual backward movement towards the pointed (or -) end of actin filaments (Cramer, 2000; Sweeney et al., 1999; Wells et al., 1999). However, the insert and the unusual directionality of movement is unknown in apicomplexan parasites.

Class	Gene name	Old classification (class/name)	IQ motifts	Localization	Function	Life stage	*Plasmodium ssp.*	*Toxoplasma gondii*
XIV a	MyoA	XIV/ MyoA	1	Inner membrane complex	Gliding/ invasion/ egress	Invasive stages	x	x
XIV c	MyoB	XIV/ MyoB	1	Apical Ring	Merozoite initiation and internalization	Merozoites, mature ookinetes and sporozoites	x	
	MyoE	XIV/ MyoE	0	Basal cap	Sporozoite traversal to the salivary glands	Merozoites, Ookinetes and sporozoites	x	
XXII	MyoF	XII/ MyoC	3-6	Apical end, cytoplasm, and apicoplast *	Organellar inheritance	Mature ookinetes, and oocyst	x	x
VI	MyoJ	VI/ MyoD	0	Posterior cup, daugter cells	Basal constriction, cell division	Mature oocyst	x	x
	MyoK	VI/ MyoF	2-3	Centrocone (the spindle pole body)	Nucleus * organization, the genome integrity * during cell division	Zygotes and early ookinetes	x	x

Table 2. Myosin heavy chains in *Plasmodium* spp. The myosin classification is based on Mueller et al., 2017. The references for the localization and cellular functions are from Frénal et al., 2020; Frénal, Jacot, et al., 2017; Robert-Paganin et al., 2019; Wall et al., 2019. The myosin expression profiles in a specific life stage were acquired from Wall et al., 2019. * A hypothesis needs to be confirmed.

Plasmodium spp. have no homologous sequences for MyoD (class XIV a), MyoB/C, MyoE from class XIV b, MyoH (XIV c), MyoL (XIV e), MyoG (XXIII), and MyoI (XXIV) (Foth et al., 2006). In *T. gondii,* some of these isoforms are involved in cell invasion. For example, *Tg*MyoC is an alternative spliced version of *Tg*MyoB; these isoforms have a different COOH-terminal tail and localization. *Tg*MyoB/C participates in the glideosome complex at the posterior pole of the parasite. Previous studies suggested that *Tg*MyoA and *Tg*MyoC may have overlapping functions; thus, both motors could be critical during invasion (Frénal et al., 2014). Another motor associated with invasion is *Tg*MyoH (class XIVc), which is localized at the tip of the parasite (Graindorge et al., 2016).

1.5. Clinical relevance of *Plasmodium* spp.

Malaria is still the most devastating parasitic infection, which a wide range of symptoms. The severity of the infection ranges from absent or mild symptoms to death, depending on the immune system of the host, age, the parasite

species, and general health. A common symptom is fever that is developed when the person contains over 50 parasites/μL of blood (Hartley et al., 2020). Other effects are chills, sweating, headache, fatigue, myalgia, cough, and nausea. Severe cases can develop cerebral malaria, renal and liver failure, respiratory distress, coma, permanent disability, and death (Mace & Arguin, 2017).

Currently, there is no satisfactory treatment for malaria. The most common treatments that have been used are chloroquine, sulfadoxine/pyrimethamine, and artemisinin-based combination therapies (ACTs), which is the recommended malaria treatment by WHO. However, *Plasmodium* has developed resistance to these treatments. The action of artemisinin depends on the cleavage of the endoperoxide bond of this compound and the subsequent formation of toxic covalent adducts for the parasites (Meshnick, 2002). Previous reports suggested that artemisinins alkylate hundreds of proteins, inducing a global degeneration of the parasite (Ismail et al., 2016; Wang et al., 2015). The resistance is associate with mutations in the Kelch 13 (K13) protein, causing a delayed parasite clearance and a high rate of parasite survival (Fairhurst & Dondorp, 2016).

Chloroquine has been used for non-severe infections in some countries (Bloland, 2001). This compound accumulates in the parasitophorous vacuole of intraerythrocytic trophozoites, disrupting the hematin detoxification (product of the hemoglobin degradation) and poisoning the parasite (Slater, 1993; Wellems & Plowe, 2001). Nevertheless, like many other antimalarial drugs, the parasites have developed resistance, which is associate with a mutation of the chloroquine resistance transporter protein (CRT). CRT is a transporter in the digestive vacuole membrane of the parasite (Wellems & Plowe, 2001).

The parasite resistance acquired to all of the antimalarial treatments owes to the wide genetic diversity of the parasite and the accumulation of mutations through sexual recombination. Additionally, parasites express different

antigens for every stage during their life cycle, which is a vast obstacle for developing an effective vaccine (Takala & Plowe, 2009). New strategies and targets must be evaluated in order to prevent a rise in malaria mortality. For this, the glideosome can be a good target for designing inhibitors that disrupt the function of the motor complex involved in motility and host cell invasion (Green et al., 2017).

1.6. Actin

The next chapters focus on actin, which is the central part of this thesis. I will start by going through the general knowledge about actins. After that, I will go into specific knowledge about apicomplexan actins, mainly focusing on *Plasmodium* spp.

The cytoskeleton is composed mainly of three types of filaments: microtubules, intermediate filaments, and actin filaments. Microtubules are formed by tubulin; these are the thickest of the polymers with a diameter of 25 nm. Intermediate filaments (diameter of 15 nm) are formed by intermediate filament proteins like keratin or desmin, vimentin and nuclear lamins. Actin filaments (diameter of 5-9 nm) are the thinnest and most flexible of these polymers. While intermediate filaments appear to have only a structural function, microtubules and actin filaments are actively involved in other cellular processes (Alberts et al., 2002).

Actin is the most abundant and one of the most conserved proteins in eukaryotic cells. The conservation is attributed to its universal scaffolding and force providing functions in essential cellular processes (Gunning et al., 2015; Pollard, 2016). For example, during cell division and specifically during cytokinesis, actin filaments in complex with myosin II and structural and regulatory proteins form a contractile ring under the surface of the plasma membrane. The contractile ring generates the mechanical force to cleave the cell and generates two daughter cells (A. L. Miller, 2011). Two mechanisms

can trigger the ring constriction; the myosin mini-filaments move towards the barbed end of anti-parallel actin filaments, or the depolymerization of cross-linked actin filaments in the presence of minus-end binding proteins and myosin can drive the ring constriction (Mendes Pinto et al., 2012; Schwayer et al., 2016) **(Fig. 6a)**.

One of the most known functions of actin is muscle contraction. Actin filaments are part of the sarcomere, which is the basic contractile unit of striated muscle. Thick filaments are the central region of the sarcomere and are composed of myosin II. The myosin filaments are flanked by two half bands of actin filaments, also called thin filaments. Actin filaments polymerize from their barbed end towards the Z-line. During this process, some regulators like Cap Z bind to actin, blocking the barbed ends of the filaments (Maruyama, 2002), while the pointed end is capped by tropomodulin (Gregorio et al., 1995; Rao et al., 2014). Besides, the polymer assembly and maintenance are regulated by formins (Taniguchi et al., 2009). During muscle contraction, the myosin heads interact with the thin filaments in an asynchronous mode. The myosins move toward the barbed ends of the actin filament (Sweeney & Hammers, 2018) **(Fig. 6b)**.

Actin is also involved in cell motility. Branched actin filament networks generated by the action of actin regulators like the capping proteins, formin, profilin, cofilin, and Arp2/3 complex, provide the force for cell motility. The cells extend the plasma membrane at the leading edge, forming protrusions called lamellipodia, consequently move the cell body and retract the back of the cell. In this way, cells are able to move long distances through the extracellular matrix *in vivo* (Lehtimaki et al., 2017; Ridley, 2011) **(Fig. 6c)**.

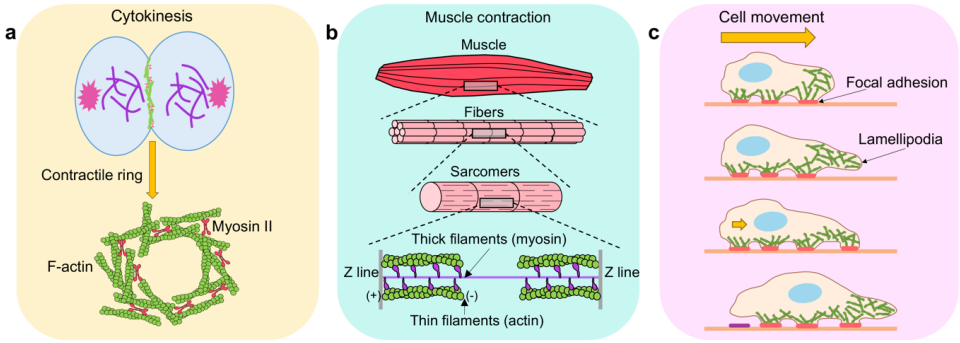

Figure 6. Role of actin filaments in essential biological processes. **a.** Cell division, **b.** muscle contraction and, **c.** cell motility. Redrawn and adapted from (Mattila & Lappalainen, 2008; A. L. Miller, 2011; Ojima, 2019).

1.6.1. Actin structure

Actin has been intensely studied for the last six decades. The structure of filamentous actin cannot be solved by X-ray crystallography because of its size, flexibility, and the heterogeneity of F-actin. In contrast, crystal structures of G-actin can be obtained by preventing polymerization, which is possible by complex formation between actin and ABPs or small molecules like latrunculin (monomer stabilizing compound) (Morton et al., 2000). In 1990, the first crystal structure of the actin-DNase I complex was solved (Kabsch et al., 1990). Nowadays, there are more than 13281 actin-related structures deposited in the Protein Data Bank (PDB).

Before the development of cryo-EM, the actin filament structure was studied using X-ray fiber diffraction (Holmes et al., 1990; Oda et al., 2001). The first cryo-EM map of an actin filament was of the actin-fimbrim complex with a resolution of 12 Å in 2008 (Galkin et al., 2008). After that, the number of structures has increased. In 2021, ~43 actin cryo-EM structures have been deposited. The improvement of the detectors has allowed to obtain density maps at resolutions of ~3 Å (Takeda et al., 2020).

1.6.1.1. Actin monomer structure

Actin belongs to the superfamily of sugar kinases, including hexokinases, Hsp70 proteins, the Arp proteins, the prokaryotic actin-like domains MreB and ParM (Bork et al., 1992; Schroer et al., 1994; Van Den Ent et al., 1999). A common characteristic of this superfamily is that the monomer folds into two major domains. For actin, these domains are referred to as the inner (ID) and outer (OD) domains, called also small and large domains **(Fig. 7a)**. The actin monomer fits in a rectangular prism of about 5.5 x 5.5 x 3.5 nm (Kühn & Mannherz, 2016). Besides, each domain is divided into two subdomains (SD1, SD2, SD3, and SD4) (Kabsch et al., 1990).

The ID and OD are connected by a polypeptide chain that crosses twice these domains. The bridge allows the rotation of both domains during the G- to F-actin transition. Besides that, this connection forms two clefts; one is associated with the nucleotide and Mg^{2+} binding, and the other cleft is located between the SD1 and SD3 and is primarily hydrophobic. This cleft allows the rotation of the two domains. It also mediates longitudinal contacts between actin monomers, and it is the primary binding site for most of the ABPs (Dominguez, 2004; Fujii et al., 2010; Oda et al., 2009). Structurally SD1 and SD3 are similar, while SD2 and SD4 contain large insertions and differ in size. In canonical actins, SD1 includes residues 1-32, 70-144, and 338-375; the C and N termini are located in this subdomain. SD2 is the smallest subdomain (residues 33-69) and contains the DNaseI-binding or D-loop; it is indispensable for polymerization (Holmes et al., 1990). Most of the crystal structures lack the D-loop because it has a disordered nature. Finally, residues 145-180 and 270-337 form the SD3, and residues 181-269 build the SD4 **(Fig. 7a)** (Dominguez & Holmes, 2011; Kühn & Mannherz, 2016).

The actin monomer has multiple conformations explained by different motions between the actin domains, such as open/twisted, closed/twisted or closed/flat conformations. The first motion is the rotation of the ID relative to OD around the rotation axis (center of mass of SD1 and SD3). The twist angle (θ) describes

this motion, which is associated with polymerization. The scissor-like motion explains the openness of the ID and OD relative to each other. It is related to the nucleotide-binding cleft size. The phosphate clamp size explains this movement (b1) and the cleft mouth size (c) **(Fig. 7)** (Oda & Maéda, 2010).

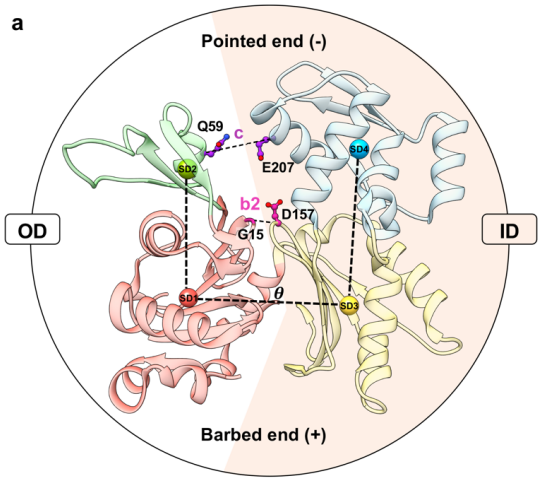

b

	Oppenness		Twistedness	
	Open	**Close**	**G-act**	**F-act**
b2	<6Å	>7Å	16-25°	8°
c	~10-11Å	~15Å		

Figure 7. Actin monomer structure. Back-face view of a profilin-G-actin state from rabbit (PDB: 5ZZA, Akıl & Robinson, 2018). The monomer has two major domains, the outer domain (OD) and the inner domain (ID). The spheres show the mass center of each subdomain. Principal parameters to determine the openness or twistedness of the monomer are indicated (c, b2, and θ). **b** Table showing the b2 and c distances and twist angle of the actin conformations (Oda & Maéda, 2010).

1.6.1.2. Filamentous actin structure

The main feature of actin is the ability to polymerize. Filaments are the active form of actin. F-actin can be defined as a long-pitch helix formed by two protofilaments. The symmetry is helical. The rise per monomer along the filament axis is 27.45 Å and the pitch of one-start helix is around 60 Å. The helical twist (α) is -166.55° for muscle chicken actin (Chou & Pollard, 2019) **(Fig. 8)**.

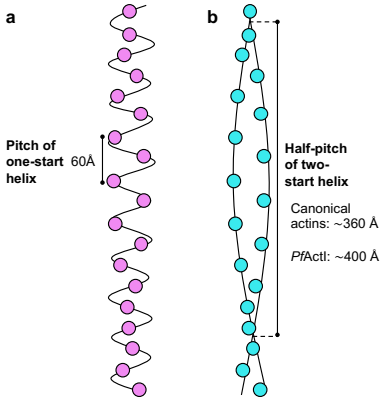

Figure 8. Schematic representation of one-start **(a)** and two-start **(b)** helices of filamentous actin, adapted from (Vahokoski et al., 2014). The pitch of the one-start helix is the distance between one monomer to the next in the one-start helix. The half-pitch is the distance that the filament requires to rotate 180°.

Actin protomers point to the same direction; in other words, actin filaments are polar; the ends are called barbed end (+) or pointed end (-) (Pollard & Cooper, 2009) **(Fig. 9)**. The transition of G-actin to F-actin involves a conformational change indispensable for polymerization. For the filament incorporation, the OD twists between 12-13° towards the ID with an axis nearly at the right angle to the helix axis. Additionally, SD2 is tilted towards SD4 by 10°. Finally, the monomer acquires a flat conformation, ~18° difference with respect to G-actin (Dominguez & Holmes, 2011; Fujii et al., 2010; Merino et al., 2018).

According to fiber diffraction data (Oda et al., 2009) and cryo-EM structures (Chou & Pollard, 2019) of canonical actins, the primary contacts between subdomains are along the long pitch strands than interstrand contacts. The contacts along the protofilament involve the SD2 (residues 61-65) and SD4 (residues 200-208 and 241-247) of the protomer n with SD1 and SD3 (residues 283-294) of the adjacent protomer (n-2). Recently, Chou & Pollard (2019) described that the primary lateral contact between protomers is the interaction of the D-loop (SD2, residues 40-50) of the n protomer with SD3 (n-2). Basically, the D-loop fits into the groove formed by the SD1 and SD3 (Oda & Maéda,

2010). The interactions between n and n-2 protomers specifically involve the residues 40-45 (SD2) with the w-loop located in the SD3 (residues 165-172) and residues R39, K61-R62 (SD2) with SD3 (D286, E167, D288). They also identify the interaction of the residue D244 (SD4) with R290 (SD3).

On the other hand, a flat protomer is required for interstrand interactions. The principal lateral contact between the long-pitch strands is an electrostatic interaction of the plug (262-273) in the n-1 (SD3) and the initial part of the D-loop (SD2) of the protomer n. The longitudinal contact residues from n protomer are 40-45 and 63-65 (SD2); and 166-171 and 285-289 (SD3) of n-2 are necessary for this interstrand interaction (Chou & Pollard, 2019; Dominguez & Holmes, 2011; Mannherz, 1992; Von Der Ecken et al., 2015) **(Fig. 9)**. Moreover, other contacts are a hydrogen bond of the backbone N of K113 of the protomer n-2 and the backbone O of E195 of the protomer n-1, and electrostatic interaction of their side chains (Chou & Pollard, 2019).

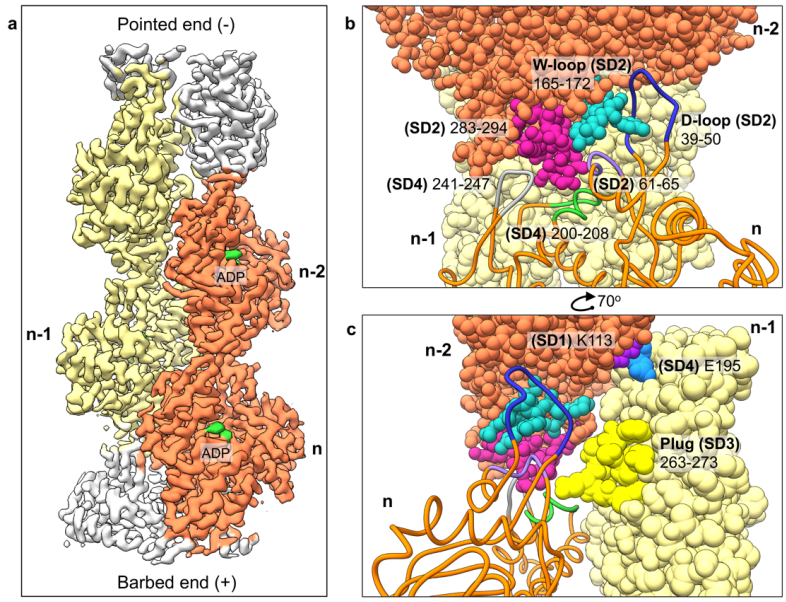

Figure 9. Canonical actin filament (PDB: 6DJO). **a.** Cryo-EM density map is depicted in different colors showing the helices. ADP-Mg^{2+} binding (green) (Chou & Pollard, 2019). **b.** Intrastrand and interstrand **(c)** interactions between protomers along the canonical actin filament.

1.6.2. Actin polymerization

Polymerization occurs by the transition of actin from G- to F-form, which involves the hydrolysis of ATP. Actin protomers bind ATP or ADP in the presence of Ca^{2+} or Mg^{2+}. The divalent cations associate with the β-and γ-phosphates of ATP, stabilizing its interaction with the protein (Kabsch et al., 1990). Actin hydrolyzes the terminal phosphate from the ATP and slowly releases the phosphate (Pollard & Cooper, 2009). *In vitro*, actin can be maintained in a globular form (G-actin) at low ionic strength in the presence of Ca^{2+}. At close to physiological conditions (100 mM KCl or 2 mM $MgCl_2$), actin polymerizes (Kühn & Mannherz, 2016).

Canonical actins polymerize by a nucleation/elongation mechanism. In a lower concentration, actin is in monomeric conformation. Dimers and trimers are very unstable; dimers dissociate at 10^6 s^{-1} and trimers at 100 s^{-1} (J A Cooper et al., 1983; Frieden, 1983). The polymerization is initiated when actin crosses the critical concentration (C_c). Above the C_c, an actin nucleus is formed by three or four monomers. Then, the filament elongates linearly. The C_c is the ratio of the dissociation (k_-) and association (k_+) rate constants. Low values indicate a higher affinity of the monomers to the filament; it is also the concentration of free monomers in the steady-state.

While the filament grows, the concentration of soluble actin monomer decreases until steady-state is reached. At steady state, actin monomers associate and dissociate at equal rates, and the length of the F-actin is constant; this process is called treadmilling **(Fig. 10)**.

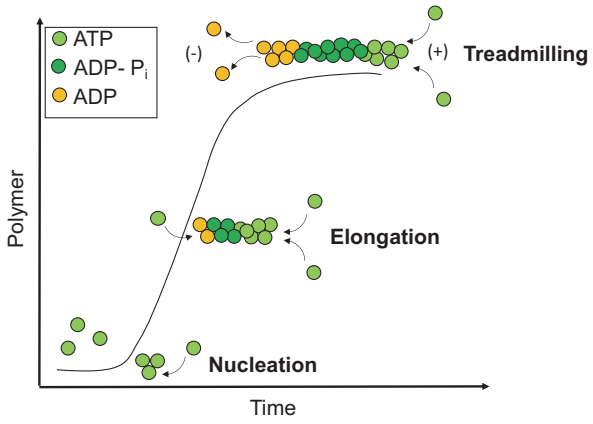

Figure 10. Nucleation-elongation mechanism. Scheme of actin polymerization over time. The polymerization occurs in three steps: nucleation, elongation, and treadmilling.

1.6.3. Polymerization kinetics

During the elongation phase, the barbed end grows much faster than the pointed end. At the barbed end, the C_c for rabbit skeletal muscle actin is 0.12 μM for ATP- and 1.8 μM for ADP-actin. At the pointed end, C_c values are higher, 0.34 μM and 2.28 μM, respectively **(Table 3)** (Fujiwara et al., 2007; Kuhn & Pollard, 2005).

In vitro, the k_+ for ATP-actin is higher ADP-actin at the barbed end (~9.5 μM^{-1} s^{-1} or ~3 μM^{-1} s^{-1}), and at the pointed end, the k_- is faster for ADP- (~0.26 s^{-1}) than for ATP-actin (~0.8 s^{-1}) **(Table 3)**. Because polymerization activates nucleotide hydrolysis, in the pointed end, ATP is already hydrolyzed to ADP + P_i and the dissociation of P_i is higher at this end because the affinity of P_i is ten times weaker than at the barbed end. Thus, the pointed end leads the depolymerization, while in the barbed end, ATP-actin and the polymerization are dominant (Drenckhahn & Pollard, 1986; Fujiwara et al., 2007; Kuhn & Pollard, 2005).

Nucleotide state	End	k_+ ($\mu M^{-1} s^{-1}$)	k_- (s^{-1})	C_c (μM)	Reference
Mg-ATP-actin	Barbed	11.6 ± 1.2	1.4 ± 0.8	0.12 ± 0.07	(Pollard, 1986)
	Pointed	1.3 ± 0.2	0.8 ± 0.3	0.62 ± 0.17	
Mg-ATP-actin	Barbed	7.5 ± 0.7	1.0 ± 1.2	0.13 ± 0.17	(Kuhn & Pollard, 2005)
	Pointed	0.66 ± 0.14	0.7 ± 0.2	1.06 ± 0.53	
Mg-ADP-actin	Barbed	3.8	7.2	1.9	(Pollard, 1986)
	Pointed	0.16	0.27	1.7	
Mg-ADP-actin	Barbed	2.9 ± 0.21	5.4 ± 0.14	1.8 ± 0.14	(Fujiwara et al., 2007)
	Pointed	0.09 ± 0.03	0.25 ± 0.04	2.8 ± 1.0	
Mg-ADP- P_i-actin	Barbed	3.4 ± 0.08	0.2 ± 0.1	0.06 ± 0.03	
	Pointed	0.11 ± 0.04	0.02 ± 0.02	0.18 ± 0.30	

Table 3. Summary of rabbit skeletal muscle actin rate constants.

The actin filament is not able to release ADP. Consequently, the depolymerization process releases actin monomers in the Mg-ADP state (Pollard, 2016). *In vivo,* this process occurs in the cytoplasm, and regulatory proteins mediate it. After the ADP is exchanged to ATP, the cycle starts over. Also, profilin binding promotes faster rates of filament turnover. The nucleotide exchange avoids defects in actin organization, cell growth, and fluid-phase endocytosis in actin from *Saccharomyces cerevisiae* (Wolven et al., 2000).

1.6.4. F-actin severing and stabilizing substances

Some commercial substances isolated from sea organisms or fungi have an effect on F-actin dynamics. The compounds can be divided into two groups: F-actin severing compounds and polymer stabilizers. The severing compounds like cytochalasins and latrunculins promote G-actin formation in different ways. While cytochalasins disrupt F-actin, latrunculins inhibit filament formation by binding to G-actin (Holzinger & Blaas, 2016). On the other hand, compounds like jasplakinolide (JAS), phalloidin, or chondramide promote and stabilize F-actin. JAS and phalloidin compete for the same binding site in actin filaments (Bubb et al., 1994). Both compounds bind at the interface of three actin

protomers (Heidecker et al., 1995). Nevertheless, JAS seems to stabilize filaments more effectively. Moreover, phalloidin has a limitation; it is membrane permeable only in hepatocytes (Wieland et al., 1984). Both compounds are extensively used in cell biology, biochemistry, and structural biology studies.

JAS affects actin nucleation. *In vitro*, JAS causes a dose-dependent decrease in the critical concentration of rabbit skeletal muscle actin (Bubb et al., 1994, 2000). *In vivo*, JAS triggers the accumulation of disorganized aggregates of F-actin in concentration and time dependence in different cell lines. For example, in prostate carcinoma cell lines, JAS disrupted actin filaments and altered the cellular architecture (Senderowicz et al., 1995). Also, at high concentrations of JAS, the F-actin concentrations increase adjacent to the plasma membrane while the stress fibers in smooth muscle cells decrease (Patterson et al., 1999).

1.6.5. Actin regulators

1.6.5.1. Actin binding proteins

In vivo, half of the total actin in cells is in G-form (~ 25-100 μM). These concentrations of actin are higher than the C_c. Why does the cell not contain a higher concentration of actin filaments? It is because actin interacts with many ABPs, which regulate the filament assembly or disassembly. Some of them participate in actin monomer sequestration, nucleation, filament barbed or pointed end capping, filament severing, nucleotide exchange, and filament cross-linking **(Table 4).**

Class	Name	Function
Nucleation	Arp2/3 [a]	Produce filament branches.
	Proteins with tandem WH2 [b]	Favoring the association of dimers or trimers.
	Formin [c]	Stabilizing dimers.
Sequestration	Thymosin $\beta 4$ [d]	Binds to the actin monomer in both ends, prevent the polymerization.
	Profilin [e, f, g]	Binds to the barbed end of the filaments. Prevent the nucleation and elongation only at the pointed end. Catalyze the exchange of ADP to ATP.
Severing	Cofilin [h, I, j]	Binds to the barbed end of the actin monomers or filaments. Inhibits nucleotide exchange. Sever actin filaments. Binds with a higher affinity for ADP-actin. Cofilin has a weak affinity to ADP-P_i-actin. Thus, it promotes dissociation of the γ-phosphate.
	Gelsolin [k]	Binds to the barbed end of the actin filaments. Sever actin filaments.
End capping	Capping [l]	Binds to the barbed end of the actin filaments and blocks the monomer addition.
	Gelsolin [k]	Capps the barbed end of actin filaments.
	Tropomodulin [m]	Capps the pointed end of skeletal muscle actin filaments.
	Arp2/3 [l]	Capps the pointed end of the former daughter filament after a branch of a mother filament is dissociated.
Cross-linking	Fimbrin [n, o]	Promote the formation of actin filament bundles.
	Filamin [n, o]	Connect less- organized networks of filaments.

Table 4. Representative regulators of canonical actin filaments. [a] (Rottner et al., 2010), [b] (Dominguez & Holmes, 2011), [c] (Pring et al., 2003), [d] (Marie France Carlier et al., 2007), [e] (Jégou et al., 2011), [f] (Courtemanche & Pollard, 2013), [g] (Ferron et al., 2007), [h] (Nishida, 1985), [i] (Cao et al., 2006), [j] (Blanchoin & Pollard, 1999), [k] (S Nag, 2013), [l] (Pollard, 2016), [m] (Rao et al., 2014), [n] (Matsudaira, 1994), [o] (Svitkina, 2018).

1.6.5.2. Post-translational modifications

One of the forms of actin regulation is post-translational modifications (PTMs). Around 45% of the amino acid sequence can be modified. PTMs include phosphorylation, ubiquitination, sumoylation, acetylation, ADP-ribosylation, arginylation, methylation, and oxidation (Terman & Kashina, 2013; Varland et al., 2019). Some of the PTMs interfere with polymerization; for example, ADP-ribosylation (Okamoto et al., 1997), the phosphorylation of a residue adjacent to the D-loop (Y53), or the oxidation of M44 (Hung et al., 2011). In contrast, the Nt-arginylation by ATE1 is required for the stability of long filaments (Saha et al., 2010).

The N-terminal actin maturation is also a process mediated by PTMs, it is caused by the successive actions of N-terminal transferases and

aminopeptidases. Fundamentally, the N terminus is acetylated (in actins class I by NatB or likely by NatA in actins class II), then the M is removed by an aminopeptidase. Finally, the N terminus is re-acetylated to produce mature actin (in actin class I by NAA80/NatH or presumably by NatA and NAA80 in actin class II) (Drazic et al., 2018; Van Damme et al., 2012; Varland et al., 2019; Wiame et al., 2018).

Some of the PTMs are involved in actomyosin interactions like acetylation by enhancing the negative charge of the N-terminal (Drazic et al., 2018) or S-glutathionylation of C374 appears to participate with the disassembly of the complex in β-actin (Fiaschi et al., 2006). The acetylation of K326 and K328 is involved in muscle contraction by modulating electrostatic interactions between F-actin, tropomyosin, and/or myosin (Viswanathan et al., 2015).

Another interesting PTM is the methylation of H73. This PTM is discussed deeply in **papers I** and **II**.

1.7. Actins from apicomplexan parasites

Actins from *Plasmodium* are among the most diverged actins in eukaryotes (Vahokoski et al., 2014). In apicomplexan parasites, filamentous actin is indispensable for motility and host cell invasion (Dobrowolski & Sibley, 1996). Unlike other apicomplexan parasites, including *T. gondii*, which have only a single actin isoform, there are two actin isoforms in *Plasmodium* (ActI and ActII). These isoforms share 79% of sequence identity (Heintzelman, 2015). On the other hand, mammals express six actin isoforms classified into two classes, class I belong to the non-muscle actins and class II, including vertebrate skeletal muscle actins (Kühn & Mannherz, 2016).

ActI is one of the components of the glideosome. It is the major isoform expressed during the entire parasite life cycle (Wesseling et al., 1989).

Experimental evidence shows the relevance of ActI in gliding motility. In *T. gondii*, parasites expressing a mutated ActI (G200M/K270M) delay their helical and circular movements. G200M/K270M mutations stabilize the actin filaments (Skillman et al., 2011). Likewise, ActI knockout in tachyzoites seems to disrupt the gliding motility but not wholly abolished it (Drewry & Sibley, 2015). Contrary to ActI, ActII is only expressed in male gametocytes (Deligianni et al., 2011) and the first mosquito midgut stages (female gametes, zygotes, and ookinetes). Additionally, ActII has an essential role during the sporogonic cycle (insect stages). The replacement of ActII by ActI showed that ookinetes were able to form oocysts. However, the oocysts were not able to release sporozoites. This study demonstrates that the function of ActII cannot be fulfilled by ActI (Andreadaki et al., 2014).

Furthermore, a proteomic study in *P. yoelii* found that ActII was detected in sporozoites located in the salivary gland (Lindner et al., 2013). Additional studies need to be done to understand the complete role of ActII in *Plasmodium*. This evidence shows that *Plasmodium* actins have specific functional roles in different stages of the parasite's life cycle.

1.7.1. Polymerization of apicomplexan actins

In apicomplexan parasites, actin polymerization is fundamental for gliding motility (Heintzelman, 2006; Meissner et al., 2013). Contrary to canonical actins, which readily form many long filaments (~1-30 µm *in vitro*; Sept et al., 1999), *Plasmodium* actins form few long filaments. *In vivo* experiments have not been successful in observing actin filaments readily. Globular and filamentous actin have been detected in a ratio of 1:2 in merozoites (Field et al., 1993). However, no distinction was made between the isoforms ActI and ActII. In contrast, actin in *T. gondii* seems to be globular (Dobrowolski et al., 1997). Furthermore, Schmitz and co-workers (2005) demonstrated that *Plasmodium* ActI forms short filaments like actin from *T. gondii* (Sahoo et al.,

2006) with an average length of ~100 nm in merozoites. Even though actins are remarkably conserved, the differences in the amino acid sequence of apicomplexan actins can explain the instability of the filaments (Pospich et al., 2017).

In vitro, kinetic studies have focused on *Pf*ActI and *Tg*ActI. There are two mechanisms of polymerization proposed for apicomplexan parasites. Skillman and co-workers (2013) reported an isodesmic polymerization mechanism for *Tg*ActI. In contrast, *Pf*ActI follows the classical nucleation-elongation model, like canonical actins (Kumpula et al., 2017). Further information on this is discussed in **paper II**.

1.7.2. *Plasmodium* spp. actin regulators

Contrary to canonical actins, which have around 160 ABPs identify so far (Kühn & Mannherz, 2016), Apicomplexan organisms have a limited set of actin regulators, about 10. This set includes profilin (PRF), coronin (COR) and capping proteins (CPs), cyclase associate protein (CAP), formin (FRMs), and cofilin or actin-depolymerizing factors (ADFs) (Frénal et al., 2020; Gordon & Sibley, 2005).

Apicomplexan parasites lack the Arp2/3 complex, which is one of the major regulators of actin dynamics. Instead, *T. gondii* owns three formins (FRM1, FRM2, and FRM3) and *Plasmodium* two (FRM1 and FRM2). FRMs interact with the F-actin barbed end and act as a nucleator (Baum et al., 2008). In *Plasmodium*, the central role of PRF and ADF1 or ADF2 is to maintain a large G-actin pool; both proteins sequester actin monomers and therefore prevent the polymerization (Moreau et al., 2017; Schüler et al., 2005). Besides, ADF2 can bind to F-actin, severing the actin filaments (Singh et al., 2011). However, ADF2 is exclusive for *Plasmodium*; *T. gondii* only codifies for ADF1 (Frénal et al., 2020). Another protein that contributes to filament disassembly is CAP by exchanging ADP for ATP during sporogony (Hliscs et al., 2010; Makkonen et

al., 2013). The CPs and COR regulate the length of the filaments. Apparently, the function of the CPs is to stop the addition of monomers to the barbed end, whereas COR increases the polymerization and facilitates the formation of parallel filament bundles (Ganter et al., 2009; Olshina et al., 2015; Salamun et al., 2014). The dynamics of assembly and disassembly of actin filaments regulated by the ABPs are crucial for the parasite survival, division, and motility at different stages of its life cycle (Frénal et al., 2020).

2. Aims of the study

In the *Plasmodium* sequence database (PlasmoDB), there are six different genes encoding myosins: MyoA (class XIVa), MyoB, and MyoE (class XIVc), MyoF (class XXII), and MyoJ and MyoK (class VI). Currently, there is no structural information on any of these, except for MyoA. Also, there are two different actin isoforms with structural and biochemical differences. This work hypothesizes that the actomyosin motors, which are essential during the different stages of the parasite, likely differ in force production mechanisms, e.g., the speed and processivity along the actin filaments. Likewise, differences in the filament structure and polymerization of *Plasmodium* actins could have a role in determining the speed of the different actomyosin motors.

Some of the research questions, which I discuss in this thesis are:

- What are the structural differences between *Plasmodium* actins?
- What are the differences in the polymerization properties of *Pf*ActI, *Pf*ActII, and canonical actins?
- How are the interactions of the different myosins with actin filaments?
- How are these proteins involved in parasite motility and other fundamental cellular functions?

The main objective of my PhD thesis was to characterize the molecular structure and the function of *Plasmodium* actin I, actin II, MyoA, MyoJ, and MyoK. Specifically, I aimed to:

- Obtain a high-resolution cryo-EM structure of *Pf*ActII in the presence and absence of the filament-stabilizing macrolide jasplakinolide (JAS).
- Compare the polymerization properties and the filament structure of *Pf*ActII to those of *Pf*ActI.
- Obtain a high-resolution cryo-EM structure of *Pf*MyoA in complex with the light chains and decorated *Pf*ActI filament.
- Characterize *Plasmodium* class VI myosins.

3. Materials and methods

The following chapters describe the methods to prepare and characterize *Plasmodium* actins, MyoA, and the class VI myosins. Only experiments performed by the author of this thesis are presented in detail.

3.1. Eucaryotic system expression

Considering that *Plasmodium* is a eucaryotic organism, and the recombinant proteins of the study require post-translational modifications and assistance in folding by co-expression with chaperones, all the proteins were expressed in a Multibac baculovirus system, which as well is adapted to co-express multiprotein complexes like the actomyosin motors.

In general terms, the gene encoding for a protein of interest is inserted into a baculovirus transfer vector under the transcriptional control of the polyhedrin promoter (p10). Afterwards, it is integrated into the Multibac baculovirus into this Tn7 site. A bacterial artificial chromosome (BAC) is present in *E. coli* cell lines like DH10multiBac, DH10MB, or the EMBacY cells. Finally, the recombinant baculovirus is usually produced in Sf9 or Sf21 from *Spodoptera frugiperda* host cell lines. During the very late phase of infection, the inserted protein is expressed under the control of the polyhedrin gene promotor (Chambers et al., 2018; Jarvis, 2009; Sari et al., 2016). Additionally, the baculovirus transfer vectors are designed to assemble many multigene expression cassettes by fusion of the LoxP site of a donor and an acceptor vector using Cre recombinase (Sari et al., 2016).

3.1.1. Cloning and expression of myosins class VI

Additional work in this thesis was the characterization of *Pf*MyoJ and *Pf*MyoK. However, more experiments need to be done in the future for publication.

Preliminary results are compiled in chapter 4.4, titled "*Plasmodium* class IV myosins".

Four constructs for *Pf*MyoJ and *Pf*MyoK removing parts of the C terminus were designed and cloned into pFASTBac I vector with a GFP and Strep tag in the N and C termini of the protein. *S. frugiperda* codon-optimized parasite MyoJ and MyoK (Invitrogen GeneArt) constructs were cloned into the pACEBacI vector using sequence and ligation–independent cloning (SLIC) (Li & Elledge, 2012). All the constructs were verified by sequencing. Plasmids were transformed into DH10 MultiBac *E. coli* strain (Geneva Biotech). After BAC DNA isolation, the samples were confirmed by PCR.

The bacmids were transfected into *Sf*9 cells using the FuGENE 6 transfection reagent (Promega). Initially, virus 0 was produced. To produce the virus 1, 5 μL of virus 0 was added into $1X10^6$ *Sf*9 cells/ml in 50 ml of insect cell medium (Sf-900 II SFM, Gibco). The supernatant was collected 2 days after proliferation arrest (DPA). The expression was tested measuring the GFP fluorescence.

3.1.1.1. Cloning of polyproteins

Polyprotein constructs were designed and used to identify the interacting light-chains of class VI myosins by co-expressing these together with MyoJ or MyoK and identify possible protein-protein interactions. Essentially, the polyprotein is a long polypeptide that contains individual proteins spaced by a proteolytic cleavage site (tcs). Tobacco etch virus (TEV) NIa protease processes the polyprotein by cleaving corresponding cleavage sites (tcs), consequently liberating the individual proteins (Bieniossek et al., 2012; Sumitra et al., 2011). Polyproteins can be used as a strategy to study protein complexes and to balance the expression levels of each protein in insect cells by a TEV NIa (Nie et al., 2014).

S. frugiperda codon-optimized polyproteins (Invitrogen GeneArt) were cloned into a pIDS vector using SLIC. All constructs contained the same expression cassette, which encompasses a polyhedrin promoter followed by the gene encoding for NIa protease from tobacco etch virus (TEV) for subunit liberation. Between 3 or 4 putative myosin light chains spaced by the TEV NIa protease cleavage site (tcs) and a flexible linker were inserted between BstEII and RsrII restriction endonuclease sites, followed by a His-tag sequence. Finally, a gene encoding for a red fluorescent protein (mCherry) was included to monitor the polyprotein expression **(Fig. 11a)**.

Multiprotein complexes were produced by the fusion of myosins, which are in an acceptor vector, and the polyproteins in a donor vector using Cre-lox recombination **(Fig 11b)**. If any of these light chains interact with the myosins, we expect to obtain a folded protein **(chapter 4.4)**.

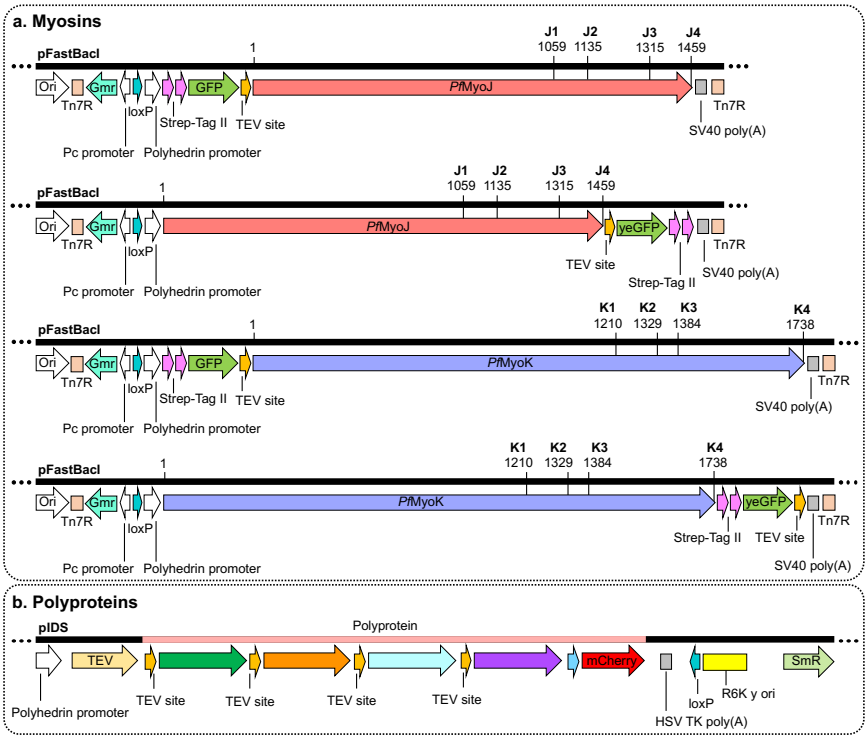

Figure 11. Representation of *Plasmodium* myosin and polyprotein constructs **a.** Myosins **b.** Polyproteins.

3.1.1.2. Buffer screening for class VI myosins

*Sf*9 cells were infected with *Pf*MyoJ or *Pf*MyoK and the chaperones (Unc45 and Hsp90). Pellets of 1.3 $X10^6$ cells were resuspended in 200 µL of the corresponding lysis buffer. To determine the optimum lysis buffer, different conditions were tested **(Table 5)**. Cells were disrupted by freeze-thawing using liquid nitrogen, then the samples were centrifuged, and the supernatant was used to measure the GFP signal using a TECAN plate reader using an excitation wavelength of 488 nm and emission wavelength of 509 nm. The GFP signal was visualized in an SDS-PAGE **(chapter 4.4)**.

Buffer	20 mM HEPES			20 mM Tris HCl			20 mM CHES			20 mM CAPS	20 mM MOPS	PBS
pH	7	7.5	8	7.5	8	8.5	8.5	9	9.5	9	7	7.4
NaCl/KCl	0-750 mM											

Table 5. Solubility screening for *Plasmodium* class VI myosins. 10 mM $MgCl_2$, 0.5 mM TCEP, 1 mM ATP, 1X SIGMAFAST protease inhibitor cocktail were added in all the conditions.

3.1.2. Expression of *Plasmodium* actins

The expression of *Plasmodium* actins was performed using a modified protocol based on Ignatev et al., 2012. *S. frugiperda* codon-optimized *Pf*ActI and *Pf*ActII (Invitrogen GeneArt) were synthesized and cloned into the pFastBac HT A vector. To follow the expression of the proteins, EMBacY cells were used. This cell line contains a constitutively expressing YFP expression cassette to monitor the expression levels by fluorescence **(Fig. 12)**.

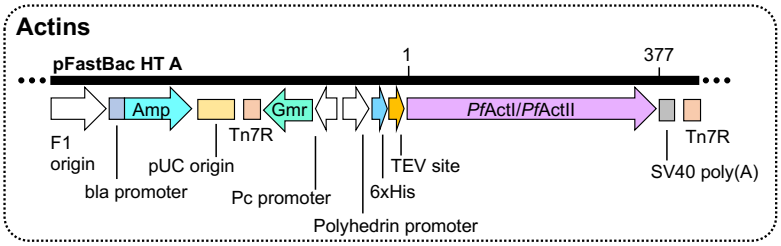

Figure 12. Representation of *Plasmodium* actin constructs.

3.2. Protein purification

3.2.1. Affinity chromatography

Affinity chromatography is a standard method to separate a protein from a mixture. Usually, the proteins of interest are tagged with a molecule like a peptide, protein, antibody, etc., which is attached covalently to the immobilized ligand (Rodriguez et al., 2020). In this study, two different stationary phases were used. *Pf*Myosins were purified using a Strep-Tactin XT superflow column (IBA). The proteins were tagged with Strep-tagII, a short peptide that binds to a modified streptavidin (Strep-Tactin resin). The *Pf*Actins were tagged with a polyhistidine (6xHis) sequence, which binds to the Ni^{2+} column.

3.2.2. Size exclusion chromatography

Size exclusion chromatography (SEC), is a fundamental technique in protein biochemistry. It has been used to separate molecules based on their hydrodynamic dimensions or the relative size with respect to the average pore size of the matrix (Barth et al., 1994). The SEC column is composed of a matrix of beads that contain pores of a particular size. Small molecules enter the beads and take more time to be eluted than large molecules. Depending on the cutoff size of the column (referring to the size of the larger molecule that can enter the beads), species of molecules larger than the cutoff size will not interact with the beads and are eluted in the void volume (volume of the column that is not occupied by the matrix) (Burgess, 2018; Duong-Ly & Gabelli, 2014).

There are three primary applications for SEC. First, it can isolate one or more components of a sample like degradation products, additional contaminants, soluble aggregates, or different oligomeric states of a protein. SEC is commonly used as the last step of protein purification after the protein is partly purified by another chromatography technique. Second, the SEC is ideal for buffer exchange, desalting, and protein refolding. Finally, SEC allows for

estimating the mass and the oligomeric stated states of a protein in solution using analytical SEC. Essentially, the systems can be coupled to highly selective detectors like multi-angle laser light scattering (SEC-MALS) to obtain the absolute molecular weight of a protein, normalizing the value of the scattered signal and the protein concentration. Other detectors can be used like mass spectrometers, photodiode arrays (DAD), or fluorescence detectors (Burgess, 2018; GEHealthcare, 2018). In this study, the SEC was used as the last step of protein purification to obtain a high grade of purity and monodisperse samples.

3.2.3. *Plasmodium falciparum* myosin purification

3.2.3.1. Class VI myosins

Buffer, pH, and salt were varied for each construct according to the buffer screening results. For *Pf*MyoK, co-expressed with the chaperones and with some of the polyproteins, it was not possible to obtain a soluble and folded protein.

The next purification protocol corresponds to *Pf*MyoJ co-expressed with the chaperones or with the polyproteins. The *Pf*MyoJ pellet was resuspended in 30 ml of lysis buffer (20 mM Tris-HCl pH 7.5, 0.5 mM ATP, 5 mM $CaCl_2$, 10 mM $MgCl_2$, 750 mM KCl, 1 mM TCEP, 1 mM EDTA, and 5% trehalose-dehydrated) and 1x Sigma Fast protease inhibitor. Cells were disrupted by sonication on ice. The cell lysate was centrifuged at 47,850 g, 1 h, at 4°C. The protein of interest was purified using 1 ml Strep-Tactin XT high capacity column (IBA). The column was equilibrated with lysis buffer.

To avoid unspecific biotin-binding from the cell lysate, 0.75 mg of avidin was added to the supernatant. Then, the supernatant was then loaded into the column. The column was then washed with 10 ml of wash buffer (20 mM Tris-

HCl pH 7.5, 0.5 mM ATP, 2 mM $CaCl_2$, 5 mM $MgCl_2$, 350 mM KCl, 1 mM TCEP, 1 mM EDTA, and 5% trehalose- dehydrated) and 10 ml of wash buffer 2 (20 mM Tris-HCl pH 7.5, 0.5 mM ATP, 2 mM $CaCl_2$, 2.5 mM $MgCl_2$, 150 mM KCl, 1 mM TCEP, 1 mM EDTA, and 5% trehalose- dehydrated).

*Pf*MyoJ was eluted in 3 ml of elution buffer (20 mM Tris-HCl pH 7.5, 0.5 mM ATP, 2 mM $CaCl_2$, 2.5 mM $MgCl_2$, 1 mM TCEP, 1 mM EDTA, 5 % trehalose-dehydrated and 50 mM d-Biotin). Eluted fractions were concentrated to 0.1ml (UFC905024, Millipore). The elution was running in an SDS-PAGE, and the fluorescence of GFP was tested before staining the gel. Because the protein concentration after affinity chromatography was low, SEC was not performed **(chapter 4.4)**.

3.2.3.2. Myosin A

MyoA co-expressed with the chaperones (Unc45 and Hp90), and the light chains (ELC, MTIP) were purified using the protocol from (Green et al., 2017) for structural biology experiments **(paper III)**.

3.2.4. *Plasmodium* actin purification

The purification of *Plasmodium* actins was performed using a modified protocol from Ignatev et al., (2012). Ammonium acetate was added to all the buffers to prevent oligomerization/polymerization (Kumpula et al., 2019).

3.2.4.1. Actin I

The *Pf*ActI pellet was resuspended in a lysis buffer (10 mM HEPES pH 7.5, 1 mM ATP, 5 mM $CaCl_2$, 7 mM β-mercaptoethanol, 5 mM imidazole, 250 mM NaCl and 300 mM ammonium acetate). Cells were disrupted by sonication on ice. The cell lysate was centrifuged at 47,850 *g*, 1h, at 4 °C.

*Pf*ActI was purified by affinity chromatography using Ni/NTA resin (Thermo Scientific). The column was equilibrated with lysis buffer 1. The supernatant was then loaded into the column, and it was washed with 30 ml of lysis buffer 1. The column was then washed three times with 40 ml of wash buffer 1A (10 mM HEPES pH 7.5, 1 mM ATP, 5 mM $CaCl_2$, 3 mM β-mercaptoethanol, and 300 mM ammonium acetate). Each wash contained different imidazole concentrations (15 to 25 mM) and NaCl (250 to 500 mM). Finally, the protein was washed with 40 ml of elution buffer 1 (10 mM HEPES pH 7.5, 0.5 mM ATP, 0.2 mM $CaCl_2$, 3 mM β-mercaptoethanol and 300 mM ammonium acetate). *Pf*ActI was eluted in 3 ml of elution buffer 1 and 350 mM imidazole.

The *Pf*ActI K270M, A272W, and H74Q mutants were purified using the same protocol as for wild-type *Pf*ActI **(paper I)**.

3.2.4.2. Actin II

For *Pf*ActII, a similar procedure to *Pf*ActI was used with some modifications. The *Pf*ActII pellet was resuspended in lysis buffer 2 (10 mM CHES pH 8.7, 1 mM ATP, 5 mM $CaCl_2$, 3 mM β-mercaptoethanol, 10 mM imidazole, 250 mM NaCl and 300 mM ammonium acetate). Further washing steps were done with high NaCl concentrations. The first wash was 50 ml of lysis buffer 2. The column was then washed two times with 50 ml of wash buffer 2 (10 mM HEPES pH 7.5, 0.5 mM ATP, 5 mM $CaCl_2$, and 300 mM ammonium acetate), 10-15 mM imidazole and 250-500 mM NaCl. Afterwards, the column was extensively washed with 100 ml wash buffer 2, 20 mM imidazole, and 1M NaCl. Finally, the protein was washed with 50 ml of elution buffer 2 (10 mM HEPES pH 7.5, 0.5 mM ATP, 0.2 mM $CaCl_2$, 1mM β-mercaptoethanol and 300 mM ammonium acetate). *Pf*ActII was eluted in 3 ml of elution buffer 2 and 350 mM imidazole **(paper II)**.

3.2.4.3. Protease digestion

The histidine tag was cleaved with Hexa-histidine-tagged tobacco etch virus (TEV) protease and dialyzed in G-buffer (10 mM HEPES pH 7.5, 0.5 mM ATP, 0.2 mM $CaCl_2$ and 0.5 mM TCEP) and 300 mM ammonium acetate overnight for both actins. After digestion, the proteins were loaded into the Ni/NTA column and washed with 10 ml G-buffer containing 300 mM ammonium acetate and 10 mM imidazole. The eluted proteins were concentrated (30,000 MWCO concentrator, Amicon Ultra-4 UFC803096 Millipore) and ultracentrifuged for 30 min at 100,000 *g*. The supernatant was collected and filtered (PVDF 0.22 μm UFC306V00). As the final step, SEC was performed using Superdex 200 Increase 10/300 GL column (GE Healthcare Life Sciences) equilibrated with G-buffer and 300 mM ammonium acetate.

3.2.5. Purification of pig skeletal muscle α-actin

Pig skeletal muscle α-actin was used as a seed for polymerization assays. The protein stored in acetone powder was purified according to standard methods and stored at 4 °C in a dialysis bag for a maximum time of a month (Doolittle et al., 2013; Hertzog & Carlier, 2005) (**paper I and paper II)**.

3.3. *Plasmodium* actin biochemical assays

The biochemical assays were performed to characterize *Pf*ActII and compare its isoform **(paper II)**. Besides, polymerization assays were performed for **paper I** to study the polymerization properties of wild-type *Pf*ActI and the K270M, A272W, and H74Q mutants. Before to perform the biochemical assays, the ammonium acetate was removed from the *Plasmodium* actins using PD SpinTrap G-25 columns (GE Healthcare) equilibrated with G-buffer.

3.3.1. Actin pyrene labeling

One of the standard methods to study actin biochemistry is using fluorescence. Labeling actin with N-(1-pyrene)iodoacetamide (here we referred to as pyrene), it is possible to follow the signal of the filament formation (Kouyama & Mihashi, 1981). Near the C terminus, on the surface of the protein, actin has a cysteine residue (C374 in canonical actins and C375 in *Plasmodium* actins), which is accessible for modification. Pyrene is attached covalently to the thiol group of the cysteine of G-actin. The emitted intensity of pyrene increases proportionally upon polymerization (Adamek & Geeves, 2014; John A. Cooper et al., 1983; Doolittle et al., 2013).

In this work, actin was labeled with pyrene for the polymerization and depolymerization assays as well as for the C_c curves. Pyrene labeling was performed using the modified protocol described by Kumpula and colleagues (2017). One-third of the *Plasmodium* actins were labeled with pyrene (Life Technologies, Invitrogen, Eugene, OR) in a ratio of concentration 1:1 of actin and pyrene. The samples were incubated for 5 min. 100 µM of 1,4-dithiothreitol (DTT) was added to stop the reaction. Afterward, two-thirds of unlabeled actin was mixed with the labeled protein (Kumpula et al., 2017). Finally, ammonium acetate was removed by desalting before performing the biochemical assays.

3.3.2. Polymerization assay

The assay was performed as described before in Kumpula et al., (2017). Two types of polymerization assays were done. The first one is the typical polymerization assay. The three phases; nucleation, elongation, and steady state, were measured. Whereas a polymerization assay using polymerize muscle α-actin as a seed only allows seeing the last two phases; the elongation and steady-state. The polymerized muscle α-actin acts as the stable nuclei to start the polymerization from the elongation phase.

The reaction mixture contained 50 µl *Plasmodium* actin in G-buffer with final concentrations between 0 to 7 µM, respectively. The reaction started by adding 100 µL of 1x F-buffer (4mM MgCl, 50 mM KCl and 10mM EGTA pH 8). The final volume of the reaction was 150 µl. For nucleated polymerization assays, muscle α-actin was added to the reaction mixture at a final concentration of 0.5 µM.

The fluorescence of nucleated and non-nucleated polymerization assays was monitored for 2 h for *Pf*ActI and *Pf*ActII at 20°C. Measurements were carried out in a Tecan Spark 20M multimode microplate reader using black 96-well plates (Greiner), λex = 365 nm (9 nm bandpass) and λem = 407 nm (20 nm bandpass), 5 flashes per measurement and 5 s of orbital mixing step at 216 rpm before commencing the measurements. The baseline of polymerization curves was corrected and normalized against the maximum value of *Pf*ActI or *Pf*ActII in GraphPad Prism 9.

3.3.3. Depolymerization assay

Depolymerization of *Plasmodium* actins was induced by the dilution of polymerized actin. 5 µM actin was labeled with 30% pyrene and polymerized in 1x F-Buffer overnight as described in 3.3.2. F-Actin was diluted at different concentrations, and the reaction started with the addition of 1x F-Buffer. The fluorescence was monitored for 10 min using the same conditions as the polymerization assay, the mixing step was omitted to reduce dead times (Kumpula et al., 2017). The data were fitted using the one-phase decay equation in GraphPad Prism 9:

$$Y=(Y0 - Plateau)*exp(-K*X) + Plateau$$

Where Y0 is the first Y value, the plateau is the Y value, K is the rate constant and that is expressed in reciprocal of the X-axis time units (seconds).

3.3.4. Critical concentration

The critical concentration (C_c) is defined as the concentration in which actin starts to polymerize. After that point, the absolute fluorescence signal values of different polymerized actin concentrations fit in a linear slope.

Different concentrations of *Plasmodium* actins were polymerized, as described before. The fluorescence was then measured from triplicate samples after 1 hour and 20 hours at 4°C. The plate reader and the optical settings were the same as in the polymerization assays. The results were fitted using a segmental linear Equation and 1/Y2 weighting in GraphPad Prism 9:

1. Y1 = intercept1 + slope1*X
2. YatX1 = slope1*X1 + intercept1
3. Y2 = YatX1 + slope2*(X – X1)
4. Y = IF(X<X1, Y1, Y2)

The first line of the equation corresponds to the first line segment. The second line of the equation calculates the Y value of the first regression when X=X1. The third line estimates the second regression segment. Since it is a continuous line, X1 is the X value where the two line segments intersect. The Y value at any other position along the second segment equals YatX1, plus the increase due to the second regression line. The final line defines Y for all values of X.

3.3.5. Sedimentation assay

Sedimentation assays are typically used to quantify the percentage of filamentous actin. Differential centrifugation is used to sediment the actin filaments. Simultaneously, the monomer form remains in the supernatant, then the sample is analyzed by SDS-PAGE or directly using an analytical ultracentrifuge. This technique is also useful for studying actin-binding proteins,

as it is well-known, actin filaments are regulated by ABPs, co-sedimentation of ABPs and F-actin, allowing the study of protein-protein interactions (Heier et al., 2017). For the thesis, sedimentation assays were performed to quantify the percentage of F-*Pf*ActI and F-*Pf*ActII at different pHs and in the presence of JAS. *Pf*Actins were polymerized overnight at 4 ºC in 1X F-Buffer (4 mM $MgCl_2$, 50 mM KCl, 1 mM EGTA pH 8), the final protein concentration was 4 µM in 100 µL of the reaction mixture. Samples were ultracentrifuged at 435000 *g* for 1 hour at 4 ºC. The supernatant and the pellet fractions were separated. The pellet was resuspended in an identical volume of the supernatant fraction. Samples were analyzed using sodium dodecyl sulphate–polyacrylamide gel electrophoresis (SDS-PAGE).

3.3.6. Mass spectrometry

Peptide mass fingerprinting (PMF) is a common strategy to identify unknown proteins, for example, from SDS-PAGE gel. Essentially, the protein gel band is destained, dried, and digested with trypsin that cleaves specifically after Arg and Lys residues when these are not followed by a Pro. The masses of the tryptic peptides are analyzed using a matrix-assisted laser desorption/ionization protein (MALDI-TOF). Then, the masses and the abundance of the tryptic peptides are used as a query to compare against the predicted mass values from in silico digestion of all the protein sequences in a given database (Hjernø, 2007; Rajawat & Jhingan, 2019).

Liquid chromatography couple with mass spectrometry (LC-MS) is very useful for determining the accurate mass measurements of full-length proteins, protein components of analytical experiments. This method uses protein in solution which is separated by LC technique such as ultra-performance liquid chromatography (UPLC). Then, the sample is identified by mass spectrometry, where the protein is further separate by their mass to charge ratio (m/z) before fragmentation (Tuli & Ressom, 2009). In this study, the cofilin from *Sf*9 cells

(paper II) and *Pf*MyoJ **(chapter 4.4)** was confirmed by MS using protein in solution and SDS-PAGE gel pieces**.** Also, the molecular weight of *Pf*ActII **(paper II)** was determined by ESI-LCMS.

3.3.7. Dynamic light scattering

Dynamic light scattering (DLS) or photon correlation spectroscopy (PCS) is a powerful method to study the diffusion behavior of particles in solution. This technique is convenient to study the homogeneity of proteins and protein complexes. Particles are in constant random thermal motion, called the Brownian motion. The speed of the diffusion is related to its size, solvent viscosity, and temperature. The diffusion speed of a particle is measured by a monochromatic laser light, which shot the particles in solution. The obtained scatter intensity of a particle at a specific angle fluctuates over time which is used to generate the autocorrelation function. Thus, based on the autocorrelation function and the Stokes-Einstein equation, the particle hydrodynamic diameter can be calculated (Maguire et al., 2018; Tatkiewicz et al., 2015).

DLS was performed to analyze the *Plasmodium* actin oligomeric state before and after polymerization and in the presence and absence of JAS **(paper II)**. The samples at 1.3 mg/ml were measured using the Zetasizer Nano ZS (Malvern Instruments) in a final volume of 70 µl at 4°C.

3.3.8. Gel electrophoresis

SDS-PAGE is a fast, sensitive method to analyze proteins under desaturating conditions. Essentially, denatured proteins with a net charge are separating by size in a solid support (polyacrylamide gel) in an electric field. It is a standard technique to verify a large variety of experiments like the purity of the protein after purification, to identify degradation, a protein-protein interaction (e.g. after

cross-linking), contaminants, and to quantify protein bands (Jeremy et al., 2002).

Another type of electrophoresis is the gel electrophoresis in native conditions (Native-PAGE), without any denaturing agent like detergents or reducing conditions. In contrast to the SDS-PAGE, Native-PAGE allows identifying different protein oligomer forms. Native-PAGE electrophoresis was used to determine the globular and filament states of *Plasmodium actins* **(paper II).**

3.4. Structural biology experiments

3.4.1. Electron microscopy

Transmission electron microscopy (TEM) is a powerful method to characterize the structure of biological samples at an atomic level. TEM operates with the same principles as light microscopy, but uses electrons instead of photons to visualize structures smaller than the wavelength of light. Fundamentally, a beam of electrons accelerated by an electron gun is focused on the sample. The transmitted electron wave is collected by electromagnetic objective lenses, which deflect the scatter signal to form images (Mitome, 2018; Reimer & Kohl, 2008).

In biological samples, the scattering contrast of the images can be increased by staining the sample. Negative staining allows to visualize small proteins and determine their oligomeric state. The protein is fixed in a tiny support called EM grid. It is then embedded in a heavy metal salt layer like uranyl acetate or phosphotungstic acid, ammonium molybdate, etc. The stain is surrounding the sample. While the electron beam can pass through the low electron density of the sample, it cannot pass through the heavy ions producing a phase-contrast where the sample is observed in a dark background (Fender et al., 2014).

In this thesis, TEM was performed to visualize *Plasmodium* actin filaments in **paper I** and **paper II**. *Pf*Actins at 20 µM were polymerized in F-buffer at 4°C for 16 h. The proteins were applied on carbon-coated 200 mesh Cu-grids (Electron Microscopy Sciences) at a final concentration of 1 µM. Grids were then washed twice with one drop of F-buffer. Subsequently, the samples were stained with 2% uranyl acetate. The excess of stain was removed from one edge of the grid using filter paper. Grids were imaged under a Jeol JEM-1230 microscope. Images were analyzed using the Ridge Detection plugin available in ImageJ 2.0.0 software (Steger, 1998). The calculated length measurement for any given filament corresponds to the portion that lies within a given frame and, therefore, cannot be used as a measurement of the actual length of the filaments.

3.4.2. Cryogenic electron microscopy

Cryogenic electron microscopy (cryo-EM) allows for determining the structures of monodisperse macromolecular assemblies imaged at cryogenic temperatures using a transmission electron microscope. The single-particle cryo-EM technique is used to determine the structure of proteins and protein complexes that cannot solve using conventional crystallographic approaches, such as membrane proteins, eukaryotic spliceosomes, large proteins, or protein structures like actin filaments (Lyumkis, 2019; Nogales, 2015). One of the advantages of cryo-EM is that only small amounts of monodisperse samples are required. Also, it is possible to determine different conformations of proteins or complexes. Vitrification is the method used for sample preparation; the protein in solution freezes under liquid ethane. Due to the fast decrease of temperature, it does not have time to crystalize. The buffer turns vitreous, and the sample maintains a near-native state (Lyumkis, 2019). Therefore, within the ice layer there are copies of the same particle in different orientations and possible conformations, known as rigid-body movements of a single object (Frank, 2002).

The EM grid has to be stored in cryogenic conditions, as well during the data collection. The electron-detection cameras or direct detectors have been essential for reconstructions with atomic resolution. This detector has little or no noise, which results in high contrast images, so contrast-enhancing agents in the samples are not needed since the contrast of the images are generated by the electron scattering from the atoms within the sample itself (Lyumkis, 2019; Nogales, 2015). The images from cryo-EM are 2D projections of the object collected as movie frames. The 3D reconstruction is obtained by merging the data collected from thousands or millions of projections of the particles in different orientations (Frank, 2002; Glaeser, 2019).

The cryo-EM experiments **(paper II and III)** were carried out through collaboration. The grid preparation and data collection of *Pf*ActI, *Pf*ActII, and *Pf*MyoA in complex with ELC and MTIP were performed by Dr. Lesley J. Calder and Dr. Peter B. Rosenthal at the Structural Biology of Cells and Viruses Laboratory, Francis Crick Institute, London, UK. Dr. Juha Vahokoski carried out the reconstruction of the density map. The protein purification of *Pf*ActI, *Pf*ActII, and *Pf*MyoA and the atomic model building and refinement of *Pf*ActII was my contribution **(Fig. 13)**.

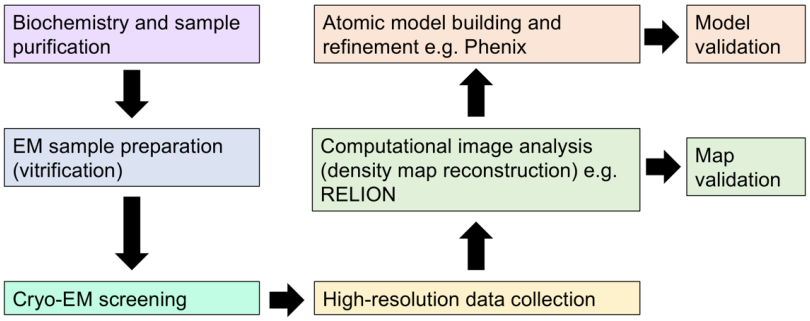

Figure 13. General workflow for single-particle cryo-EM analysis. Redrawn and adapted from (Lyumkis, 2019).

3.4.2.1. Atomic model building and refinement

The atomic model of *Pf*ActII was built from the cryo-EM structure of *Pf*ActI (5OGW) (Pospich et al., 2017) using the mutation tool from Coot 0.9-pre (P Emsley, 2010), it was placed in the density map using Chimera 1.14 (Pettersen et al., 2004). Namdinator was used to fit the initial atomic model to the density map and correct the geometry of the model (Kidmose et al., 2019). The refinement was carried out for several rounds in reciprocal space with Phenix 1.19.2 (Liebschner et al., 2019).

3.4.2.2. Structure analysis

The figures and videos of the structures were generated in Chimera 1.14 (Pettersen et al., 2004) and ChimeraX 1.2.5. The mass centers of the subdomains were calculated in Pymol v1.7.4, and the distances d2-4, b2, and the θ angle were calculated with Chimera 1.14. The rise (translation) and twist (rotation) for the helices were computed with Chimera 1.14 using two adjacent subunits (match showMatrix command). The electrostatic potentials and hydrophobicity surface were generated in Chimera 1.14. The density map was segmented using ChimeraX 1.2.5 (Goddard et al., 2018).

4. Results

4.1. Paper I

This paper describes in atomic detail the *Plasmodium falciparum* actin I polymerization. ATP hydrolysis during polymerization was studied using high-resolution crystallography and biochemical assays. We found that the switching of Arg178/Asp180-containing A-loop between two conformations (1a/b and 2a) is related to the short length of *Pf*ActI filaments **(Paper I, Fig 3)**. To probe the effect of residues in or around the A-loop on filament stability, three mutants (K270M, A272W, and H74Q) were constructed. In addition to the crystal structures, the P_i release rate was measured for all of the actin mutants and wild type **(Paper I, Fig 1a)**.

My contribution to this article was to study the polymerization properties of these mutants. These three mutants, along with the wild type (wild-type *Pf*ActI), were expressed and purified. The wild-type *Pf*ActI and mutants eluted at around 15.5-17.5 mL of Superdex 200 Increase 10/300 GL column **(Fig. 14)**. K270M, A272W mutations caused hyperactivation of the P_i release rate by Mg^{2+} **(Paper I, Fig 1a)**. Seeded polymerization assays were performed to determine if the increase of the P_i release in the mutants promote faster elongation rates. No changes were found in the elongation rates of the mutants compared with the wild-type *Pf*ActI **(Paper I, Fig 1b)**.

To investigate the effect of the mutations in the filament stability, the abundance of filaments was quantified using TEM images with negative staining of the filamentous *Pf*ActI and the mutants. The canonical-type mutants K270M and A272W formed many long filaments in the absence of JAS compared to wild-type *Pf*ActI. In contrast, the H74Q mutant did not form any long filaments **(Paper I, Fig 4)**.

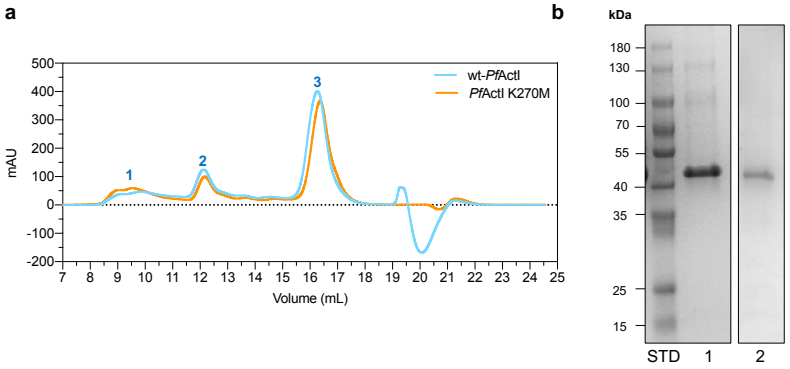

Figure 14. *Pf*ActI purification. **a.** Size exclusion chromatogram of wild-type *Pf*ActI and K270M. Peaks 1-2 indicate aggregates and oligomers; peak 3 represents the monomeric actin. **b.** SDS-PAGE, combined elution fractions from gel filtration. **1**, wild-type *Pf*ActI and **2**, *Pf*ActI K270M. STD, Protein Standard Marker.

The effect of pH on the polymerization in wild-type *Pf*ActI and the K270M mutant, which mimics canonical muscle actin, was studied. Although this experiment was not included in the paper, it is part of the thesis. At pH 7.5, the pellet fraction increased in *Pf*ActI. Only at this pH, few long filaments were observed in EM samples (**Paper I, Fig. 4)**. In contrast, the K270M mutant formed long filaments at pH 6 **(Fig 15)**.

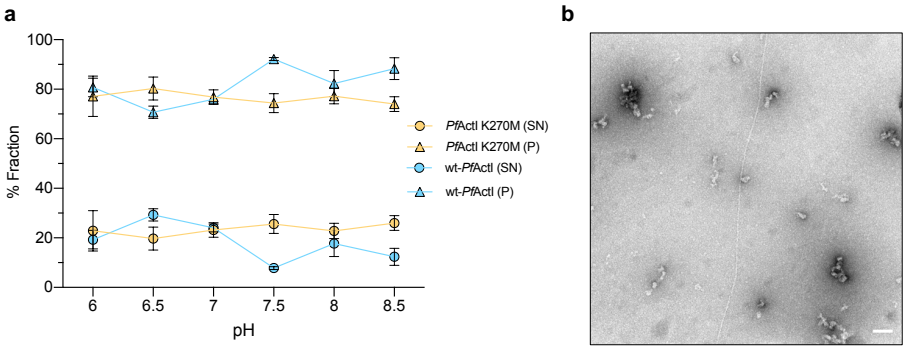

Figure 15. Sedimentation assay at different pHs and EM image of polymerized K270M. **a.** Polymerized wild-type *Pf*ActI and K270M samples at different pHs. After ultracentrifugation pellets and supernatants, were collected, and the corresponding bands in an SDS-PAGE were quantified. **b.** EM microgram of polymerized *Pf*ActI-K270M (1 µM) at pH 6. The scale bar represents 100 nm.

4.2. Paper II

4.2.1. Expression and purification of *Plasmodium* actins

Escherichia coli is the classic and simple organism for heterologous expression of recombinant proteins. However, for proteins that require post-translational modifications, with a larger size, disorder regions or proteins which require specific proteins for proper folding that *E. coli* does not encode, are not suitable for this kind of expression system. This is the case of *Plasmodium* actins, which require a eucaryotic expression system like yeast or insects. The expression system adopted in this thesis was insect cell expression using Sf9 cells due to its reported positive expression of actin 1 from *P. falciparum* and *T. gondii* actin (Bhargav et al., 2013; Skillman et al., 2011). The expression cultures were harvested 96 h post-infection. *Pf*ActII eluted at around 15.5-18 ml of Superdex 200 Increase 10/300 GL column **(Fig. 16)**.

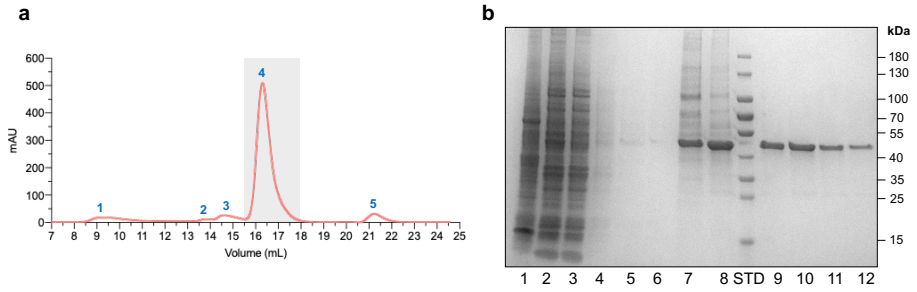

Figure 16. *Pf*ActII purification. **a.** Size exclusion chromatogram of *Pf*ActII. Peaks 1-3 indicate aggregates and oligomers, peak 4 represents the monomeric actin, and peak 5 is not visible by SDS-PAGE. **b.** SDS-PAGE showing all the steps of actin purification. **1** Pellet, **2** Supernatant, **3** Flowthrough, **4-6** Washes, **7** Elution after affinity chromatography, **8** Concentrated protein after TEV cleavage, **9-12** Elution fractions after gel filtration. STD, Protein Standard Marker.

Interestingly, *Pf*ActII showed a strong affinity to *Sf*9 cofilin, which was confirmed by MS. The purification was thus extensively optimized to remove any detectable cofilin contamination.

4.2.2. Molecular weight of *Pf*ActII

The theoretical molecular weight (MW) is 42,718 Da, which includes two extra residues in the N terminus (G-A) owing to our expression system. The MW of *Pf*ActII was determined by ESI-LC-MS. A peak of 42,732 Da with a relative abundance of ~92.7% was identified, showing that *Pf*ActII expressed in insect cells is post-translationally modified, specifically the His73, contrary to *Pf*ActI that lacks the methylation of H74. However, a fraction of the *Pf*ActII population appeared not to have a methylated H73, a second peak of 42,715 Da was identified, which corresponds to the theoretical molecular weight of the construct, the relative abundance was ~77.4% **(Table 6)**. The methylation of H73 was included in the cryo-EM model.

	Teorical MW (Da)	Experimental MW (Da)	Comments
***Pf*ActI**	41,999	41,996 [a]	Non methylated H74
***Pb*ActII**	42,809	42,822 [b]	Methylated H73 (+13Da)
***Pf*ActII**	42,718	42,715 ± 0.5 [c]	Non methylated H73
		42,732 ± 1.2 [c]	Methylated H73 (+13Da)

Table 6. Molecular weight of *Plasmodium spp.* actins. [a] (Kumpula et al., 2017), [b] **paper I** and [c] **paper II**, each value is an average from the masses from 4 separate experiments ± standard deviations.

4.2.3. Polymerized *Pf*ActII populations

Most of the biochemical experiments before have been performed for *Pf*ActI, and it is well known that this isoform forms short filaments compared to canonical actins (Kumpula et al., 2017; Skillman et al., 2011). In contrast, the second isoform is not yet characterized. To understand the distribution of *Pf*ActII filaments during polymerization, a sedimentation assay was performed by applying a high relative centrifugal force of 100,000*,* 200,000*,* and 435,000 *g.* At the maximum speed, the efficiency of the *Pf*ActI or *Pf*ActII pellets is similar (p=0.38, two-tailed Student's t-test). These results agree with previous work on *Pf*ActI and skeletal muscle α-actin (70% compared to 99%) (Kumpula et al., 2017). It implies that skeletal muscle α-actin can form longer or a higher

proportion of filaments than *Plasmodium* actins. On the other hand, at lower speeds, 100,000 *g,* 200,000 *g,* the efficiency is 45% and 60.2%, respectively. Interestingly in the presence of JAS, the pelleting efficiency at 100,000 *g* is the same as the protein ultracentrifuged at maximum speed without JAS (70.3%); the Student's t-test did not show a significant difference (p=0.48). In contrast, the pellet of *Pf*ActII-JAS at 435,000 *g* increased around 9% compared with the *Pf*ActII without JAS **(Paper II, Fig. 1 a-b).**

To study the filament size distribution of the sample and compare it with *Pf*ActI, DLS was employed. F-*Pf*ActII showed a distribution into three populations with a hydrodynamic radius (r_H) of 8.1, 42,9, 412.5 nm with volume percentage contributions of 50.6, 32.7 and 16.7%, whereas G-*Pf*ActII is distributed in one peak with r_H of 5.1 nm. On the other hand, F-*Pf*ActI is distributed in two peaks with r_H of 5.4 nm (91.6%) and a wide second peak, including sizes between 10.7 to 39 nm (8.33%). The G-form is distributed in one population of 5.6 nm. These values are similar to the previous report (Kumpula et al., 2017). Compared with the size of the G-α-actin (2.7 nm) previously reported, *Plasmodium* actins appear to be in a dimeric form **(Paper II, Fig. S2 a)**. Likewise, the supernatant of F-*Pf*ActII-JAS was presented in four larger populations: 15.6 nm, 69.3 nm, 214.9 nm, and 678 nm (total volume of 46.5%, 16%, 1.2%, and 33.4%) **(Paper II, Fig. 1 c)**.

The size distribution of the samples was measured after ultracentrifugation. The r_H of the supernatant ultracentrifuged at 100,000 *g* is 5.4 nm, and the peak moved to 2.7 nm when the sample was ultracentrifuged at higher speed. For *Pf*ActII-JAS, ultracentrifugated protein at higher speed presented a r_H of 5.8 nm. Also, the pellet fractions of *Pf*ActII, after resuspension, maintain apparently as dimers with a r_H of ~5.5. In the case of *Pf*ActII-JAS, the pellet showed two oligomeric populations with a r_H of 47 nm (50.6%), and a wide peak between 156.3 and 654.7 nm (49.1%) respectively **(Paper II, Fig. 1 d-e)**.

Samples were visualized by native-PAGE. The running buffer contained 0.35 mM ATP, 0.1 mM ADP, 25 mM Tris-Cl, 125 mM glycine pH 8.5, and 0.1 mM $MgCl_2$. This method allows resolving oligomers up to ~12 units (Vahokoski et al., 2014). 30 µM actin was polymerized overnight and the samples were analyzed before and after ultracentrifugation. Ultracentrifugation at the lower speed removed all oligomeric material. However, there were some differences in the pellet efficiency. At 100,000 *g,* 42.1% of the protein in the supernatant appears to be monomeric, 2.1% dimeric and 2.3% trimeric (extremely weak bands). At high speed, the percentage in the supernatant decreased to 21.8% in monomer and 1.9% in dimer forms. Dimeric forms are not visible in the supernatant of *Pf*ActII-JAS, the monomeric form was around 24%. On the other hand, after resuspension in 1x F-buffer, the pellets retained a small fraction of the actin in oligomeric form. In the sample without JAS around 3.3% and 12.8% in *Pf*ActII-JAS. These observations confirm that JAS stabilizes the filaments, even after ultracentrifugation **(Paper II, Fig. 1f)**.

Furthermore, 16 h after the initial ultracentrifugation, the supernatant was re-pelleted. The native-PAGE showed that the remaining protein in the supernatant is in monomers and dimers but no large oligomers were observed. The concentration of these dimers decreased according to the total concentration of protein. The efficiency of the supernatant material obtained by ultracentrifugation at 435,000 *g* had a similar ratio compared to the first step of centrifugation in SDS-PAGE (25% for the supernatant and 75% for the pellet). In contrast, the pelleting efficiency of the supernatant of *Pf*ActII-JAS decreased (40.5% for the supernatant and 59.5% for the pellet). A possible explanation is that the concentration of the supernatant *Pf*ActII-JAS is lower in comparison with *Pf*ActII **(Paper II, Fig. S2)**.

These results showed that the populations of F-*Pf*ActII are larger than F-*Pf*ActI. According to the predicted r_H calculated for α-actin monomers (2.7 nm) and dimers (3.4, 4.4-4.6 nm) (Kumpula et al., 2017). The F-*Pf*ActII species correspond approximately to 4, 18, and 179 units, and for G- *Pf*ActII, it is

presented likely as a dimer. For F-*Pf*ActI, the first peak corresponds to dimers, and the second peak to filaments with 4 to 17 units.

4.2.4. Filament length

To compare the filament length of *Plasmodium* actins, 1 µM filamentous *Pf*ActII and F-*Pf*ActI were visualized by negatively stained EM. Previously, **paper I** showed that wild-type *Pf*ActI forms short filaments, also known as sausages, and only few long filaments. In contrast, F-*Pf*ActII in equilibrium is distributed mainly in two populations, few long filaments and the other fraction of proteins remain in a monomeric or dimeric form **(Paper II, Fig. 1g)**.

4.2.5. The critical concentration of *Pf*ActII

The C_c at the steady-state of *Pf*ActII was measured as described previously for canonical actins and *Pf*ActII (Hertzog & Carlier, 2005; Kumpula et al., 2017). The C_c was found at 0.112 ± 0.016 µM (n=5). A similar value has been reported for *Pf*ActI (0.13 µM) **(Paper II, Fig. 2)**.

A previous publication of the polymerization kinetics using TIRF microscopy of *Pf*ActI suggested a higher C_c for *Pf*ActI (4 µM) than the value reported by Kumpula et al. (2017). They argued that the measurements were done after more than 16 h of polymerization, at this point the long filaments are not stable (Lu et al., 2019). Possibly, they did not observe the shorter filaments because of the resolution of the microscope or because they did not use fresh protein. In order to identify if the C_c changes over the time, the C_c curves were done using concentrations higher than 5 µM (maximum value tested for *Pf*ActI), and the samples were measured after 1 and 20 h of polymerization. Interestingly, the C_c curve of *Pf*ActII was segmented into two slopes, which means that the polymerization is not linear. The intersection point after 20 h (3.12 ± 0.616 µM,

n=2) decreased 1.4 µM over 1 h of incubation (4.5 ± 0.141 µM, n=2). Unexpectedly, the *Pf*ActI C_c curve after 1 h of polymerization was linear. However, the curve was segmented into two slopes after 20 h, 2 ± 0.141 µM (n=2). The minimum value evaluated for the *Pf*ActI C_c curve was 0.2 µM, which is slightly above over the C_c reported. However, first slope was fitted starting at C_c reported previously **(Paper II, Fig. 2)**.

On the other hand, the C_c plot of polymerized *Pf*ActII in non-polymerizing buffer showed that *Pf*ActII was oligomerized in the presence of ATP like *Pf*ActI. Contrary to the C_c curve in F-Buffer, this plot had a linear behavior. However, the C_c changed over the time. After 1 h of polymerization, the determined C_c was 0.2. The C_c decreased after 20 h of incubation to 0.06 µM **(Fig. 17 a- b)**. A linear regression curve was also observed for *Pf*ActII polymerized in the presence of JAS (ratio 1:1). The C_c did not increase significantly after 20 h of polymerization 0.14 ± 0.09 µM (1 h) and 0.12 ± 0.15 µM (20 h) (n=2) **(Fig. 17)**. These results suggested that the C_c of the *Plasmodium* actins reach the equilibrium after 20 h of incubation.

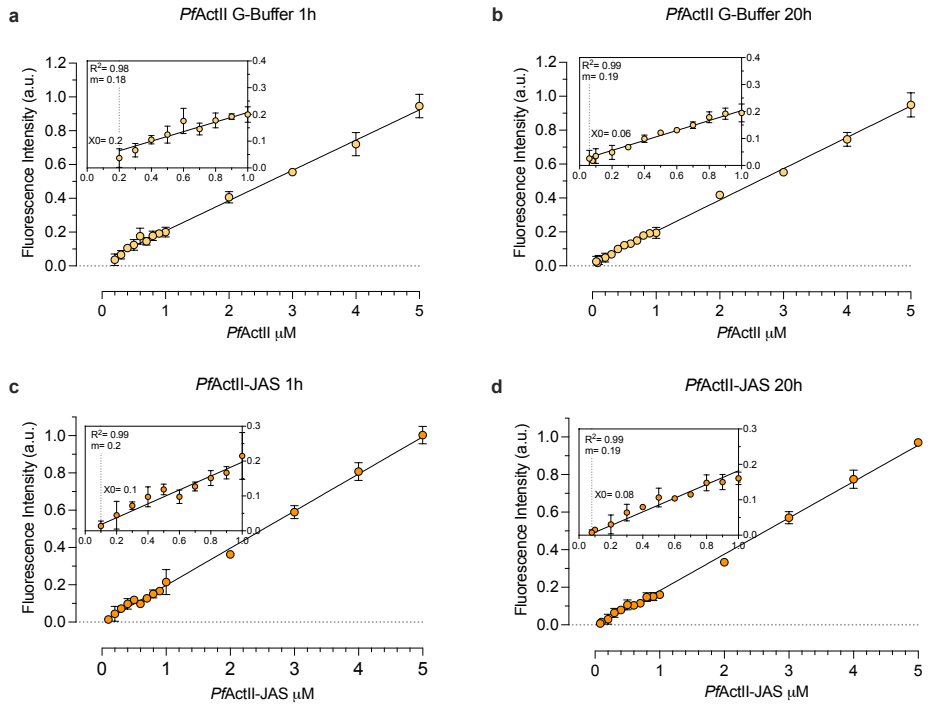

Figure 17. C_c plots of *Pf*ActII. *Pf*ActII polymerized with G-Buffer**, a.** Samples were incubated for 1 h or 20 h in **(b)** at 4°C**.** *Pf*ActII polymerized 1x-F buffer in the presence of JAS (in a ratio 1:1). **c.** Samples after 1 h and 20 h of incubation in **(d)** at 4°C. The data fit in a linear regression equation. X0 represents the critical concentration. The lower concentration points are magnified on the left. Error bars representing the standard deviation, a.u.= arbitrary units.

4.2.6. Polymerization kinetics

Spontaneous polymerization of *Plasmodium* actins was performed at different concentrations, the pyrene fluorescence was measured over time. The curves showed a sigmoidal behavior and a lag phase for both actins as canonical actins. However, the lag phase of *Pf*ActII was less pronounced than *Pf*ActI. Additionally, *Pf*ActII reached the equilibrium faster than *Pf*ActI. In around 100 min, concentrations below 5 µM reached the plateau in *Pf*ActII, while in *Pf*ActI, it takes more than 110 min. Moreover, *Pf*ActII presented an overshoot which is an unusual peak, likely during the elongation phase (during the first 10 min of

polymerization). This peak was less pronounced when the actin concentrations gradually decreased **(Paper II Fig. 2 a- b)**.

To determine the elongation rate constant of *Pf*ActII, actin was polymerized in the presence of 0.5 µM of F-*Pf*ActII or skeletal muscle F-α-actin, which served as seeds. The first 20 min of polymerization exhibited two different phases, as previously observed for *Pf*ActI with F-α-actin seeds (Kumpula et al., 2017). The first phase is ~3.8 fold higher than the second slope. The peak observed in the polymerization assays without seeding appeared less pronounced when actin is polymerized with nuclei **(Fig. 18 and paper II, Fig. 3 c- d)**. The magnitude of the relative kinetic parameters changed in presence of F-*Pf*ActII or F-α-actin seeds. However, only one experiment using α-actin seeds was performed. Additional replicates need to be done to determine the significant differences. Using the C_c value from the steady-state and the equation from the second phase using F-*Pf*ActII seeds, the corresponding relative value of k_- is 0.003 ± 0.003 s^{-1} **(Table 7)**.

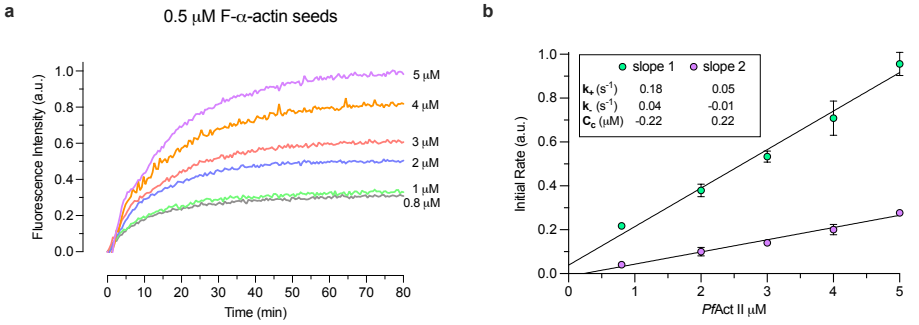

Figure 18. Nucleated polymerization curve of *Pf*ActII. **a.** Polymerization curves induced by the addition of 1x F-buffer using pyrene fluorescence of *Pf*ActII and F-α-actin seeds. **b.** Elongation rate constants plot of *Pf*ActII, the slope 1 is the initial phase (~29-264 s) and, the slope 2 corresponds to the second phase from ~6.8 to 19.5 min. a.u.= arbitrary units.

Nucleated polymerization (NP)				
	***Pf*ActII seeds**		**α-actin seeds**	
	Slope 1	*Slope 2*	*Slope 1*	*Slope 2*
k_+	0.04 ± 0.01	0.01 ± 0.002	0.18	0.05
C_c (μM)	1.12 ± 0.29	0.36 ± 0.19	-0.22	0.22
k_-	-0.04 ± 0.02	-0.004 ± 0.003	0.04	-0.01
Steady state (SS)				
C_c (μM)	0.11 ± 0.02			
k_- *	-0.003 ± 2e-004			

Table 7. Relative kinetic parameters of *Pf*ActII. All values reported as mean ± standard deviation (*Pf*ActII seeds: n=3 NP, n= 5 in SS). NP with F-α-actin seeds: n=1. * Relative k_- calculated using the steady state C_c and relative elongation constant (k_+) from slope 2 of nucleated polymerization assays.

4.2.7. Depolymerization kinetics

Depolymerization dynamics are challenging to quantify; the rate constant depends on the length of the filaments. The preliminary results showed one phase of depolymerization at 100 nM, 50 nM, and 35 nM. The half time of the slope increased significantly with the dilutions (11.5 ± 2.38 s^{-1}, 20.35 ± 1.81 s^{-1} and 37.7 ± 3.14 s^{-1}, n=3) (p=0.0001, one-way ANOVA test). The rate of depolymerization is similar between the *Plasmodium* actins at 50 nM **(Fig. 19)**. Additional experiments have to be done to compare the depolymerization kinetics between the *Plasmodium* actins.

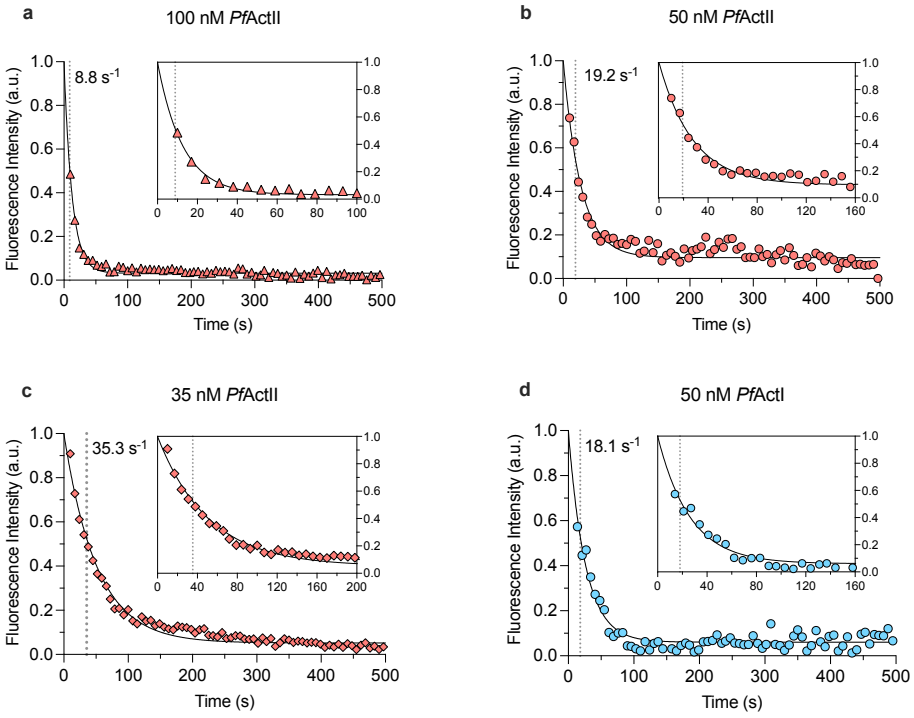

Figure 19. Depolymerization curves of *Plasmodium* actins. The depolymerization was induced by dilution of 5 µM polymerized *Pf*ActII to **a.** 100 nM, **b.** 50 nM and, **c.** 35 nM. **d.** *Pf*ActI depolymerization curve at 50 nM. The data was fit to the one-phase decay equation. The lower time points are zoomed in.

4.2.8. Filament structure

The filament structure of canonical actin has been determined to near-atomic resolution for several groups (Chou & Pollard, 2019, 2020; Merino et al., 2018; Von Der Ecken et al., 2015, 2016). For *Plasmodium* actin, there are two structures of the *Pf*ActI filament (Pospich et al., 2017) (6TU4, **Paper III**) and medium resolution reconstructions of JAS-stabilized *Pf*ActI, *Pb*ActII (Vahokoski et al., 2014). In collaboration with the Francis Crick Institute, London, UK, the filament of *Pf*ActII was obtained in the presence and absence of JAS. The structure was determined using helical averaging methods (He & Scheres, 2017). The average resolution was 3.3 Å and 3.5 Å, according to the Fourier

correlation using the 0.143 criteria **(Paper II, Fig S3)**. Six subunits of the filament were modeled into the density. The filament structure was determined in the Mg^{2+}-ADP state.

The aim was to determine the filament structure of *Pf*ActII that was previously unknown and identify the structural differences between *Plasmodium* and canonical actins. The results are described in the following sections.

4.2.9. Conformation of the filament subunits

Like other actins, F-*Pf*ActII has a helical symmetry **(Fig. 20)**. The helical twist angle of *Pf*ActII with and without JAS was -166.9°. There is a difference of ~0.6° and ~0.75° relative to α-actin (-166.6) and *Pf*AcI (-167.65) (Chou & Pollard, 2019; Pospich et al., 2020). Furthermore, the protomers present a flat and close conformation which is the opposite conformation of the monomeric actin form. The interdomain dihedral angle (θ) of subunits was larger in *Pf*ActII structures (10.1° and 9.7°). The most significant difference of the θ angle is a rotation of 3.9° (*Pf*ActII) and 3.5° (*Pf*ActII-JAS) relative to the F-*Pf*ActI structure (6TU4) **(Paper II, Fig S7)**.

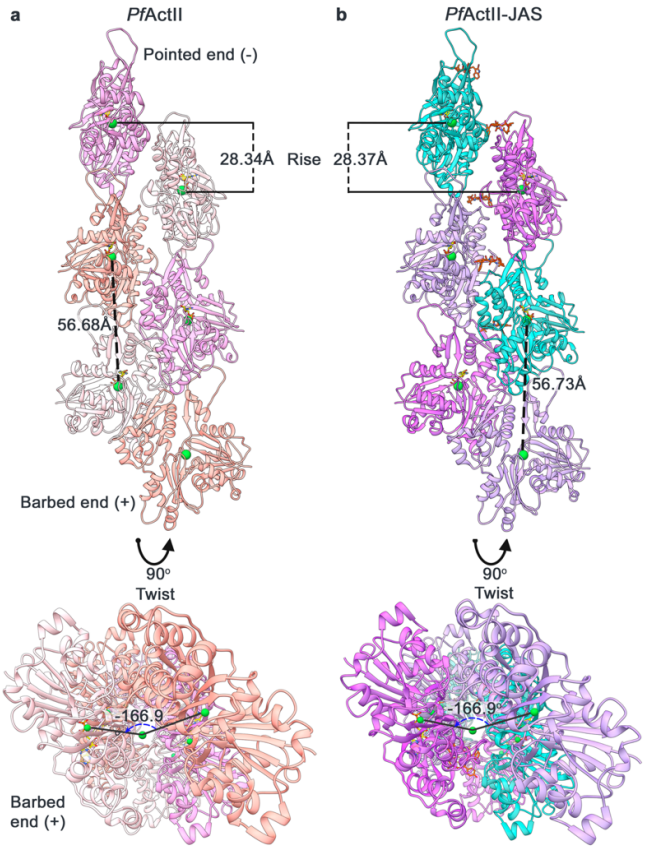

Figure 20. Helical assembly of *Pf*ActII and JAS-stabilized *Pf*ActII filaments with six subunits (side view). The center of mass (green sphere) of each subunit is located next to the β-phosphate of the ADP molecule. In the bottom panel, the filament is shown from the top view (from the pointed end to the barbed end). The rise per subunit along the short pitch helix and the helical twist angle are indicated.

4.2.10. The nucleotide-binding pocket

ADP and Mg^{2+} occupy the nucleotide-binding pocket located between the inner and outer domains (ID and OD). Because the resolution is not at the atomic level, detailed information of the active site is unknown, like the density map of the water molecules around the phosphate and the Mg^{2+}. General differences were identified between the F-*Pf*ActII and other actin filament structures. H161

structures. H161 of *Pf*ActII flipped to the opposite side of H161 in G-Actins, and Q137 moved around 70° in the opposite direction of the ADP **(Paper II, Fig 5)**.

To understand the mechanisms of F-actin ATP hydrolysis, structures with atomic resolution are targeted. As a side part of the project, Mg-ADP-*Pf*ActII complexed with fragmin (domain F1) from *Physarum polycephalum* was purified **(Fig. 21a)**. As reported previously, fragmin binds to the barbed end actin subunit, mimicking the F-actin state, which allows studying the ATP hydrolysis (Takeda et al., 2020). 576 conditions were screened around the crystallization conditions in which *Pf*ActI-Fragmin (data not published) and α-actin-Fragmin complexes were obtained **(Fig. 21b)**. The protein crystallized in three conditions **(Fig. 21c)**. However, the diffraction quality of the crystals was low. We are in the process of optimizing the crystallization conditions of Mg-ADP-*Pf*ActII.

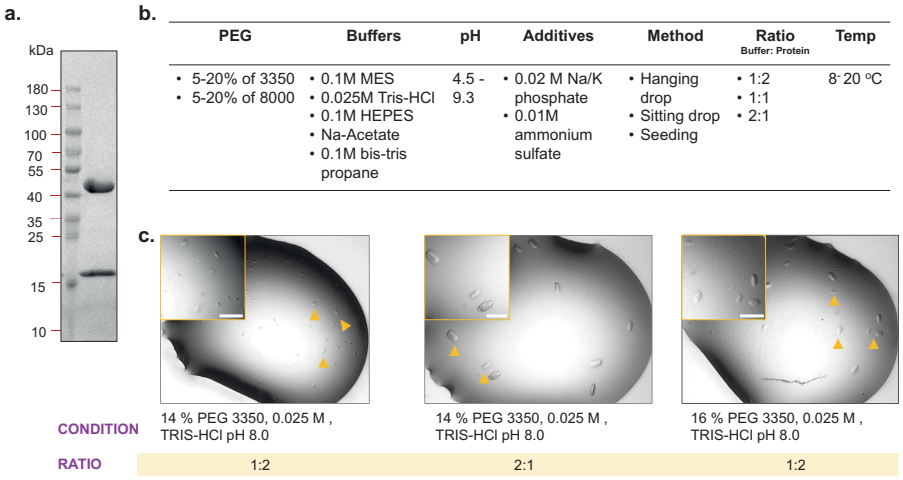

Figure 21. Mg-ADP-*Pf*ActII- F1 domain complex. **a.** SDS-PAGE of purified *Pf*ActII-F1 domain complex. ~60 μM was mixed with F1 domain in a ratio of 1:1.2. *Pf*ActII 40 kDa, F1 domain 18.2 kDa. **b.** Summary of the crystallization conditions tested for *Pf*ActII-F1 complex. **c.** Crystals of *Pf*ActII-F1 domain complex. The length of the crystals was ~ 0.75 mm. The top left of the image is zoomed in. Scale bars (white) represent 100 µm.

4.2.11. Lateral and longitudinal contacts

4.2.11.1. Intrastrand interactions

- **D-loop**

Actin filaments grow towards the pointed end, and the DNaseI-binding or D-loop inserts into the C terminus (SD3), which includes the W-loop of the next protomer. Hydrophobic interactions mediate the interaction between the D-loop and the adjacent protomer. In F-*Pf*ActII, the hydrophobicity surface of the SD3 that interacts with the D-loop increased by the substitution of V139 and A170 (canonical actins) by I139 and V170. Other differences in the D-loop composition between canonical and *Plasmodium* actins involve the substitution of some residues. The amino acids R39, Q41, V43, and G48 are substituted by K40, P42, I44, and E49 in *Pf*ActI or K39, P41, I43, and E48 in *Pf*ActII **(Paper II, Fig 7)**.

- **Hydrophobic key and lock interaction**

This interaction involves the SD3, particularly I287 (canonical actins), which insert into a groove of SD4 from the adjacent protomer, producing a hydrophobic key and lock interaction. In *Plasmodium* actins, S199 and V201 from α-actins are replaced by T199 and T201 in *Pf*ActII, and G200 and S202 in *Pf*ActI. These substitutions reduce the hydrophobicity area around the key-lock interaction. Clearly, the key-lock contact is weaker in F-*Pf*ActI because of the substitution of I287 (in α-actins) by a V288 (Pospich et al., 2017). Contrary, F-*Pf*ActII contains isoleucine (288) like α-actins **(Paper II, Fig. 6)**. Besides that, we observed the distance between the α carbons of I208 and I288 in α-actins is slightly closer than *Plasmodium* actins. In α-actins, the distance is 9.6 Å (6DJO, 6KLL) and 9.7 Å in the presence of JAS (5OOC, 6T23), whereas in *Plasmodium* actins it is ~0.3 Å larger. *Pf*ActII is 9.9 Å, and both *Pf*ActII-JAS and *Pf*ActI-JAS are 10.1 Å. This suggests that the distance between protomers

could affect the key-lock interaction. Other intrastrand interactions involve two salt bridges between the residues R62 and D289 and D245 and R291 **(Paper II, Fig. 10)**.

4.2.11.2. Interstrand interactions

The plug region (SD3) of n-1 and the SD2 of n-2 protomer **(Fig. 9)** are involved in an essential interaction between opposite actin strands. It is an electrostatic interaction very conserved among actins. The main difference between *Plasmodium* and canonical actins is the inversion of the electrostatic potential by the substitution of M269 (canonical actins) by K270 (*Pf*ActI) or R270 (*Pf*ActII). In the case of F-*Pf*ActII, this substitution does not interfere with the length of the filaments, which is the opposite effect in *Pf*ActI **(Paper II, Fig. 8)**. Additional lateral interactions involve the residues H173 and L113 (SD3 and SD1) of one protomer with L39 (SD2) and the residues E195 and G269 (SD4) of the contrary protomer **(Paper II, Fig. S9)**.

4.2.12. Phosphate release

The structures available for canonical actins polymerized in the presence of JAS show a filament structure retaining the P_i. However, this is not the case for the *Plasmodium* actins. The density map does not show the density of the phosphates *Pf*ActI or *Pf*ActII polymerized with JAS. On the other hand, the side chain of S14 (S15 in *Pf*ActI) which is a nucleotide sensor, pointing in the direction of H73, S14 does not form a hydrogen bond with the β-phosphate of ADP or G74, the distance between Ser14 and β-phosphate of ADP is more than 5Å**.** In contrast, this interaction has been observed in actin from *Drosophila* (Rould et al., 2006). The backdoor is closed, the distance between the side chains of N111 and R177 is 2.5Å (F-*Pf*ActII) and 2.3 Å (F-*Pf*ActII-JAS), similar to the canonical actin in ADP- P_i state (Chou & Pollard, 2019). The backdoor

in most of the filamentous canonical actins appears to be closed. In contrast, the G-Actins in ATP-Ca^{2+} or ADP-Mg^{2+} have an open backdoor (7.6-11.1 Å distance between side chains). As we proposed in **paper III**, an alternative path of P_i release could be a closed or open channel, depending on the rotamer conformation of N115 and W79 (N116 and Y80 in *Pf*ActI) **(Fig. 22)**.

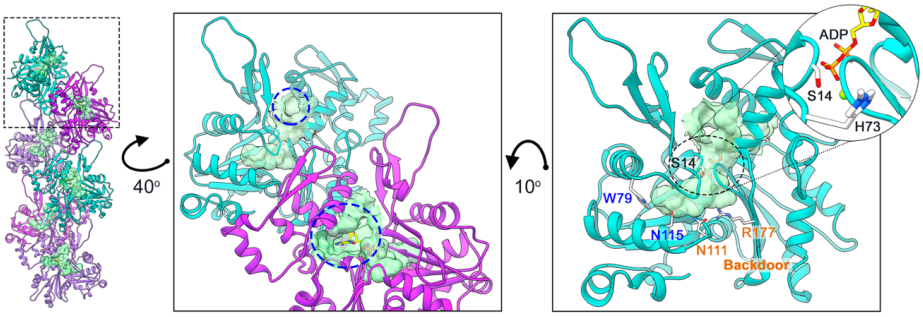

Figure 22. Internal tunnel for phosphate release in *Pf*ActII.The internal cavity was calculated using the CASTp server (Tian et al., 2018) and visualized as surfaces in Chimera. The residues that form the backdoor (Chou & Pollard, 2019) showed a close conformation.

4.2.13. Effect of JAS on the filamentous actin

As described previously, the *Plasmodium* actins filaments do not behave as canonical actins, which means that the length and proportion of filaments are shorter and lower for the *Pf*Actins. Actin filaments stabilized by JAS have been used for Cryo-EM experiments before (Pospich et al., 2017; Vahokoski et al., 2014). This compound polymerizes G-actin in a large proportion than the natural polymerization process doing it very convenient for data collection. The structures of JAS stabilized and non-stabilized *Pf*ActII were obtained with a similar resolution, and the architecture of the filament was not affected by JAS. The helical twist angle is the same (-166.9°) for both structures. There is a minor rise of 0.03 Å between *Pf*ActII (28.34 Å) and *Pf*ActII-JAS (28.37 Å).

The binding site of JAS is located between three subdomains. The inole group is inserted into a pocket created by the outer domain between the P loop (SD1) and H loop (SD2) and the top part of the SD3 of the adjacent protomer. The third contact is the pointed end site of SD4. The interacting residues around 4 Å include H73, I75, R177, N179, L110, P112, T114, G197, H198, T199, E205, L243, L248, and I288. In contrast, the binding site of JAS in *Pf*ActI showed fewer ionic or hydrogen bonding interactions around the P loop (residues 109-114) and the SD4.

Furthermore, Merino (2018) and co-workers found some conformational changes when JAS-cLys was added immediately before polymerization of monomeric α-actin in ATP or ADP state: *(a)* an open conformation of the D-loop, *(b)* the phosphate release is blocked, and *(c)* the disordered C terminus. In contrast, JAS-stabilized *Plasmodium* actins did not show the same effects. Either JAS-stabilized (F-*Pf*ActI and F-*Pf*ActII) or non-stabilized F-*Pf*ActII has a closed D-loop conformation **(Paper II, Fig. S11)**. The density of P_i is absent, and the C terminus is stabilized in all the structures. In **paper I**, we suggested that the substitutions of Q41 and G48 (α-actin) by P42 and E49 in *Pf*ActI or P41 and E48 *Pf*ActII are contributing to the closed D-loop conformation. This conformation and the effect of other residues, F54 and G200 (Y53 and S199 in α-actin), could contribute with the instability of *Pf*ActI filaments. However, it does not have the same effect in the filamentous *Pf*ActII, possibly because Y53 remains as in α-actin and S199 is substituted by T199.

4.3. Paper III

In **paper III**, the first high-resolution structure of the actomyosin motor complex from *P. falciparum* (3.1 Å) and a *Pf*Act1 filament structure (2.6 Å) were obtained. My contribution to this paper was the purification of the actomyosin motor complex. Myosin A in complex with the light chains (ELC and MTIP) was expressed and purified. As reported before, the complex requires specific

chaperones to fold correctly. Thus, *Pf*MyoA/ELC/MTIP was expressed in the presence of Unc45 and Hsp90 to produce a functional complex (Green et al., 2017) **(Fig. 23)**.

Also, *Pf*ActI was expressed and purified **(Fig 16)**. The actin 1 filament model with atomic resolution was used in **paper III** to compare it with the F-*Pf*ActII structure.

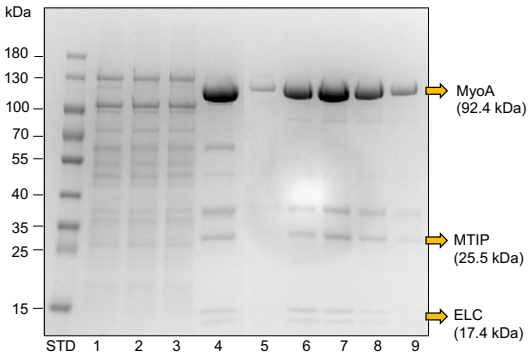

Figure 23. SDS-PAGE of *Pf*MyoA-ELC-MTIP purification. **1** Supernatant, **2** Flowthrough, **3** Washes, **4** Elution after affinity chromatography, **5-9** Elution fractions after gel filtration. STD, Protein Standard Marker.

4.4. *Plasmodium* class VI myosins

4.4.1. Cloning and expression of *Plasmodium* class VI myosins

The conserved regions of the *Plasmodium* class VI myosins - the motor domain, the neck, and the tail - were identified using the platform myHits (SIB) (http://myhits.isb-sib.ch) (Pagni et al., 2004) and InterPro BETA (https://www.ebi.ac.uk/interpro/). 3D models of *Pf*MyoJ and *Pf*MyoK were generated by threading using Phyre2 (Kelley et al., 2015). According to the 3D model and predictions, four constructs for each myosin were designed; the

constructs were named J1, J2, J3, J4 for *Pf*MyoJ and K1, K2, K3, K4 for *Pf*MyoK **(Fig 24)**.

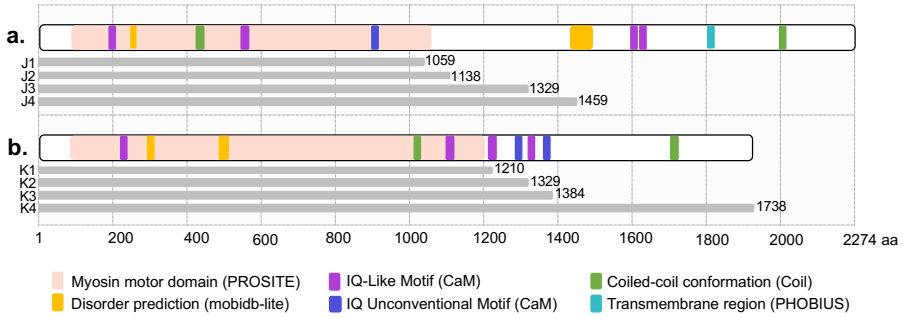

Figure 24. Conserved regions of *Pf* class VI myosins. **(a).** The motor domain of *Pf*MyoJ is predicted around amino acids 106-1065, two disordered regions in the N terminus (237-272) and C terminus (1457-1529), two coiled-coil regions at 466-486 and 2003-2030, and 5 IQ-Like motifs and one unconventional motif. **(b).** The *Pf*MyoK sequence predicts a motor domain covering amino acids 102-1208, 2 disordered regions in the N terminus (274-327 and 465-543), and two coiled-coil regions (1002-1029, and 1534-1554). Four IQ-Like motifs and two unconventional motifs were identified. The grey boxes depict the designed constructs.

*Pf*Myosin constructs were cloned into the pFASTBacI vector (acceptor vector) with Strep-tag II, and these were used for expression using baculovirus-infected insect cells. Because some myosins require specific chaperones for correct folding (Bookwalter et al., 2017; Green et al., 2017)**,** the proteins were coexpressed with the parasites myosin chaperones *Pf*Unc45 and *Pf*Hsp90. To standardize the expression conditions for each protein, different amounts of virus to infect cells were tested. To optimize the solubility conditions, buffer screening was made for all the constructs, using the GFP fluorescence signal. The highest GFP signal was detected with KCl (500-750 mM) in Tris Buffer pH 7.5 for *Pf*MyoK (K1, K2, K4 constructs) and J4 for *Pf*MyoJ, indicated that these proteins are expressed at least partly in a soluble form **(Fig 25)**.

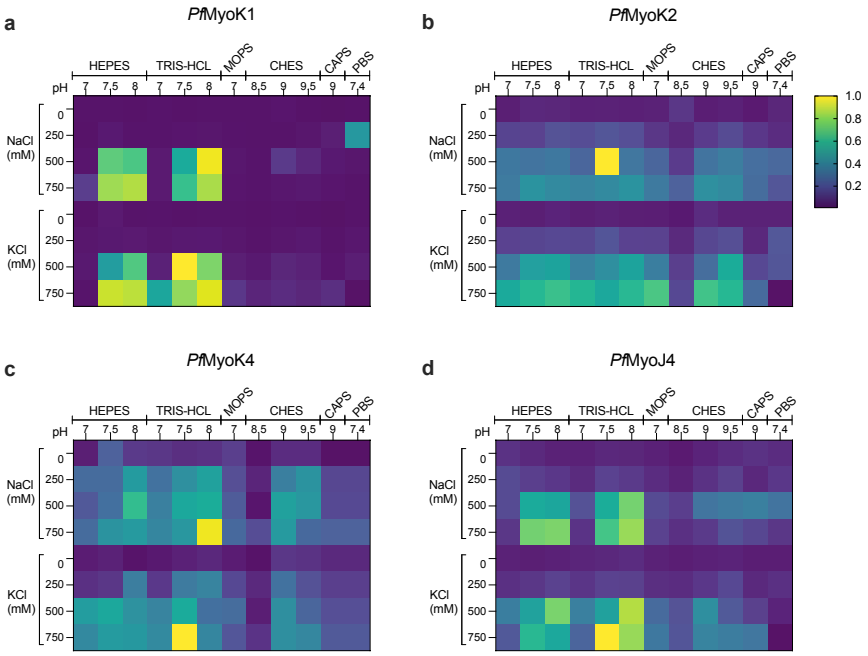

Figure 25. Buffer screening. The fluorescence intensity of the GFP of the *Pf*Myosin constructs was measured at 488 nm. The fluorescence was higher for all the constructs using Tris-Buffer at pH 7.5-8 in a high salt concentration.

Purification of these constructs was attempted by affinity chromatography using Strep-Tactin magnetic beads. The soluble fraction of the proteins did not bind to the resin **(Fig 26a and 27a)**. These myosins are likely present as soluble aggregates after expression. In addition to chaperones, the coexpression of light chains promotes the proper folding of myosins. As the correct light chains for MyoJ and MyoK are unknown, coexpression was attempted with the MyoA light chains MTIP and ELC. The co-expression increased the protein solubility **(Fig 26b and 27b)**.

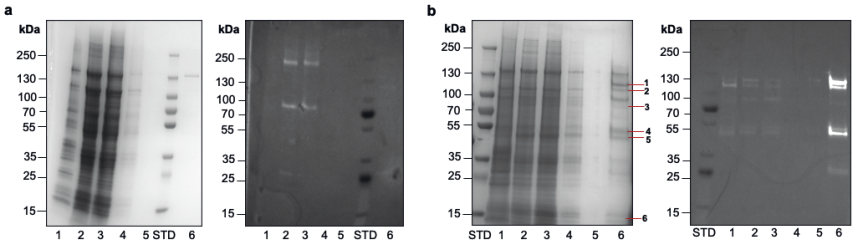

Figure 26. SDS-PAGE of *Pf*MyoJ4 purification. **1** Pellet, **2** Supernatant, **3** Flowthrough, **4** Wash 1, **5** Wash 2, **6** Concentrated elution. GFP signal is shown on the right. **a.** *Pf*MyoJ4 purification co-expressed with *Pf*Unc45 and *Pf*Hsp90. **b.** *Pf*MyoJ4 was co-expressed and purified with *Pf*Unc45, *Pf*Hsp90, and *Pf*ELC (selected bands were sent for identification by MS). The expected molecular weight of the protein, including GFP and Strep-tag, is 203.4 kDa.

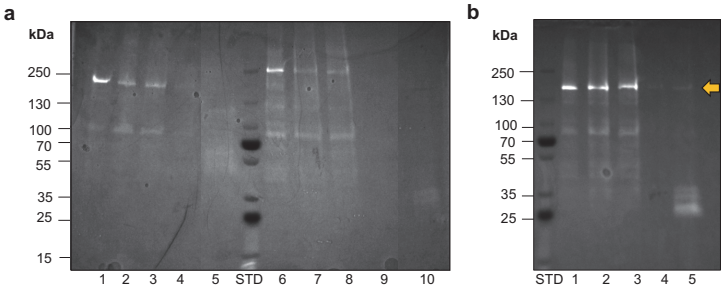

Figure 27. SDS-PAGE showing GFP signal. Purification of *Pf*MyoK tagged with GFP. **a** *Pf*MyoK1. **1** Pellet, **2** Supernatant, **3** Flowthrough, **4** Wash, **5** Concentrated elution. *Pf*MyoK4. **6** Pellet, **7** Supernatant, **8** Flowthrough, **9** Wash **10** Concentrated elution. **b** *Pf*MyoK1-ELC purification, **1** Pellet, **2** Supernatant, **3** Flowthrough, **4** Wash **5** Concentrated elution.

4.4.2. Cloning and expression of the putative light chains

There are 11 putative myosin light chains identified in *Plasmodium falciparum***.** As the specific light chains for these two class VI myosins are unknown and there is a multitude of possible combinations, it is difficult to decide which ones to use for coexpression. To identify the specific light chains for *Pf*MyoJ and *Pf*MyoK, three polyproteins were designed and cloned in a pIDS vector **(Fig 11 b and Table 8)**. The polyprotein is a strategy to study protein complexes and

to balance the expression levels of each protein in insect cells by a TEV NIa (Nie et al., 2014).

Polyprotein	Gene ID	Annotation
Poly 1	PF3D7_1017500	Myosin light chain (ELC)
	PF3D7_1246400	Myosin A tail domain interacting protein (MTIP)
	PF3D7_1118700	Myosin light chain (MLC-B)
	PF3D7_0627200	Myosin light chain, putative
Poly 2	PF3D7_0816400	Conserved Plasmodium protein, unknown function
	PF3D7_0728500	Conserved Plasmodium protein, unknown function
	PF3D7_0605400	Calcium-binding protein, putative/troponin C
	PF3D7_0414200.2	Calmodulin-like protein
Poly 3	PF3D7_0816400	EF-hand calcium-binding domain-containing protein, putative
	PF3D7_0728500	Conserved Plasmodium protein, unknown function
	PF3D7_0414200	Calmodulin-like protein

Table 8. List of the putative light chains of the polyproteins.

Multiprotein complexes were produced by the fusion of the myosins and the polyproteins (hereafter referred to as Poly). The viruses were produced, whereafter the fluorescence intensity of GFP (Tag of myosin) and mCherry (Tag of the polyproteins) was measured. The expression levels of the best hits were tested using different amounts of virus and density of the cells. There was no significant change between the different concentrations of virus 1 (data not shown). Regarding the density of the cells, the GFP fluorescence of the construct J4N/Poly3 using $2x10^6$ cells/ml decreased in comparison with $1x10^6$ cells/ml.

For *Pf*MyoJ, the larger construct with the N-terminal tag, co-expressed with the polyproteins 2 and 3, showed higher fluorescence than the construct with the C-terminal tag. On the other hand, one of the shorter constructs of *Pf*MyoK (K2), co-expressed with the polyprotein 3, showed red and green fluorescence **(Fig. 28)**. Further experiments were performed with *Pf*MyoJ4 co-expressed

with the polyproteins. The protein was purified by affinity chromatography. The visible band in the elution fraction (concentrated sample) was confirmed by GFP fluorescence and MS. However, the yield from the purification was meager **(Fig. 29)**. As these experiments are in progress, more work needs to be done on both myosins to identify their specific light chains and to get enough protein for structural and biochemical assays.

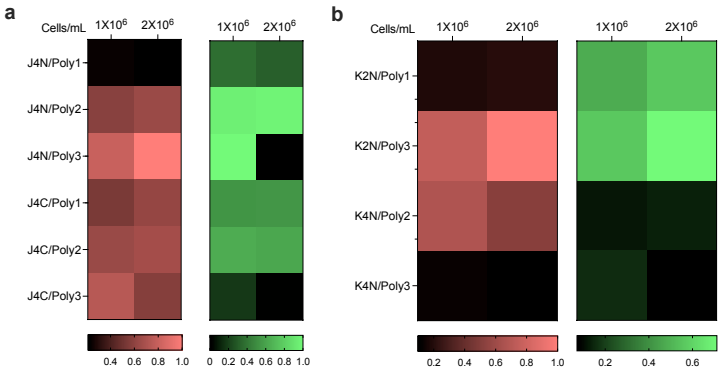

Figure 28. Expression test of *Pf*Myosins class VI co-expressed with *Pf*Unc45, *Pf*Hsp90, and the polyproteins. **a.** *Pf*MyoJ and **b.** *Pf*MyoK. The fluorescence intensity values were normalized against the higher value of each measurement. N or C refers to the position of the fluorescence tag.

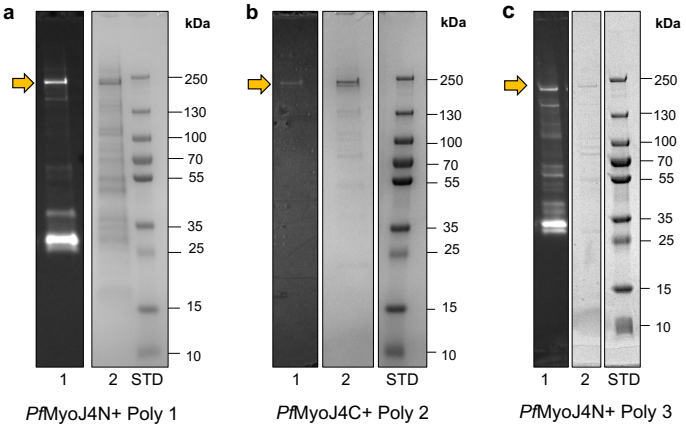

Figure 29. *Pf*MyoJ4 purification co-expressed with *Pf*Unc45/*Pf*Hsp90 and the polyproteins. **1** GFP signal, **2** SDS-PAGE. **a.** *Pf*MyoJN/Polyprotein 1. **b.** *Pf*MyoJC/Polyprotein 2. **c.** *Pf*MyoJC/Polyprotein 3. Selected bands were sent for MS.

5. Discussion

Around 40 to 60% of the amino acid sequence identity is the threshold to determine the conservation of a protein (Addou et al., 2009). Actins are very conserved among the eukariotic organisms, owing to their essential function in different cellular processes. On the other hand, *Plasmodium actins* are the most divergent actins; *Pf*ActI shares 81.55% of sequence identity with human skeletal muscle alpha-actin while *Pf*ActII shares 75.67%. Even though the amino acid sequence identity of *Pf*ActII is the lowest, compared with α-actins, the protein structure, *Pf*ActII is more similar to α-actins than *Pf*ActI.

The significant difference in terms of sequence of apicomplexan actins is between the residues 228-233. *Pf*ActII has an insertion of E in position 232. Moreover, *Pf*ActI has five unique substitutions; M16, Q49, A144, T194, and M283 (in α-actins) by N17, E50, S145, H195, and K292. In the case of *Pf*ActII, it has twelve substitutions: A19, G42, A97, N128, A135, L193, S235, K238, S239, F266, T277, G308 (in α-actins) by S19, N42, S97, D128 S135, F193, D235, E239, I240, L267, A279, N309 **(Paper II, Fig S1)**. Most of the changes are substitutions between neutral amino acids. However, there are a few exceptions; in *Pf*ActI, the replacement of a neutral amino acid (M) by K292 (basic and positive) in SD3 and the addition of acidic residues D235 and E239 in *Pf*ActII (SD4). These differences in sequence involve structural changes in the *Plasmodium* actins. The implications of these modifications in filament length, phosphate release, and polymerization will be discussed below.

5.1. Polymerization mechanism of *Plasmodium* actins

The first alternative mechanism of polymerization proposed for apicomplexan actins was an isodesmic mechanism for *Tg*ActI (Skillman et al., 2013), which differs from the classic nucleation-elongation process described for canonical actins. This polymerization mechanism is a non-cooperative process, in which

the rates of association and dissociation (k_+ and k_-) are constant for each monomer added to the filament. However, the affinity of the monomer to the polymer is independent of the filament length. In contrast, the nucleation-elongation mechanism is cooperative, and the polymerization occurs after a nucleation process, in which the free energy change (ΔG) increases after forming a stable nucleus. During the elongation phase, the ΔG decreases gradually with each added monomer to the filament (De Greef et al., 2009).

The isodesmic mechanism implies polymerization in the absence of nucleation. It means that a C_c is not required to induce an elongation phase. Thus, the lag phase is absent. However, recent publications and the results of this thesis disagree with the polymerization process suggested by Skillman and co-workers (2013). First, a C_c was reported for *Pf*ActI (Kumpula et al., 2017). Second, in **paper II**, the polymerization curves of *Plasmodium* actins showed a lag phase that disappears in the presence of α-actin seed. Finally, a C_c of *Pf*ActII was calculated with a similar value to *Pf*ActI and α-actins. There is only one publication that disagrees with the C_c of *Pf*ActI. They reported a C_c of 4μM. (Lu et al., 2019). Moreover, *Pf*ActI polymerization curves showed a lag phase that was not identified previously (Kumpula et al., 2017). Due to technical differences, it is likely that the time to set up the polymerization experiment has to be faster (less than 10s between the F-buffer is added to the samples and the first measurement) since monomeric actin tends to polymerize after the ammonium acetate is removed.

The aforementioned agrees with the classic nucleation-elongation mechanism. However, some of the experimental results could question this model: *(i)* The polymerization curves using α-actin seed show two slopes in the elongation phase, in which the first slope is higher than the second. *(ii)* The *Pf*ActII polymerization curve with or without seeding shows an unusual peak during the first 10 minutes. *(iii)* The C_c curves of *Plasmodium* actins exhibit two slopes, and the curve is linear in the presence of JAS or in G-Buffer conditions. *(iiii)* There is an excess of nucleation, which is more evident in *Pf*ActI than *Pf*ActII,

possibly influenced by the unstable conformation of the A-loop that apparently only *Pf*ActI can adopt (Kumpula et al., 2017 and Paper I). For *Pf*ActII, the excess of nucleation or dimers can be observed in the supernatant of pelleting assay after 36 h of incubation.

According to the evidence described above, the nucleation-elongation mechanism cannot explain all these unusual events thoroughly. Can the formation of the dimers be energetically more favored than larger oligomers (elongation phase) in *Plasmodium* actins? Such a situation occurs in the so-called anticooperative mechanism (Gershberg et al., 2016; Wehner & Würthner, 2020). This polymerization model could explain the excessive nucleation and the low numbers of long filaments. On the other hand, it is possible to consider that fragmentation is favored in *Plasmodium* actins, more so in *Pf*ActI than *Pf*ActII. This could explain the peculiar peak appearing during the elongation phase of *Pf*ActII polymerization.

Alternatively, in this study, a strong interaction of *Pf*ActII with a cofilin from *Sf*9 cells was detected. A cofilin band was not visible in SDS-PAGE in the purified samples used to perform the experiments. However, minute amounts, undetectable by Coomassie staining, could impact the polymerization kinetics. The overshoot during polymerization was observed in proteins with and without ADF contamination. Thus, it is not possible to exclude that the peak is an artifact produced by an undetectable cofilin concentration in SDS-PAGE. A similar overshoot is reported for other actins, the peak appeared close to the plateau in the polymerization curve. It is likely owing to a fast ATP hydrolysis that cause a partial depolymerization of the actin-ADP subunits at the pointed end of the filament. This overshoot can increase by the induction of branching, severing by sonication or ADF/cofilin, and seed filaments (Brooks & Carlsson, 2008; M. F. Carlier et al., 1985; Conchaudron et al., 2006). Further experiments need to be carried out, where the polymerization process can be visualized with the possibility to distinguish between monomers/dimers or trimers and filaments to understand the proper mechanisms of polymerization.

5.2. Differences between *Plasmodium* actins affect the length of the filaments

The main functional difference between *Pf*ActI, *Pf*ActII, and canonical actins is the short length of the filaments observed *in vitro* (Schmitz et al., 2005, 2010; Vahokoski et al., 2014 and **paper I**). The first explanation suggested for this was an isodesmic mechanism of *Tg*ActI assembly (Skillman et al., 2013), which cannot be possible, given the results discussed above. Another explanation for the filament length differences is the fragmentation process proposed in **paper I** for *Pf*ActI. This model determines the stability of the filaments by the interactions of D180 in the A-loop with either K270 (plug) or H74 in the H-loop (depending on its protonation state). This promotes a ping-pong movement of the A-loop, causing a change of the θ angle which acts as a switch between stable and unstable filament conformations.

While the spontaneous fragmentation appears to be more favorable for *Pf*ActI, it does not seem to be the case for *Pf*ActII. However, the length of the filaments in *Pf*ActII seems to be shorter and the occurrence of long filaments lower than in canonical actins (Vahokoski et al., 2014). This raises more questions: How does the fragmentation process of *Plasmodium* actins occur *in vivo*? Are the ABPs from the parasite and the host involved in this process? Do differences in fragmentation of *Pf*ActI and *Pf*ActII affect the speed of the parasite motility?

Fragmentation in canonical actins is dependent on filament length (Schmoller et al., 2011). Possibly, it is the case also for *Pf*ActII, since there is no evidence of a ping-pong movement of the A-loop. In comparison with *Pf*ActI, the fragmentation of *Pf*ActII could be less favorable due to some structural differences that do not permit the second conformation of the A-loop (2a). The methylation of H73, which is conserved in most of the actins, is one possible difference affecting this. The methylation of this histidine is involved in the actin monomer stability and flexibility of the OD and ID domains (Terman & Kashina, 2013). H73 is not methylated in *Pf*ActI **(Paper I, Fig. 3)**, contrary to *Pf*ActII in which the methylation of H73 ensures the interaction with D179 favoring the A-

loop (1b) conformation **(Paper II, Fig. S10)**. Other residues that must play a role in the instability of the *Pf*ActI filaments: G115, K270, and A272 (in *Pf*ActI) are substituted by T115, R270, and C272 in *Pf*ActII.

In *Pf*ActII, fragmentation could be mediated *in vivo* by other mechanisms like ABPs or the oxidation of C272. Yet another difference between *Plasmodium* actins is the content of cysteines. Human α-actin has five C (C10, C217, C257, C285, C374) while *Pf*ActI contains four (C218, C258, C286, C375) and *Pf*ActII has seven cysteines (C29, C52, C217, C258, C272, C286, and C375). Interestingly, *Pf*ActII has a C in the position 272 like non-muscle β and γ-actins, which showed to be the most reactive residue towards H_2O_2 in solution. The oxidation of actin caused negative effects in ABPs interactions and depolymerization (Wilson et al., 2016). In contrast, the residue 272 is replaced by an A in *Pf*ActI. Indeed, this substitution caused structural differences between *Plasmodium* actins. In **paper I**, the mutation A272C in *Pf*ActI that mimics *Pf*ActII favored the stable A-loop conformation (1ab). Perhaps, the influence of ROS in the actin dynamics could have different effects in the *Plasmodium* actins *in vivo,* like the induction of depolymerization or fragmentation in *Pf*ActII under specific conditions. This is something that should be studied in the future.

5.3. Changes in the D-loop promote different effects in *Plasmodium* actins

While the lateral contacts between actin monomers are important for filament stability, the longitudinal contacts are also essential. The D-loop plays the main role in those interactions. The major difference in the *Plasmodium* actins' D-loop in relation to α-actin is the tip of the loop. Both actins have a substitution of Q42 and G49 (in α-actins) by P41 and E48 (in *Pf*ActII). In *Pf*ActI, these residues (P42 and E49) showed an effect on the P_i release and are possibly related to the closed conformation of the D-loop **(Paper I)**. The mutation P42Q

that increases the filament stability *in vitro* is lethal *in vivo* (Douglas et al., 2018). Also, it has been observed in filamentous α-actins that Y169 forms an N-H···π bond with the side chain of Q49 (Chou & Pollard, 2019). However, E50 (in F-*Pf*ActI) or Q49 (in F-*Pf*ActII) adopt an opposite orientation.

Despite the similarity of this loop between both isoforms, possibly a few changes in the D-loop, in addition to the lateral contacts and the A-loop conformation, contributes to the instability of *Pf*ActI filaments. However, in *Pf*ActII, the P41 and E48 substitutions in the D-loop do not drastically affect the length of the filaments. Another factor that could induce filament stability in *Pf*ActII involves the residues M40, I139, and V170, which may contribute to strengthening the hydrophobic interactions between the SD3 of one monomer and the D-loop of the adjacent monomer **(Paper II, Fig. 7)**.

5.4. Phosphate release

Details of how phosphate is released from the active site of actin remain controversial. The last cryo-EM structures of canonical actins (Chou & Pollard, 2019) and *Pf*ActI **(Paper III)** proposed two possible paths for phosphate leaving. The first one describes a tunnel from the active site to the "backdoor," which is closed by N111 and R177 in the AMP-PNP and ADP- P_i states but is partially open in the filament structure in the ADP state (4.2 Å distance between side chains). On the other hand, in **paper III**, we proposed an alternative path, a closed or open channel, depending on the rotamer conformation of N115 and W79 (N116 and Y80 in *Pf*ActI) **(Paper II, Fig. 22 and paper III, Fig. 4)**.

Additionally, the second path suggested for phosphate leaving is blocked by N115 and W79, as F-*Pf*ActI and most canonical actins in a filament form. Nevertheless, the G-*Pf*ActI (4CBU and 6I4E) crystal structures in ATP-Ca^{2+} and ADP-Mg^{2+} state show a double rotamer conformation of N115, one of the

conformations turns to the opposite side. Further experiments need to be done to confirm if an alternative path of phosphate release is possible.

5.5. Effect of JAS in the filamentous *Plasmodium* actins

Like canonical actins, JAS stabilizes the *Plasmodium* actin filaments without disturbing the architecture of the polymer. The binding site of JAS is the same as for phalloidin; between three protomers. Studies in canonical actins suggested that the D-loop state could contribute to the filament stability. An open D-loop state is reported in rabbit skeletal muscle α-actin in the presence of a modified JAS (JAS-cLys), phalloidin in ADP-Mg^{2+} state, and α-actin-ADP–BeFx state (Merino et al., 2018; Pospich et al., 2020). A recent publication also showed an open D-loop conformation in F-actin-ADP-Mg^{2+} from *Zea mays.* They also suggest that the F-*Zm*Act is more stable and rigid than α-actins and JAS-stabilized *Pf*ActI (Ren et al., 2019). On the other hand, other cryo-EM structures of α-actin bound to JAS or with ADP-Mg^{2+}, AMPPNP or ADP-P_i did not have changes in the D-loop state (Chou & Pollard, 2019, 2020). In *Plasmodium* actins, JAS stabilizes the filaments without affecting the D-loop conformation **(paper II and paper III)**. However, a salt bridge formed by R62 (SD2) and D289 (SD3) of two adjacent protomers in the JAS-stabilized F-*Pf*ActII structure is stronger. The distance in JAS-stabilized *Pf*ActII is 1.2 Å shorter in comparison with F-*Pf*ActII without JAS **(Paper II, Fig. 8)**. Possibly, F-*Pf*ActI has the same weak interaction. However, it is challenging to prove since a filament structure has not been possible to obtain without JAS.

Moreover, it has been shown that JAS inhibits P_i release without modifying the polymerization rate (Bubb et al., 2000; Vig et al., 2011). Consequently, it was observed that the phosphate is present in cryo-EM structures of α-actins polymerized in the presence of JAS (Chou & Pollard, 2019, 2020; Merino et al., 2018). In contrast, the density map of the phosphate is missing in JAS-

stabilized F-*Pf*Actins (Pospich et al., 2017, **paper II**, and **paper III**). Though, the conformation of S14 and the backdoor appear as in canonical actins when the phosphate is not released yet. Perhaps, the dynamics of phosphate release in *Plasmodium* actins are different, supporting the hypothesis of an additional path for the phosphate release **(Paper III, Fig. 4)**. Another option to consider is that JAS does not retain the phosphate as in α-actins, or that technical factors like the time between actin polymerization and grid preparation would affect the results.

5.6. Actin filaments are indispensable for the development of the *Plasmodium* life cycle

The distribution of filamentous *Plasmodium* actins is dynamic and associated with the nuclear periphery, pellicular membranes (motile of invasive stages), and during invasion (merozoites) at the tight junction (Angrisano et al., 2012). Numerous studies reveal the importance of *Pf*ActI for parasite motility, where the actin filaments are being one of the main components of the glideosome and other actomyosin motors. Additionally, Act1 is involved in other functions like apicoplast inheritance, host cell invasion (Das et al., 2017), endocytic trafficking (Smythe et al., 2008), and the morphology of the ring (asexual stage) (Grüring et al., 2011).

Indeed, *in vivo,* many factors can affect the actin filament dynamics like ABPs, interacting proteins of the actomyosin motor complexes, different intracellular environments (mosquito gut, salivary glands, kidney, erythrocytes), and post-translational modifications. For example, the actin nucleator *Pf*FRM2 (cytosol) and *Pf*ActI are shown to participate during cytokinesis in schizonts (Stortz et al., 2019), while *Pf*FRM1 is associated with gliding motility and invasion. It is proposed that *Pf*FRM1 initiates the actin polymerization at the apical end of the parasites, and GAC stabilizes the filaments along the pellicle that, in complex

with the other components of the glideosome, move towards the pole end (Baum et al., 2008; Jacot et al., 2016).

The instability of filamentous *Pf*ActI reported *in vitro* is consistent with the *in vivo* results. The speed of the sporozoites is co-related with the length of the filaments. When the concentration of F-actin is high or the polymerization is inhibited, the adhesion forces produced by the interaction of TRAP and extracellular substrate are weaker. Subsequently, the parasites move slower (Münter et al., 2009). Indeed, the high population of short filaments in *Pf*ActI is owed to structural changes explained before. Also, the mutation P42Q that increases the filament stability is lethal *in vivo* (Douglas et al., 2018).

On the other hand, most of the studies have focused on the first actin isoform. It is still not known if *Pf*ActII interacts with the glideosome or other actomyosin complexes. *Pf*ActII is exclusive to the mosquito stages. It is involved in exflagellation during gametocytogenesis (Deligianni et al., 2011; Vahokoski et al., 2014) and ookinete formation (Andreadaki et al., 2014). The polymerization dynamics of *Pf*ActII are different from *Pf*ActI. Filamentous *Pf*ActII appears to be more stable, and structural features like the A-loop conformation, longitudinal and lateral contacts can explain the stability of the filaments. Clearly, this isoform does not form long filaments at the same proportion and length as canonical actins. However, it is still unknown if *Pf*ActII forms short filaments *in vivo*. In such a scenario, the ABPs have to regulate depolymerization. This agrees with a previous report where the disruption of *Pb*CPβ (capping protein) showed to have a negative effect in the mosquito stages. Thus, sporozoites could not colonize the salivary glands because of a motility defect (Ganter et al., 2009). Other effects which occur in the cytosol redox regulation would contribute to the fragmentation (Wilson et al., 2016). On the other hand, if the length of the filaments is related to the speed of motility, long filaments of *Pf*ActII can explain why these mosquito stages are not motile or as fast as sporozoites. Further investigation needs to be carried out to

understand how the fragmentation process is in *Pf*ActII and the effects of the ABPs in the polymerization dynamics.

5.7. The interface of MyoA in complex with *Pf*ActII

Actin undergoes significant conformational changes from a monomeric to filamentous form (Oda & Maéda, 2010). However, it is not the case of the actomyosin complex (*Pf*ActI: MyoA); neither MyoA or *Pf*ActI induce considerable conformational changes. The actomyosin complex also encompasses the light chains which are indispensable to produce the active "power stroke" of the motor. Presumably, the short neck of MyoA works as a rigid lever arm. When ELC and MTIP bind to the neck region of MyoA causes stiffening of this region **(Paper III, Fig. 2)**. On the other hand, the actomyosin interface is highly conserved (Robert-Paganin et al., 2021); the main actomyosin interface involves contacts between the HTH motif and the HCM loop, additional contacts are produced by the loop 2, 3 and 4 **(Paper III, Fig. 3)**.

5.8. Looking for the interacting light chains of myosins class VI

Class VI myosins are implicated in critical cellular processes like motility, vesicular membrane traffic, in the maintenance of the stereocilia in cochlear hair cells and cellular adhesion (Buss et al., 2004; Hasson, 2003; Millo et al., 2004; Self et al., 1999). In *Plasmodium*, the function of these myosins is related to cell division. However, it is not entirely clear if they can participate in other cellular events.

In the initial stage of the project, three IQ motifs were predicted for MyoJ, and none for MyoK (Foth et al., 2006). Possibly because these sites are

degenerated in the apicomplexan parasites (Herm-Götz et al., 2002). The Calmodulin database and Meta-analysis predictor (CaM) is currently available (Mruk et al., 2014). This script predicts calmodulin target sites (8 different types of IQ motifs) from an entered sequence **(Table 9)**. Two types of motifs were identified: IQ-like [FILV]Qxxx[RK]xxxxxxxx and unconventional IQ [IVL]Qxxx[RK]xxxx[RK]xx[FILVWY]. For the predicted IQ-like motifs, the binding of myosin to the light chain could require the presence or absence of Ca^{2+}.

Myosin	Sequence	Residue number	Motif
*Pf*MyoJ	IQKKKRQTIVVSGH	195-208	IQ-Like
	LQNIIKYKNINVSS	574-587	IQ-Like
	IQGDEKKKEIRRNV	910-923	Unconventional
	IQSDEKNVPTTYLP	1589-1602	IQ-Like
	LQNKDKTINKIDNV	1614-1627	IQ-Like
*Pf*MyoK	FQKGYKKKKKKMIP	225-238	IQ-Like
	LQEDMKRYLTPKMF	1158-1171	IQ-Like
	IQCVYKYWLHIRKR	1218-1231	IQ-Like
	IQKNYRTYILRKKF	1302-1315	Unconventional
	FQKYFKQRVKAANI	1331-1344	IQ-Like
	IQRAFKKYMKKKYI	1368-1381	Unconventional

Table 9. Predicted IQ motifs of Myosins class VI using CaM, available at https://cam.umassmed.edu/.

Likely some of the predicted IQ-motifs participate in the myosin-light chain interaction, which should be investigated in the future. Moreover, class VI myosins contain two unique insertions (Ménétrey et al., 2005). In *Plasmodium* class VI myosins, the first insertion (insert 1) maintains the conservation of some amino acids. Since this insert is characteristic of this class, it could possibly be involved in nucleotide-binding similarly to mammalian myosins. On the other hand, the second insert is degenerated. It is an unconventional calmodulin motif that binds to $4Ca^{2+}$-CaM, and it is crucial for reverse directionality of the myosin toward the minus end of actin filaments **(Fig. 40)** (Ménétrey et al., 2005, 2007; Sweeney et al., 1999).

*Pf*Myosins of class VI are challenging to study *in vitro*. The interacting light chains are unknown, the IQ domains are degenerated, consequently the binding sites of the light chains remain unidentified. Besides, it is unclear if class VI myosins from *Plasmodium* can move towards the minus end of actin filaments. Identifying the specific light chains for *Pf*MyoJ and *Pf*MyoK would help improve protein expression and purification.

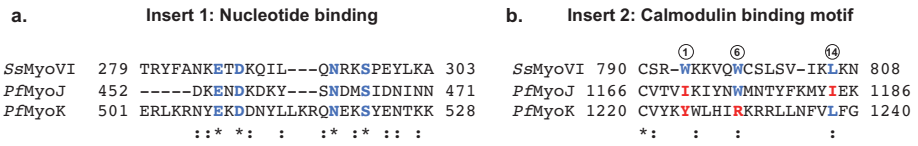

Figure 30. Alignment of the inserts 1 and 2 identified in Myosin VI from *Sus Scrofa* (Ménétrey et al., 2005). The following sequences were used for the alignment: *Sus scrofa* Myosin VI (SsMyoVI), *Plasmodium falciparum* Myosin J (*Pf*MyoJ), and Myosin K (*Pf*MyoK). The sequence alignment was performed in JalView using the T coffee server.

6. Conclusions and remarks

Actins are very well-studied proteins in many prokaryotic and eukaryotic organisms. Malaria parasites contain two actin isoforms. One isoform, *Pf*ActI is rather well characterized. However, there is a lack of knowledge concerning the second actin isoform. The general scope of this thesis was the biochemical and structural characterization of the malaria parasite actomyosin system, focusing on *Pf*ActII. This work provides *in vitro* evidence of functional and structural differences of *Plasmodium* and canonical actins. Few changes on the monomer structure of the *Pf*ActII compared to *Pf*ActI are involved in the stability of the actin filaments by spontaneous polymerization, like the A-loop conformation, the content of cysteines, and the plug. Also, the biochemical characterization of *Pf*ActII confirmed some unique features observed previously in *Pf*ActI, but not in canonical actins, like the non-linear slope during the elongation phase, C_c curves and excess of nucleation, suggesting the possibility of a different polymerization mechanism than in canonical actins. Further experiments need to be done to prove this hypothesis and study the polymerization properties in the presence of ABPs.

This work also contributes to the biochemical characterization of *Pf*ActI and the model of filament fragmentation proposed. Detailed structural information of filamentous actins and the glideosome complex are also provided in this thesis. Moreover, additional studies are needed *in vivo* to understand the role of these proteins in different cellular processes in the parasite life cycle and the function of each isoform in complex with the different actomyosin motors.

This information is a basis for generating a combination of antimalaria-drugs targeting the insect and human stages in order to prevent the spreading of the parasite and treat the acute infection. Since *Pf*ActII is the most diverse actin and exclusive to the insect cell stages, it could be a good target to design compounds that disrupt the development of the parasite during the mosquito

stages. Furthermore, this thesis provides structural actin filament information to generate analogs of JAS, specific for malaria actins.

This thesis also contributes to the structural determination of *Pf*ActI filaments decorated with MyoA:ELC:MTIP complex, giving molecular details of the actin: myosin interface and the active site. Also, a preliminary characterization of the myosins class VI. *Plasmodium* has six myosins, and the specific interacting light chains are only known for MyoA and MyoB. This work also provides a molecular biology tool (polyproteins) that could be used for the other myosins (in *Plasmodium*) to identify the interacting light chains.

Understanding the biology of the actomyosin components and its molecular differences between the malaria parasite and human may pave the way towards developing novel drugs targeting the actomyosin motors of the malaria parasites.

7. Future considerations

This work provided the first overview of the *Pf*ActII polymerization kinetics. The method to study actin polymerization used in this thesis was based on the increase of pyrene fluorescence upon polymerization. However, It will be interesting to study the polymerization dynamics also using a method that allows monitoring the actin polymerization and depolymerization in real-time, like TIRF microscopy. Lu and co-workers (2019) demonstrated that it is possible to observe *Plasmodium* actin filaments using TIRF. However, short filaments of *Pf*ActI (< 400 µm) were not likely to visualize using this method. In the case of *Pf*ActII, this isoform does not form short filaments, which is an advantage to study the kinetics of the protein using this technique.

On the other hand, the F-actin ATP hydrolysis and phosphate release mechanism are still unclear; structures of F-actin at atomic resolution will allow us to understand this process. Optimizing the crystallization conditions of Mg-ADP-*Pf*ActII in a complex with Fragmin is the next step. Alternatively, commercial fluorescence nucleotides that bind to canonical actins and hydrolyze within actin filaments are used to monitor actin polymerization and nucleotide exchange using TIFR microscopy (Colombo et al., 2021). Since actins are highly conserved proteins, it may be possible to adapt these methods to *Plasmodium* actins

Additionally, the biochemical experiments in this thesis were performed in the presence of polymerization buffer. However, *in vivo*, actin interacts with numerous proteins, like the ABPs from the parasite and possibly from the host. The next step in this project will be to study the polymerization properties in the presence of the ABPs using the biochemical methods already established, also crystallography, and TIRF microscopy.

In vivo, parasites develop into different cellular stages during their life cycle, and some of these forms move faster than the others; for example, sporozoites are the fastest form and merozoites are almost nonmotile (Carruthers &

Tomley, 2008; Frénal, Dubremetz, et al., 2017). Understanding the differences of force generation by the different myosins in complex with *Pf*ActI or *Pf*ActII will give us information on the roles of different actomyosin motors during the different stages of the parasite life cycle. Thus, motility assays using the different actomyosin motors in *Plasmodium* could complement our study.

In the future, it will be interesting to obtain cryo-EM structures of the actomyosin motor with additional components of the glideosome, like the proteins that form the bridge between the PM and the IMC to GAP and GAC proteins will give us information about the 3D geometry of the entire glideosome complex.

Finally, the characterization of class VI myosins is in progress. Identifying the interacting light chains is a key to obtain soluble protein for the biochemical and structural characterization. Additionally, pull-down experiments *in vivo* using a tagged protein could complement the experiments to elucidate the interacting proteins.

References

Adamek, N., & Geeves, M. A. (2014). Use of pyrene-labelled actin to probe actin-myosin interactions: kinetic and equilibrium studies. *Exp Suppl*, *105*, 87–104. https://doi.org/10.1007/978-3-0348-0856-9_5

Addou, S., Rentzsch, R., Lee, D., & Orengo, C. A. (2009). Domain-Based and Family-Specific Sequence Identity Thresholds Increase the Levels of Reliable Protein Function Transfer. *Journal of Molecular Biology*, *387*(2), 416–430. https://doi.org/10.1016/j.jmb.2008.12.045

Akıl, C., & Robinson, R. C. (2018). Genomes of Asgard archaea encode profilins that regulate actin. *Nature*, *562*(7727), 439–443. https://doi.org/10.1038/s41586-018-0548-6

Alberts, B., Johnson, A., Lewis, J., Raff, M., Roberts, K., & Walter, P. (2002). The Self-Assembly and Dynamic Structure of Cytoskeletal Filaments. In *Molecular Biology of the Cell* (4th ed., Vol. 3111, pp. 1–5). Garland Science. https://www.ncbi.nlm.nih.gov/books/NBK26862/

Aly, A. S. I., Vaughan, A. M., & Kappe, S. H. I. (2009). Malaria parasite development in the mosquito and infection of the mammalian host. *Annual Review of Microbiology*, *63*, 195–221. https://doi.org/10.1146/annurev.micro.091208.073403

Andreadaki, M., Morgan, R. N., Deligianni, E., Kooij, T. W. A., Santos, J. M., Spanos, L., Matuschewski, K., Louis, C., Mair, G. R., & Siden-Kiamos, I. (2014). Genetic crosses and complementation reveal essential functions for the *P lasmodium* stage-specific actin2 in sporogonic development. *Cellular Microbiology*, *16*(5), 751–767. https://doi.org/10.1111/cmi.12274

Angrisano, F., Riglar, D. T., Sturm, A., Volz, J. C., Delves, M. J., Zuccala, E. S., Turnbull, L., Dekiwadia, C., Olshina, M. A., Marapana, D. S., Wong, W., Mollard, V., Bradin, C. H., Tonkin, C. J., Gunning, P. W., Ralph, S. A., Whitchurch, C. B., Sinden, R. E., Cowman, A. F., … Baum, J. (2012). Spatial localisation of actin filaments across developmental stages of the malaria parasite. *PLoS ONE*, *7*(2), 32188. https://doi.org/10.1371/journal.pone.0032188

Antinori, S., Galimberti, L., Milazzo, L., & Corbellino, M. (2012). Biology of human malaria plasmodia including Plasmodium knowlesi. *Mediterranean Journal of Hematology and Infectious Diseases*, *4*(1), 201. https://doi.org/10.4084/MJHID.2012.013

Bannister, L. H., Mitchell, G. H., Butcher, G. A., Dennis, E. D., & Cohen, S. (1986). Structure and development of the surface coat of erythrocytic merozoites of Plasmodium knowlesi. *Cell and Tissue Research*, *245*(2), 281–290. https://doi.org/10.1007/BF00213933

Barth, H. G., Jackson, C., & Boyes, B. E. (1994). Size Exclusion Chromatography. *Analytical Chemistry*, *66*(12), 595–620. https://doi.org/10.1021/ac00084a022

Baum, J., Richard, D., Healer, J., Rug, M., Krnajski, Z., Gilberger, T. W., Green, J. L., Holder, A. A., & Cowman, A. F. (2006). A conserved molecular motor drives cell invasion and gliding motility across malaria life cycle stages and other apicomplexan parasites. *Journal of Biological Chemistry*, *281*(8), 5197–5208. https://doi.org/10.1074/jbc.M509807200

Baum, J., Tonkin, C. J., Paul, A. S., Rug, M., Smith, B. J., Gould, S. B., Richard, D., Pollard, T. D., & Cowman, A. F. (2008). A Malaria Parasite Formin Regulates Actin Polymerization and Localizes to the Parasite-Erythrocyte Moving Junction during Invasion. *Cell Host and Microbe*, *3*(3), 188–198. https://doi.org/10.1016/j.chom.2008.02.006

Becker, K. (2011). Apicomplexan Parasites: Molecular Approaches toward Targeted Drug Development. In K. Becker (Ed.), *Apicomplexan Parasites: Molecular Approaches toward Targeted Drug Development*. Wiley-VCH Verlag GmbH & Co. KGaA. https://doi.org/10.1002/9783527633883

Bergman, L. W. (2003). Myosin A tail domain interacting protein (MTIP) localizes to the inner membrane complex of Plasmodium sporozoites. *Journal of Cell Science*, *116*(1), 39–49. https://doi.org/10.1242/jcs.00194

Besteiro, S., Dubremetz, J.-F. F., & Lebrun, M. (2011). The moving junction of apicomplexan parasites: A key structure for invasion. *Cellular Microbiology0*, *13*(6), 797–805. https://doi.org/10.1111/j.1462-5822.2011.01597.x

Bhargav, S. P., Vahokoski, J., Kumpula, E. P., & Kursula, I. (2013). Crystallization and preliminary structural characterization of the two actin isoforms of the malaria parasite. *Acta Crystallographica Section F: Structural Biology and Crystallization Communications*, *69*(10), 1171–1176. https://doi.org/10.1107/S174430911302441X

Blackman, M. J., & Carruthers, V. B. (2013). Recent insights into apicomplexan parasite egress provide new views to a kill. *Current Opinion in Microbiology*, *16*(4), 459–464. https://doi.org/10.1016/j.mib.2013.04.008

Blake, T. C. A., Haase, S., & Baum, J. (2020). Actomyosin forces and the energetics of red blood cell invasion by the malaria parasite Plasmodium falciparum. *BioRxiv*, *44*, 2020.06.25.171900. https://doi.org/10.1101/2020.06.25.171900

Blanchoin, L., & Pollard, T. D. (1999). Mechanism of interaction of Acanthamoeba actophorin (ADF/Cofilin) with actin filaments. *Journal of Biological Chemistry*, *274*(22), 15538–15546. https://doi.org/10.1074/jbc.274.22.15538

Bloland, P. B. (2001). Drug resistance in malaria Drug resistance in malaria. In *World Health Organization*. http://www.who.int/emc

Bookwalter, C. S., Tay, C. L., Mccrorie, R., Previs, M. J., Lu, H., Krementsova, E. B., Fagnant, P. M., Baum, J., & Trybus, K. M. (2017). *Reconstitution of the Malaria Parasite Glideosome Reconstitution of the core of the malaria parasite glideosome with recombinant Plasmodium class XIV myosin A and Plasmodium actin*. https://doi.org/10.1074/jbc.M117.813972

Bork, P., Sander, C., & Valencia, A. (1992). An ATPase domain common to prokaryotic cell cycle proteins, sugar kinases, actin, and hsp70 heat shock proteins. *Proceedings of the National Academy of Sciences of the United States of America*, *89*(16), 7290–7294. https://doi.org/10.1073/pnas.89.16.7290

Boucher, L. E., & Bosch, J. (2015). The apicomplexan glideosome and adhesins - Structures and function. In *Journal of Structural Biology* (Vol. 190, Issue 2, pp. 93–114). Academic Press Inc. https://doi.org/10.1016/j.jsb.2015.02.008

Bourgard, C., Albrecht, L., Kayano, A. C. A. V., Sunnerhagen, P., & Costa, F. T. M. (2018). Plasmodium vivax biology: Insights provided by genomics, transcriptomics and proteomics. *Frontiers in Cellular and Infection Microbiology*, *8*(FEB), 34. https://doi.org/10.3389/fcimb.2018.00034

Brooks, F. J., & Carlsson, A. E. (2008). Actin polymerization overshoots and ATP hydrolysis as assayed by pyrene fluorescence. *Biophysical Journal*, *95*(3), 1050–1062. https://doi.org/10.1529/biophysj.107.123125

Bubb, M. R., Senderowicz, A. M. J., Sausville, E. A., Duncan, K. L. K., & Korn, E. D. (1994). Jasplakinolide, a cytotoxic natural product, induces actin polymerization and competitively inhibits the binding of phalloidin to F-actin. *Journal of Biological Chemistry*, *269*(21), 14869–14871. https://pubmed.ncbi.nlm.nih.gov/8195116/

Bubb, M. R., Spector, I., Beyer, B. B., & Fosen, K. M. (2000). Effects of jasplakinolide on the kinetics of actin polymerization. An explanation for certain in vivo observations. *Journal of Biological Chemistry*, *275*(7), 5163–5170. https://doi.org/10.1074/jbc.275.7.5163

Burgess, R. R. (2018). A brief practical review of size exclusion chromatography: Rules of thumb, limitations, and troubleshooting. *Protein Expression and Purification*, *150*, 81–85. https://doi.org/10.1016/j.pep.2018.05.007

Buss, F., Spudich, G., & Kendrick-Jones, J. (2004). Myosin VI: Cellular functions and motor properties. *Annual Review of Cell and Developmental Biology*, *20*, 649–676. https://doi.org/10.1146/annurev.cellbio.20.012103.094243

Cao, W., Goodarzi, J. P., & De La Cruz, E. M. (2006). Energetics and Kinetics of Cooperative Cofilin-Actin Filament Interactions. *Journal of Molecular Biology*, *361*(2), 257–267. https://doi.org/10.1016/j.jmb.2006.06.019

Carlier, M. F., Pantaloni, D., & Korn, E. D. (1985). Polymerization of ADP-actin and ATP-actin under sonication and characteristics of the ATP-actin equilibrium polymer. *Journal of Biological Chemistry*, *260*(11), 6565–6571. https://doi.org/10.1016/s0021-9258(18)88819-6

Carlier, Marie France, Hertzog, M., Didry, D., Renault, L., Cantrelle, F. X., Van Heijenoort, C., Knossow, M., & Guittet, E. (2007). Structure, function, and evolution of the β-thymosin/WH2 (WASP-homology2) actin-binding module. *Annals of the New York Academy of Sciences*, *1112*, 67–75. https://doi.org/10.1196/annals.1415.037

Carruthers, V. B., & Tomley, F. M. (2008). Microneme proteins in apicomplexans.

Subcellular Biochemistry, *47*, 33–45. https://doi.org/10.1007/978-0-387-78267-6_2

Chambers, A. C., Aksular, M., Graves, L. P., Irons, S. L., Possee, R. D., & King, L. A. (2018). Overview of the Baculovirus Expression System. In *Current Protocols in Protein Science* (Vol. 91, Issue 1, pp. 5.4.1-5.4.6). Blackwell Publishing Inc. https://doi.org/10.1002/cpps.47

Chou, S. Z., & Pollard, T. D. (2019). Mechanism of actin polymerization revealed by cryo-EM structures of actin filaments with three different bound nucleotides. *Proceedings of the National Academy of Sciences of the United States of America*, *116*(10), 4265–4274. https://doi.org/10.1073/pnas.1807028115

Chou, S. Z., & Pollard, T. D. (2020). Cryo-electron microscopy structures of pyrene-labeled ADP-Pi- and ADP-actin filaments. *Nature Communications*, *11*(1), 1–9. https://doi.org/10.1038/s41467-020-19762-1

Colombo, J., Antkowiak, A., Kogan, K., Kotila, T., Elliott, J., Guillotin, A., Lappalainen, P., & Michelot, A. (2021). A functional family of fluorescent nucleotide analogues to investigate actin dynamics and energetics. *Nature Communications*, *12*(1), 1–13. https://doi.org/10.1038/s41467-020-20827-4

Conchaudron, A. P., Didry, D., Le, K. H. D., Larquet, E., Boisset, N., Pantaloni, D., & Carlier, M. F. (2006). Analysis of tetramethylrhodamine-labeled actin polymerization and interaction with actin regulatory proteins. *Journal of Biological Chemistry*, *281*(33), 24036–24047. https://doi.org/10.1074/jbc.M602747200

Cooper, J A, Buhle, E. L., Walker, S. B., Tsong, T. Y., & Pollard, T. D. (1983). Kinetic evidence for a monomer activation step in actin polymerization. *Biochemistry*, *22*(9), 2193–2202. http://www.ncbi.nlm.nih.gov/pubmed/6860660

Cooper, John A., Walker, S. B., & Pollard, T. D. (1983). Pyrene actin: documentation of the validity of a sensitive assay for actin polymerization. *Journal of Muscle Research and Cell Motility*, *4*(2), 253–262. https://doi.org/10.1007/BF00712034

Courtemanche, N., & Pollard, T. D. (2013). Interaction of profilin with the barbed end of actin filaments. *Biochemistry*, *52*(37), 6456–6466. https://doi.org/10.1021/bi400682n

Cowman, A. F., Berry, D., & Baum, J. (2012). The cellular and molecular basis for malaria parasite invasion of the human red blood cell. *Journal of Cell Biology*, *198*(6), 961–971. https://doi.org/10.1083/jcb.201206112

Cramer, L. P. (2000). Myosin VI: Roles for a minus end-directed actin motor in cells. In *Journal of Cell Biology* (Vol. 150, Issue 6). Rockefeller University Press. https://doi.org/10.1083/jcb.150.6.F121

Crick, A. J., Theron, M., Tiffert, T., Lew, V. L., Cicuta, P., & Rayner, J. C. (2014). Quantitation of malaria parasite-erythrocyte cell-cell interactions using optical tweezers. *Biophysical Journal*, *107*(4), 846–853. https://doi.org/10.1016/j.bpj.2014.07.010

Crompton, P. D., Moebius, J., Portugal, S., Waisberg, M., Hart, G., Garver, L. S., Miller, L. H., Barillas-Mury, C., & Pierce, S. K. (2014). Malaria Immunity in Man and Mosquito: Insights into Unsolved Mysteries of a Deadly Infectious Disease. *Annual Review of Immunology*, *32*(1), 157–187. https://doi.org/10.1146/annurev-immunol-032713-120220

Das, S., Lemgruber, L., Tay, C. L., Baum, J., & Meissner, M. (2017). Multiple essential functions of Plasmodium falciparum actin-1 during malaria blood-stage development. *BMC Biology*, *15*(1), 70. https://doi.org/10.1186/s12915-017-0406-2

De Greef, T. F. A., Smulders, M. M. J., Wolffs, M., Schenning, A. P. H. J., Sijbesma, R. P., & Meijer, E. W. (2009). Supramolecular polymerization. *Chemical Reviews*, *109*(11), 5687–5754. https://doi.org/10.1021/cr900181u

De Niz, M., Burda, P.-C., Kaiser, G., del Portillo, H. A., Spielmann, T., Frischknecht, F., & Heussler, V. T. (2016). Progress in imaging methods: insights gained into Plasmodium biology. *Nature Reviews Microbiology*, *15*(1), 37–54. https://doi.org/10.1038/nrmicro.2016.158

Deligianni, E., Morgan, R. N., Bertuccini, L., Kooij, T. W. A., Laforge, A., Nahar, C., Poulakakis, N., Schüler, H., Louis, C., Matuschewski, K., & Siden-Kiamos, I. (2011). Critical role for a stage-specific actin in male exflagellation of the malaria parasite. *Cellular Microbiology*, *13*(11), 1714–1730. https://doi.org/10.1111/j.1462-5822.2011.01652.x

Dobrowolski, J. M., Niesman, I. R., & Sibley, L. D. (1997). Actin in the parasite toxoplasma gondii is encoded by a single copy gene, act1 and exists primarily in a globular form. *Cell Motility and the Cytoskeleton*, *37*(3), 253–262. https://doi.org/10.1002/(SICI)1097-0169(1997)37:3<253::AID-CM7>3.0.CO;2-7

Dobrowolski, J. M., & Sibley, L. D. (1996). Toxoplasma invasion of mammalian cells is powered by the actin cytoskeleton of the parasite. *Cell*, *84*(6), 933–939. https://doi.org/10.1016/S0092-8674(00)81071-5

Dominguez, R. (2004). Actin-binding proteins - A unifying hypothesis. *Trends in Biochemical Sciences*, *29*(11), 572–578. https://doi.org/10.1016/j.tibs.2004.09.004

Dominguez, R., & Holmes, K. C. (2011). Actin structure and function. *Annual Review of Biophysics*, *40*(1), 169–186. https://doi.org/10.1146/annurev-biophys-042910-155359

Dondorp, A. M., & Von Seidlein, L. (2017). Malaria. In J. Cohen, W. G. Powderly, & S. M. Opal (Eds.), *Infectious Diseases* (4th ed., Vol. 2, Issue 10130, pp. 1014–1024). Elsevier. https://doi.org/10.1016/S0140-6736(18)30324-6

Doolittle, L. K., Rosen, M. K., & Padrick, S. B. (2013). Measurement and Analysis of In Vitro Actin Polymerization. In *Methods Mol Biol* (Vol. 1046, pp. 273–293). https://doi.org/10.1007/978-1-62703-538-5_16

Douglas, R. G., Nandekar, P., Aktories, J. E., Kumar, H., Weber, R., Sattler, J. M.,

Singer, M., Lepper, S., Sadiq, S. K., Wade, R. C., & Frischknecht, F. (2018). Inter-subunit interactions drive divergent dynamics in mammalian and Plasmodium actin filaments. *PLoS Biology*, *16*(7), e2005345–e2005345. https://doi.org/10.1371/journal.pbio.2005345

Drazic, A., Aksnes, H., Marie, M., Boczkowska, M., Varland, S., Timmerman, E., Foyn, H., Glomnes, N., Rebowski, G., Impens, F., Gevaert, K., Dominguez, R., & Arnesen, T. (2018). NAA80 is actin's N-terminal acetyltransferase and regulates cytoskeleton assembly and cell motility. *Proceedings of the National Academy of Sciences of the United States of America*, *115*(17), 4399–4404. https://doi.org/10.1073/pnas.1718336115

Drenckhahn, D., & Pollard, T. D. (1986). Elongation of actin filaments is a diffusion-limited reaction at the barbed end and is accelerated by inert macromolecules. *Journal of Biological Chemistry*, *261*(27), 12754–12758.

Drewry, L. L., & Sibley, L. D. (2015). Toxoplasma actin is required for efficient host cell invasion. *MBio*, *6*(3). https://doi.org/10.1128/mBio.00557-15

Duong-Ly, K. C., & Gabelli, S. B. (2014). Gel filtration chromatography (size exclusion chromatography) of proteins. In *Methods in Enzymology* (Vol. 541, pp. 105–114). Academic Press Inc. https://doi.org/10.1016/B978-0-12-420119-4.00009-4

Fairhurst, R. M., & Dondorp, A. M. (2016). Artemisinin-Resistant Plasmodium falciparum Malaria. In *Microbiology Spectrum* (Vol. 4, Issue 3, pp. 409–429). American Society of Microbiology. https://doi.org/10.1128/microbiolspec.ei10-0013-2016

Fender, P., Moriscot, C., Ruigrok, R. W. ., & Schoehn, G. (2014). Electron Microscopy of Viruses: Techniques to Prepare Viruses and Viral Proteins for Observation by Electron Microscopy☆. In *Reference Module in Biomedical Sciences*. Elsevier. https://doi.org/10.1016/b978-0-12-801238-3.02563-0

Ferron, F., Rebowski, G., Lee, S. H., & Dominguez, R. (2007). Structural basis for the recruitment of profilin-actin complexes during filament elongation by Ena/VASP. *EMBO Journal*, *26*(21), 4597–4606. https://doi.org/10.1038/sj.emboj.7601874

Fiaschi, T., Cozzi, G., Raugei, G., Formigli, L., Ramponi, G., & Chiarugi, P. (2006). Redox regulation of β-actin during integrin-mediated cell adhesion. *Journal of Biological Chemistry*, *281*(32), 22983–22991. https://doi.org/10.1074/jbc.M603040200

Field, S. J., Pinder, J. C., Clough, B., Dluzewski, A. R., Wilson, R. J. M., & Gratzer, W. B. (1993). Actin in the merozoite of the malaria parasite, Plasmodium falciparum. *Cell Motility and the Cytoskeleton*, *25*(1), 43–48. https://doi.org/10.1002/cm.970250106

Foth, B. J., Goedecke, M. C., & Soldati, D. (2006). New insights into myosin evolution and classification. *Proceedings of the National Academy of Sciences of the United States of America*, *103*(10), 3681–3686. https://doi.org/10.1073/pnas.0506307103

Frank, J. (2002). Single-particle imaging of macromolecules by cryo-electron microscopy. *Annual Review of Biophysics and Biomolecular Structure*, *31*, 303–319. https://doi.org/10.1146/annurev.biophys.31.082901.134202

Frénal, K., Dubremetz, J.-F., Lebrun, M., & Soldati-Favre, D. (2017). Gliding motility powers invasion and egress in Apicomplexa. *Nature Reviews Microbiology*, *15*(11), 645–660. https://doi.org/10.1038/nrmicro.2017.86

Frénal, K., Jacot, D., Hammoudi, P. M., Graindorge, A., MacO, B., & Soldati-Favre, D. (2017). Myosin-dependent cell-cell communication controls synchronicity of division in acute and chronic stages of Toxoplasma gondii. *Nature Communications*, *8*(1), 1–18. https://doi.org/10.1038/ncomms15710

Frénal, K., Krishnan, A., & Soldati-Favre, D. (2020). The Actomyosin Systems in Apicomplexa. In *Advances in Experimental Medicine and Biology* (Vol. 1239, pp. 331–354). Springer. https://doi.org/10.1007/978-3-030-38062-5_14

Frénal, K., Marq, J. B., Jacot, D., Polonais, V., & Soldati-Favre, D. (2014). Plasticity between MyoC- and MyoA-glideosomes: an example of functional compensation in Toxoplasma gondii invasion. *PLoS Pathogens*, *10*(10), e1004504. https://doi.org/10.1371/journal.ppat.1004504

Frieden, C. (1983). Polymerization of actin: Mechanism of the Mg2+-induced process at pH 8 and 20°C. *Proceedings of the National Academy of Sciences of the United States of America*, *80*(21 I), 6513–6517. https://doi.org/10.1073/pnas.80.21.6513

Fujii, T., Iwane, A. H., Yanagida, T., & Namba, K. (2010). Direct visualization of secondary structures of F-actin by electron cryomicroscopy. *Nature*, *467*(7316), 724–728. https://doi.org/10.1038/nature09372

Fujiwara, I., Vavylonis, D., & Pollard, T. D. (2007). Polymerization kinetics of ADP- and ADP-Pi-actin determined by fluorescence microscopy. *Proc Natl Acad Sci U S A*, *104*(21), 8827–8832. https://doi.org/10.1073/pnas.0702510104

Galkin, V. E., Orlova, A., Cherepanova, O., Lebart, M. C., & Egelman, E. H. (2008). High-resolution cryo-EM structure of the F-actin-fimbrin/plastin ABD2 complex. *Proceedings of the National Academy of Sciences of the United States of America*, *105*(5), 1494–1498. https://doi.org/10.1073/pnas.0708667105

Ganter, M., Schüler, H., & Matuschewski, K. (2009). Vital role for the Plasmodium actin capping protein (CP) beta-subunit in motility of malaria sporozoites. *Molecular Microbiology*, *74*(6), 1356–1367. https://doi.org/10.1111/j.1365-2958.2009.06828.x

GEHealthcare. (2018). *Handbooks from GE Healthcare Life Sciences For more information refer to gelifesciences.com/handbooks Affinity Chromatography ÄKTA™ Laboratory-scale Chromatography Systems Isolation of mononuclear cells Microcarrier Cell Culture Nucleic Acid Sample Prepar*.

Gershberg, J., Fennel, F., Rehm, T. H., Lochbrunner, S., & Würthner, F. (2016). Anti-cooperative supramolecular polymerization: A new K2-K model applied to the

self-assembly of perylene bisimide dye proceeding via well-defined hydrogen-bonded dimers. *Chemical Science*, *7*(3), 1729–1737. https://doi.org/10.1039/c5sc03759j

Glaeser, R. M. (2019). How Good Can Single-Particle Cryo-EM Become? What Remains before It Approaches Its Physical Limits? *Annual Review of Biophysics*, *48*, 45–61. https://doi.org/10.1146/annurev-biophys-070317-032828

Goddard, T. D., Huang, C. C., Meng, E. C., Pettersen, E. F., Couch, G. S., Morris, J. H., & Ferrin, T. E. (2018). UCSF ChimeraX: Meeting modern challenges in visualization and analysis. *Protein Science*, *27*(1), 14–25. https://doi.org/10.1002/pro.3235

Gordon, J. L., & Sibley, L. D. (2005). Comparative genome analysis reveals a conserved family of actin-like proteins in apicomplexan parasites. *BMC Genomics*, *6*, 179. https://doi.org/10.1186/1471-2164-6-179

Graindorge, A., Frénal, K., Jacot, D., Salamun, J., Marq, J. B., & Soldati-Favre, D. (2016). The Conoid Associated Motor MyoH Is Indispensable for Toxoplasma gondii Entry and Exit from Host Cells. *PLoS Pathogens*, *12*(1), 1–26. https://doi.org/10.1371/journal.ppat.1005388

Green, J. L., Martin, S. R., Fielden, J., Ksagoni, A., Grainger, M., Yim Lim, B. Y. S., Molloy, J. E., & Holder, A. A. (2006). The MTIP-myosin A complex in blood stage malaria parasites. *Journal of Molecular Biology*, *355*(5), 933–941. https://doi.org/10.1016/j.jmb.2005.11.027

Green, J. L., Wall, R. J., Vahokoski, J., Yusuf, N. A., Ridzuan, M. A. M., Stanway, R. R., Stock, J., Knuepfer, E., Brady, D., Martin, S. R., Howell, S. A., Pires, I. P., Moon, R. W., Molloy, J. E., Kursula, I., Tewari, R., & Holder, A. A. (2017). Compositional and expression analyses of the glideosome during the *Plasmodium* life cycle reveal an additional myosin light chain required for maximum motility. *Journal of Biological Chemistry*, jbc.M117.802769. https://doi.org/10.1074/jbc.M117.802769

Gregorio, C. C., Weber, A., Bondad, M., Pennise, C. R., & Fowler, V. M. (1995). Requirement of pointed-end capping by tropomodulin to maintain actin filament length in embryonic chick cardiac myocytes. *Nature*, *377*(6544), 83–86. https://doi.org/10.1038/377083a0

Grüring, C., Heiber, A., Kruse, F., Ungefehr, J., Gilberger, T.-W., & Spielmann, T. (2011). Development and host cell modifications of Plasmodium falciparum blood stages in four dimensions. *Nature Communications*, *2*, 165. https://doi.org/10.1038/ncomms1169

Gunning, P. W., Ghoshdastider, U., Whitaker, S., Popp, D., & Robinson, R. C. (2015). The evolution of compositionally and functionally distinct actin filaments. *Journal of Cell Science*, *128*(11), 2009–2019. https://doi.org/10.1242/jcs.165563

Håkansson, S., Morisaki, H., Heuser, J., & Sibley, L. D. (1999). Time-lapse video microscopy of gliding motility in Toxoplasma gondii reveals a novel, biphasic

mechanism of cell locomotion. *Molecular Biology of the Cell*, *10*(11), 3539–3547. https://doi.org/10.1091/mbc.10.11.3539

Hartley, M. A., Hofmann, N., Keitel, K., Kagoro, F., Moniz, C. A., Mlaganile, T., Samaka, J., Masimba, J., Said, Z., Temba, H., Gonzalez, I., Felger, I., Genton, B., & D'Acremont, V. (2020). Clinical relevance of low-density Plasmodium falciparum parasitemia in untreated febrile children: A cohort study. *PLoS Medicine*, *17*(9). https://doi.org/10.1371/journal.pmed.1003318

Hasson, T. (2003). Myosin VI: Two distinct roles in endocytosis. *Journal of Cell Science*, *116*(17), 3453–3461. https://doi.org/10.1242/jcs.00669

He, S., & Scheres, S. H. W. (2017). Helical reconstruction in RELION. *Journal of Structural Biology*, *198*(3), 163–176. https://doi.org/10.1016/j.jsb.2017.02.003

Heidecker, M., Yan-Marriott, Y., & Marriott, G. (1995). Proximity Relationships and Structural Dynamics of the Phalloidin Binding Site of Actin Filaments in Solution and on Single Actin Filaments on Heavy Meromyosin. *Biochemistry*, *34*(35), 11017–11025. https://doi.org/10.1021/bi00035a007

Heier, J. A., Dickinson, D. J., & Kwiatkowski, A. V. (2017). Measuring protein binding to F-actin by co-sedimentation. *Journal of Visualized Experiments*, *2017*(123), 55613. https://doi.org/10.3791/55613

Heintzelman, M. B. (2006). Cellular and Molecular Mechanics of Gliding Locomotion in Eukaryotes. *International Review of Cytology*, *251*, 79–129. https://doi.org/10.1016/S0074-7696(06)51003-4

Heintzelman, M. B. (2015). Gliding motility in apicomplexan parasites. *Seminars in Cell & Developmental Biology*, *46*, 135–142. https://doi.org/10.1016/j.semcdb.2015.09.020

Herm-Götz, A., Weiss, S., Stratmann, R., Fujita-Becker, S., Ruff, C., Meyhöfer, E., Soldati, T., Manstein, D. J., Geeves, M. A., & Soldati, D. (2002). Toxoplasma gondii myosin A and its light chain: A fast, single-headed, plus-end-directed motor. In *EMBO Journal* (Vol. 21, Issue 9). European Molecular Biology Organization. https://doi.org/10.1093/emboj/21.9.2149

Hertzog, M., & Carlier, M.-F. (2005). Functional Characterization of Proteins Regulating Actin Assembly. In *Current Protocols in Cell Biology* (Vol. 26, Issue 1, pp. 13.6.1-13.6.23). John Wiley & Sons, Inc. https://doi.org/10.1002/0471143030.cb1306s26

Hjernø, K. (2007). Protein identification by peptide mass fingerprinting. In *Mass Spectrometry Data Analysis in Proteomics* (Vol. 367, pp. 61–75). Humana Press. https://doi.org/10.1385/1-59745-275-0:61

Hliscs, M., Sattler, J. M., Tempel, W., Artz, J. D., Dong, A., Hui, R., Matuschewski, K., & Schüler, H. (2010). Structure and function of a G-actin sequestering protein with a vital role in malaria oocyst development inside the mosquito vector. *Journal of Biological Chemistry*, *285*(15), 11572–11583. https://doi.org/10.1074/jbc.M109.054916

Holmes, K. C., Popp, D., Gebhard, W., & Kabsch, W. (1990). The Structure of F-actin Calculated from X-ray Fibre Diagrams and the 0.6 nm Crystal Structure. In *Molecular Mechanisms in Muscular Contraction* (pp. 65–75). Macmillan Education UK. https://doi.org/10.1007/978-1-349-09814-9_3

Holzinger, A., & Blaas, K. (2016). Actin-dynamics in plant cells: The function of actin-perturbing substances: Jasplakinolide, chondramides, phalloidin, cytochalasins, and latrunculins. *Methods in Molecular Biology*, *1365*, 243–261. https://doi.org/10.1007/978-1-4939-3124-8_13

Hung, R. J., Pak, C. W., & Terman, J. R. (2011). Direct redox regulation of F-actin assembly and disassembly by Mical. *Science*, *334*(6063), 1710–1713. https://doi.org/10.1126/science.1211956

Ignatev, A., Bhargav, S. P., Vahokoski, J., Kursula, P., & Kursula, I. (2012). The lasso segment is required for functional dimerization of the Plasmodium formin 1 FH2 domain. *PLoS ONE*, *7*(3), 33586. https://doi.org/10.1371/journal.pone.0033586

Ismail, H. M., Barton, V., Phanchana, M., Charoensutthivarakul, S., Wong, M. H. L., Hemingway, J., Biagini, G. A., O'Neill, P. M., & Ward, S. A. (2016). Artemisinin activity-based probes identify multiple molecular targets within the asexual stage of the malaria parasites Plasmodium falciparum 3D7. *Proceedings of the National Academy of Sciences of the United States of America*, *113*(8), 2080–2085. https://doi.org/10.1073/pnas.1600459113

Jacot, D., Tosetti, N., Pires, I., Stock, J., Graindorge, A., Hung, Y.-F. F., Han, H., Tewari, R., Kursula, I., & Soldati-Favre, D. (2016). An Apicomplexan Actin-Binding Protein Serves as a Connector and Lipid Sensor to Coordinate Motility and Invasion. *Cell Host and Microbe*, *20*(6), 731–743. https://doi.org/10.1016/j.chom.2016.10.020

Jarvis, D. L. (2009). Chapter 14 Baculovirus-Insect Cell Expression Systems. In *Methods in Enzymology* (1st ed., Vol. 463, Issue C). Elsevier Inc. https://doi.org/10.1016/S0076-6879(09)63014-7

Jégou, A., Niedermayer, T., Orbán, J., Didry, D., Lipowsky, R., Carlier, M. F., & Romet-Lemonne, G. (2011). Individual actin filaments in a microfluidic flow reveal the mechanism of ATP hydrolysis and give insight into the properties of profilin. *PLoS Biology*, *9*(9). https://doi.org/10.1371/journal.pbio.1001161

Jeremy, M. B., John, L. T., & Lubert, S. (2002). Biochemistry - NCBI Bookshelf. In *Biochemistry, 5th edition*. W H Freeman. https://www.ncbi.nlm.nih.gov/books/NBK21154/

Jones, M. L., Collins, M. O., Goulding, D., Choudhary, J. S., & Rayner, J. C. (2012). Analysis of protein palmitoylation reveals a pervasive role in Plasmodium development and pathogenesis. *Cell Host and Microbe*, *12*(2), 246–258. https://doi.org/10.1016/j.chom.2012.06.005

Kabsch, W., Mannherz, H. G., Suck, D., Pai, E. F., & Holmes, K. C. (1990). Atomic structure of the actin: DNase I complex. *Nature*, *347*(6288), 37–44.

https://doi.org/10.1038/347037a0

Keeley, A., & Soldati, D. (2004). The glideosome: a molecular machine powering motility and host-cell invasion by Apicomplexa. *Trends in Cell Biology*, *14*(10), 528–532. https://doi.org/10.1016/j.tcb.2004.08.002

Kidmose, R. T., Juhl, J., Nissen, P., Boesen, T., Karlsen, J. L., & Pedersen, B. P. (2019). Namdinator - Automatic molecular dynamics flexible fitting of structural models into cryo-EM and crystallography experimental maps. *IUCrJ*, *6*(Pt 4), 526–531. https://doi.org/10.1107/S2052252519007619

Kooij, T. W. A., Janse, C. J., & Waters, A. P. (2006). Plasmodium post-genomics: Better the bug you know? In *Nature Reviews Microbiology* (Vol. 4, Issue 5, pp. 344–357). Nat Rev Microbiol. https://doi.org/10.1038/nrmicro1392

Kouyama, T., & Mihashi, K. (1981). Fluorimetry Study of N-(1-Pyrenyl)iodoacetamide-Labelled F-Actin: Local Structural Change of Actin Protomer both on Polymerization and on Binding of Heavy Meromyosin. *European Journal of Biochemistry*, *114*(1), 33–38. https://doi.org/10.1111/j.1432-1033.1981.tb06167.x

Kuhn, J. R., & Pollard, T. D. (2005). Real-time measurements of actin filament polymerization by total internal reflection fluorescence microscopy. *Biophysical Journal*, *88*(2), 1387–1402. https://doi.org/10.1529/biophysj.104.047399

Kühn, S., & Mannherz, H. G. (2016). Actin: Structure, function, dynamics, and interactions with bacterial toxins. In *Current Topics in Microbiology and Immunology* (Vol. 399, pp. 1–34). Springer Verlag. https://doi.org/10.1007/82_2016_45

Kumpula, E. P., Lopez, A. J., Tajedin, L., Han, H., & Kursula, I. (2019). Atomic view into plasmodium actin polymerization, ATP hydrolysis, and fragmentation. *PLoS Biology*, *17*(6), e3000315. https://doi.org/10.1371/journal.pbio.3000315

Kumpula, E. P., Pires, I., Lasiwa, D., Piirainen, H., Bergmann, U., Vahokoski, J., & Kursula, I. (2017). Apicomplexan actin polymerization depends on nucleation. *Scientific Reports*, *7*(1), 12137. https://doi.org/10.1038/s41598-017-11330-w

Lehtimaki, J., Hakala, M., & Lappalainen, P. (2017). Actin filament structures in migrating cells. *Handbook of Experimental Pharmacology*, *235*, 1–30. https://doi.org/10.1007/164_2016_28

Li, M. Z., & Elledge, S. J. (2012). *SLIC: A Method for Sequence- and Ligation-Independent Cloning* (pp. 51–59). Humana Press. https://doi.org/10.1007/978-1-61779-564-0_5

Liebschner, D., Afonine, P. V., Baker, M. L., Bunkoczi, G., Chen, V. B., Croll, T. I., Hintze, B., Hung, L. W., Jain, S., McCoy, A. J., Moriarty, N. W., Oeffner, R. D., Poon, B. K., Prisant, M. G., Read, R. J., Richardson, J. S., Richardson, D. C., Sammito, M. D., Sobolev, O. V., … Adams, P. D. (2019). Macromolecular structure determination using X-rays, neutrons and electrons: Recent developments in Phenix. *Acta Crystallographica Section D: Structural Biology*,

75(10), 861–877. https://doi.org/10.1107/S2059798319011471

Lindner, S. E., Swearingen, K. E., Harupa, A., Vaughan, A. M., Sinnis, P., Moritz, R. L., & Kappe, S. H. I. (2013). Total and putative surface proteomics of malaria parasite salivary gland sporozoites. *Molecular and Cellular Proteomics*, *12*(5), 1127–1143. https://doi.org/10.1074/mcp.M112.024505

Lu, H., Fagnant, P. M., & Trybus, K. M. (2019). Unusual dynamics of the divergent malaria parasite PfAct1 actin filament. *Proceedings of the National Academy of Sciences of the United States of America*, *116*(41), 20418–20427. https://doi.org/10.1073/pnas.1906600116

Lyumkis, D. (2019). Challenges and opportunities in cryo-EM single-particle analysis. *Journal of Biological Chemistry*, *294*(13), 5181–5197. https://doi.org/10.1074/jbc.REV118.005602

Mace, K. E., & Arguin, P. M. (2017). Malaria surveillance - United States, 2014. *MMWR Surveillance Summaries*, *66*(12), 1–24. https://doi.org/10.15585/mmwr.ss6612a1

Maguire, C. M., Rösslein, M., Wick, P., & Prina-Mello, A. (2018). Characterisation of particles in solution–a perspective on light scattering and comparative technologies. *Science and Technology of Advanced Materials*, *19*(1), 732–745. https://doi.org/10.1080/14686996.2018.1517587

Makkonen, M., Bertling, E., Chebotareva, N. A., Baump, J., & Lappalainen, P. (2013). Mammalian and malaria parasite cyclase-associated proteins catalyze nucleotide exchange on G-actin through a conserved mechanism. *Journal of Biological Chemistry*, *288*(2), 984–994. https://doi.org/10.1074/jbc.M112.435719

Mannherz, H. G. (1992). Crystallization of actin in complex with actin-binding proteins. *Journal of Biological Chemistry*, *267*(17), 11661–11664. https://pubmed.ncbi.nlm.nih.gov/1318297/

Maruyama, K. (2002). β-Actinin, Cap Z, Connectin and Titin: What's in a name? *Trends in Biochemical Sciences*, *27*(5), 264–266. https://doi.org/10.1016/S0968-0004(02)02068-6

Matsudaira, P. (1994). Actin crosslinking proteins at the leading edge. *Seminars in Cell and Developmental Biology*, *5*(3), 165–174. https://doi.org/10.1006/scel.1994.1021

Mattila, P. K., & Lappalainen, P. (2008). Filopodia: Molecular architecture and cellular functions. *Nature Reviews Molecular Cell Biology*, *9*(6), 446–454. https://doi.org/10.1038/nrm2406

McGhee, R. B. (1953). The infection by Plasmodium lophurae of duck erythrocytes in the chicken embryo. *The Journal of Experimental Medicine*, *97*(6), 773–782. https://doi.org/10.1084/jem.97.6.773

Meissner, M., Ferguson, D. J., & Frischknecht, F. (2013). Invasion factors of apicomplexan parasites: essential or redundant? *Current Opinion in*

Microbiology, *16*, 438–444. https://doi.org/10.1016/j.mib.2013.05.002

Mendes Pinto, I., Rubinstein, B., Kucharavy, A., Unruh, J. R., & Li, R. (2012). Actin Depolymerization Drives Actomyosin Ring Contraction during Budding Yeast Cytokinesis. *Developmental Cell*, *22*(6), 1247–1260. https://doi.org/10.1016/j.devcel.2012.04.015

Ménétrey, J., Bahloul, A., Wells, A. L., Yengo, C. M., Morris, C. A., Sweeney, H. L., & Houdusse, A. (2005). The structure of the myosin VI motor reveals the mechanism of directionality reversal. *Nature*, *435*(7043), 779–785. https://doi.org/10.1038/nature03592

Ménétrey, J., Llinas, P., Mukherjea, M., Sweeney, H. L., & Houdusse, A. (2007). The Structural Basis for the Large Powerstroke of Myosin VI. *Cell*, *131*(2), 300–308. https://doi.org/10.1016/j.cell.2007.08.027

Merino, F., Pospich, S., Funk, J., Wagner, T., Küllmer, F., Arndt, H. D., Bieling, P., & Raunser, S. (2018). Structural transitions of F-actin upon ATP hydrolysis at near-atomic resolution revealed by cryo-EM /631/535/1258/1259 /631/45/612/1228 /101 /101/28 article. *Nature Structural and Molecular Biology*, *25*(6), 528–537. https://doi.org/10.1038/s41594-018-0074-0

Meshnick, S. R. (2002). Artemisinin: Mechanisms of action, resistance and toxicity. *International Journal for Parasitology*, *32*(13), 1655–1660. https://doi.org/10.1016/S0020-7519(02)00194-7

Miller, A. L. (2011). The contractile ring. *Current Biology*, *21*(24), R976. https://doi.org/10.1016/j.cub.2011.10.044

Miller, L. H., Baruch, D. I., Marsh, K., & Doumbo, O. K. (2002). The pathogenic basis of malaria. *Nature*, *415*(6872), 673–679. https://doi.org/10.1038/415673a

Millo, H., Leaper, K., Lazou, V., & Bownes, M. (2004). Myosin VI plays a role in cell-cell adhesion during epithelial morphogenesis. *Mechanisms of Development*, *121*(11), 1335–1351. https://doi.org/10.1016/j.mod.2004.06.007

Mitome, M. (2018). Transmission Electron Microscope. In *Compendium of Surface and Interface Analysis* (Issue 1, pp. 1–9). Springer Singapore. https://doi.org/10.1007/978-981-10-6156-1_124

Moreau, C. A., Bhargav, S. P., Kumar, H., Quadt, K. A., Piirainen, H., Strauss, L., Kehrer, J., Streichfuss, M., Spatz, J. P., Wade, R. C., Kursula, I., & Frischknecht, F. (2017). A unique profilin-actin interface is important for malaria parasite motility. *PLoS Pathogens*, *13*(5). https://doi.org/10.1371/journal.ppat.1006412

Morrissette, N. S., & Sibley, L. D. (2002). *Cytoskeleton of Apicomplexan Parasites Cytoskeleton of Apicomplexan Parasites*. *66*(1). https://doi.org/10.1128/MMBR.66.1.21

Morton, W. M., Ayscough, K. R., & Mclaughlin, P. J. (2000). Latrunculin alters the actin-monomer subunit interface to prevent polymerization. *Nature Cell Biology*, *2*(6), 376–378. https://doi.org/10.1038/35014075

Mruk, K., Farley, B. M., Ritacco, A. W., & Kobertz, W. R. (2014). Calmodulation meta-analysis: Predicting calmodulin binding via canonical motif clustering. *Journal of General Physiology*, *144*(1), 105–114. https://doi.org/10.1085/jgp.201311140

Mueller, C., Graindorge, A., & Soldati-Favre, D. (2017). Functions of myosin motors tailored for parasitism. In *Current Opinion in Microbiology* (Vol. 40, pp. 113–122). Elsevier Ltd. https://doi.org/10.1016/j.mib.2017.11.003

Münter, S., Sabass, B., Selhuber-Unkel, C., Kudryashev, M., Hegge, S., Engel, U., Spatz, J. P., Matuschewski, K., Schwarz, U. S., & Frischknecht, F. (2009). Plasmodium Sporozoite Motility Is Modulated by the Turnover of Discrete Adhesion Sites. *Cell Host and Microbe*, *6*(6), 551–562. https://doi.org/10.1016/j.chom.2009.11.007

Nie, Y., Bellon-Echeverria, I., Trowitzsch, S., Bieniossek, C., & Berger, I. (2014). Multiprotein Complex Production in Insect Cells by Using Polyproteins. In C. Y. Wai (Ed.), *Structural Genomics: General Applications, Methods in Molecular Biology* (2nd ed., Vol. 1091, pp. 576–580). Springer Science+Business Media. https://doi.org/10.1016/B978-0-12-374984-0.01487-X

Nishida, E. (1985). Opposite Effects of Cofilin and Profilin from Porcine Brain on Rate of Exchange of Actin-Bound Adenosine 5′-Triphosphate. *Biochemistry*, *24*(5), 1160–1164. https://doi.org/10.1021/bi00326a015

Nogales, E. (2015). The development of cryo-EM into a mainstream structural biology technique. *Nature Methods*, *13*(1), 24–27. https://doi.org/10.1038/nmeth.3694

Oda, T., Iwasa, M., Aihara, T., Maéda, Y., & Narita, A. (2009). The nature of the globular- to fibrous-actin transition. *Nature*, *457*(7228), 441–445. https://doi.org/10.1038/nature07685

Oda, T., & Maéda, Y. (2010). Multiple Conformations of F-actin. In *Structure* (Vol. 18, Issue 7, pp. 761–767). Cell Press. https://doi.org/10.1016/j.str.2010.05.009

Oda, T., Makino, K., Yamashita, I., Namba, K., & Maéda, Y. (2001). Distinct structural changes detected by x-ray fiber diffraction in stabilization of F-actin by lowering pH and increasing ionic strength. *Biophysical Journal*, *80*(2), 841–851. https://doi.org/10.1016/S0006-3495(01)76063-8

Ojima, K. (2019). Myosin: Formation and maintenance of thick filaments. *Animal Science Journal*, *90*(7), 801–807. https://doi.org/10.1111/asj.13226

Okamoto, H., Fujita, H., Matsuyama, S., & Tsuyama, S. (1997). Purification, characterization, and localization of an ADP-ribosylactin hydrolase that uses ADP-ribosylated actin from rat brains as a substrate. *Journal of Biological Chemistry*, *272*(44), 28116–28125. https://doi.org/10.1074/jbc.272.44.28116

Olshina, M. A., Angrisano, F., Marapana, D. S., Riglar, D. T., Bane, K., Wong, W., Catimel, B., Yin, M.-X., Holmes, A. B., Frischknecht, F., Kovar, D. R., & Baum, J. (2015). Plasmodium falciparum coronin organizes arrays of parallel actin filaments potentially guiding directional motility in invasive malaria parasites. *Malaria Journal*, *14*(1), 280. https://doi.org/10.1186/s12936-015-0801-5

Opitz, C., & Soldati, D. (2002). “The glideosome”: a dynamic complex powering gliding motion and host cell invasion by Toxoplasma gondii. *Molecular Microbiology*, *45*(3), 597–604. http://www.ncbi.nlm.nih.gov/pubmed/12139608

P Emsley, B. L. W. S. K. C. (2010). Features and development of Coot. *Acta Crystallogr D*, *66*, 486–501.

Pagni, M., Ioannidis, V., Cerutti, L., Zahn-Zabal, M., Jongeneel, C. V., & Falquet, L. (2004). MyHits: a new interactive resource for protein annotation and domain identification. *Nucleic Acids Research*, *32*(Web Server issue), W332. https://doi.org/10.1093/NAR/GKH479

Patterson, R. L., Van Rossum, D. B., & Gill, D. L. (1999). Store-operated Ca2+ entry: Evidence for a secretion-like coupling model. *Cell*, *98*(4), 487–499. https://doi.org/10.1016/S0092-8674(00)81977-7

Pettersen, E. F., Goddard, T. D., Huang, C. C., Couch, G. S., Greenblatt, D. M., Meng, E. C., & Ferrin, T. E. (2004). UCSF Chimera - A visualization system for exploratory research and analysis. *Journal of Computational Chemistry*, *25*(13), 1605–1612. https://doi.org/10.1002/jcc.20084

Pinder, J. C., Fowler, R. E., Dluzewski, A. R., Bannister, L. H., Lavin, F. M., Mitchell, G. H., Wilson, R. J., & Gratzer, W. B. (1998). Actomyosin motor in the merozoite of the malaria parasite, Plasmodium falciparum: implications for red cell invasion. *Journal of Cell Science*, *111*, 1831–1839.

Plattner, F., & Soldati-Favre, D. (2008). Hijacking of host cellular functions by the apicomplexa. In *Annual Review of Microbiology* (Vol. 62, pp. 471–487). https://doi.org/10.1146/annurev.micro.62.081307.162802

Pollard, T. D. (2016). Actin and actin-binding proteins. *Cold Spring Harbor Perspectives in Biology*, *8*(8), a018226. https://doi.org/10.1101/cshperspect.a018226

Pollard, T. D., & Cooper, J. A. (2009). Actin, a central player in cell shape and movement. In *Science* (Vol. 326, Issue 5957, pp. 1208–1212). https://doi.org/10.1126/science.1175862

Pospich, S., Kumpula, E. P., Von Der Ecken, J., Vahokoski, J., Kursula, I., & Raunser, S. (2017). Near-atomic structure of jasplakinolide-stabilized malaria parasite F-actin reveals the structural basis of filament instability. *Proceedings of the National Academy of Sciences of the United States of America*, *114*(40), 10636–10641. https://doi.org/10.1073/pnas.1707506114

Pospich, S., Merino, F., & Raunser, S. (2020). Structural Effects and Functional Implications of Phalloidin and Jasplakinolide Binding to Actin Filaments. *Structure*, *28*(4), 437-449.e5. https://doi.org/10.1016/j.str.2020.01.014

Pring, M., Evangelista, M., Boone, C., Yang, C., & Zigmond, S. H. (2003). Mechanism of formin-induced nucleation of actin filaments. *Biochemistry*, *42*(2), 486–496. https://doi.org/10.1021/bi026520j

Rajawat, J., & Jhingan, G. (2019). Mass spectroscopy. In *Data Processing Handbook for Complex Biological Data Sources* (pp. 1–20). Elsevier. https://doi.org/10.1016/B978-0-12-816548-5.00001-0

Rao, J. N., Madasu, Y., & Dominguez, R. (2014). Mechanism of actin filament pointed-end capping by tropomodulin. *Science*, *345*(6195), 463–467. https://doi.org/10.1126/science.1256159

Reimer, L., & Kohl, H. (2008). *Transmission Electron Microscopy* (Fifth, Vol. 36). Springer New York. https://doi.org/10.1007/978-0-387-40093-8

Ren, Z., Zhang, Y., Zhang, Y., He, Y., Du, P., Wang, Z., Sun, F., & Ren, H. (2019). Cryo-EM Structure of Actin Filaments from Zea mays Pollen[OPEN]. *Plant Cell*, *31*(12), 2855–2867. https://doi.org/10.1105/tpc.18.00973

Ridley, A. J. (2011). Life at the leading edge. In *Cell* (Vol. 145, Issue 7, pp. 1012–1022). Cell Press. https://doi.org/10.1016/j.cell.2011.06.010

Robert-Paganin, J., Robblee, J. P., Auguin, D., Blake, T. C. A., Bookwalter, C. S., Krementsova, E. B., Moussaoui, D., Previs, M. J., Jousset, G., Baum, J., Trybus, K. M., & Houdusse, A. (2019). Plasmodium myosin A drives parasite invasion by an atypical force generating mechanism. *Nature Communications*, *10*(1). https://doi.org/10.1038/s41467-019-11120-0

Robert-Paganin, J., Xu, X. P., Swift, M. F., Auguin, D., Robblee, J. P., Lu, H., Fagnant, P. M., Krementsova, E. B., Trybus, K. M., Houdusse, A., Volkmann, N., & Hanein, D. (2021). The actomyosin interface contains an evolutionary conserved core and an ancillary interface involved in specificity. *Nature Communications*, *12*(1), 1–11. https://doi.org/10.1038/s41467-021-22093-4

Rodriguez, E. L., Poddar, S., Iftekhar, S., Suh, K., Woolfork, A. G., Ovbude, S., Pekarek, A., Walters, M., Lott, S., & Hage, D. S. (2020). Affinity chromatography: A review of trends and developments over the past 50 years. *Journal of Chromatography B: Analytical Technologies in the Biomedical and Life Sciences*, *1157*. https://doi.org/10.1016/j.jchromb.2020.122332

Roos, D. S., Donald, R. G. K., Morrissette, N. S., & Moulton, A. L. C. (1995). Molecular Tools for Genetic Dissection of the Protozoan Parasite Toxoplasma gondii. *Methods in Cell Biology*, *45*(C), 27–63. https://doi.org/10.1016/S0091-679X(08)61845-2

Rottner, K., Hänisch, J., & Campellone, K. G. (2010). WASH, WHAMM and JMY: Regulation of Arp2/3 complex and beyond. *Trends in Cell Biology*, *20*(11), 650–661. https://doi.org/10.1016/j.tcb.2010.08.014

Rould, M. A., Wan, Q., Joel, P. B., Lowey, S., & Trybus, K. M. (2006). Crystal structures of expressed non-polymerizable monomeric actin in the ADP and ATP states. *Journal of Biological Chemistry*, *281*(42), 31909–31919. https://doi.org/10.1074/jbc.M601973200

Rueckert, S., Betts, E. L., & Tsaousis, A. D. (2019). The Symbiotic Spectrum: Where Do the Gregarines Fit? *Trends in Parasitology*, *35*(9), 687–694.

https://doi.org/10.1016/j.pt.2019.06.013

S Nag, M. L. R. R. L. B. (2013). Gelsolin: the tail of a molecular gymnast. *Cytoskeleton*, *70*, 360–384.

Saha, S., Mundia, M. M., Zhang, F., Demers, R. W., Korobova, F., Svitkina, T., Perieteanu, A. A., Dawson, J. F., & Kashina, A. (2010). Arginylation regulates intracellular actin polymer level by modulating actin properties and binding of capping and severing proteins. *Molecular Biology of the Cell*, *21*(8), 1350–1361. https://doi.org/10.1091/mbc.E09-09-0829

Sahoo, N., Beatty, W., Heuser, J., Sept, D., & Sibley, L. D. (2006). Unusual kinetic and structural properties control rapid assembly and turnover of actin in the parasite Toxoplasma gondii. *Molecular Biology of the Cell*, *17*(2), 895–906. https://doi.org/10.1091/mbc.E05-06-0512

Salamun, J., Kallio, J. P., Daher, W., Soldati-Favre, D., & Kursula, I. (2014). Structure of Toxoplasma gondii coronin, an actin-binding protein that relocalizes to the posterior pole of invasive parasites and contributes to invasion and egress. *FASEB Journal*, *28*(11), 4729–4747. https://doi.org/10.1096/fj.14-252569

Sari, D., Gupta, K., Raj, D. B. T. G., Aubert, A., Drncová, P., Garzoni, F., Fitzgerald, D., & Berger, I. (2016). The multibac baculovirus/insect cell expression vector system for producing complex protein biologics. In *Advances in Experimental Medicine and Biology* (Vol. 896, pp. 199–215). Springer New York LLC. https://doi.org/10.1007/978-3-319-27216-0_13

Schmitz, S., Grainger, M., Howell, S., Calder, L. J., Gaeb, M., Pinder, J. C., Holder, A. A., & Veigel, C. (2005). Malaria parasite actin filaments are very short. *Journal of Molecular Biology*, *349*(1), 113–125. https://doi.org/10.1016/j.jmb.2005.03.056

Schmitz, S., Schaap, I. A. T., Kleinjung, J., Harder, S., Grainger, M., Calder, L., Rosenthal, P. B., Holder, A. A., & Veigel, C. (2010). Malaria parasite actin polymerization and filament structure. *Journal of Biological Chemistry*, *285*(47), 36577–36585. https://doi.org/10.1074/jbc.M110.142638

Schmoller, K. M., Niedermayer, T., Zensen, C., Wurm, C., & Bausch, A. R. (2011). Fragmentation is crucial for the steady-state dynamics of actin filaments. *Biophysical Journal*, *101*(4), 803–808. https://doi.org/10.1016/j.bpj.2011.07.009

Schroer, T. A., Fyrberg, E., Cooper, J. A., Waterston, R. H., Helfman, D., Pollard, T. D., & Meyer, D. I. (1994). Actin-related protein nomenclature and classification. In *Journal of Cell Biology* (Vol. 127, Issue 6 II, pp. 1777–1778). The Rockefeller University Press. https://doi.org/10.1083/jcb.127.6.1777

Schüler, H., Mueller, A. K., & Matuschewski, K. (2005). A Plasmodium actin-depolymerizing factor that binds exclusively to actin monomers. *Molecular Biology of the Cell*, *16*(9), 4013–4023. https://doi.org/10.1091/mbc.E05-02-0086

Schwayer, C., Sikora, M., Slováková, J., Kardos, R., & Heisenberg, C. P. (2016). Actin Rings of Power. *Developmental Cell*, *37*(6), 493–506. https://doi.org/10.1016/j.devcel.2016.05.024

Self, T., Sobe, T., Copeland, N. G., Jenkins, N. A., Avraham, K. B., & Steel, K. P. (1999). Role of myosin VI in the differentiation of cochlear hair cells. *Developmental Biology*, *214*(2), 331–341. https://doi.org/10.1006/dbio.1999.9424

Senderowicz, A. M. J., Kaur, G., Sainz, E., Laing, C., Inman, W. D., Rodriguez, J., Crews, P., Malspeis, L., Grever, M. R., Sausville, E. A., & Duncan, K. L. K. (1995). Jasplakinolide's inhibition of the growth of prostate carcinoma cells in vitro with disruption of the actin cytoskeleton. *Journal of the National Cancer Institute*, *87*(1), 46–51. https://doi.org/10.1093/jnci/87.1.46

Sept, D., Xu, J., Pollard, T. D., & McCammon, J. A. (1999). Annealing accounts for the length of actin filaments formed by spontaneous polymerization. *Biophysical Journal*, *77*(6), 2911–2919. https://doi.org/10.1016/S0006-3495(99)77124-9

Singh, B. K., Sattler, J. M., Chatterjee, M., Huttu, J., Schuler, H., & Kursula, I. (2011). Crystal Structures Explain Functional Differences in the Two Actin Depolymerization Factors of the Malaria Parasite. *Journal of Biological Chemistry*, *286*(32), 28256–28264. https://doi.org/10.1074/jbc.m111.211730

Skillman, K. M., Diraviyam, K., Khan, A., Tang, K., Sept, D., & Sibley, L. D. (2011). Evolutionarily Divergent, Unstable Filamentous Actin Is Essential for Gliding Motility in Apicomplexan Parasites. *PLoS Pathogens*, *7*(10), e1002280. https://doi.org/10.1371/journal.ppat.1002280

Skillman, K. M., Ma, C. I., Fremont, D. H., Diraviyam, K., Cooper, J. A., Sept, D., & Sibley, L. D. (2013). The unusual dynamics of parasite actin result from isodesmic polymerization. *Nature Communications*, *4*, 1–8. https://doi.org/10.1038/ncomms3285

Slater, A. F. G. (1993). Chloroquine: Mechanism of drug action and resistance in plasmodium falciparum. *Pharmacology and Therapeutics*, *57*(2–3), 203–235. https://doi.org/10.1016/0163-7258(93)90056-J

Smythe, W. A., Joiner, K. A., & Hoppe, H. C. (2008). Actin is required for endocytic trafficking in the malaria parasite Plasmodium falciparum. *Cellular Microbiology*, *10*(2), 452–464. https://doi.org/10.1111/j.1462-5822.2007.01058.x

Steger, C. (1998). An Unbiased Detector of Curvilinear Structures. In *IEEE TRANSACTIONS ON PATTERN ANALYSIS AND MACHINE INTELLIGENCE* (Vol. 20, Issue 2). https://pdfs.semanticscholar.org/86de/a10b5c7b831a24132db3e4b50a01f9f001b0.pdf

Stortz, J. F., Del Rosario, M., Singer, M., Wilkes, J. M., Meissner, M., & Das, S. (2019). Formin-2 drives polymerisation of actin filaments enabling segregation of apicoplasts and cytokinesis in Plasmodium Falciparum. *ELife*, *8*. https://doi.org/10.7554/eLife.49030

Sultan, A. A., Thathy, V., Frevert, U., Robson, K. J. H., Crisanti, A., Nussenzweig, V., Nussenzweig, R. S., & Ménard, R. (1997). TRAP is necessary for gliding motility

and infectivity of Plasmodium sporozoites. *Cell*, *90*(3), 511–522. https://doi.org/10.1016/S0092-8674(00)80511-5

Svitkina, T. (2018). The actin cytoskeleton and actin-based motility. *Cold Spring Harbor Perspectives in Biology*, *10*(1). https://doi.org/10.1101/cshperspect.a018267

Sweeney, H. L., & Hammers, D. W. (2018). Muscle contraction. *Cold Spring Harbor Perspectives in Biology*, *10*(2). https://doi.org/10.1101/cshperspect.a023200

Sweeney, H. L., Wells, A. L., Lin, A. W., Chen, L.-Q., Safer, D., Cain, S. M., Hasson, T., Carragher, B. O., & Milligan, R. A. (1999). Myosin VI is an actin-based motor that moves backwards. *Nature*, *401*(6752), 505–508. https://doi.org/10.1038/46835

Takala, S. L., & Plowe, C. V. (2009). Genetic diversity and malaria vaccine design, testing and efficacy: Preventing and overcoming "vaccine resistant malaria." *Parasite Immunology*, *31*(9), 560–573. https://doi.org/10.1111/j.1365-3024.2009.01138.x

Takeda, S., Fujiwara, I., Sugimoto, Y., Oda, T., Narita, A., & Maéda, Y. (2020). Novel inter-domain Ca2+-binding site in the gelsolin superfamily protein fragmin. *Journal of Muscle Research and Cell Motility*, *41*(1), 153–162. https://doi.org/10.1007/s10974-019-09571-5

Taniguchi, K., Takeya, R., Suetsugu, S., Kan-o, M., Narusawa, M., Shiose, A., Tominaga, R., & Sumimoto, H. (2009). Mammalian formin Fhod3 regulates actin assembly and sarcomere organization in striated muscles. *Journal of Biological Chemistry*, *284*(43), 29873–29881. https://doi.org/10.1074/jbc.M109.059303

Tatkiewicz, W., Elizondo, E., Moreno, E., Díez-Gil, C., Ventosa, N., Veciana, J., & Ratera, I. (2015). Methods for characterization of protein aggregates. In *Methods in Molecular Biology* (Vol. 1258, pp. 387–401). Humana Press Inc. https://doi.org/10.1007/978-1-4939-2205-5_22

Terman, J. R., & Kashina, A. (2013). Post-translational modification and regulation of actin. In *Current Opinion in Cell Biology* (Vol. 25, Issue 1, pp. 30–38). Elsevier Ltd. https://doi.org/10.1016/j.ceb.2012.10.009

Tian, W., Chen, C., Lei, X., Zhao, J., & Liang, J. (2018). CASTp 3.0: Computed atlas of surface topography of proteins. *Nucleic Acids Research*, *46*(W1), W363–W367. https://doi.org/10.1093/nar/gky473

Tuli, L., & Ressom, H. W. (2009). LC-MS based detection of differential protein expression. *Journal of Proteomics and Bioinformatics*, *2*(10), 416–438. https://doi.org/10.4172/jpb.1000102

Vahokoski, J., Bhargav, S. P., Desfosses, A., Andreadaki, M., Kumpula, E. P., Martinez, S. M., Ignatev, A., Lepper, S., Frischknecht, F., Sidén-Kiamos, I., Sachse, C., & Kursula, I. (2014). Structural Differences Explain Diverse Functions of Plasmodium Actins. *PLoS Pathogens*, *10*(4). https://doi.org/10.1371/journal.ppat.1004091

Van Damme, P., Lasa, M., Polevoda, B., Gazquez, C., Elosegui-Artola, A., Kim, D. S., De Juan-Pardo, E., Demeyer, K., Hole, K., Larrea, E., Timmerman, E., Prieto, J., Arnesen, T., Sherman, F., Gevaert, K., & Aldabe, R. (2012). N-terminal acetylome analyses and functional insights of the N-terminal acetyltransferase NatB. *Proceedings of the National Academy of Sciences of the United States of America*, *109*(31), 12449–12454. https://doi.org/10.1073/pnas.1210303109

Van Den Ent, F., Lockhart, A., Kendrick-Jones, J., & Löwe, J. (1999). Crystal structure of the N-terminal domain of MukB: A protein involved in chromosome partitioning. *Structure*, *7*(10), 1181–1187. https://doi.org/10.1016/S0969-2126(00)80052-0

Varland, S., Vandekerckhove, J., & Drazic, A. (2019). Actin Post-translational Modifications: The Cinderella of Cytoskeletal Control. *Trends in Biochemical Sciences*, *44*(6), 502–516. https://doi.org/10.1016/j.tibs.2018.11.010

Vig, A., Ohmacht, R., Jámbor, É., Bugyi, B., Nyitrai, M., & Hild, G. (2011). The effect of toxins on inorganic phosphate release during actin polymerization. *European Biophysics Journal*, *40*(5), 619–626. https://doi.org/10.1007/s00249-010-0659-y

Viswanathan, M. C., Blice-Baum, A. C., Schmidt, W., Foster, D. B., & Cammarato, A. (2015). Pseudo-acetylation of K326 and K328 of actin disrupts Drosophila melanogaster indirect flight muscle structure and performance. *Frontiers in Physiology*, *6*(MAR), 1–30. https://doi.org/10.3389/fphys.2015.00116

Volz, J. C., Yap, A., Sisquella, X., Thompson, J. K., Lim, N. T. Y., Whitehead, L. W., Chen, L., Lampe, M., Tham, W. H., Wilson, D., Nebl, T., Marapana, D., Triglia, T., Wong, W., Rogers, K. L., & Cowman, A. F. (2016). Essential Role of the PfRh5/PfRipr/CyRPA Complex during Plasmodium falciparum Invasion of Erythrocytes. *Cell Host and Microbe*, *20*(1), 60–71. https://doi.org/10.1016/j.chom.2016.06.004

Von Der Ecken, J., Heissler, S. M., Pathan-Chhatbar, S., Manstein, D. J., & Raunser, S. (2016). Cryo-EM structure of a human cytoplasmic actomyosin complex at near-atomic resolution. *Nature*, *534*(7609), 724–728. https://doi.org/10.1038/nature18295

Von Der Ecken, J., Müller, M., Lehman, W., Manstein, D. J., Penczek, P. A., & Raunser, S. (2015). Structure of the F-actin-tropomyosin complex. *Nature*, *519*(7541), 114–117. https://doi.org/10.1038/nature14033

Wall, R. J., Zeeshan, M., Katris, N. J., Limenitakis, R., Rea, E., Stock, J., Brady, D., Waller, R. F., Holder, A. A., & Tewari, R. (2019). Systematic analysis of Plasmodium myosins reveals differential expression, localisation, and function in invasive and proliferative parasite stages. *Cellular Microbiology*, *21*(10). https://doi.org/10.1111/cmi.13082

Wang, J., Zhang, C. J., Chia, W. N., Loh, C. C. Y., Li, Z., Lee, Y. M., He, Y., Yuan, L. X., Lim, T. K., Liu, M., Liew, C. X., Lee, Y. Q., Zhang, J., Lu, N., Lim, C. T., Hua, Z. C., Liu, B., Shen, H. M., Tan, K. S. W., & Lin, Q. (2015). Haem-activated promiscuous targeting of artemisinin in Plasmodium falciparum. *Nature Communications*, *6*. https://doi.org/10.1038/ncomms10111

Wehner, M., & Würthner, F. (2020). Supramolecular polymerization through kinetic pathway control and living chain growth. *Nature Reviews Chemistry*, *4*(1), 38–53. https://doi.org/10.1038/s41570-019-0153-8

Weiss, L. M., & Kim, K. (Eds.). (2007). *Toxoplasma gondii. The Model Apicomplexan: Perspectives and Methods*.

Wellems, T. E., & Plowe, C. V. (2001). Chloroquine-resistant malaria. In *Journal of Infectious Diseases* (Vol. 184, Issue 6, pp. 770–776). J Infect Dis. https://doi.org/10.1086/322858

Wells, A. L., Lin, A. W., Chen, L. Q., Safer, D., Cain, S. M., Hasson, T., Carragher, B. O., Milligan, R. A., & Sweeney, H. L. (1999). Myosin VI is an actin-based motor that moves backwards. *Nature*, *401*(6752), 505–508. https://doi.org/10.1038/46835

Wesseling, J. G., Snijders, P. J. F., van Someren, P., Jansen, J., Smits, M. A., & Schoenmakers, J. G. G. (1989). Stage-specific expression and genomic organization of the actin genes of the malaria parasite Plasmodium falciparum. *Molecular and Biochemical Parasitology*, *35*(2), 167–176. https://doi.org/10.1016/0166-6851(89)90119-9

White, N. J. (2016). Why Do Some Primate Malarias Relapse? In *Trends in Parasitology* (Vol. 32, Issue 12, pp. 918–920). Elsevier Ltd. https://doi.org/10.1016/j.pt.2016.08.014

Wiame, E., Tahay, G., Tyteca, D., Vertommen, D., Stroobant, V., Bommer, G. T., & Van Schaftingen, E. (2018). NAT6 acetylates the N-terminus of different forms of actin. *FEBS Journal*, *285*(17), 3299–3316. https://doi.org/10.1111/febs.14605

Wieland, T., Nassal, M., Kramer, W., Fricker, G., Bickel, U., & Kurz, G. (1984). Identity of hepatic membrane transport systems for bile salts, phalloidin, and antamanide by photoaffinity labeling. *Proceedings of the National Academy of Sciences of the United States of America*, *81*(16 I), 5232–5236. https://doi.org/10.1073/pnas.81.16.5232

Wilson, C., Terman, J. R., González-Billault, C., & Ahmed, G. (2016). Actin filaments—A target for redox regulation. In *Cytoskeleton* (Vol. 73, Issue 10, pp. 577–595). John Wiley and Sons Inc. https://doi.org/10.1002/cm.21315

Wolven, A. K., Belmont, L. D., Mahoney, N. M., Almo, S. C., & Drubin, D. G. (2000). In vivo importance of actin nucleotide exchange catalyzed by profilin. *Journal of Cell Biology*, *150*(4), 895–903. https://doi.org/10.1083/jcb.150.4.895

World Health Organization. (2019). *World malaria report 2019*. https://www.who.int/publications-detail/world-malaria-report-2019

World Health Organization. (2020). World malaria report 2020: 20 years of global progress and challenges. In *WHO* (Vol. 73, Issue 1). https://www.who.int/publications/i/item/9789240015791

Wright, G. J., & Rayner, J. C. (2014). Plasmodium falciparum Erythrocyte Invasion:

Combining Function with Immune Evasion. *PLoS Pathogens*, *10*(3), e1003943. https://doi.org/10.1371/journal.ppat.1003943

Yahata, K., Hart, M. N., Davies, H., Asada, M., Templeton, T. J., Treeck, M., Moon, R. W., & Kaneko, O. (2020). Gliding motility of Plasmodium merozoites. *BioRxiv*, 2020.05.01.072637. https://doi.org/10.1101/2020.05.01.072637

Yusuf, N. A., Green, J. L., Wall, R. J., Knuepfer, E., Moon, R. W., Schulte-Huxel, C., Stanway, R. R., Martin, S. R., Howell, S. A., Douse, C. H., Cota, E., Tate, E. W., Tewari, R., & Holder, A. A. (2015). The Plasmodium class XIV Myosin, MyoB, has a distinct subcellular location in invasive and motile stages of the malaria parasite and an unusual light chain. *Journal of Biological Chemistry*, *290*(19), 12147–12164. https://doi.org/10.1074/jbc.M115.637694

Paper I

Atomic view into *Plasmodium* actin polymerization, ATP hydrolysis, and fragmentation

Kumpula EP, **Lopez AJ**, Tajedin L, Han H & Kursula I.

PLoS Biol 17(6): e3000315. doi: 10.1371/journal.pbio.3000315. (2019)

I

Abstract

Plasmodium actins form very short filaments and have a noncanonical link between ATP hydrolysis and polymerization. Long filaments are detrimental to the parasites, but the struc- tural factors constraining *Plasmodium* microfilament lengths have remained unknown. Using high-resolution crystallography, we show that magnesium binding causes a slight flat- tening of the *Plasmodium* actin I monomer, and subsequent phosphate release results in a more twisted conformation. Thus, the Mg-bound monomer is closer in conformation to fila- mentous (F) actin than the Ca form, and this likely facilitates polymerization. A coordinated potassium ion resides in the active site during hydrolysis and leaves together with the phos- phate, a process governed by the position of the Arg178/Asp180-containing A loop. Asp180 interacts with either Lys270 or His74, depending on the protonation state of the histidine, while Arg178 links the inner and outer domains (ID and OD) of the actin protomer. Hence, the A loop acts as a switch between stable and unstable filament conformations, the latter leading to fragmentation. Our data provide a comprehensive model for polymerization, ATP hydrolysis and phosphate release, and fragmentation of parasite microfilaments. Similar mechanisms may well exist in canonical actins, although fragmentation is much less favor- able due to several subtle sequence differences as well as the methylation of His73, which is absent on the corresponding His74 in *Plasmodium* actin I.

PLOS BIOLOGY

RESEARCH ARTICLE

Atomic view into *Plasmodium* actin polymerization, ATP hydrolysis, and fragmentation

Esa-Pekka Kumpula[1], **Andrea J. Lopez**[2], **Leila Tajedin**[2], **Huijong Han**[1,3], **Inari Kursula**[1,2,3]*

1 Biocenter Oulu and Faculty of Biochemistry and Molecular Medicine, University of Oulu, Oulu, Finland, **2** Department of Biomedicine, University of Bergen, Bergen, Norway, **3** European XFEL GmbH, Schenefeld, Germany

* inari.kursula@uib.no

OPEN ACCESS

Citation: Kumpula E-P, Lopez AJ, Tajedin L, Han H, Kursula I (2019) Atomic view into *Plasmodium* actin polymerization, ATP hydrolysis, and fragmentation. PLoS Biol 17(6): e3000315. https://doi.org/10.1371/journal.pbio.3000315

Academic Editor: Laura Machesky, The Beatson Institute, UNITED KINGDOM

Received: November 29, 2018

Accepted: May 23, 2019

Published: June 14, 2019

Data Availability Statement: The protein structure coordinates and structure factor amplitudes have been deposited at the Protein Data Bank (PDB) with the codes 6I4D, 6I4E, 6I4F, 6I4G, 6I4H, 6I4I, 6I4J, 6I4K, 6I4L, and 6I4M. All other relevant data are within the paper and its Supporting Information files.

Funding: This work was funded by grants to IK from the Academy of Finland (aka.fi), the Emil Aaltonen Foundation (emilaaltonen.fi), the Jane and Aatos Erkko Foundation (jaes.fi), the Norwegian Research Council (forskningsradet.no), and the

Abstract

Plasmodium actins form very short filaments and have a noncanonical link between ATP hydrolysis and polymerization. Long filaments are detrimental to the parasites, but the structural factors constraining *Plasmodium* microfilament lengths have remained unknown. Using high-resolution crystallography, we show that magnesium binding causes a slight flattening of the *Plasmodium* actin I monomer, and subsequent phosphate release results in a more twisted conformation. Thus, the Mg-bound monomer is closer in conformation to filamentous (F) actin than the Ca form, and this likely facilitates polymerization. A coordinated potassium ion resides in the active site during hydrolysis and leaves together with the phosphate, a process governed by the position of the Arg178/Asp180-containing A loop. Asp180 interacts with either Lys270 or His74, depending on the protonation state of the histidine, while Arg178 links the inner and outer domains (ID and OD) of the actin protomer. Hence, the A loop acts as a switch between stable and unstable filament conformations, the latter leading to fragmentation. Our data provide a comprehensive model for polymerization, ATP hydrolysis and phosphate release, and fragmentation of parasite microfilaments. Similar mechanisms may well exist in canonical actins, although fragmentation is much less favorable due to several subtle sequence differences as well as the methylation of His73, which is absent on the corresponding His74 in *Plasmodium* actin I.

Introduction

Actin is the constituent protein of microfilaments with essential roles in central processes in the cell, including transport, cell division, and motility [1–3]. The primary biological activity of actin is its polymerization to form filaments that can generate force at cell membranes or act as scaffolding structures or tracks for motor proteins [4]. These filaments are on a timer, based on the hydrolysis of tightly bound ATP, formation of the stable intermediate ADP-inorganic phosphate (P_i) actin, and finally, the release of P_i [5]. The physiological tightly bound divalent cation coordinating the bound nucleotide in actin is Mg^{2+} (reviewed in [6]). However, actin is

Sigrid Jusélius Foundation (sigridjuselius.fi). The funders had no role in study design, data collection and analysis, decision to publish, or preparation of the manuscript.

Competing interests: The authors have declared that no competing interests exist.

Abbreviations: EGTA, ethylene glycol-bis[2-aminoethyl ether]-N,N,N',N'-tetraacetic acid; F, filamentous; G, globular; Hsc70, Heat shock cognate 71 kDa protein; ID, inner domain; MDCC-PBP, 7-diethylamino-3-[N-(2-maleimidoethyl) carbamoyl]coumarin-labeled phosphate-binding protein; mHis73, methylated His73; OD, outer domain; *Pb*ActII, *Plasmodium berghei* actin II; PC, principal component; PCA, principal component analysis; PDB, Protein Data Bank; *Pf*ActI, *P. falciparum* actin I; P_i, inorganic phosphate; RMSD, root-mean-square deviation; *Sc*Act, *Saccharomyces cerevisiae* actin; SD, subdomain; TEV, tobacco etch virus; *Tg*Act, *Toxoplasma gondii* actin.

usually purified in the calcium-bound form, which has a higher critical concentration of polymerization [7]. In addition to magnesium and calcium, at least potassium affects actin polymerization by decreasing the critical concentration by approximately 2-fold [7].

In model actins, which typically represent actins of opisthokonts from yeast to mammals, the coupling of nucleotide hydrolysis to filament stability is well established. In general, ADP actin depolymerizes much faster than ATP or ADP-P_i actin and is therefore the main depolymerizing species [7]. Although ADP actin can polymerize, its critical concentration is much higher than that of ATP actin [7], which leads to domination of ATP actin in polymerization kinetics. Outliers of this functional consensus are actins of the phylum Apicomplexa, including *Plasmodium* spp. and *Toxoplasma gondii*—both notorious human pathogens. With less than 80% sequence identity to their canonical counterparts, actins of these parasites are among the most evolutionarily diverged eukaryotic actins while still retaining most of the core features [8–11]. The primary actin of *P. falciparum* and the only one of *T. gondii* are the best understood of the phylum, whereas others remain virtually uncharacterized.

In vitro, apicomplexan actins tend to form only short filaments of approximately100 nm without the filament-stabilizing macrolide jasplakinolide [8–10,12]. *T. gondii* actin (*Tg*Act) has been proposed to follow an isodesmic polymerization mechanism [11], which would differ fundamentally from the classical nucleation-elongation pathway. However, *P. falciparum* actin I (*Pf*ActI) has a critical concentration close to that of mammalian α-actin and a very similar elongation rate [13]. Under ADP-rich conditions, *Pf*ActI forms oligomers of 3 to 12 subunits while forming larger polymeric species in polymerizing conditions containing magnesium and potassium, together with a significant pool of dimers [9,13]. These properties are in stark contrast to what is seen for the well-characterized model systems.

Despite the functional differences, the *Pf*ActI monomer largely resembles canonical actins in structure [9]. The most pronounced differences are at the pointed end, namely, subdomain (SD) 2 (containing the DNaseI-binding D loop) and parts of SD4, which both connect to SD3 of the next longitudinal protomer in the filament. The D loop and the C terminus are both important functional factors but are disordered in the crystal structure of *Pf*ActI, reflecting their flexibility [9]. In jasplakinolide-stabilized *Pf*ActI filaments, the D loop is in a clearly altered conformation compared with α-actin filaments [10]. Yet the main hydrophobic interactions are conserved, and the amino acid substitutions are primarily located at the base of the D loop [9]. In addition, differences in the plug region (residues Ser266-Ala273, especially Lys270) and some other residues along the filament interface (in particular Val288, Gly200) also likely contribute to filament instability [10]. However, a single key factor driving the inherent instability of the parasite microfilaments has not been identified.

The large-scale conformational transition of the actin monomer from globular (G) to filamentous (F) form has been described from a series of high-resolution filament structures of α-actin [14–18]. Yet experimental evidence on what exactly triggers the structural transition and the subsequent activation of ATP hydrolysis is still lacking. Among key questions are the following: (i) Why does Mg-ATP actin polymerize more readily than Ca-ATP actin or Mg-ADP actin? (ii) What is the role of K^+ in polymerization and ATP hydrolysis? Unlike the extensively studied model actins, *Pf*ActI forms short oligomers also in classical nonpolymerizing conditions in the presence of ADP and, on the other hand, stable dimers—in addition to short filamentous structures—in conditions in which canonical actins polymerize into long filaments [9,13]. Thus, it seems that hydrolysis of ATP and subsequent P_i release is favorable for oligomerization of *Pf*ActI. Associated structural changes could thus favor nucleus formation—i.e., result in a conformation closer to the F than the G state. Here, we analyze phosphate release rates and high-resolution structures of wild-type and mutant *Plasmodium* actins in different nucleotide states, bridging the gap between structure and function in understanding the

polymerization mechanism and the instability of the parasite microfilaments. Many of the conclusions may be relevant for understanding these mechanisms also in canonical actins.

Results

Unusual coupling between nucleotide hydrolysis and polymerization in *Pf*ActI

In skeletal muscle α-actin, conformational changes upon polymerization activate nucleotide hydrolysis in the actin protomers, and the subsequent P_i release leads to destabilization of the "aged" filament [14,15]. Throughout this text, we refer to this activation of P_i release or nucleotide hydrolysis by the word "activation" unless otherwise stated. Actins are predominantly purified in their nonphysiological Ca^{2+} bound form, due to improved stability and higher critical concentration of polymerization. In physiological conditions, actin binds Mg^{2+} and is therefore mostly studied in this state. Polymerization is fastest and the critical concentration the lowest in physiological conditions with Mg^{2+} and K^+ [7]. Critical concentrations of canonical actins and *Pf*ActI in such polymerizing conditions are similar [13]. In addition, P_i release rates have been studied earlier for canonical actins as well as *Pf*ActI and *Plasmodium berghei* actin II (*Pb*ActII). Filamentous α-actin releases P_i at rates of 14.8×10^{-4} s^{-1} during the elongation phase of polymerization and 0.15 to 0.47×10^{-4} s^{-1} once equilibrium (steady state) between polymerization and depolymerization has been reached [19,20] (S1 Table). By comparison, P_i release rates in equilibrium measured from *Pf*ActI and *Pb*ActII were $>1.3 \times 10^{-4}$ s^{-1} in the presence of Ca^{2+} and Mg^{2+} [9]. These measurements were conducted above the critical concentration of either filament end in the ATP state (1.5 μM for the barbed end, 4.5 μM for the pointed end in 1 mM Mg^{2+}, as measured for α-actin [7]). To further characterize the relationship between phosphate release and polymerization, we measured P_i release rates from *Pf*ActI, *Pb*ActII, and α-actin in 0.2 mM Ca^{2+}, 1 mM Mg^{2+}, and 4 mM Mg^{2+}/50 mM K^+ at protein concentrations around 1 and 3 to 6 μM each. Contrary to α-actin, P_i release rates of the parasite actins did not increase in the polymerizing MgK conditions at low actin concentrations (Fig 1A, S2 Table). This was true also for higher concentrations of *Pf*ActI but not for *Pb*ActII (S3 Table). At higher concentrations, P_i release from *Pf*ActI was instantaneous with no identifiable lag phase in any of the conditions, whereas P_i release curves from *Pb*ActII and α-actin showed a lag phase in Mg and MgK states (S1 Fig). This is in line with our earlier report, in which spontaneous polymerization of *Pf*ActI showed a very short or nonexistent lag phase [13]. These data suggest that the coupling of nucleotide hydrolysis and P_i release with polymerization is different in *Pf*ActI compared with canonical actins and *Pb*ActII.

Steps of ATP hydrolysis and phosphate release in *Pf*ActI can be followed in crystallo

Since the major activation of P_i release from *Pf*ActI is caused by Mg^{2+}, we decided to study the process in detail by analyzing crystal structures of monomeric *Pf*ActI and *Pb*ActII in the Mg state and compare those to the published high-resolution structures of the Ca states [9] (Fig 2, S4 Table). Both *Plasmodium* actins were crystallized as complexes with mouse gelsolin segment 1 (hereafter gelsolin) in the presence of 0.5 mM ethylene glycol-bis[2-aminoethyl ether]-N,N,N',N'-tetraacetic acid (EGTA) and 1 mM $MgCl_2$ as well as 200 mM potassium thiocyanate from the crystallization solution (S3 Table). In addition to the wild-type proteins, we also determined several structures of 4 *Pf*ActI mutants (A272W, H74Q, F54Y, and G115A) in different nucleotide states—altogether 10 structures—which will be discussed in the sections below.

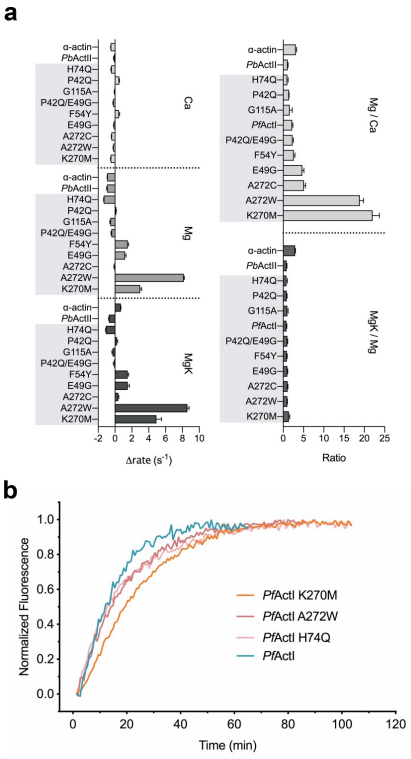

Fig 1. Phosphate release rates and elongation kinetics of *Plasmodium* and canonical actins. (A) Phosphate release rates of *Pf*ActI, *Pb*ActII, and α-actin as well as a collection of mutants of *Pf*ActI, expressed as rates compared with *Pf*ActI wild type by subtraction (left) and as ratios of Mg/Ca or MgK/Mg (right). In the text and S2 Table, the ratios are referred to as "activation." The underlying data for this figure can be found in S1 Data. (B) Polymerization of 10% pyrene-labeled *Pf*ActI, *Pf*ActI K270M, *Pf*ActI A272W, and *Pf*ActI H74Q seeded with α-actin nuclei. *Pb*ActII, *Plasmodium berghei* actin II; *Pf*ActI, *P. falciparum* actin I.

https://doi.org/10.1371/journal.pbio.3000315.g001

The wild-type crystals diffracted to high resolution (1.2–1.85 Å, S5 and S6 Tables), enabling a detailed structural analysis. Actin-gelsolin complexes crystallized in the presence of Mg^{2+} may undergo complete or no hydrolysis of ATP [16,21,22]. To our surprise, in Mg-*Pf*ActI crystals from which diffraction data were collected soon after crystal formation, a model with partial occupancies for both ATP and ADP (and associated conformational changes in the protein such as Ser15) in the active site was found to best explain the data (Fig 2C, S2 Fig). We call this model Mg-ATP/ADP-*Pf*ActI. Only after aging the crystals for several months could we obtain data explained by an ADP-only model (Fig 2D), termed Mg-ADP-*Pf*ActI. Crystals grown after exchanging the nucleotide in solution after complex formation also contained a similar mixed nucleotide state. These findings were corroborated by anomalous difference density maps, in which peaks of >4 σ were found for Pα, Pβ, and Pγ in Mg-ATP/ADP-*Pf*ActI but only for Pα and Pβ in the Mg-ADP-*Pf*ActI. It therefore seems that gelsolin inhibits nucleotide exchange in *Pf*ActI as in α-actin [23], and that ATP hydrolysis happens in crystallo, with no exchange of the nucleotide with the solvent. The pH dependence of P_i release from free *Pf*ActI monomers

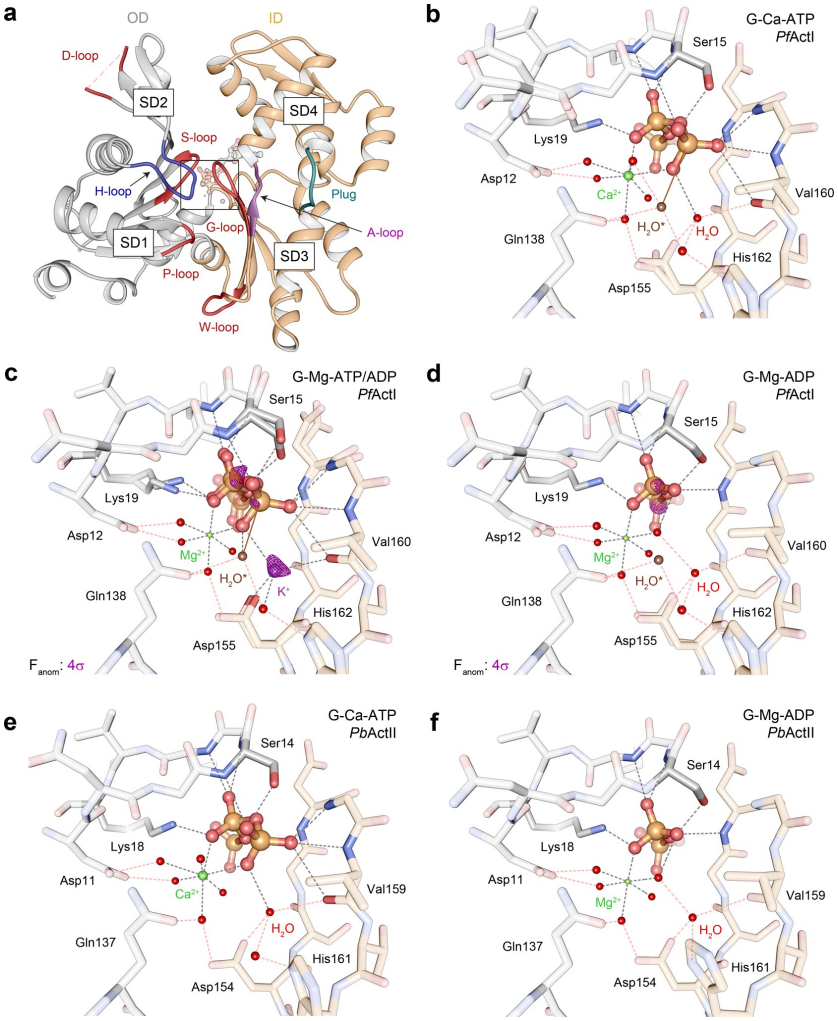

Fig 2. Active site configurations in the *Pf*ActI and *Pb*ActII structures. (A) Overview of the Mg-ATP/ADP-*Pf*ActI monomer with the D loop, S loop, H loop, G loop, P loop, and W loop as well as the plug and A loop indicated. The region of interest enlarged in the other panels is boxed. (B–D) *Pf*ActI structures in the (B) Ca-ATP [9], (C) Mg-ATP/ADP, and (D) Mg-ADP states. (E, F) *Pb*ActII structures in (E) Ca-ATP [9] and (F) Mg-ADP states. In all panels, hydrogen bonds with ATP, ADP, or ions are indicated with black dashed lines and the outer shell hydrogen bonding via water molecules with red dashed lines. In (B, C), the brown solid line indicates the nucleophilic attack vector of the putative catalytic water [21] (H_2O^*). In (C, D), anomalous difference density is shown as a purple mesh at a 4-σ contour level. The ID and OD are colored in orange and gray, respectively, in all panels. ID, inner domain; OD, outer domain; *Pb*ActII, *P. berghei* actin II; *Pf*ActI, *P. falciparum* actin I; SD, subdomain.

https://doi.org/10.1371/journal.pbio.3000315.g002

was 60% to 114% at the crystallization pH range of 5.7 to 6.5 relative to the standard assay conditions at pH 7.5 (S3 Fig). Despite the mixed nucleotide state, we were unable to locate free P_i

anywhere within the structure, even after soaking the Mg-ADP-*Pf*ActI crystals in P_i. Contrary to *Pf*ActI, Mg-*Pb*ActII crystals contained only ADP just 2 weeks after crystallization, despite showing a slightly lower P_i release rate in solution than *Pf*ActI (S1 Fig and S3 Table). Thus, the effects of gelsolin and/or the crystalline environment apparently slow down the hydrolysis but not the P_i release rate of *Pf*ActI. This combination of high resolution and slow hydrolysis provides a convenient window to visualize the structural changes upon ATP hydrolysis, P_i release, and polymerization.

The overall structures of the different nucleotide states of *Pf*ActI appear very similar, but principal component analysis (PCA) with a set of 147 unique actin structures identified 2 conformational shifts during the reaction pathway (S4 Fig, S1 Movie): (i) opening of the nucleotide-binding cleft and (ii) slight flattening upon inclusion of Mg^{2+}, followed by twisting of the monomer upon completion of hydrolysis. A data set comprising only *Plasmodium* actins shows a similar trend (S4 Fig), although principal component (PC)2 in this data set depicts a change in SD2 and not so much in SD1, as in the full data set (S1 Movie). The twist angles of the mass centers of the SDs (θ) were used as an independent measure and showed angles of 19.0˚, 17.9˚, and 20.0˚ for Ca-ATP, Mg-ATP/ADP, and Mg-ADP structures, respectively (S7 Table). The opening-closing motion was not evident from distances of the mass centers of SD2 and SD4 (d_{2-4}) or phosphate clamp distances (b_2) as defined before [24]. However, anisotropic B factors indicate a directional destabilization of SD2 toward SD4 (S5 Fig). It has to be kept in mind that all these crystal structures contain gelsolin bound to the cleft between SDs 1 and 3, which likely has an effect on both the twist and the opening motion of the actin monomer. We expect gelsolin to limit the flexibility of the domains with respect to each other, and thus the direction of these movements could be taken as indicative of the real situation, with the magnitude likely smaller than in a free actin monomer. A comparable data set of *Dictyostelium discoideum* actins is characterized in PCA by a combination of opening and twisting upon inclusion of Mg^{2+} and a reversal of the opening upon completion of hydrolysis [16].

*Pf*ActI binds potassium during ATP hydrolysis

In the Mg-ATP/ADP-*Pf*ActI, we found excess electron density, not explained by water, between the side chain of Asp155, the backbone nitrogen of Gly157, and the backbone carbonyl of Val160 (Fig 2C and S2 Fig). An anomalous difference density map revealed a 6.5-σ peak at this site (Fig 2C). In other Mg-actin structures, no other metals have been identified in the active site besides the divalent cation. Considering ions present, coordination distances, and geometry as well as anomalous scattering lengths at the used wavelength (1.032 Å), K^+ is the most likely explanation for this density. Furthermore, this site corresponds to one of the K^+-binding sites identified in the homologous Heat shock cognate 71 kDa protein (Hsc70) nucleotide-binding domain [25]. We therefore modeled K^+ at this site with a final refined occupancy of 0.7, which is close to the occupancy of ATP (0.8). Considering all the possible ions present in the crystals, the only other possibilities in addition to K^+ would be Mg^{2+} or Cl^-. We excluded Mg^{2+} based on coordination geometry. However, distinguishing between K^+ and Cl^- is more difficult. To address this, we refined a chloride ion at this site and subsequently analyzed the models with K^+ and with Cl^- using the CheckMyMetal server [26]. The results showed that K^+ is coordinated in a tetrahedral configuration, whereas Cl^- is unliganded, which favors our assignment of K^+. In addition, because of the coordinating negative side chain (Asp155) and the negatively charged phosphate tail of ATP, an anion would be very unlikely at this site.

The active site of actin is highly conserved, including the residues coordinating this K^+. Yet there is no evidence of K^+ or any other ions at this site in published actin structures, other than the Cd-ATP-*Pf*ActI structure [27], where Cd^{2+} was refined at this site. The Mg-ADP structure

does not contain excess electron density or anomalous difference density at this site (Fig 2D), despite showing anomalous difference density for the Pα and Pβ atoms of ADP. This suggests that K^+ leaves the active site upon P_i release. Because K^+ does not activate P_i release from *Pf*ActI (Fig 1A, S2 and S3 Tables), this interaction most likely does not directly influence the mechanism of P_i release in *Pf*ActI but may rather be relevant for hydrolysis.

Nonmethylated His74 and Lys270 play ping-pong on the A loop in *Pf*ActI

Three loops in the actin fold are considered primary sensors of the nucleotide state (Fig 2A): the S loop (residues 11–16 [28–30]), the H loop (residues 70–78 [29]), and the G loop (residues 154–161 [30]). Other, more distant sensors of the nucleotide state are the W loop (residues 165–172 [31]), the D loop (residues 38–52 [28–30]), and the C terminus (residues 349–375 [32]). The foremost nucleotide state sensor in canonical actins is Ser14 in the S loop, whose side chain rotates toward the β-phosphate of ADP upon P_i release. The conformation of the corresponding Ser15 in *Pf*ActI moves from the ATP state [9] through a double conformation with occupancies 0.8/0.2 in the ATP/ADP state to a complete ADP conformation (Fig 2B–2D). This conformational switch is further propagated to the flipping of the peptide bond between Glu73 and His74 in the nearby H loop (S6 Fig), as seen also in *Pb*ActII and the uncomplexed ATP and ADP structures of several actin structures [16,28,30].

Asp180 is located in a short loop following β14 (S7 Fig), sandwiched between the H loop and the plug residues, including Lys270 (Figs 1A and 3). We call this loop the A loop because of its anionic nature (described below), its central residues being arginine and aspartate, and because its relevance is here described from an apicomplexan parasite. The A loop serves as a linker between SD3 and SD4. In the Ca-ATP structure, the A loop resides close to the H loop (Fig 3A). Asp180 is in 2 conformations: either interacting with the Nδ of His74 (3.2 Å, conformation 1a) or oriented toward Arg178 (conformation 1b). In the Mg-ATP/ADP structure, the backbone of the A loop has a second conformation (conformation 2a) with an occupancy of 0.4 (Fig 3C). In the Mg-ADP structure, only conformations 1b and 2a are present at equal occupancies. B factors match the environment in both Mg structures (S8 Fig), and the occupancies are in agreement with the estimated protonation state (55%) of a histidine side chain in solution at pH 6.0. In conformation 2a, Asp180 forms a salt bridge with Lys270. In conformation 1a, Asp180 moves to form a salt bridge with His74. Thus, the A loop is engaged in a ping-pong movement between the 2 positive charges. Conformation 1b is analogous to the position of the side chain in the jasplakinolide-stabilized *Pf*ActI filament model (Fig 3G) and in many canonical actin filament models [10,33–35].

Most model actins, except for that of *Saccharomyces cerevisiae*, presumably have a methylated His74 (*Pf*ActI numbering) in the H loop [36], although this is not evident from the majority of structures in the Protein Data Bank (PDB). Histidine methylation is a rare post-translational modification that lowers the pK_a of the side chain by donating electrons to the π-system and thus stabilizing the positive charge. Our crystal structures are of sufficiently high resolution to verify the previous observations that in native or recombinant *Pf*ActI, His74 is not methylated [12,13]. Curiously, recombinant *Pb*ActII expressed and purified similarly is methylated at this position (S2 Fig). In actins with a methylated histidine at this site, Nδ is mostly protonated and free to interact with the carbonyl of Gly159 (*Pf*ActI numbering), which together with Val160 is involved in coordinating the active site K^+ (Fig 2C). As protonated histidines act as cations in electrostatic interactions and as π-systems in cation-π interactions, protonation constitutes a credible interaction switch between $His74^+/Asp180^-$ and $His74/Arg178^+$, particularly for a nonmethylated histidine. A methylated histidine in canonical actins and *Pb*ActII would favor interactions of the A loop with the H loop.

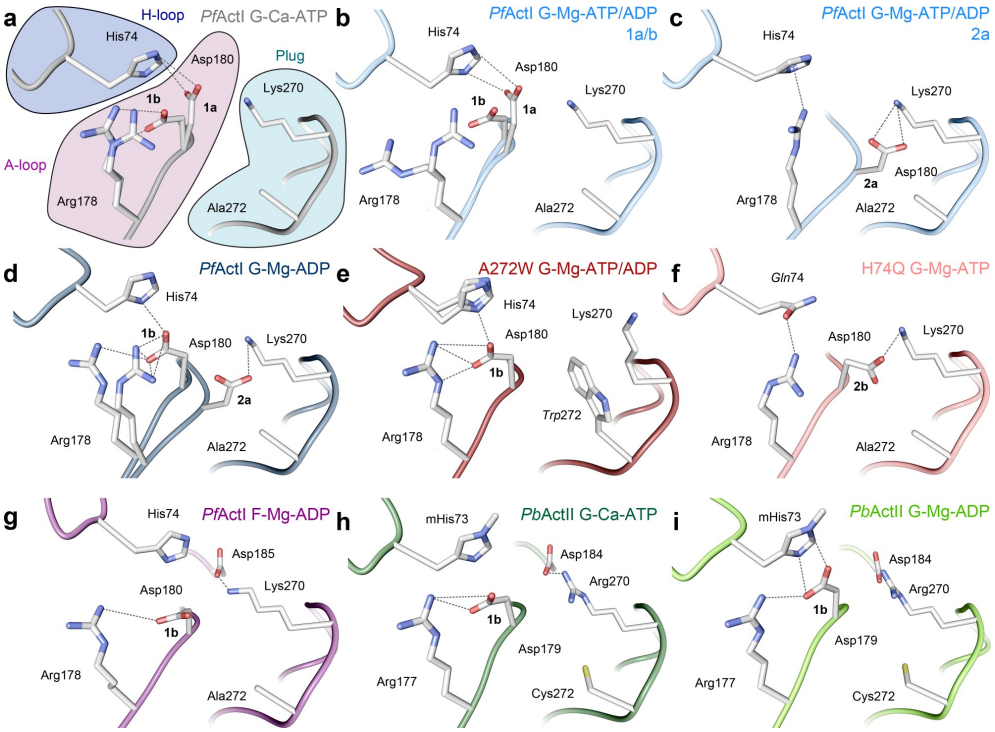

Fig 3. Orientation of the A loop in *Pf*ActI and *Pb*ActII. (A–D) Wild-type *Pf*ActI in the (A) Ca-ATP state [9] (1a and 1b), (B) Mg-ATP/ADP state (1a and 1b), (C) Mg-ATP/ADP state (2a), and (D) Mg-ADP state (1b and 2a). Note that panels (B) and (C) represent alternative conformations from the same crystal structure. (E–F) *Pf*ActI mutants (E) A272W in the Mg-ATP/ADP state (1b) and (F) H74Q in the Mg-ATP state (2b). (G) Wild-type *Pf*ActI in the F state [10] (1b), stabilized by jasplakinolide (not depicted). (H–I) Wild-type *Pb*ActII in the (H) Ca-ATP [9] (1b) and (I) Mg-ADP states (1b). In (H), His73 is methylated for consistency even though it is not in the deposited model. The most probable ionic and hydrogen bonding interactions are indicated with dashed lines. The conformers of the H loop are attributed to each conformation based on overlap of van der Waals radii as well as distances and geometry for hydrogen bonding. F, filamentous; G, globular; mHis73, methylated His73; *Pb*ActII, *Plasmodium berghei* actin II; *Pf*ActI, *P. falciparum* actin I.

https://doi.org/10.1371/journal.pbio.3000315.g003

Arg178 in the A loop participates in connecting the inner domain (ID) and the outer domain (OD). In the Mg-ATP/ADP structure, Arg178 moves toward the carbonyl groups of His74 and Pro110 in conformation 1b, thus connecting the P loop in SD1 (residues 109–114) and H loop in SD2 (S9 Fig). Conversely in conformation 2a, Arg178 interacts with His74 via a cation-π interaction, which only maintains the contact between SD3 and SD2. Because the 2 conformations of the A loop backbone (1a/b and 2a) are evident in the presence of Mg^{2+} but not with Ca^{2+} and are still present in the Mg-ADP structure, the movement of the loop is either connected directly to Mg^{2+} binding or is an indirect result facilitated by Mg^{2+} binding and the resulting accelerated P_i release.

Structural differences in the Ca and Mg states of *Pb*ActII

According to PCA, Mg-ADP *Pb*ActII is less open and more twisted than the Ca-ATP form, situating toward the twinfilin–C complex [37] and the cofilin-decorated filament structure [38].

Measurements of θ, d_{2-4}, and b_2 support these findings (S7 Table). However, the largest changes appear in SD2, which has high B factors and relatively weak electron density (S10 Fig). The active site configurations in the Ca states are similar between *Pf*ActI and *Pb*ActII (Fig 2B and 2E). However, in the presence of Mg^{2+}, the His161 side chain adopts a different conformation in *Pb*ActII than that seen in any of the structures of *Pf*ActI and most other gelsolin-bound structures in the PDB (Fig 2F). The exception to this is the *D. discoideum* actin structure in the presence of Li-ATP (1NMD), in which a similar conformation was proposed to be more amenable to hydrolytic activity [21]. However, the side chain is rotated 180˚ about the Cβ-Cγ bond in 1NMD compared with *Pb*ActII and most other actin structures. The new conformation of His161 in *Pb*ActII changes the water network by occupying the space of one of the waters coordinating the active site K^+ in *Pf*ActI. In canonical F actin, His161 adopts a conformation similar to that seen in *Pb*ActII but even closer to Pγ [18,35].

There is no evidence of conformations 1a or 2a in the *Pb*ActII Mg-ADP structure (Fig 3H and 3I). This can be rationalized as follows: (i) methylation of His73 ensures that it is mostly protonated and therefore repels Arg177, interacting with Asp179; (ii) Gly115 of *Pf*ActI is threonine in *Pb*ActII, and the G115A mutant also lacks conformation 2a (see below); and (iii) Ala272 of *Pf*ActI is cysteine in *Pb*ActII, which may sterically block the backbone position of conformation 2a. The fact that the alternative conformations of the A loop have not been built in the majority of actin structures does not unambiguously prove that they would not exist, and indeed in several cases, this loop has high B factors. However, based on available data, we expect that a stable conformation 2a may be unique to *Pf*ActI and that *Pb*ActII resembles canonical actins in this respect.

Canonical-type K270M mutation in *Pf*ActI hyperactivates phosphate release and stabilizes filaments

We proposed earlier that differences in the plug region and especially Lys270 (corresponding to Met269 in α-actin) are among the determining factors for *Pf*ActI filament instability [10]. Because Asp180 interacts with Lys270 directly, we generated a canonical-type K270M mutant. Indeed, this mutant formed many more long filaments in the absence of jasplakinolide than wild-type *Pf*ActI (Fig 4). Curiously, considering this stabilizing effect, the K270M mutation caused hyperactivation of the P_i release rate by Mg^{2+}. This activation effect was manifested by a reduction of the rate in Ca conditions to α-actin levels and a moderate increase in Mg. Furthermore, in contrast to the wild type, K270M was no longer insensitive to K^+ (S2 Table) and also showed a lag phase at high concentration (S3 Fig), thus behaving essentially as α-actin but with a faster rate in Mg and MgK conditions. In order to rule out that the differences in the P_i release rates would be caused by an altered elongation rate in the mutant, we performed seeded polymerization assays to compare the elongation rates. The elongation rates of K270M and wild-type *Pf*ActI are essentially identical (Fig 1B), meaning that the increased P_i release rate is not due to faster elongation. Because the K270M mutation should make conformation 2a less favorable by disrupting the interaction with Asp180, these results can be taken as indication that conformation 2a is counterproductive to P_i release.

Mutations affecting the conformational space of the A loop affect phosphate release in *Pf*ActI

As the A loop moves into conformation 2a to interact with Lys270, it fills a space otherwise occupied by water molecules. On the opposite side, Ala272 points toward the A loop (Fig 3A–3G). This alanine is conserved in *Tg*Act and in nearly all alveolates but is replaced by serine in most model actins and by cysteine in *Pb*ActII or asparagine in *Arabidopsis thaliana* actin 1 (S7

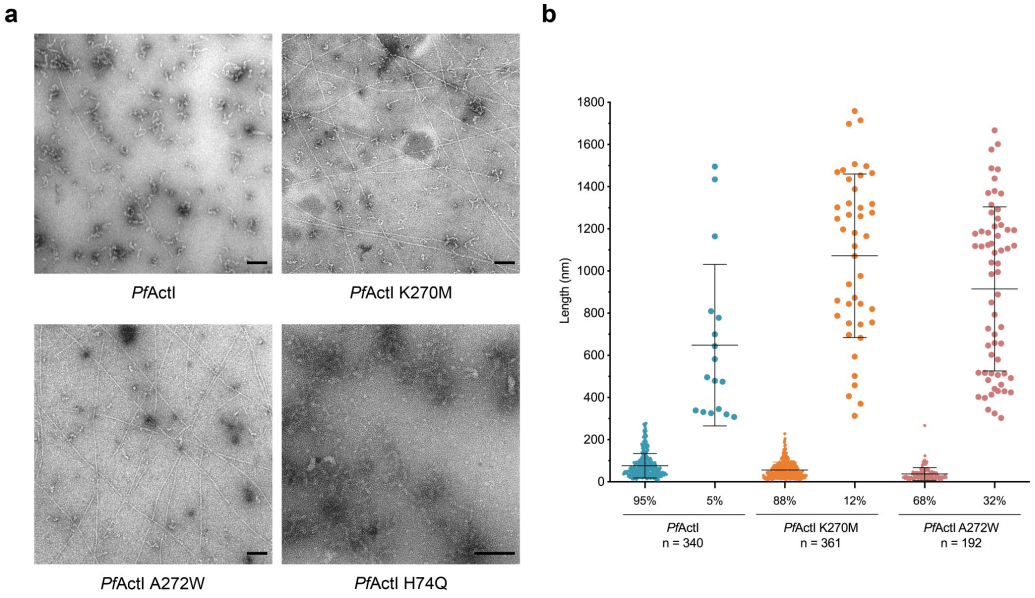

Fig 4. Abundance of long filaments is increased in *Pf*ActI mutations blocking conformation 2a. (A) Representative electron micrographs of negatively stained, polymerized wild-type *Pf*ActI and the K270M, A272W, and H74Q mutants. Wild-type *Pf*ActI formed mostly irregular short filament-like structures with the occasional appearance of long filaments. The K270M mutant formed longer helical filaments at an over double frequency, whereas the A272W mutant formed long filaments 6 times as often as the wild type. No long helical filaments were observed for the H74Q mutant. (B) Quantitative analysis of filament lengths of wild-type *Pf*ActI and the mutants K270M and A272W. Note that the maximum length is defined by the field of view, and in reality, the long filaments are much longer than what was measured. The underlying data for this figure can be found in S2 Data. Scale bars in (A) represent 100 nm. *Pf*ActI, *P. falciparum* actin I.

https://doi.org/10.1371/journal.pbio.3000315.g004

Fig). We reasoned that if the disappearance of the positive charge by the K270M mutation changed the P_i release dramatically, P_i release might be directly related to the conformation of the A loop. Thus, large side chains at position 272 that affect the movement of the A loop should also modulate the P_i release rate. We therefore prepared A272C and A272W mutants—the first to provide a side chain of moderate size, also mimicking *Pb*ActII, and the second to block the movement of the loop completely, both presumably favoring conformation 1a/b. The A272C mutant caused a moderate 5.1-fold activation upon Mg^{2+} binding, whereas the A272W mutant showed a large 18.9-fold activation and the largest observed rate ($9.78 \pm 0.06 \times 10^{-4}$ s^{-1}) in Mg conditions (Fig 1A, S2 Table). As with K270M, the increased P_i release rate in the A272W mutant is not due to faster elongation (Fig 1B), and there are more long filaments of this mutant at equilibrium (Fig 4).

The A272W structure in MgK conditions resembles overall the mixed structure (root-mean-square deviation (RMSD)(Cα) = 0.269) more than the Mg-ADP structure (RMSD(Cα) = 0.410) and is positioned close to the Ca-ATP structure in the PCA analysis. The A loop is forced into conformation 1b by the Trp272 side chain (Fig 3E). Glu73 is in a double conformation, one similar to the Mg-ADP structure and another to that of the Mg-ATP/ADP structure (Fig 3E, S6 Fig). In addition to limiting the conformational space of the A loop, Trp272 forces Lys270 away from the Asp180 side chain and toward the solvent, widening the gap between His74 and Lys270 from 7.7 to 10.4 Å and only slightly altering the conformation of residues

Leu268-Asn281 (RMSD = 0.27 Å, Mg-ATP/ADP-*Pf*ActI compared with Mg-ATP/ADP-*Pf*ActI-A272W; Fig 3E). The occupancy of ATP in the active site of this relatively fresh crystal is only 0.3 (S5 Table).

To generate a mutant that would favor conformation 2a of the A loop, we further prepared a neutralizing H74Q mutant, which negates the charge on the histidine side chain, forcing an unfavorable interaction of the glutamine with Asp180. This mutant was severely compromised in terms of P_i release, with α-actin levels of P_i release in the Ca state ($0.27 \pm 0.03 \times 10^{-4}$ s^{-1}) and no activation by either Mg^{2+} or K^+ or by using a higher protein concentration (Fig 1A, S2 Table). Moreover, H74Q did not form any long filaments, even though its elongation rate appeared rather similar to the wild type. (Figs 1B and 4). In this mutant (MgK conditions), the Asp180 side chain is oriented away from Gln74, which interacts with Arg178 (Fig 3F). However, the backbone of the loop did not adopt conformation 2a, and we therefore call this conformation 2b, because the carboxylic acid group of the Asp180 side chain occupies the same space as that in conformation 2a, preserving the interaction with Lys270 (Fig 3F).

Arg184 interactions with the H loop in SD2

Interactions across the interdomain cleft mediate twist angle stability and the openness of actin [39]. Upon ATP hydrolysis in *Pf*ActI, Glu73 in the H loop undergoes a conformational shift, whereby the backbone is flipped and the side chain orients toward the ID and interacts with Arg184 (Fig 5A–5E, S9 Fig). This conformational shift happens also in *Pb*ActII (Fig 5H and 5I) and in several canonical actin structures [16,28,30]. In Ca-ATP-*Pf*ActI, Arg184 is engaged in a cation-π interaction with Tyr70. This interaction is preserved in the mixed structure but is dissipated in the pure Mg-ADP state (Fig 5B–5D), after an interaction transfer of Arg184 from Tyr70 to the flipped backbone carbonyl of Glu73. In F-*Pf*ActI, the interaction between Arg184 and Glu73 is enhanced by a hydrogen bond between Arg184 and the Ile72 carbonyl. In the *Pf*ActI H74Q and A272W mutants, the conformations in this area resemble those of the Ca-ATP (in H74Q) and Mg-ADP (in A272W) states (Fig 5F and 5G, S6 Fig).

The effects of canonical-type mutations in the D loop on phosphate release

The major substitutions in the D loop of *Pf*ActI are Pro42, Glu49, and Phe54 (Gln41, Gly48, and Tyr53 in α-actin; S7 Fig). Tyr53 is a conserved phosphoregulation site in canonical actins [22], whereas the other 2 sites are interesting because of their possible conformational effects. These residues are invisible or only barely visible (in the case of Phe54) in the crystal structures. However, in the filament, the tip of the D loop of *Pf*ActI differs from canonical actins [10]. We therefore measured P_i release rates for the mutants F54Y [9], P42Q, E49G, and the double mutant P42Q/E49G of *Pf*ActI. P42Q and E49G showed opposite effects in Mg^{2+} activation with P42Q reducing and E49G increasing it, but both were similarly insensitive to K^+ (Fig 1A, S2 Table). However, the negative effect of P42Q is due to an increase in the Ca rate compared with wild type, whereas the positive effect of E49G on Mg^{2+} activation is caused by both reduced rate in Ca and an increased rate in Mg. The double mutant has reduced Mg^{2+} activation with levels indistinguishable from the wild type while still remaining insensitive to K^+. Thus, it seems to be dominated by the effect of E49G in the Ca state and shows a compounded negative effect that is not shown by either of the mutations alone.

At high concentration (10 μM), the F54Y mutation reduces the rate of hydrolysis in the Ca state to α-actin levels [9]. Here, we measured the rates at a concentration of 1 μM. The Mg^{2+}- and K^+-activation levels of F54Y were similar to the wild type, but the absolute rates were approximately doubled (Fig 1A, S2 Table). In the Ca condition, the F54Y mutant behaves similarly to P42Q (S3 Table), whereas the rates in the Mg and MgK conditions were most similar

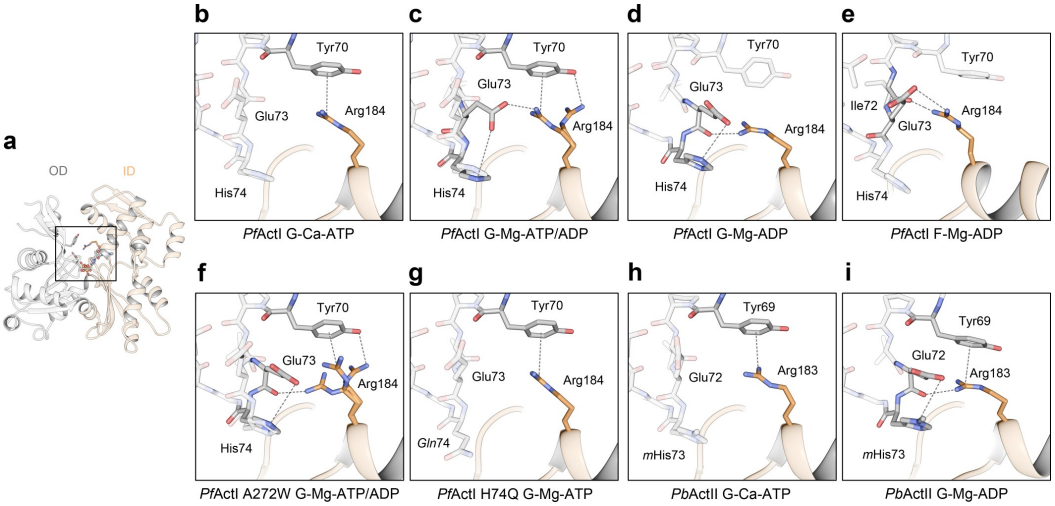

Fig 5. Conformation of the H loop residues 70–74 as well as the domain cleft spanning Arg184 in *Pf*ActI and corresponding residues 69–73 and Arg183 in *Pb*ActII. (A) Overview of the wild-type *Pf*ActI monomer in the Ca-ATP state [9] for positional reference. (B–E) Wild-type *Pf*ActI in the (B) Ca-ATP state [9], (C) Mg-ATP/ADP state, (D) Mg-ADP state, and (E) F state [10]. (F–G) *Pf*ActI mutants (F) A272W in the Mg-ATP/ADP and (G) H74Q in Mg-ATP states. (H–I) Wild-type *Pb*ActII in the (H) Ca-ATP [9] and (I) Mg-ADP states. The ID and OD are colored in orange and gray, respectively, in all panels. His73 of *Pb*ActII in (H) is methylated for consistency even though it is nonmethylated in the original PDB entry. Interatomic distances amenable to ionic interactions or hydrogen bonding (≤4 Å) are shown as dashed lines. F, filamentous; G, globular; ID, inner domain; mHis73, methylated His73; OD, outer domain; *Pb*ActII, *Plasmodium berghei* actin II; *Pf*ActI, *P. falciparum* actin I.

https://doi.org/10.1371/journal.pbio.3000315.g005

to the E49G mutant. Thus, these canonical-type mutations in the D loop area all have similar effects on P_i release. However, whereas P42Q and E49G directly affect the tip of the D loop in the filament, F54Y presents no foreseeable structural changes besides the added H bonds to Lys62 of monomer n and to Tyr170 of monomer n − 2 in the filament.

G115A mutation structures the C terminus of *Pf*ActI

Gly115 in *Pf*ActI is located in the P loop of SD1 and is Thr, Ser, or Ala in other reference actins (S7 Fig). Nearby, Pro110 interacts with Arg178 in conformation 1b, and the backbone flexibility conveyed by Gly115 could control the positioning of this interaction. We previously generated a mutant G115A that did not rescue long filament formation in the absence of jasplakinolide but showed slightly longer filaments than the wild type in its presence [9]. We crystallized the mutant using the same conditions as the wild-type *Pf*ActI with either Ca^{2+} or Mg^{2+} to compare these structures. Unlike the wild type (Fig 6A), the C terminus of G115A is more ordered, with interpretable electron density up to Cys375 in the Ca^{2+} and up to His372 in the Mg^{2+} structure (Fig 6B and 6C). In contrast, all other structures of *Pf*ActI, with the exception of H74Q (Fig 6D) and the *Pb*ActI-α-actin D-loop chimera [9], have a disordered C terminus after Ser366.

The G115A mutation straightens α3 and moves the P loop slightly away from the C terminus. This in turn favors a cation-π interaction between Lys114 and His372 (3.7 Å) and a hydrogen bond between Glu118 and His372 (2.8 Å). In the wild type, the position of Lys114 does not allow both interactions to take place simultaneously, which is the likely reason for the disordered C terminus (Fig 6A). In filaments, this interaction is preserved with corresponding

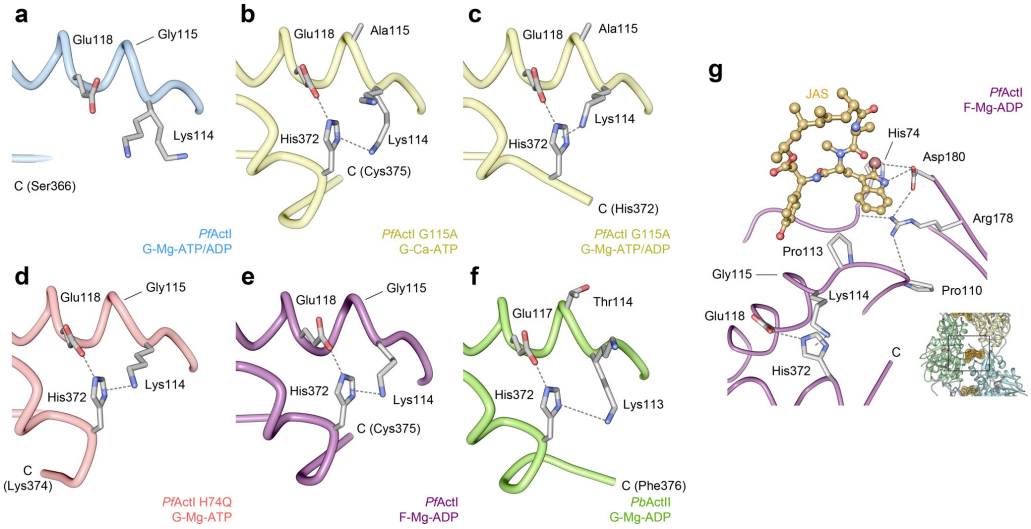

Fig 6. Interaction of the C termini of *Pf*ActI and *Pb*ActII with Lys114 (Lys113 in *Pb*ActII) and Glu118 (Glu117 in *Pb*ActII) of α3. (A) Wild-type *Pf*ActI in the Mg-ATP/ADP state has a disordered C terminus. The *Pf*ActI G115A mutant, in contrast, shows an ordered C terminus in the Ca-ATP state (B) and in the Mg-ATP/ADP state (C), similarly to the H74Q mutant in the Mg-ATP state (D). (E) Wild-type *Pf*ActI in the JAS-stabilized F state [10] and (F) *Pb*ActII in the Mg-ADP state also have stabilized C termini. The C-terminal His372 interacts with Lys114 and Glu118 of α3 due to the displacement of the N-terminal tip of the helix. In G115A, this is caused by the altered backbone conformation. In H74Q, the effect is likely indirect. In wild-type *Pf*ActI, the C terminus is not stabilized in any gelsolin-bound structure by the His372 interactions, which however are retained in the JAS-stabilized filament structure due to interactions of the P loop with the bromoindole moiety in JAS. In *Pb*ActII (F), residue 114 (corresponding to Gly115 in *Pf*ActI) is threonine and elicits a stabilization of the C terminus. (G) JAS interactions with the P loop and the A loop in the F-*Pf*ActI structure [10]. Interaction distances amenable to ionic or hydrogen bonding interactions (≤4 Å) are indicated with dashed lines. The inset in (G) shows the position in the filament. C, C terminus (with the terminal residue indicated); F, filamentous; G, globular; JAS, jasplakinolide; *Pb*ActII, *Plasmodium berghei* actin II; *Pf*ActI, *P. falciparum* actin I.

https://doi.org/10.1371/journal.pbio.3000315.g006

distances of 3.1 Å (Lys114-His372) and 3.0 Å (Glu118-His372; Fig 6E). *Pb*ActII, which has an ordered C terminus in both Ca and Mg states (Fig 6F), has a threonine in the corresponding position 114. The distances from Lys113 and Glu117 to His372 are 2.7 Å and 5.0 Å in Mg-ADP-*Pb*ActII. The altered position of the P loop does not extend to Pro110 and therefore does not directly influence the interactions of Arg178 at the interface of SD1 and SD2. Trp357 and Phe353 are in a double conformation in both structures, the former facilitating a recently identified cation binding site [40]. The conformations 1a and 1b of the A loop are evident in these structures, but conformation 2a is not visible in the Mg^{2+} structure. G115A has only slightly decreased P_i release rates in Mg and MgK conditions (Fig 1A, S2 Table).

Discussion

On the roles of ions in actin polymerization

The fortunate coincidence that our crystallization condition for both *Plasmodium* actins and the mutant forms contained K^+ provided direct evidence of Mg^{2+}-dependent K^+ binding in the active site of *Pf*ActI. This is, to the best of our knowledge, the first experimental evidence of K^+ in the active site of actin. The presence of K^+ is in conjunction with the Mg-ATP state but not with the Ca-ATP or Mg-ADP states. Thus, K^+ seems to be involved in hydrolysis and leave the active site together with the P_i. Compared with the nonphysiological, inactive

calcium-bound state, Mg^{2+} binding in the presence of K^+ causes a slight flattening and possibly a tendency toward opening of the *Pf*ActI monomer, followed by a closing and twisting back upon hydrolysis. The slightly flattened conformation may well be the explanation why Mg-K-ATP actin is the fastest polymerizing actin species [7]. Conversely, Mg-K-ADP actin polymerizes weakly in canonical systems [7], and the twisting (i.e., moving further away from the F conformation) upon ATP hydrolysis, as seen for *Pf*ActI, may explain this. However, because the path of the G-F transition may have major intermediates that are off the linear path and cannot be captured by crystallographic analysis, the validity of the connection between polymerization propensity and twist of a G-actin structure remains to be confirmed. It should also be noted that the response of *Pf*ActI to ADP differs from canonical actins [9], and we do not yet completely understand the dependency of ATP hydrolysis and polymerization in the parasite actins.

A structural homolog of actin, Hsc70, has a conserved K^+ binding site at the same location as *Pf*ActI [25]. The activity of Hsc70 decreases slightly in the presence of ammonium [41], which is in line with our previous finding that CH_3COONH_4 is able to "protect" *Pf*ActI from oligomerization, which in turn is dependent on ATP hydrolysis [9,13]. However, because *Pf*ActI did not respond to K^+ in P_i release assays, the exact role of the active site K^+ in P_i release remains to be investigated. The positive charge on the K^+ may play a role in orientation of the γ-phosphate or the catalytic water or charge complementation of its conjugate base OH^- in the reaction pathway, as has been suggested for Hsc70 [42]. Unlike Hsc70, however, the presence of K^+ is not mandatory for hydrolysis in *Pf*ActI. Yet its presence may challenge previous hydrolysis mechanisms proposed based on simulations [43,44].

The A loop enables fragmentation but at the same time likely also contributes to increased nucleation

Apicomplexan microfilaments are short but display a relatively normal critical concentration of polymerization, which means that the filament length distribution must result from the overabundance of nucleation, fragmentation, or both. Because the lag phase is very short [13], increased nucleation likely contributes. However, we believe fragmentation is at least equally important, and these 2 are likely interconnected. The conformation of the A loop clearly connects to the stability of long filaments in *Pf*ActI. This is evidenced by increased proportion of long filaments when conformation 1a/b is favored by mutations K270M and A272W and, on the other hand, by a complete lack of long filaments in the 2a-favoring H74Q mutant. The K270M mutant also releases phosphate quantitatively faster and qualitatively similarly to α-actin. In the *Pf*ActI filament model, conformation 2a is not seen, likely because jasplakinolide binds both Arg178 and Asp180, fixing them in a stable conformation. In its absence, the filament structure would permit this conformation. Because these mutations affecting phosphate release rate and filament length do not significantly modulate polymerization kinetics, it is likely that a mechanism distinct from simple weakening of interprotomer contacts exists. However, because short filaments are still present in K270M and A272W, other factors such as the ones at the base of the D loop (discussed below) may be involved. In vivo, the mutation K270M is lethal in the blood stages of the *Plasmodium* life cycle, which serves to illustrate the significance of filament length to parasite survival [45].

The interplay between the H loop, the A loop, and the plug is complex, but our data provide important insights into how the movement of this triad connects to the mechanism of P_i release and (de)polymerization. P_i release is strongly influenced by the conformational distribution of the A loop into the 2 configurations 1a/b and 2a/b, as we show by P_i release measurements and structures. Conformation 2b is counterproductive to P_i release, whereas

elimination of 2a by steric hindrance (as in the mutants A272W and A272C) or by charge neutralization (K270M) favors P_i release, suggesting that interactions of the A loop with the H loop and the P loop are required for native activity levels. Methylation of His73/74 and the resulting change in side-chain charge distribution is a key modulator of P_i release. A methylated histidine, as found in most actins, is approximately 11-fold more protonated in the cellular pH than a nonmethylated histidine would be. The only other species with a nonmethylated histidine at this position, and for which there are structures available, is *S. cerevisiae*, which—like *Pf*ActI—has a shorter lag phase of polymerization and no lag in phosphate release upon polymerization [46]. However, in structures of *S. cerevisiae* actin (*Sc*Act), conformation 2a/b is not present, possibly due to the presence of Leu269 and Ala114 instead of Lys270 and Gly115 [47].

F-actin–like interactions in the Mg-ATP state can be considered favorable for polymerization. We consider interactions spanning the cleft between ID and OD on the back face of the monomer the most favorable for flattening and thus nucleation and polymerization. There are only 2 such interaction sites: (i) between Arg184 of SD4 and Tyr70 and Glu73 of SD2 (Fig 5) and (ii) between Arg178 of SD3 and Pro110 and His74 of SD1 and SD2, respectively (S9 Fig). In (i), the interaction of Arg184 via a cation-π interaction to Tyr70 is supplemented by an ionic bond with Glu73 in the Mg-ATP/ADP structure, followed by a movement of Glu73 toward SD2 and a consequent hydrogen bond to the backbone of Ile72 in the F state. Yet, although the polymerization rate of the β-actin R183W mutant was significantly decreased [39], the α-actin R183G mutant displayed unaltered polymerization kinetics [48]. In (ii), the Arg178 interaction is absent in Ca-ATP actin but present in conformation 1b of Mg-ATP/ADP-*Pf*ActI. The interaction is preserved between His74 and Arg178 and further strengthened by hydrogen bonding to the carbonyl of Leu111. An R177H mutant in yeast actin results in an extended lag phase in polymerization [49], which corroborates that this interaction promotes nucleation. Arg177 is also the site for polymerization-inhibiting ADP ribosylation by iota toxins [50,51].

Based on our observations, we propose a model for *Pf*ActI filament fragmentation (Fig 7, S2 Movie). In this model, conformation 2a in the naked *Pf*ActI filament severs the contact between the ID and OD, leading to destabilization of the monomer twist and filament contacts, eventually causing a break in the filament. The model provides an alternative, perhaps complementary, explanation to the electrostatic effects we presented based on the filament model [10] and would also explain the increased pelleting of native *Pf*ActI at low pH [8].

On the role of the D loop

The 2 substitutions in the D loop (Pro42 and Glu49 in *Pf*ActI) contribute to the unstable nature of *Pf*ActI filaments. These mutations favor the unstable closed D-loop conformation [35] to such an extent that even in the presence of jasplakinolide, which forces the stable open D-loop conformation in α-actin, the *Pf*ActI filament adopts the closed conformation [10]. Pro42 and Glu49 are in close proximity to the stiffness and polymerization cation sites [52], which in turn are close to 2 substitutions in *Pf*ActI, namely, Gly200 and Phe54. Together, these residues seem to participate in a complex interplay that is likely one of the major components of filament instability in *Pf*ActI. Because P_i release of E49G is activated 2.2-fold more by Mg^{2+} than wild type, whereas the activation of P42Q/E49G and P42Q is equal or less, respectively, one can conclude that these mutations are complementary to each other and that conformational restrictions of the D loop and P_i release rates are reciprocally connected. Like K270M, the mutation P42Q is lethal in vivo, highlighting the fact that the conformational rigidity of the D loop is critical to parasite biology [45]. Additionally, the effects of the F54Y mutation on

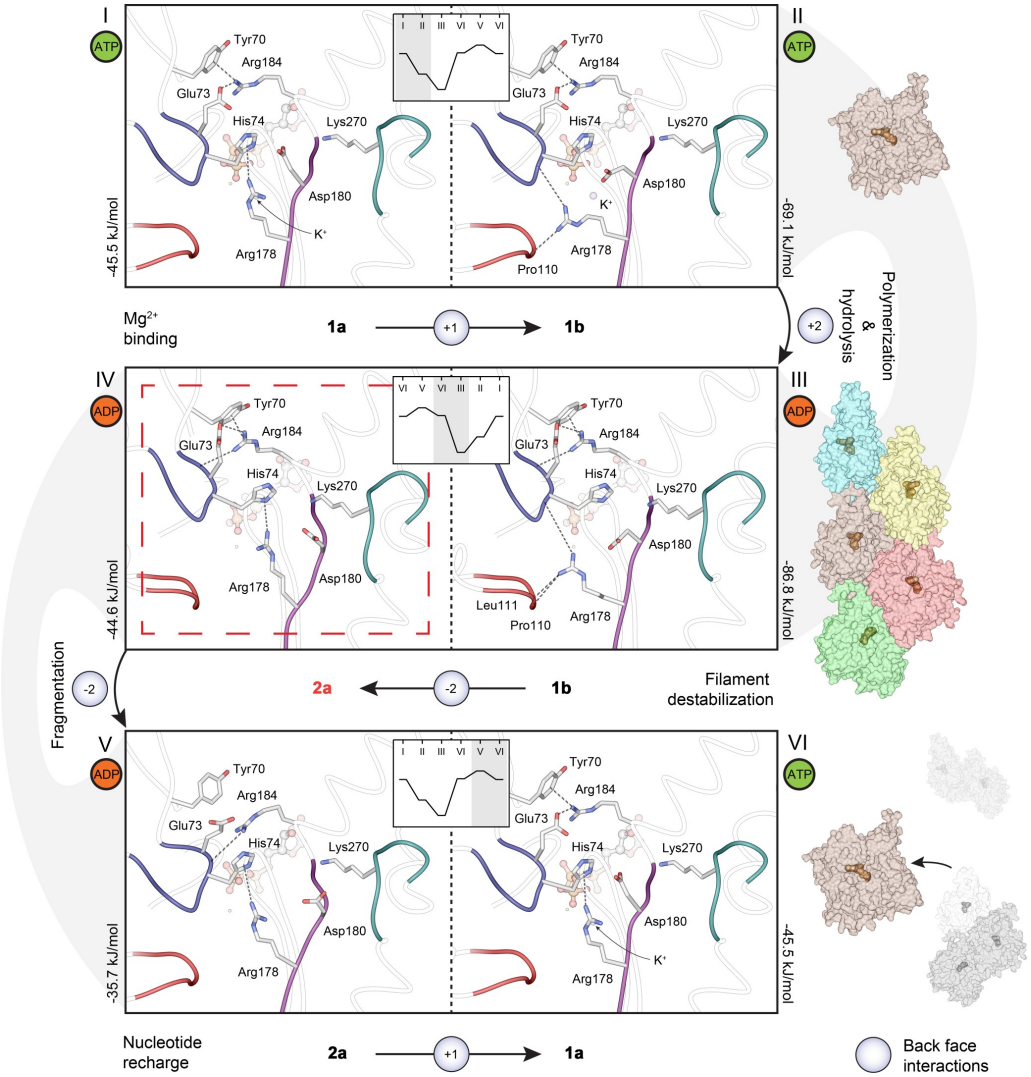

Fig 7. Mechanistic model of conformational changes in the *Pf*ActI monomer during polymerization, fragmentation, and nucleotide recharge. The exchange of Ca^{2+} to Mg^{2+} in vitro causes a conformational change from conformation 1a (I) to 1b (II), conferring 2 new back-face interactions that stabilize an F-like conformation. Upon polymerization (III), 2 new interactions are formed (Arg178 to backbone of Leu111 and Arg184 to backbone of Glu73), further stabilizing the flat conformation. In F-*Pf*ActI, ATP is hydrolyzed to ADP, and the P_i is released without major rearrangements [18], causing a further reduction in interactions spanning the ID–OD cleft via the G and S loops (loss of 5 hydrogen bonds between *Pf*ActI and Pγ; not depicted). In a hypothetical model of F-*Pf*ActI, in which conformation 2a is adopted (IV), 2 interactions formed by the adoption of 1b (II) are broken, causing a destabilization of the OD in respect to the ID, promoting a filament break. Upon fragmentation and dissociation of the monomer from the newly formed pointed end, conformation 2a is retained (V) in the ADP-*Pf*ActI monomer, the nucleotide is exchanged, and conformation 1a is reassumed (VI). Changes in the number of interactions on the back face of the monomer (on the inside of the filament) across the ID–OD cleft are highlighted in blue circles. Total interactions (hydrogen bonds, ionic interactions, and cation-π interactions) across the ID–OD cleft are 1, 3, 5, 2, and 1 in G-Mg-ATP 1a, G-Mg-ATP 1b, F-Mg-ADP 1b, F-Mg-ADP 2a, and G-Mg-ADP 2a, respectively, excluding changes caused by loss of Pγ. In the insets, interaction energies from Arg178, Asp180, and Arg184 to H and P loops are indicated in graphical form, whereas the absolute interaction energies are indicated next to each panel. Note that

the inset is mirrored in panels III and IV to reflect the overall flow of the figure. The underlying data for this figure can be found in S3 Data. F, filamentous; G, globular; ID, inner domain; OD, outer domain; *Pf*ActI, *P. falciparum* actin I; P_i, inorganic phosphate.

https://doi.org/10.1371/journal.pbio.3000315.g007

overall rates (but not the activation) show that this mutation has a role beyond post-translational modifications. Interestingly, structural information on P_i release seems to be "erased" from α-actin filaments by jasplakinolide, which is attributed to the D-loop conformation [35]. The fact that *Pf*ActI filaments can be stabilized by adding jasplakinolide into filaments after polymerizing to equilibrium [10] shows that the binding of jasplakinolide can overcome the effects of the constantly closed conformation of the D loop.

Concluding remarks

Although there are several structural factors contributing to the unique properties of *Plasmodium* microfilaments, the A loop seems to be a major switch between stable and unstable filament conformations. As such, it would be responsible for faster breakdown of the filaments but, on the other hand, also for lowering the energy barrier for polymerization, leading to increased nucleation. There are no known actin-binding proteins that can directly affect this region of the filament, suggesting that this mechanism could be a major intrinsic determinant of filament lengths in vivo. Importantly, although less favorable due to increased protonation of the methylated His73, the lack of attraction between Asp179 and Met269, and the apparent absence of conformation 2a caused by the G115A substitution, the proposed mechanism could work also in canonical actins. As crystal structures represent low-energy states, it is possible that fragmentation in canonical actins proceeds through the same mechanism, simply less frequently.

Materials and methods

Unless otherwise stated, all materials were purchased from Sigma (St. Louis, MO).

Mutagenesis

*Pf*ActI mutants were generated by site-directed mutagenesis as described for F54Y and G115A by Vahokoski and colleagues [9]. Mutants A272W, A272C, H74Q, P42Q, E49G, and P42Q/E49G were prepared using similar methods as before, with different primers. All mutants were confirmed by capillary sequencing at the Biocenter Oulu Sequencing Core or at the Center for Medical Genetics and Molecular Medicine, Haukeland University Hospital, Bergen.

Protein expression and purification

Wild-type and mutant *Plasmodium* actins were purified as described by Vahokoski and colleagues [9,13]. Briefly, insect-cell–expressed His-tagged *Plasmodium* actins were purified using Ni-NTA (Qiagen, Hilden, Germany) affinity chromatography, cleaved with a recombinantly expressed protease (tobacco etch virus [TEV] protease for *Pf*ActI and rhinoviral 3C protease for *Pb*ActII). The cleaved protein was then passed through a second Ni-NTA column to remove the His tag and uncleaved protein. Finally, the purification was finalized by gel filtration over a Superdex 200 column (GE Healthcare, Chicago, IL). Mouse gelsolin segment 1 was purified as described by Bhargav and colleagues [53] and included in actin samples (where applicable) before gel filtration at a 1.2-fold molar excess.

Phosphate release assays

P_i release was measured using the 7-diethylamino-3-[N-(2-maleimidoethyl)carbamoyl]coumarin-labeled phosphate-binding protein (MDCC-PBP) biosensor [54,55] that produces a fluorescence signal upon P_i binding. To reduce P_i, ATP, and ADP background, monomeric actins used for P_i release assays were pretreated with DOWEX 1X8 resin equilibrated with G_0 buffer (10 mM HEPES [pH 7.5], 0.2 mM $CaCl_2$, 0.5 mM TCEP) for 3 min at 298 K and further diluted using G_0 buffer to 1.6-fold higher concentration than that used for measurements. Before initiating the kinetic measurements, components for the different conditions were supplied as 8-fold concentrated stocks such that the desired final concentrations of all components were reached. Final compositions of the 3 conditions were 10 mM HEPES (pH 7.5), 0.2 mM $CaCl_2$, 0.5 mM TCEP, 50 μM ATP (Ca condition), Ca condition with added 1 mM $MgCl_2$ (Mg condition), and Ca condition with added 4 mM $MgCl_2$, 1 mM EGTA, and 50 mM KCl (MgK condition). Fluorescence was recorded using a Tecan Infinite M1000 plate reader (Tecan, Männedorf, Switzerland) and black 384-well plates (Greiner, Kremsmünster, Austria) at λ_{ex} = 430 nm and λ_{em} = 465 nm using bandpass filters with 5-nm bandwidth and a 10-s measurement interval. Fluorescence versus time data were converted to μM P_i by linear interpolation of a standard series of P_i and analyzed by linear regression at the linear portion of the kinetic curve. The slope of the regression line was then divided by the protein concentration measured after DOWEX treatment to yield the final rates. For the P_i release curves, the abscissa units are values of μM phosphate released divided by μM actin, which describes the average turnover of the hydrolytic cycle in each sample.

In the presence of Mg and in MgK, α-actin displays an initial lag phase, followed by an exponential P_i release curve, which, at high concentrations, plateaus close to the upper limit of the linear range of the system (S1 Fig). We therefore decided to consider only the first 2 phases for our analyses. We further calculated the activation of P_i release by Mg^{2+} and by K^+ by dividing the Mg rate by the Ca rate in the former and the MgK rate by the Mg rate in the latter. These ratios are a sensitive measure for comparing actins to one another, because they are insensitive to changes in residual nucleotide contamination in the samples. These contaminants are of the order of <10% of the 50-μM ATP added to each reaction. Because the total nucleotide concentration is in a >50-fold excess over the nM-range dissociation constant of ATP to actin [56], we assume that in the assay, actin is saturated and not affected by small fluctuations in the nucleotide concentration. All plotting and analysis were performed in Prism 8.0.0 (GraphPad, San Diego, CA).

Actin polymerization assays

*Pf*ActI wild type and mutants were labeled with N-(1-pyrene)iodoacetamide (Life technologies, Invitrogen, Eugene, OR) as described by Kumpula and colleagues [13]. Labeled and unlabeled actin samples were mixed in a volume ratio of 1:2 (labeled:unlabeled) by volume at a concentration of 8.1-μM actin to reach a labeling ratio of approximately 10%. Polymerization assays nucleated by α-actin filaments were prepared as described by Kumpula and colleagues and Pollard [13,57]. Briefly, 50 μl of the above mixture was transferred into each well followed by the addition of 100 μl of 0.75-μM polymerized muscle α-actin seed solution that was freshly prepared in 1.5× F buffer from a 5-μM stock to initiate the polymerization reaction. The resulting 150-μl reaction mixture contained 1× F buffer with final *Plasmodium* actin and α-actin concentrations of 2.7 μM and 0.5 μM, respectively. Measurements were carried out in a Tecan Spark 20M multimode microplate reader using black 96-well plates (Greiner), λ_{ex} = 365 nm (9 nm bandpass) and λ_{em} = 407 nm (20 nm bandpass), 5 flashes per measurement and a 2-s

orbital mixing step performed at 250 rpm before commencing the measurements. The resulting polymerization curves were normalized and plotted in GraphPad Prism 8.0.0.

Electron microscopy

*Pf*ActI wild-type and mutant samples were polymerized for 16 h at 298 K at a concentration of 20 μM in F buffer. Prior to application on carbon-coated 200-mesh Cu grids (Electron Microscopy Sciences, Hatfield, PA), samples were diluted to a final concentration of 1 μM and immediately applied on the grids. Samples were incubated for 60 s on the grids, dried from the side using prewetted Whatman paper, and washed with 3 drops of F buffer. Then, they were stained with 2% uranyl acetate, first for 2 s and then for 60 s, in a fresh drop before drying from the side as before and then drying in air. The grids were imaged using a JEOL JEM-1230 microscope (JEOL Ltd., Tokyo, Japan) operated at 80 kV and with a final pixel size of 1.22 nm. The images were analyzed using the ridge detection plugin available in ImageJ 2.0.0 [58]. The calculated length measurement for any given filament corresponds to the portion that lies within a given frame and therefore cannot be used as a measure of the actual length of the long filaments.

Protein crystallization

*Pf*ActI-G1 and *Pb*ActII-G1 complexes in the Mg state were prepared essentially as described by Panneerselvam and colleagues [27], with the exception that $CdCl_2$ was replaced by 1 mM $MgCl_2$. In some cases, crystals were grown by streak seeding as described by Panneerselvam and colleagues [27], and in others, crystals were obtained directly from optimization screens without seeding. Cryoprotection was achieved by soaking for 5 to 30 s using the same condition as for the crystallization with a higher precipitant concentration (PEG3350, 22%–28%) and PEG400 at 10% to 20% as the cryoprotectant. Protein buffer components were also included in the cryosolutions at concentrations of 1 mM $MgCl_2$, 0.5 mM ADP, and 0.5 mM TCEP for the Mg conditions and 0.2 mM $CaCl_2$, 0.5 mM ATP, and 0.5 mM TCEP for the Ca conditions. The pH of the crystallization reservoir buffer (0.1 M Bis-Tris) varied from 5.8 to 6.5. Mg-ADP-*Pf*ActI-G1 crystals were cryoprotected in a solution containing 50 mM potassium phosphate. Mg-ADP-AlF_n-*Pf*ActI(F54Y)-G1 crystals were prepared by adding a solution of 20% PEG3350, 0.1 M Bis-Tris (pH 6.0), 0.2 M KSCN, and 1 mM AlF_n solution directly into the drops and incubated for a few minutes before cryoprotection with a solution as described above. The AlF_n solution consisted of premixed $AlCl_3$ and NaF in a 1:4 molar ratio. The minimum time between data collection from a crystal yielding structures with ATP/ADP mixtures and ADP only was 6 mo for Mg-*Pf*ActI-F54Y crystals, whereas the time from crystallization to data collection from Mg-*Pb*ActII was only 2 wk.

Diffraction data collection, processing, and structure refinement

Crystallization data were collected at 100 K at several beamlines. Mg-ATP/ADP-*Pf*ActI, Mg-ADP-P_i-*Pf*ActI, Mg-ADP-F54Y, and Mg-*Pb*ActII were collected at beamline P13 of PETRA III, DESY (Hamburg, Germany); Ca-F54Y and Mg-AlF_n-F54Y were collected at I24 of Diamond Light Source (Didcot, UK); Mg-F54Y, Mg-H74Q, and Mg-A272W were collected at I04-1 of Diamond Light Source (Didcot, UK), Ca-G115A was collected at ID23-1 of ESRF (Grenoble, France); and Mg-G115A was collected at MX-14.1 of BESSY (Berlin, Germany). Diffraction images were processed using the XDS package [59]. Structure determination and refinement were carried out using programs of the PHENIX suite [60]. Initial phases were found by molecular replacement with PHASER [61], using the Ca-ATP-*Pf*ActI-G1 structure (PDB ID 4CBU) as the search model for the *Pf*ActI structures and the Ca-ATP-*Pb*ActI-G1

structure (PDB ID 4CBX) for the *Pb*ActII structure. Additionally, MR-SAD using Autosol [62] was used to reduce model bias in the Mg-ADP-AlF_n-F54Y structure. Structure refinement was carried out using phenix.refine [63].

PCA

There are 2 main structural rearrangements recognized in actin: the twistedness of the 2 main domains (SD1–2 and SD3–4) along an axis that pierces SD1 and SD3 at their respective centers and the openness of the nucleotide-binding cleft as a rotation around an axis perpendicular to the twist axis and to the plane of the F-actin monomer. We analyzed 147 unique actin structures found in the PDB using BIO3D [64] at resolution $\leq$4 Å, together with the structures reported here, and found that these movements are captured well by PCA in PC1 (twistedness) and PC2 (openness) that contain 78% of total variance (S1 Movie). All actin sequences were first aligned using MUSCLE [65], and the sequence gaps were removed. Then, the structures were aligned on a common core before PCA analysis [66]. The common core was determined by iterative pruning of atoms until a preset volume threshold of 0.5 was reached [64]. In structures with multiple chains of actins, all chains were used for the PCA analysis, but a single chain was used for plotting.

In a plot of PC1 versus PC2 (S4 Fig), most actin structures cluster at the center of the plot. This large cluster contains all structures reported in this study as well as structures of actin bound to ABPs such as gelsolin and profilin. Several outliers to this large cluster form their own distinct groups. Filament structures cluster at low twistedness and average openness, open profilin-actin structures cluster at high openness and average twistedness, free G-actin structures cluster at high twistedness and average openness, and finally, ADF/cofilin bound actin structures cluster at high twistedness and low openness. We also analyzed *Plasmodium* actin structures as their own set by similar PCA analysis. PC1 and PC2 contain 84% of total variance in this data set, and their trajectories are toned-down versions of the twistedness and openness of the full data set (S1 Movie). Although PC1 in the limited data set can easily be recognized as the twisting motion of the full data set (due to the presence of the F-*Pf*ActI model), the opening-closing motion is slightly ambiguous (due to the lack of an open *Pf*ActI model) and is therefore indicated with an asterisk.

Domain motion analysis

To support the PCA analysis, we measured 3 parameters of 4 sets of structures: the domain distance between SD2 and SD4 (d_{2-4}), the phosphate clamp distance (b_2 [24]), and the torsion angle defined by all 4 SDs (θ). The d_{2-4} distance was measured by a distance between the mass centers of the Cα atoms of residues 35–39 and 52–73 for SD2 and 183–269 for SD4. The phosphate clamp distance was measured as the distance between α-carbons of Gly16 and Asp158. The torsion angle θ was measured using the mass centers of α-carbons from all 4 domains using the residue assignment defined above for SD2 and SD4, as well as residues 6–32, 77–137, and 340–366 for SD1 and residues 140–182 and 270–337 for SD3. The models used were (i) wild-type *Pf*ActI structures in the Ca-ATP, Mg-ATP/ADP, Mg-ADP, and F-ADP states; (ii) *Pf*ActI F54Y structures in Ca-ATP, Mg-ADP-AlF_3, and Mg-ADP; (iii) *Pb*ActII structures in Ca-ATP and Mg-ADP states; and (iv) *D. discoideum* actin structures of mutant E205A/R206A/E207A/P109I in Ca-ATP and Mg-ATP and mutant E205A/R206A/E207A/P109A in Ca-ATP and Mg-ADP. The results are presented in S7 Table. For the *D. discoideum* structures, all residue assignments are −1 relative to the numbers presented above. For *Pb*ActII, residue assignments for residue numbers smaller than 232 were −1 relative to *Pf*ActI and others as for *Pf*ActI.

Analysis of ID–OD interaction energies

The ID–OD contacts were analyzed using the Amino Acid Interaction (INTAA) server [67] that uses point-charge electrostatics and Lennard-Jones potentials to calculate an interaction energy term between selected amino acids. Three key residues from the ID (Arg178, Asp180, and Arg184) were selected, and interaction energies were calculated for 2 patches on the OD side (Lys69-Ile76 of the H loop and Glu108-Lys114) for the 5 models presented in Fig 7. Individual models were generated by selecting conformations with the least number of clashes in the area of interest. Hydrogen atoms were then added to these models using the AddH module in Chimera [68], resulting in singly protonated His74 at the δN. In the case of the F-*Pf*ActI model in conformation 2a (IV in Fig 7), the original F-actin model was superposed with the 2a conformation model derived from the Mg-ATP/ADP structure using SD3 only. The coordinates of the A loop were then transferred from the Mg-ATP/ADP model to the F-actin model, and the model was subsequently energy minimized in UCSF Chimera. One hundred steps of steepest descent minimization with 0.02-Å step size was followed by 10 steps of conjugate gradient minimization with 0.02-Å step size and keeping all the atoms except the A loop static, which kept in line with the hypothesis that the loop movement is the singular event affecting the ID–OD stability.

Supporting information

S1 Table. P_i release rates reported in the literature. P_i, inorganic phosphate.
(DOCX)

S2 Table. Phosphate release rates of actins in Ca, Mg, and MgK conditions and activation by Mg^{2+} and K^+ at actin concentrations of 1 μM.
(DOCX)

S3 Table. Phosphate release rates of actins in Ca, Mg, and MgK conditions and activation by Mg^{2+} and K^+ at actin concentrations of 3 to 6 μM.
(DOCX)

S4 Table. Crystallization conditions for the structures reported in this study.
(DOCX)

S5 Table. Crystallization states, ATP occupancies, pH, and resolution.
(DOCX)

S6 Table. Crystallographic data collection and refinement statistics.
(DOCX)

S7 Table. Distances and angles describing the SD positions from 4 sets of structures. SD, subdomain.
(DOCX)

S1 Fig. P_i release as a function of time from high concentrations of *Pf*ActI, *Pb*ActII, and α-actin. P_i release curves of (A) *Pf*ActI at 3.5 μM, (B) *Pb*ActII at 3.8 μM, and (C) α-actin at 5.9 μM in Ca-ATP (dashed black line), Mg-ATP (black line) and MgK (red line) conditions. The underlying data for this figure can be found in S4 Data. *Pb*ActII, *Plasmodium berghei* actin II; *Pf*ActI, *P. falciparum* actin I; P_i, inorganic phosphate.
(TIF)

S2 Fig. Alternate refinements of the active site of Mg-ATP/ADP-*Pf*ActI and identification of mHis73 in *Pb*ActII. Presence of ATP/ADP mixture and K in the active site of *Pf*ActI and

the presence of mHis73 in *Pb*ActII evidenced by electron density maps and mass spectrometry. Difference density maps (mF_o-dF_c) at 4 σ of *Pf*ActI active site refined with (A) ADP only, (B) ATP only, and (C) K replaced by full-occupancy water. (D) Electron density ($2mF_o$-dF_c) and difference density (mF_o-dF_c) maps around His73 at 1 σ and 4 σ, respectively, with a model refined as methylated and unmethylated His73. (E) Mass spectrum of full-length *Pb*ActII expressed in Sf21 insect cells. Spectrum measured by ESI-LCMS from 12 μM *Pb*ActII with 1.45% (v/v) TFA. The 42,822-Da peak corresponds to methylated *Pb*ActII, whereas the theoretical average molecular weight for unmethylated *Pb*ActII is 42,809 Da (Δm = 13 Da). The peak at 42,805 Da is unknown but could result from, e.g., intramolecular disulfides (2 × −2 Da). The underlying data for this figure can be found in S5 Data. ESI-LCMS, electrospray ionization liquid chromatography mass spectrometry; mHis73, methylated His73; *Pb*ActII, *Plasmodium berghei* actin II; *Pf*ActI, *P. falciparum* actin I; Sf21, *Spodoptera frugiperda* cell line; TFA, trifluoroacetic acid.
(TIF)

S3 Fig. Delayed P_i release in K270M and A272W mutants of *Pf*ActI and pH dependence of P_i release in wild-type *Pf*ActI. (A) The effect of pH on P_i release by *Pf*ActI. The P_i release rate was measured in Mg-ATP conditions at a range of pH values. The rates were normalized relative to the sample at pH 7.34, which corresponds to the standard assay conditions. (B) Delayed phosphate release in mutants K270M and A272W of *Pf*ActI. P_i release curves of *Pf*ActI wild-type (3.5 μM), K270M (6.4 μM), and A272W (4.3 μM) mutants in Mg-ATP (black lines) and MgK (red lines) conditions. The inset shows the complete curves with the same units as the main plot. The curves have been translated in Y to improve clarity. The underlying data for this figure can be found in S6 Data. *Pf*ActI, *Plasmodium falciparum* actin I; P_i, inorganic phosphate.
(TIF)

S4 Fig. PCA of actin structures in the PDB and from this study. (A) Plot of twistedness (PC1) versus openness (PC2) of the full data set of 147 actin structures (see also S1 Movie). Defined structural groups of filament structures (dark purple), Pfn-bound open structures (orange), free G actin structures (light purple), and ADF/cofilin-bound structures (pink) are indicated with F, Pfn, G, and C, respectively. The large heterogeneous group in the middle is shaded in gray. Structures of interest are indicated with circles or squares and names or PDB identifiers, whereas others are indicated with black dots. (B) Zoomed view of (A) containing the *Plasmodium* actin structures (excluding *Pb*ActII Mg-ADP) as well as 4 mutant *D. discoideum* actin structures [16] constituting a full set of nucleotide and divalent cation states. (C) PCA of *Plasmodium* actin structures only, with similar notation as in (A). (D) Zoomed view of (C) containing all relevant *Pf*ActI structures excluding the H74Q mutant and the *Pb*ActI–α-actin chimera [9]. The lines and dashed lines between the *Pf*ActI and *Pb*ActII structures indicate the path in the hydrolytic direction (ATP–ATP/ADP–ADP) as appropriate for each set of structures. F structures are underlined, all other structures are of the G form. The underlying data for this figure can be found in S7 Data. ADF, actin depolymerizing factor; C, ADF/cofilin-bound structures; F, filamentous; G, globular; *Pb*ActII, *Plasmodium berghei* actin II; PC, principal component; PCA, principal component analysis; PDB, Protein Data Bank; *Pf*ActI, *P. falciparum* actin I; Pfn, profilin.
(TIF)

S5 Fig. Residue-level anisotropic B factors of *Pf*ActI in Ca-ATP, Mg-ATP/ADP, and Mg-ADP states. Anisotropic B factors show relative destabilization of SD2 of *Pf*ActI during ATP hydrolysis. The size of the ellipsoids is proportional to residue-level B factors and the shape to

the direction of anisotropy. Presence of Mg induces an opening of the interdomain cleft and a directional destabilization of SD2 along the rotation of the G–F transition axis (through the mass centers of SD1 and SD3). (Front) View from the side of nucleotide entry (ID on the left, OD on the right). (Back) View from the opposite side of nucleotide entry. (OD) Side view from the OD side with ID faded out. (ID) Side view from the ID side with OD faded out. Numbers 1 through 4 indicate the respective SDs, and the arrows indicate the main direction of anisotropy. F, filamentous; G, globular; ID, inner domain; OD, outer domain; *Pf*ActI, *Plasmodium falciparum* actin I; SD, subdomain.
(TIF)

S6 Fig. Backbone conformations of residues around His74 in *Pf*ActI and His73 in *Pb*ActII. Orientations of the H-loop Glu73-His74 backbone in *Pf*ActI wild type and mutants A272W and H74Q as well as those of Glu72-His73 backbone in *Pb*ActII. *Pb*ActII, *Plasmodium berghei* actin II; *Pf*ActI, *P. falciparum* actin I.
(TIF)

S7 Fig. Multiple sequence alignment of actins from various kingdoms of life. Sequence alignment of selected actin amino acid sequences with secondary structure elements from *Pf*ActI [9]. α-helices and β-strands are indicated with helical symbols and arrows as well as Greek letters and numbers, whereas 3_{10} helices are only indicated by helical symbols. The loops and the plug region discussed in the text are highlighted under the sequences. The sequences are divided into 2 groups: (1) apicomplexan actins, including *Pf*ActI (Q8I4X0), *Pb*ActII (Q4YU79), and *Tg*Act (P53476) and (2) canonical actins from *Dd*Act (P07830), *Sc*Act (P60010), *At*Act (P0CJ46), *Hs*Act_alpha_sk (P68133), *Hs*Act_beta (P60709), *Hs*Act_gamma (P63261). Human actins are identical in sequence to corresponding other mammalian actins. Arrowheads indicate mutations studied in this work. The sequence numbering corresponds to that of *Pf*ActI. *At*Act, *Arabidopsis thaliana* actin; *Dd*Act, *Dictyostelium discoideum* actin; *Hs*Act_alpha_sk, *Homo sapiens* skeletal muscle α actin; *Hs*Act_beta, *H. sapiens* β actin; *Hs*Act_gamma, *H. sapiens* γ actin; *Pb*ActII, *Plasmodium berghei* actin II; *Pf*ActI, *P. falciparum* actin I; *Sc*Act, *Saccharomyces cerevisiae* actin; *Tg*Act, *Toxoplasma gondii* actin.
(TIF)

S8 Fig. Atomic-level B factors in the A loop of different *Plasmodium* actin structures. Temperature factors of protein side-chain atoms in the vicinity of the A loop. *Pf*ActI in (A) Ca-ATP state (all conformers), Mg-ATP/ADP state conformers A, B, and C (B–D), Mg-ADP state conformers A and B (E, F). *Pb*ActII in Ca-ATP state (G) and Mg-ADP state (H). The size of the sphere relates to the maximum and minimum B factors of each structure, whereas the color relates to the first quartile (Q1, dark cyan), median (Q2, white), and third quartile (Q3, maroon) of the total distribution of B factors in each structure. *Pb*ActII, *Plasmodium berghei* actin II; *Pf*ActI, *P. falciparum* actin I.
(TIF)

S9 Fig. Interactions of Arg178 of ID with the P loop of OD. Connections formed by Arg178 between the P loop of SD1 and the H loop of SD2 in the *Pf*ActI Mg-ATP/ADP structure. (A) Arg178 forms hydrogen bonds with backbone O of Pro110 in SD1 and His74 in SD2 in conformation 1b. (B) Interaction between Arg178 and SD2 is maintained by the cation-π interaction via His74 in conformation 2a, but the connection to SD1 is lost. (C) Contacts between the ID and OD are preserved in the F-*Pf*ActI model that is also in conformation 1b. OD residues are indicated in orange carbon atoms, whereas ID residues are indicated in gray. F, filamentous; ID, inner domain; OD, outer domain; *Pf*ActI, *Plasmodium falciparum* actin I; SD,

subdomain.
(TIF)

S10 Fig. Plot of residue-level B factors in *Pf*ActI and *Pb*ActII. Plot of residue-level B factors of *Pf*ActI in (gray line) Ca-ATP, (blue line) Mg-ATP/ADP and (black line) Mg-ADP states as well as *Pb*ActII in (brown line) Ca-ATP and (orange line) Mg-ADP states. The SDs are annotated as SD1 (yellow), SD2 (red), SD3 (cyan), and SD4 (magenta). The approximate site of residues 61–66 that are built into weak density is marked by a black arrow. The underlying data for this figure can be found in S8 Data. *Pb*ActII, *Plasmodium berghei* actin II; *Pf*ActI, *P. falciparum* actin I, SD, subdomain.
(TIF)

S1 Movie. Principal component trajectories of Cα traces from PCA of actins. PC1 (twistedness) and PC2 (openness) are shown for the full data set of 147 actin chains and for the limited data set comprising only *Plasmodium* actin structures. PC, principal component; PCA, principal component analysis.
(MP4)

S2 Movie. Interpolated trajectories of the models used in Fig 7 to generate a comprehensive view of conformational changes taking place in *Pf*ActI during the polymerization and fragmentation processes. *Pf*ActI, *Plasmodium falciparum* actin I.
(MP4)

S1 Data. The underlying raw data for Fig 1A.
(XLSX)

S2 Data. The underlying raw data for Fig 4B.
(XLSX)

S3 Data. The underlying raw data for Fig 7.
(XLSX)

S4 Data. The underlying raw data for S1 Fig.
(XLSX)

S5 Data. The underlying raw data for S2 Fig.
(XLSX)

S6 Data. The underlying raw data for S3 Fig.
(XLSX)

S7 Data. The underlying raw data for S4 Fig.
(XLSX)

S8 Data. The underlying raw data for S10 Fig.
(XLSX)

Acknowledgments

We are grateful for the skillful assistance of Ju Xu and Dr. Juha Vahokoski in constructing some of the *Pf*ActI mutants, Dr. Henni Piirainen for help with the purification of some of them, Dr. Juha Kallio for help with data collection, and Arne Raasakka for critical reading and helpful discussions on the manuscript. We thank the Biocenter Oulu Electron Microscopy core facility, in particular Dr. Ilkka Miinalainen, as well as the Molecular Imaging Center, University of Bergen (in particular Dr. Endy Spriet) for assistance with electron microscopy. We

also thank the Biocenter Oulu Proteomics and Protein Analysis core facility and Dr. Ulrich Bergmann for assistance with mass spectrometry. The MDCC-PBP plasmid was a kind gift from Dr. Martin R. Webb from the Francis Crick Institute. We gratefully acknowledge the use of the Diamond Light Source beamlines I24 and I04-1, the European Synchrotron Radiation Facility beamline ID23-1, the European Molecular Biology Laboratory/German Electron Synchrotron beamline P13 on PETRA III, and the Berliner Elektronenspeicherring-Gesellschaft für Synchrotronstrahlung beamline MX-14.1. We also thank the facilities for excellent user support during data collection for the structures published here.

Author Contributions

Conceptualization: Esa-Pekka Kumpula, Inari Kursula.

Data curation: Esa-Pekka Kumpula, Inari Kursula.

Formal analysis: Esa-Pekka Kumpula, Inari Kursula.

Funding acquisition: Inari Kursula.

Investigation: Esa-Pekka Kumpula, Andrea J. Lopez, Leila Tajedin, Huijong Han, Inari Kursula.

Methodology: Esa-Pekka Kumpula, Andrea J. Lopez, Leila Tajedin, Huijong Han, Inari Kursula.

Project administration: Inari Kursula.

Resources: Inari Kursula.

Supervision: Inari Kursula.

Validation: Esa-Pekka Kumpula, Inari Kursula.

Visualization: Esa-Pekka Kumpula.

Writing – original draft: Esa-Pekka Kumpula.

Writing – review & editing: Andrea J. Lopez, Leila Tajedin, Huijong Han, Inari Kursula.

References

1. Titus MA. Myosin-Driven Intracellular Transport. Cold Spring Harb Perspect Biol 2018; 10: a021972. https://doi.org/10.1101/cshperspect.a021972 PMID: 29496823.
2. Svitkina T. The Actin Cytoskeleton and Actin-Based Motility. Cold Spring Harb Perspect Biol 2018; 10: a018267. https://doi.org/10.1101/cshperspect.a018267 PMID: 29295889.
3. Glotzer M. Cytokinesis in Metazoa and Fungi. Cold Spring Harb Perspect Biol 2017; 9: a022343. https://doi.org/10.1101/cshperspect.a022343 PMID: 28007751.
4. Sweeney HL, Holzbaur ELF. Motor Proteins. Cold Spring Harb Perspect Biol 2018; 10: a021931. https://doi.org/10.1101/cshperspect.a021931 PMID: 29716949.
5. Pollard TD. Actin and Actin-Binding Proteins. Cold Spring Harb Perspect Biol 2016; 8: a018226. https://doi.org/10.1101/cshperspect.a018226 PMID: 26988969.
6. Estes JE, Selden LA, Kinosian HJ, Gershman LC. Tightly-bound divalent cation of actin. J. Muscle Res. Cell Motil. 1992; 13: 272–284. PMID: 1527214.
7. Pollard TD. Rate constants for the reactions of ATP- and ADP-actin with the ends of actin filaments. J Cell Biol 1986; 103: 2747–54. https://doi.org/10.1083/jcb.103.6.2747 PMID: 3793756.
8. Schmitz S, Schaap IAT, Kleinjung J, Harder S, Grainger M, Calder L et al. Malaria parasite actin polymerization and filament structure. J Biol Chem 2010; 285: 36577–85. https://doi.org/10.1074/jbc.M110.142638 PMID: 20826799.

9. Vahokoski J, Bhargav SP, Desfosses A, Andreadaki M, Kumpula E-P, Martinez SMet al. Structural Differences Explain Diverse Functions of Plasmodium Actins. PLoS Pathog 2014; 10: e1004091. https://doi.org/10.1371/journal.ppat.1004091 PMID: 24743229.
10. Pospich S, Kumpula E-P, von der Ecken J, Vahokoski J, Kursula I, Raunser S. Near-atomic structure of jasplakinolide-stabilized malaria parasite F-actin reveals the structural basis of filament instability. Proc Natl Acad Sci U S A 2017; 114: 10636–10641. https://doi.org/10.1073/pnas.1707506114 PMID: 28923924.
11. Skillman KM, Ma CI, Fremont DH, Diraviyam K, Cooper JA, Sept Det al. The unusual dynamics of parasite actin result from isodesmic polymerization. Nat Commun 2013; 4: 2285. https://doi.org/10.1038/ncomms3285 PMID: 23921463.
12. Schmitz S, Grainger M, Howell S, Calder LJ, Gaeb M, Pinder JCet al. Malaria parasite actin filaments are very short. J Mol Biol 2005; 349: 113–25. https://doi.org/10.1016/j.jmb.2005.03.056 PMID: 15876372.
13. Kumpula E-P, Pires I, Lasiwa D, Piirainen H, Bergmann U, Vahokoski Jet al. Apicomplexan actin polymerization depends on nucleation. Sci Rep 2017; 7: 12137. https://doi.org/10.1038/s41598-017-11330-w PMID: 28939886.
14. Oda T, Iwasa M, Aihara T, Maéda Y, Narita A. The nature of the globular- to fibrous-actin transition. Nature 2009; 457: 441–445. https://doi.org/10.1038/nature07685 PMID: 19158791.
15. Fujii T, Iwane AH, Yanagida T, Namba K. Direct visualization of secondary structures of F-actin by electron cryomicroscopy. Nature 2010; 467: 724–728. https://doi.org/10.1038/nature09372 PMID: 20844487.
16. Murakami K, Yasunaga T, Noguchi TQP, Gomibuchi Y, Ngo KX, Uyeda TQPet al. Structural basis for actin assembly, activation of ATP hydrolysis, and delayed phosphate release. Cell 2010; 143: 275–87. https://doi.org/10.1016/j.cell.2010.09.034 PMID: 20946985.
17. von der Ecken J, Müller M, Lehman W, Manstein DJ, Penczek PA, Raunser S. Structure of the F-actin–tropomyosin complex. Nature 2014; 519: 114–117. https://doi.org/10.1038/nature14033 PMID: 25470062.
18. Chou SZ, Pollard TD. Mechanism of actin polymerization revealed by cryo-EM structures of actin filaments with three different bound nucleotides. Proc Natl Acad Sci U S A 2019; 116: 4265–4274. https://doi.org/10.1073/pnas.1807028115 PMID: 30760599.
19. Melki R, Fievez S, Carlier M-F. Continuous Monitoring of P_i Release Following Nucleotide Hydrolysis in Actin or Tubulin Assembly Using 2-Amino-6-mercapto-7-methylpurine Ribonucleoside and Purine-Nucleoside Phosphorylase as an Enzyme-Linked Assay. Biochemistry 1996; 35: 12038–12045. https://doi.org/10.1021/bi961325o PMID: 8810908.
20. Schmoller KM, Niedermayer T, Zensen C, Wurm C, Bausch AR. Fragmentation is crucial for the steady-state dynamics of actin filaments. Biophys J 2011; 101: 803–8. https://doi.org/10.1016/j.bpj.2011.07.009 PMID: 21843470.
21. Vorobiev S, Strokopytov B, Drubin DG, Frieden C, Ono S, Condeelis Jet al. The structure of nonvertebrate actin: implications for the ATP hydrolytic mechanism. Proc Natl Acad Sci U S A 2003; 100: 5760–5. https://doi.org/10.1073/pnas.0832273100 PMID: 12732734.
22. Baek K, Liu X, Ferron F, Shu S, Korn ED, Dominguez R. Modulation of actin structure and function by phosphorylation of Tyr-53 and profilin binding. Proc Natl Acad Sci U S A 2008; 105: 11748–53. https://doi.org/10.1073/pnas.0805852105 PMID: 18689676.
23. Tellam RL. Gelsolin inhibits nucleotide exchange from actin. Biochemistry 1986; 25: 5799–804. PMID: 3022803.
24. Dalhaimer P, Pollard TD, Nolen BJ. Nucleotide-mediated conformational changes of monomeric actin and Arp3 studied by molecular dynamics simulations. J Mol Biol 2008; 376: 166–83. https://doi.org/10.1016/j.jmb.2007.11.068 PMID: 18155236.
25. Wilbanks SM, McKay DB. How potassium affects the activity of the molecular chaperone Hsc70. II. Potassium binds specifically in the ATPase active site. J Biol Chem 1995; 270: 2251–7. https://doi.org/10.1074/jbc.270.5.2251 PMID: 7836458.
26. Zheng H, Cooper DR, Porebski PJ, Shabalin IG, Handing KB, Minor W. CheckMyMetal: a macromolecular metal-binding validation tool. Acta Crystallogr Sect D Struct Biol 2017; 73: 223–233. https://doi.org/10.1107/S2059798317001061 PMID: 28291757.
27. Panneerselvam S, Kumpula E-P, Kursula I, Burkhardt A, Meents A. Rapid cadmium SAD phasing at the standard wavelength (1 Å). Acta Crystallogr Sect D Struct Biol 2017; 73: 581–590. https://doi.org/10.1107/S2059798317006970 PMID: 28695858.
28. Otterbein LR, Graceffa P, Dominguez R. The crystal structure of uncomplexed actin in the ADP state. Science 2001; 293: 708–11. https://doi.org/10.1126/science.1059700 PMID: 11474115.

29. Graceffa P, Dominguez R. Crystal structure of monomeric actin in the ATP state. Structural basis of nucleotide-dependent actin dynamics. J Biol Chem 2003; 278: 34172–80. https://doi.org/10.1074/jbc.M303689200 PMID: 12813032.

30. Rould MA, Wan Q, Joel PB, Lowey S, Trybus KM. Crystal structures of expressed non-polymerizable monomeric actin in the ADP and ATP states. J Biol Chem 2006; 281: 31909–19. https://doi.org/10.1074/jbc.M601973200 PMID: 16920713.

31. Kudryashov DS, Grintsevich EE, Rubenstein PA, Reisler E. A nucleotide state-sensing region on actin. J Biol Chem 2010; 285: 25591–601. https://doi.org/10.1074/jbc.M110.123869 PMID: 20530485.

32. Strzelecka-Gołaszewska H, Mossakowska M, Woźniak A, Moraczewska J, Nakayama H. Long-range conformational effects of proteolytic removal of the last three residues of actin. Biochem J 1995; 307 (Pt 2): 527–34. https://doi.org/10.1042/bj3070527 PMID: 7733893.

33. von der Ecken J, Heissler SM, Pathan-Chhatbar S, Manstein DJ, Raunser S. Cryo-EM structure of a human cytoplasmic actomyosin complex at near-atomic resolution. Nature 2016; 534: 724–8. https://doi.org/10.1038/nature18295 PMID: 27324845.

34. Mentes A, Huehn A, Liu X, Zwolak A, Dominguez R, Shuman Het al. High-resolution cryo-EM structures of actin-bound myosin states reveal the mechanism of myosin force sensing. Proc Natl Acad Sci U S A 2018; 115: 1292–1297. https://doi.org/10.1073/pnas.1718316115 PMID: 29358376.

35. Merino F, Pospich S, Funk J, Wagner T, Küllmer F, Arndt H-Det al. Structural transitions of F-actin upon ATP hydrolysis at near-atomic resolution revealed by cryo-EM. Nat Struct Mol Biol 2018; 25: 528–537. https://doi.org/10.1038/s41594-018-0074-0 PMID: 29867215.

36. Yao X, Grade S, Wriggers W, Rubenstein PA. His(73), often methylated, is an important structural determinant for actin. A mutagenic analysis of HIS(73) of yeast actin. J Biol Chem 1999; 274: 37443–9. https://doi.org/10.1074/jbc.274.52.37443 PMID: 10601317.

37. Paavilainen VO, Oksanen E, Goldman A, Lappalainen P. Structure of the actin-depolymerizing factor homology domain in complex with actin. J Cell Biol 2008; 182: 51–59. https://doi.org/10.1083/jcb.200803100 PMID: 18625842.

38. Tanaka K, Takeda S, Mitsuoka K, Oda T, Kimura-Sakiyama C, Maéda Yet al. Structural basis for cofilin binding and actin filament disassembly. Nat Commun 2018; 9: 1860. https://doi.org/10.1038/s41467-018-04290-w PMID: 29749375.

39. Hundt N, Preller M, Swolski O, Ang AM, Mannherz HG, Manstein DJet al. Molecular mechanisms of disease-related human β-actin mutations p.R183W and p.E364K. FEBS J 2014; 281: 5279–91. https://doi.org/10.1111/febs.13068 PMID: 25255767.

40. Scipion CPM, Ghoshdastider U, Ferrer FJ, Yuen T-Y, Wongsantichon J, Robinson RC. Structural evidence for the roles of divalent cations in actin polymerization and activation of ATP hydrolysis. Proc Natl Acad Sci U S A 2018; 115: 10345–10350. https://doi.org/10.1073/pnas.1806394115 PMID: 30254171.

41. O'Brien MC, McKay DB. How potassium affects the activity of the molecular chaperone Hsc70. I. Potassium is required for optimal ATPase activity. J Biol Chem 1995; 270: 2247–50. https://doi.org/10.1074/jbc.270.5.2247 PMID: 7836457.

42. Boero M, Ikeda T, Ito E, Terakura K. Hsc70 ATPase: an insight into water dissociation and joint catalytic role of K+ and Mg2+ metal cations in the hydrolysis reaction. J Am Chem Soc 2006; 128: 16798–807. https://doi.org/10.1021/ja064117k PMID: 17177430.

43. McCullagh M, Saunders MG, Voth GA. Unraveling the mystery of ATP hydrolysis in actin filaments. J Am Chem Soc 2014; 136: 13053–8. https://doi.org/10.1021/ja507169f PMID: 25181471.

44. Akola J, Jones RO. Density Functional Calculations of ATP Systems. 2. ATP Hydrolysis at the Active Site of Actin. J Phys Chem B 2006; 110: 8121–8129. https://doi.org/10.1021/jp054921d PMID: 16610915.

45. Douglas RG, Nandekar P, Aktories J-E, Kumar H, Weber R, Sattler JMet al. Inter-subunit interactions drive divergent dynamics in mammalian and Plasmodium actin filaments. PLoS Biol 2018; 16: e2005345. https://doi.org/10.1371/journal.pbio.2005345 PMID: 30011270.

46. Ti S-C, Pollard TD. Purification of actin from fission yeast Schizosaccharomyces pombe and characterization of functional differences from muscle actin. J Biol Chem 2011; 286: 5784–92. https://doi.org/10.1074/jbc.M110.199794 PMID: 21148484.

47. Vorobiev S, Strokopytov B, Drubin DG, Frieden C, Ono S, Condeelis J et al. The structure of nonvertebrate actin: implications for the ATP hydrolytic mechanism. Proc Natl Acad Sci U S A 2003; 100: 5760–5. https://doi.org/10.1073/pnas.0832273100 PMID: 12732734.

48. Miller BM, Trybus KM. Functional effects of nemaline myopathy mutations on human skeletal alpha-actin. J Biol Chem 2008; 283: 19379–88. https://doi.org/10.1074/jbc.M801963200 PMID: 18477565.

49. Wen K-K, Rubenstein PA. Biochemical consequences of the cardiofunk (R177H) mutation in yeast actin. J Biol Chem 2003; 278: 48386–94. https://doi.org/10.1074/jbc.M308980200 PMID: 13129918.

50. Vandekerckhove J, Schering B, Bärmann M, Aktories K. Clostridium perfringens iota toxin ADP-ribosylates skeletal muscle actin in Arg-177. FEBS Lett 1987; 225: 48–52. PMID: 2891567.

51. Aktories K, Bärmann M, Ohishi I, Tsuyama S, Jakobs KH, Habermann E. Botulinum C2 toxin ADP-ribosylates actin. Nature 1986; 322: 390–2. https://doi.org/10.1038/322390a0 PMID: 3736664.

52. Kang H, Bradley MJ, Elam WA, De La Cruz EM. Regulation of actin by ion-linked equilibria. Biophys J 2013; 105: 2621–8. https://doi.org/10.1016/j.bpj.2013.10.032 PMID: 24359734.

53. Bhargav SP, Vahokoski J, Kumpula E-P, Kursula I. Crystallization and preliminary structural characterization of the two actin isoforms of the malaria parasite. Acta Crystallogr Sect F Struct Biol Cryst Commun 2013; 69: 1171–6. https://doi.org/10.1107/S174430911302441X PMID: 24100575.

54. Brune M, Hunter JL, Howell SA, Martin SR, Hazlett TL, Corrie JET et al. Mechanism of Inorganic Phosphate Interaction with Phosphate Binding Protein from *Escherichia coli*. Biochemistry 1998; 37: 10370–10380. https://doi.org/10.1021/bi9804277 PMID: 9671505.

55. Brune M, Hunter JL, Corrie JE, Webb MR. Direct, real-time measurement of rapid inorganic phosphate release using a novel fluorescent probe and its application to actomyosin subfragment 1 ATPase. Biochemistry 1994; 33: 8262–71. PMID: 8031761.

56. De La Cruz EM, Pollard TD. Nucleotide-free actin: stabilization by sucrose and nucleotide binding kinetics. Biochemistry 1995; 34: 5452–61. PMID: 7727403.

57. Pollard TD. Measurement of rate constants for actin filament elongation in solution. Anal Biochem 1983; 134: 406–12. PMID: 6650826.

58. Steger C. An unbiased detector of curvilinear structures. IEEE Trans Pattern Anal Mach Intell 1998; 20: 113–125.

59. Kabsch W. XDS. Acta Crystallogr D Biol Crystallogr 2010; 66: 125–32. https://doi.org/10.1107/S0907444909047337 PMID: 20124692.

60. Adams PD, Afonine P V, Bunkóczi G, Chen VB, Davis IW, Echols N et al. PHENIX: a comprehensive Python-based system for macromolecular structure solution. Acta Crystallogr D Biol Crystallogr 2010; 66: 213–21. https://doi.org/10.1107/S0907444909052925 PMID: 20124702.

61. McCoy AJ, Grosse-Kunstleve RW, Adams PD, Winn MD, Storoni LC, Read RJ. Phaser crystallographic software. J Appl Crystallogr 2007; 40: 658–674. https://doi.org/10.1107/S0021889807021206 PMID: 19461840.

62. Terwilliger TC, Adams PD, Read RJ, McCoy AJ, Moriarty NW, Grosse-Kunstleve RW et al. Decision-making in structure solution using Bayesian estimates of map quality: the PHENIX AutoSol wizard. Acta Crystallogr D Biol Crystallogr 2009; 65: 582–601. https://doi.org/10.1107/S0907444909012098 PMID: 19465773.

63. Afonine P V, Grosse-Kunstleve RW, Echols N, Headd JJ, Moriarty NW, Mustyakimov M et al. Towards automated crystallographic structure refinement with phenix.refine. Acta Crystallogr D Biol Crystallogr 2012; 68: 352–67. https://doi.org/10.1107/S0907444912001308 PMID: 22505256.

64. Grant BJ, Rodrigues APC, ElSawy KM, McCammon JA, Caves LSD. Bio3d: an R package for the comparative analysis of protein structures. Bioinformatics 2006; 22: 2695–6. https://doi.org/10.1093/bioinformatics/btl461 PMID: 16940322.

65. Edgar RC. MUSCLE: multiple sequence alignment with high accuracy and high throughput. Nucleic Acids Res 2004; 32: 1792–7. https://doi.org/10.1093/nar/gkh340 PMID: 15034147.

66. Kabsch W, IUCr. A discussion of the solution for the best rotation to relate two sets of vectors. Acta Crystallogr Sect A 1978; 34: 827–828.

67. Galgonek J, Vymětal J, Jakubec D, Vondrášek J. Amino Acid Interaction (INTAA) web server. Nucleic Acids Res 2017; 45: W388–W392. https://doi.org/10.1093/nar/gkx352 PMID: 28472475.

68. Pettersen EF, Goddard TD, Huang CC, Couch GS, Greenblatt DM, Meng EC, Ferrin TE. UCSF Chimera—a visualization system for exploratory research and analysis. J Comput Chem 2004; 25: 1605–12. https://doi.org/10.1002/jcc.20084 PMID: 15264254.

Paper III

High-resolution structures of malaria parasite actomyosin and actin filaments.

Vahokoski J, Calder LJ, **Lopez AJ**, Molloy JE, Rosenthal PB & Kursula I
bioRxiv doi: https://doi.org/10.1101/2020.07.02.183871. (2020)

III

Abstract

Malaria is responsible for half a million deaths annually and poses a huge economic burden on the developing world. The mosquito-borne parasites (*Plasmodium* spp.) that cause the disease depend upon an unconventional actomyosin motor for both gliding motility and host cell invasion. The motor system, often referred to as the glideosome complex, remains to be understood in molecular terms and is an attractive target for new drugs that might block the infection pathway. Here, we present the first high-resolution structure of the actomyosin motor complex from *Plasmodium falciparum* at an average resolution of 3.1 Å. Our structure includes the malaria parasite actin filament (*Pf*Act1) complexed with the myosin motor (*Pf*MyoA) and its two associated light-chains. The high-resolution core structure reveals the *Pf*Act1:*Pf*MyoA interface in atomic detail, while at lower-resolution, we visualize the *Pf*MyoA light-chain binding region, including the essential light chain (*Pf*ELC) and the myosin tail interacting protein (*Pf*MTIP). Finally, we report the bare *Pf*Act1 filament structure at an average resolution of 2.6 Å, which gives new information about the nucleotide-binding site, including the orientation of the ATP/ADP sensor, Ser15, and the presence of a channel, which we propose as a possible phosphate exit path after ATP hydrolysis.

High-resolution structures of malaria parasite actomyosin and actin filaments

Juha Vahokoski[1], Lesley J. Calder[2], Andrea J. Lopez[1], Justin E. Molloy[2], Peter B. Rosenthal[2*] & Inari Kursula[1,3*]

[1]Department of Biomedicine, University of Bergen, Jonas Lies vei 91, 5009 Bergen, Norway

[2]Structural Biology of Cells and Viruses Laboratory, Francis Crick Institute, NW1 1AT London, UK

[3]Biocenter Oulu and Faculty of Biochemistry and Molecular Medicine, University of Oulu, Aapistie 7, 90220 Oulu, Finland

[*]**Corresponding authors:** Peter B. Rosenthal (peter.rosenthal@crick.ac.uk) & Inari Kursula (inari.kursula@uib.no)

Authors' ORCIDs: 0000-0001-8956-3931 (Andrea Lopez); 0000-0002-8307-2450 (Justin Molloy); 0000-0002-0387-2862 (Peter Rosenthal); 0000-0001-5236-7056 (Inari Kursula)

Classification: Biological Sciences - Biophysics and Computational Biology

Keywords: actin, cryo-EM, gliding motility, malaria, myosin, phosphate release, protein-protein complex

Author contributions: JV, LJC, AJL, JEM, and PBR performed experiments, JV, JEM, PBR, and IK analyzed the data and wrote the manuscript, all authors approved the final version of the manuscript.

Abstract

Malaria is responsible for half a million deaths annually and poses a huge economic burden on the developing world. The mosquito-borne parasites (*Plasmodium* spp.) that cause the disease depend upon an unconventional actomyosin motor for both gliding motility and host cell invasion. The motor system, often referred to as the glideosome complex, remains to be understood in molecular terms and is an attractive target for new drugs that might block the infection pathway. Here, we present the first high-resolution structure of the actomyosin motor complex from *Plasmodium falciparum*. Our structure includes the malaria parasite actin filament (*Pf*Act1) complexed with the myosin motor (*Pf*MyoA) and its two associated light-chains. The high-resolution core structure reveals the *Pf*Act1:*Pf*MyoA interface in atomic detail, while at lower-resolution, we visualize the *Pf*MyoA light-chain binding region, including the essential light chain (*Pf*ELC) and the myosin tail interacting protein (*Pf*MTIP). Finally, we report a bare *Pf*Act1 filament structure at an improved resolution, which gives new information about the nucleotide-binding site, including the orientation of the ATP/ADP sensor, Ser15, and the presence of a channel, which we propose as a possible phosphate exit path after ATP hydrolysis.

Significance statement

We present the first structure of the malaria parasite motor complex; actin 1 (*Pf*Act1) and myosin A (*Pf*MyoA) with its two light chains. We also report a high-resolution structure of filamentous *Pf*Act1 that reveals new atomic details of the ATPase site, including a channel, which may provide an exit route for phosphate and explain why phosphate release is faster in *Pf*Act1 compared to canonical actins. *Pf*Act1 goes through no conformational changes upon *Pf*MyoA binding. Our *Pf*MyoA structure also superimposes with a recent crystal structure of *Pf*MyoA alone, though there are small but important conformational changes at the interface. Our structures serve as an

47 excellent starting point for drug design against malaria, which is one of the most
48 devastating infectious diseases.

49 **Introduction**

50 Malaria parasites belong to the phylum *Apicomplexa*, which are all obligate
51 intracellular parasites many of which infect humans and livestock, causing
52 immeasurable human tragedy and vast economic losses worldwide. Among the best-
53 known members of the phylum are *Plasmodium* spp. (the causative agents of
54 malaria), *Toxoplasma gondii* (toxoplasmosis), and *Cryptosporidium* spp.
55 (gastrointestinal and respiratory cryptosporidiosis), all life-threatening human
56 pathogens. Apicomplexan parasites are critically dependent on an actomyosin based
57 motor system that drives gliding motility that they use to enter and exit cells of the
58 host organisms (1, 2). The motor complex, called the glideosome, is located in a
59 narrow space between the parasite plasma membrane and an inner membrane
60 complex (IMC), which is structurally unique to this class of parasites (1-3).

61 Myosins are a large and diverse family of motor proteins, with >30 classes, found
62 across all eukaryotic organisms (4). Although the myosin classes are functionally and
63 structurally distinct, they share several conserved domains (5, 6) and produce force
64 and movement *via* the same basic mechanism, making cyclical interactions with
65 actin, coupled to the break-down of ATP to ADP and inorganic phosphate (P_i). Most
66 myosins characterized to date move towards the plus-end of actin filaments, with the
67 exception of the reverse-directed, class VI myosins. The myosin heavy chain consists
68 of an N-terminal motor domain that is well-conserved and contains the catalytic site
69 and actin binding site, which attaches and releases actin during the ATPase-cycle.
70 The motor domain is followed by a “neck” region, which binds one or more
71 calmodulin-like light chains. This region is functionally important because structural
72 rearrangements within the motor domain cause it to rotate through a large angle
73 (>60^o), and it acts as a lever arm to amplify the motion, producing the active “power

stroke". Class VI myosins have a unique insert within the neck sequence that reverses the power stroke direction. Following the neck region, most myosins have an extended, C-terminal "tail", which is highly diverse in both sequence and structure and is responsible for targeting the motor to its cellular cargo. Some myosins have a coiled-coil forming region within the tail that causes the heavy chains to dimerize (7).

Plasmodium spp. have six myosin genes; three parasite-specific class XIV myosins, two reverse-directed class VI myosins, and one class XXII myosin (8). One of the class XIV myosins, *Pf*MyoA, is essential for gliding motility and is the best-characterized of the parasite myosins. It is unusually small, consisting of just the canonical motor domain and neck region that bears two light chains; essential light chain (*Pf*ELC) and myosin tail interacting protein (*Pf*MTIP) (9). As *Pf*MyoA completely lacks a tail region, it is thought to be unable to dimerize on its own. *Pf*MyoA is anchored to the IMC by binding two glideosome-associated proteins (*Pf*GAP45 and *Pf*GAP50) *via* MTIP (10). To generate gliding motility, *Pf*MyoA interacts with *Pf*Act1 filaments (11-13) that are linked to the plasma membrane *via* the glideosome-associated connector (GAC; (14)), which binds to transmembrane adhesins of the thrombospondin-related anonymous protein family (15). During gliding, *Pf*MyoA moves along actin, pulling the IMC towards the anterior (front end) of the parasite, while pushing the actin filaments and associated plasma membrane, rearwards (16). Recently, X-ray crystal structures have been determined for the truncated motor domains of two *Pf*MyoA orthologs from *T. gondii* (*Tg*MyoA) and *P. falciparum* (*Pf*MyoA) (17, 18). For brevity, herein we refer to the *P. falciparum* proteins without the species-specific prefix "*Pf*".

Apicomplexan actins differ from the well-characterized canonical actins from yeasts, plants, and animals in some important aspects. While canonical actins form filaments, which can be micrometers to tens of micrometers in length, apicomplexan actin filaments tend to be short, typically around 100 nm (13). For *T. gondii* actin, an isodesmic polymerization mechanism was suggested to be the reason behind the

short filament length (19). However, we have shown that the polymerization pathway and kinetics of *P. falciparum* actin 1 (Act1) are very similar to canonical actins (20), and the short length of the filaments is likely caused by a high fragmentation rate (21). In a recent study based on TIRF microscopy, it was suggested that the critical concentration for polymerization of Act1 is at least an order of magnitude higher than that of canonical actins (22). Also the link between ATP hydrolysis and polymerization seems to be different in apicomplexan compared to canonical actins (11, 20, 21). Whereas canonical actins polymerize preferably in the ATP form and only catalyze ATP hydrolysis in the filamentous (F) form, ATP hydrolysis in the monomer causes *Plasmodium* actins to form short oligomers (11). Furthermore, Act1 forms stable dimers, which does not occur in other actins characterized to date (20). These differences indicate that there may be differences in the catalytic mechanism of ATP hydrolysis and phosphate release and in the activation of polymerization between the apicomplexan and higher eukaryotic actins.

Malaria parasites go through several transformations between very different cell types during their life cycle, and some of these forms are among the fastest moving cells. Merozoites penetrate red blood cells in seconds, the midgut-penetrating ookinetes can move at ~5 µm/min (23) and the mosquito-transmitted sporozoites move with impressive average speeds of 1-2 µm/s (Hopp *et al.* 2015) for tens of minutes. Recently, it was proposed that the speed and force generation of MyoA are fine-tuned by phosphorylation of Ser19 in the N-terminal helix (18). In addition, the light chains are required for maximal speed as measured by *in vitro* actin-gliding assays (9, 24). Structures of the full-length MyoA:ELC:MTIP complex are necessary for understanding the role of the light chains in determining force, speed, and step size of the motor complex as well as its association with other glideosome components.

Here, we report the first structure of full-length MyoA, with its native ELC and MTIP light chains, bound to the Act1 filament and a new high-resolution structure of the

bare Act1 filament. Our high-resolution structures show the binding mode of MyoA to Act1, the positioning of the two light chains (ELC and MTIP) on the short MyoA neck, and also reveal a possible route for the leaving phosphate after ATP hydrolysis in the Act1 active site.

Results and discussion

High-resolution structures of malaria parasite actomyosin and actin filaments

We reconstituted the malaria parasite actomyosin filament in the rigor state *in vitro* using recombinantly expressed Act1 and MyoA:ELC:MTIP complex in the presence of a small cyclic peptide, jasplakinolide, which stabilizes actin filaments and has been used for cryo-EM studies on undecorated Act1 filaments previously (11, 12). After plunge-freezing and cryo-EM imaging, we observed three types of filaments: bare Act1 filaments and filaments either partially or fully decorated by the MyoA:ELC:MTIP complex. By picking well-decorated filaments from the micrographs **(Fig. S1)**, we determined the malaria parasite actomyosin structure using helical averaging methods (25) to an overall resolution of 3.1 Å, as estimated by Fourier shell correlation with the 0.143 criterion **(Figs. 1 and S1, Table 1)**. For direct comparison, we also determined the structure of the bare Act1 filament at an average resolution of 2.6 Å **(Figs. 1 and S2, Table 1)**. Visual inspection of the density maps of both complexes agrees with the global resolution estimations **(Figs. 1, S3, and S4 and Movies S1-S4)**. We modelled a filament consisting of five Act1 and four MyoA (in the actomyosin filament) subunits modelled into the density **(Fig. S5)**.

As typical for actomyosin cryo-EM structures (26-29), the resolution in the Act1:MyoA:ELC:MTIP structure decays radially away from the helical axis, having a well-resolved core, consisting of the actin filament and the myosin motor domain, whereas density for the MyoA neck region is weaker, but nevertheless allowed us to locate density for the light chains, ELC and MTIP (**Fig. 2**). The actin core in both of our structures is particularly well resolved compared to other actin filament structures

(Fig. S3, S4). Thus, the molecular details of F-actin, including the small molecules ADP and jasplakinolide as well as the active site metal and several water molecules, can be visualized in greater detail **(Fig. 1)** than in myosin-decorated or undecorated actin filament structures to date (12, 26-31). The majority of the MyoA motor domain is well-ordered, and most of the side chains can be placed into density, especially within the actomyosin interface, allowing us to analyze specific contacts between MyoA and Act1 in detail.

ELC and MTIP bind to the short neck of MyoA in a compact manner, presumably stiffening the neck region so that it acts as a relatively rigid lever arm **(Fig. 2)**, consistent with the requirement of both light chains for maximal actin gliding speed as measured in *in vitro* motility assays. A consequence of the rigid neck region is that the space taken up by the actomyosin complex in the sub-pellicular compartment must remain rather fixed. The length of the MyoA:ELC:MTIP complex would occupy approximately half the distance between the IMC and the plasma membrane (~30 nm; **Fig. 2**), which is similar to the spacing between thick and thin filaments in the muscle sarcomere (32). In the parasite, when the additional space taken up by the actin filament (diameter ~6.5 nm) and GAC (D_{max} ~25 nm; (14)) is considered, there are significant geometric and steric constraints on how the actomyosin complex might be arranged. It is possible that the attachment of MyoA *via* its MTIP light chain to the GAP45:GAP50 complex in the IMC might allow azimuthal movement so the motor domain might approach the actin helix from different angles. These structural considerations will need to be revisited when the 3D geometry of the full glideosome complex is understood.

The MyoA motor domain has a conserved overall structure with several known subdomains common to functional myosin motors **(Fig. S6)**. The upper and lower 50 kDa subdomains are separated by the actin-binding cleft, which is in a closed conformation in our complex **(Fig. 3)**. The central transducer region consists of seven β strands **(Fig. S6)**. The lower 50 kDa subdomain contains a helix-turn-helix (HTH)

motif, involved in intimate contacts with Act1, while the rest of the actin-contacting residues are in the hypertrophic cardiomyopathy (HCM) loop and in loops 2, 3, and 4 **(Fig. 3)**. The more distal parts, the converter and the relay helix, are involved directly in the conformational change upon the power stroke **(Fig. 2, (33))**. Additionally, class XIV myosins have an N-terminal SH3 domain, the role of which is unclear but could be related to the regulation of myosin function during different stages of the parasite life cycle (34). Our actomyosin rigor structure shows that neither the SH3 domain nor the N-terminal helix is in direct contact with the actin filament **(Fig. 3)**.

Overall, the MyoA structure in complex with actin is very similar (with an overall root mean square deviation (r.m.s.d.) for the C_α positions ~1.3 Å) to the rigor-like conformer found as one of the molecules in the asymmetric unit in the recently determined MyoA crystal structure (18). However, there are several small but important changes in the complex. Notable differences allow interactions and avoid clashes with actin, including movement of the HCM loop (Ile409-Arg422) by nearly 4 Å, slightly smaller shifts in loop 3 (Glu369-Ala378), loop 4 (Thr571-Lys579), and the HTH motif (Val538-Asn563) as well as the ordering of loop 2 (Lys632-Ser639), which is not visible in the crystal structure (18). In addition, there are several smaller rearrangements in more distal areas, in particular in the converter domain. The N-terminal helix, which is specific to apicomplexan MyoAs and accommodates the phosphorylated Ser19, is stacked between the SH3 domain and the motor domain, suggesting an intimate structural or functional role **(Figs. 3 and S6)**. In the crystal structure of TgMyoA, the entire N-terminal helical extension is not visible in the electron density map (35) but is seen in the most recent MyoA crystal structures (18).

Actomyosin interface

The MyoA domain architecture is conserved, as in other myosins, regardless of the myosin class **(Figs. 2 and 3)**, but residues in the actin-binding interface are generally not conserved (**Fig. S6)**. The Act1 surface is relatively flat, and thus MyoA also lacks

large protrusions, which would penetrate deep into the filament **(Fig. 3A)**. The interface is mainly formed by contacts between the HTH motif, the HCM loop, and loops 2, 3, and 4 **(Fig. 3)** similarly to previous structures (28, 29).

The majority of specific contacts are formed by the HTH motif in the lower 50K domain, which contacts the actin-actin interface (buried surface area 386 $Å^2$), where the D-loop of one subunit inserts into the cleft between subdomains 1 and 3 of an adjacent subunit **(Fig. 3B and C)**. The first half of the HTH motif (Ser540-Gly550) forms extensive contacts with both actin subunits, whereas the latter part (Gly551-Lys565) interacts mostly with the D-loop. The Asp544 side chain of MyoA forms hydrogen bonds with the backbone amine of Thr352 in Act1 and the side chain or backbone amine of Ser351. Asp544 also interacts *via* its backbone carbonyl with the backbone amine of Ala548 in MyoA. This interaction network between Act1 and MyoA occurs just before the kink in the relay helix, possibly stabilizing it. The tip of the HTH motif (Ala548-Pro549-Gly550) inserts into a hydrophobic cleft in Act1, lined by Ile347-Leu352 and Tyr145-Thr150 as well as the D-loop residues Met46-Val47 from the adjacent actin subunit.

The HCM loop **(Fig. 3B)** forms a second important interface to Act1 (buried surface area 295 $Å^2$) that is complementary in shape and hydrophobic in nature. Suprisingly, there are no side chain interactions contributing to this interface, which is rather mediated by main chain atoms. Additional contact points are created by loop 2, which is in close vicinity of the HCM loop. The backbone atoms of Gly24 and Asp26 in Act1 form hydrogen bonds with the backbone atoms of Ile635 and Gly633, respectively, in MyoA. Ile635 of MyoA inserts into a small patch on Act1 lined by Gly25, Asp26, Ser345, Ile346, and Ser349. The MyoA basic residues Arg606, Lys634, and Lys637 are close to Asp26, Asp25, and Ser349/Ser351, respectively, distances ranging between 3.8 and 4.5 Å.

Details of the actin 1 filament and implications on phosphate release

We reconstructed the Act1 filament alone and obtained helical parameters that were highly similar to the Act1:MyoA complex. As previously noted for other actomyosin complexes (26, 27, 29), neither MyoA nor Act1 undergo large conformational changes when compared to the structures in isolation. However, our highly-resolved structures of the Act1 filament allow us to see most of the side chain orientations and details of the binding of the ligands, ADP-Mg and jasplakinolide, as well as putative water molecules, including several in the vicinity of the active site **(Fig. 1, Movies S3 and S4)**.

Based on crystal structures, the side chain of Ser15 (14 in canonical actins) has been established as a nucleotide sensor, which is turned away from bound ATP but hydrogen bonded to the β-phosphate of ADP (36). In our structure of the ADP-bound form, the side chain of Ser15 points away from the nucleotide, not contacting the ADP phosphates, thus more closely resembling the conformation in crystal structures of the ATP state **(Fig. 4)**. Interestingly, the Ser15 side chain points towards a channel with additional density, which in our high-resolution maps is close to where P_i is bound in the recent F-actin structures in the ADP-P_i state (37). The channel extends towards solvent, but its opening is partly blocked by the side chains of Asn116 and Trp80 **(Fig. 4A and B, Movie S4)**. We have modelled this density as a chain of water molecules **(Figs. 4 and S7)**, but it cannot be excluded that the channel could be partly occupied by for example phosphate or other solute molecules. The corresponding channel in monomeric Act1 is much shorter compared to the F-form and does not extend to solvent **(Fig. 4C)**. In F-form, this channel appears to be the most favorable way out from the active site. Thus, we propose it may be an alternative path for the leaving phosphate after hydrolysis, instead of or in addition to the proposed backdoor (37). In this pathway, Asn116 and Trp80, would act as "gatekeepers" that switch conformation to allow the phosphate to leave, as simply

changing the rotamers of these side chains is sufficient to fully open the channel to solvent **(Fig. 4D)**.

Similar density as seen in our structure has been described at this site in the recent AMP-PNP and ADP-P_i structures of muscle actin (38). In muscle actin, also in F-form, the cavity is, however, much shorter due to the presence of the bulkier Ile76 instead of V77 in Act1 **(Fig. 4E)**; phosphate release would be restricted and could possibly be an additional reason for the differences in phosphate release rates in different actins. Notably, residue 76/77 is an Ile in α- and γ-actins, but is also Val in β-actin as well as plant and yeast actins. We have previously noticed the importance of the substitution of the residue preceding Asn116 from an Ala in canonical actins to Gly in Act1. Ala at this position is responsible for structuring the C terminus and slightly slows down phosphate release compared to a Gly, in particular in the Mg-bound form (11, 21). In addition to allowing more flexibility to the C terminus, a Gly at this position would enable more conformations for Asn116 and thus faster opening of the phosphate release channel, contributing together with the movement of the A-loop (21) to the faster P_i release in the parasite actins. In concordance with this, jasplakinolide, which inhibits phosphate release and stabilizes filaments, is bound very close to this proposed exit route.

Interestingly, Asn115 and Arg116 in skeletal or smooth muscle α-actin are sites of disease-associated mutations (N115S, N115T, R116Q, R116H). The mechanisms by which these mutations disrupt actin function are not known but have been postulated to be linked to nucleotide binding or association with actin-binding proteins, such as CAP or α-actinin (39, 40). The mutations N115T and R116Q in yeast actin affect both nucleotide exchange as well as polymerization kinetics, in particular in the nucleation phase (41).

Concluding remarks

The first malaria parasite actomyosin filament structure reported here will serve as a foundation for understanding gliding motility in Apicomplexa as well as force generation in a variety of actomyosin motor systems. We visualize the actin-myosin interface at high-resolution and also present the structure of the entire core motor complex including the light chains which are essential for fast motility. The structure of the complex will also be an important tool for evaluating the actomyosin motor as a drug target and describes several protein-protein interfaces that may be targeted by inhibitors. The bare Act1 filament assigns accurate side chain conformations and reveals new active site features including a channel, which we propose as a possible release pathway for the leaving phosphate in Act1.

Materials and methods

Preparation of proteins and cryo-EM grids

MyoA:ELC:MTIP and Act1 were expressed and purified as previously described (9, 20). For Act1 samples, ammonium acetate was removed by a spin column, and Act1 (13.1 µM) was polymerized in the presence of 13 µM jasplakinolide by adding 10X KMEI (10 mM Hepes, pH 7.5, 500 mM KCl, 40 mM MgCl2, 10 mM EGTA). Polymerized filamentous Act1 was diluted down to 0.13 µM, and treated with apyrase (77 µg/ml) for 20 min before addition of the MyoA:ELC:MTIP complex in a 1:1 ratio. For Act1-only samples, no apyrase was used. After 30 min incubation, negatively stained or cryo-EM grids were prepared. Quality of the decorated filaments was first checked with negative staining, and after confirming presence of decorated Act1 filaments, frozen-hydrated samples were prepared on Quantifoil 2/2, 200 mesh air-glowed grids using an Mk III Vitrobot (FEI). 3 µl sample was applied on a grid and blotted for 3 s before plunge-freezing in liquid ethane.

Data collection and image processing

Actin 1:myosin A filament

Data consisting of 2815 movies were collected with a Titan Krios electron microscope equipped with a Falcon 3 camera, operated at 300 kV in counting mode. The magnification was 75000x, corresponding to 1.09 Åpixel^{-1}, using dose rate 0.539 e/Å^{2}s^{-1} with exposure time 92 s for a stack of 46 frames. The dose per frame was 1.07 e/Å^2, and we used defoci from 0.8 to 2.6 µm. The movies were aligned with MotionCor2 (42) within the Scipion framework (43). Contrast transfer function was estimated by CTFFind 4.1.5 (44), and the resulting 2786 good images were used for further data processing. To confirm data processability, we picked decorated filaments by hand and performed low-resolution reconstructions from 2x binned images from a few hundred particles using symmetry parameters defined for Act1 (12) or refined helical symmetry parameters in Relion 2.1 (25, 45) using a featureless cylinder as a starting reference. The reconstruction converged into a filamentous structure with protruding densities typical for actomyosin structures. Further inspection revealed that homologous myosin motor domains (28) as well as a filamentous Act1 model (PDB code: 5ogw (12)) fit the density well. Decorated filaments were iteratively picked with Relion autopick using reference-free Relion 2D classes as templates with an inter-box distance of two subunits with a rise of 28 Å. The resulting 381256 particles were subjected to reference-free 2D classification in Relion, resulting in 239225 fully decorated actomyosin particles. High-resolution volumes were generated in Relion 2.1 auto-refine using low-resolution models from 2x binned data as reference. A soft mask was applied on a reference model, and reconstruction was continued from the last iteration. When the reconstruction converged, we continued refinement of the contrast transfer function and subsequent reconstructions with Relion 3 beta for two additional rounds. Refined half-maps were sharpened automatically (46), and global resolution was corrected for the effects of a mask (47) using the Relion postprocessing tool. The global resolution reached 3.1 Å based on the 0.143 Fourier shell criterion. The local resolution was calculated with

Blocres in Bsoft package version 1.8.6 with a Fourier shell correlation threshold of 0.3 (48, 49).

Actin 1 filament

We collected 3953 movies with a Titan Krios electron microscope fitted with Falcon III camera in electron counting mode, operated at 300 kV. We used a nominal magnification of 75000x, corresponding to 1.09 Åpixel^{-1}. Each movie was recorded as 46 frames with 1.17 e^-/Å^2 dose/frame 1.17 e/Å^2 using defoci from 0.8 to 2.6 µm. The fractionated movies were aligned globally in Relion 3.0.7. Contrast transfer function was estimated by CtfFind 4.1.10 from dose-weighted micrographs. Particles were picked automatically using four times the rise (28 Å). The resulting 336552 particles were extracted and binned two times at 2.18 Å/pixel in a 328 pixel box before they were subjected to a reference free 2D classification, and resulted in 305480 particles in the final data set. These particles were re-extracted as unbinned, and processed with Relion auto-refine with a reference mask and solvent flattening from a previous reconstruction at nominal resolution 4.4 Å low pass filtered to 20 Å. After polishing and contrast transfer function refinement, the resulting map reached an average resolution of 2.57 Å, based on the 0.143 Fourier shell criterion. Visual inspection of the density map features agreed with the resolution estimate. After reconstruction, the map was masked and sharpened by the Relion postprocessing tool.

Model Building

Actin 1:myosin A filament

Act1 (PDB code 5ogw; (12)) was docked in density using Chimera (50), and we generated four additional symmetry copies. Two copies of MyoA crystal structure in the rigor-state (PDB code 6i7d; (18)) were placed into the density using Chimera. We iteratively built a model using tools in ISOLDE 1.0b (51), Coot (52), and real-space refinement in Phenix 1.16 (53). When the model was complete, model geometry was

373 optimized by Namdinator (54, 55). The local resolution of the reconstruction was
374 estimated by Blocres (47) and Chimera and ChimeraX (50, 56).

375 In addition, we note that the experimental map is of high quality. Before the MyoA
376 crystal structure became available, we built a complete model of MyoA, *de novo*,
377 based on a homology model of MyoA, the density map, and myosin models 1DFK
378 and 6C1D (28, 57) to guide manual model building. MyoA was correctly built into
379 density, and we have assigned the sequence register correctly, excluding the last 25
380 amino acids, which were better resolved in the X-ray crystal-structure (PDB code:
381 6i7d). Additionally, phosphorylation of Ser19 was resolved with the correct sequence
382 register.

383 *Actin 1 filament*

384 Our previous model of the Act1 filament (PDB code: 5ogw; (12)) was placed in the
385 density map in Chimera (50), and was manually build using model building tools in
386 ISOLDE 1.0b3.dev6 (51), Coot (52), and real-space refinement in Phenix 1.17 (53).
387 We built five copies of Act1, re-assigning side chain rotamers as required, and waters
388 around Act1 monomers into density. Additionally, we built the active site with the
389 Mg^{2}-coordinated waters. Density for the Mg^{2+}-water complex at the active site was
390 elongated in the plane of the atoms, and the Mg^{2+}-coordinated waters were merged
391 together with the Mg^{2+} ion density. Therefore, we created tighter custom restraints to
392 accommodate ideal coordination around the Mg^{2+} ion.

393 *Low-resolution model of light-chain-decorated myosin A*

394 I-TASSER server (58) was used to build a homology model of ELC
395 (PF3D7_1017500). The resulting map and model from the high-resolution refinement
396 (see above) worked as a basis for atomic model building. An alanine helix was
397 placed into density with Coot (52) continuing from the last residue (Lys768) of the
398 high-resolution MyoA model to residue 817. The homology model of ELC and a

crystal structure of MTIP (residues 60-204) in complex with a MyoA peptide (2QAC, (59)) were placed into density using Chimera (50). The resulting coordinates were refined using Namdinator (54). For analysis, we generated a density presentation of each chain with Molmap low-pass filtered down to 5Å: The ELC, MTIP, MyoA, and their density fits were further optimized manually.

Acknowledgements

We thank the Francis Crick Structural Biology Scientific Technology Platform for instrument access, Andrea Nans for help with data cryo-EM data collection, and Phil Walker for help with computing. We thank Donald Benton and Oliver Acton for helpful advice with image processing. I.K. and J.V. were supported by grants from the Academy of Finland, the Sigrid Jusélius Foundation, and the Norwegian Research Council. P.B.R. and J.E.M. are supported by the Francis Crick Institute, which receives its core funding from Cancer Research UK (FC001143, FC001178), the UK Medical Research Council (FC001143, FC001119), and the Wellcome Trust (FC001143, FC001119). The maps and models have been deposited in the Electron Microscopy Data Bank, http://www.ebi.ac.uk/pdbe/emdb/ (accession nos. EMD-10590 and EMD-10587). The atomic models have been deposited in the Protein Data Bank, https://www.ebi.ac.uk/pdbe/ (PDB ID codes 6TU7 and 6TU4).

References

1. K. Frenal, J. F. Dubremetz, M. Lebrun, D. Soldati-Favre, Gliding motility powers invasion and egress in Apicomplexa. *Nat Rev Microbiol* **15**, 645-660 (2017).
2. M. B. Heintzelman, Gliding motility in apicomplexan parasites. *Semin Cell Dev Biol* **46**, 135-142 (2015).
3. E. P. Kumpula, I. Kursula, Towards a molecular understanding of the apicomplexan actin motor: on a road to novel targets for malaria remedies? *Acta Crystallogr F Struct Biol Commun* **71**, 500-513 (2015).
4. A. Sebe-Pedros, X. Grau-Bove, T. A. Richards, I. Ruiz-Trillo, Evolution and classification of myosins, a paneukaryotic whole-genome approach. *Genome Biol Evol* **6**, 290-305 (2014).

5. Y. Kato, T. Miyakawa, M. Tanokura, Overview of the mechanism of cytoskeletal motors based on structure. *Biophys Rev* **10**, 571-581 (2018).
6. M. Preller, D. J. Manstein, Myosin structure, allostery, and mechano-chemistry. *Structure* **21**, 1911-1922 (2013).
7. J. R. Sellers, Myosins: a diverse superfamily. *Biochim. Biophys. Acta-Mol. Cell Res.* **1496**, 3-22 (2000).
8. R. J. Wall *et al.*, Systematic analysis of Plasmodium myosins reveals differential expression, localisation, and function in invasive and proliferative parasite stages. *Cell Microbiol* **21**, e13082 (2019).
9. J. L. Green *et al.*, Compositional and expression analyses of the glideosome during the Plasmodium life cycle reveal an additional myosin light chain required for maximum motility. *J Biol Chem* **292**, 17857-17875 (2017).
10. J. L. Green *et al.*, The MTIP-myosin A complex in blood stage malaria parasites. *J. mol. Biol.* **355**, 933-941 (2006).
11. J. Vahokoski *et al.*, Structural differences explain diverse functions of Plasmodium actins. *PLoS Pathog* **10**, e1004091 (2014).
12. S. Pospich *et al.*, Near-atomic structure of jasplakinolide-stabilized malaria parasite F-actin reveals the structural basis of filament instability. *Proc Natl Acad Sci U S A* **114**, 10636-10641 (2017).
13. S. Schmitz *et al.*, Malaria parasite actin filaments are very short. *J. mol. Biol.* **349**, 113-125 (2005).
14. D. Jacot *et al.*, An Apicomplexan Actin-Binding Protein Serves as a Connector and Lipid Sensor to Coordinate Motility and Invasion. *Cell Host Microbe* **20**, 731-743 (2016).
15. S. Kappe *et al.*, Conservation of a gliding motility and cell invasion machinery in Apicomplexan parasites. *J Cell Biol* **147**, 937-944 (1999).
16. R. E. Farrow *et al.*, The mechanism of erythrocyte invasion by the malarial parasite, Plasmodium falciparum. *Seminars In Cell & Developmental Biology* **22**, 953-960 (2011).
17. C. J. Powell *et al.*, Dissecting the molecular assembly of the Toxoplasma gondii MyoA motility complex. *J Biol Chem* **292**, 19469-19477 (2017).
18. J. Robert-Paganin *et al.*, Plasmodium myosin A drives parasite invasion by an atypical force generating mechanism. *Nat Commun* **10**, 3286 (2019).
19. K. M. Skillman *et al.*, The unusual dynamics of parasite actin result from isodesmic polymerization. *Nat Commun* **4**, 2285 (2013).
20. E. P. Kumpula *et al.*, Apicomplexan actin polymerization depends on nucleation. *Sci Rep* **7**, 12137 (2017).
21. E. P. Kumpula, A. J. Lopez, L. Tajedin, H. Han, I. Kursula, Atomic view into Plasmodium actin polymerization, ATP hydrolysis, and fragmentation. *PLoS Biol* **17**, e3000315 (2019).
22. H. Lu, P. M. Fagnant, K. M. Trybus, Unusual dynamics of the divergent malaria parasite PfAct1 actin filament. *Proc Natl Acad Sci U S A* **116**, 20418-20427 (2019).
23. T. Lammermann *et al.*, Neutrophil swarms require LTB4 and integrins at sites of cell death in vivo. *Nature* **498**, 371-375 (2013).
24. C. S. Bookwalter *et al.*, Reconstitution of the core of the malaria parasite glideosome with recombinant Plasmodium class XIV myosin A and Plasmodium actin. *J Biol Chem* **292**, 19290-19303 (2017).
25. S. He, S. H. W. Scheres, Helical reconstruction in RELION. *J Struct Biol* **198**, 163-176 (2017).

26. T. Fujii, K. Namba, Structure of actomyosin rigour complex at 5.2 A resolution and insights into the ATPase cycle mechanism. *Nat Commun* **8**, 13969 (2017).
27. P. S. Gurel *et al.*, Cryo-EM structures reveal specialization at the myosin VI-actin interface and a mechanism of force sensitivity. *Elife* **6** (2017).
28. A. Mentes *et al.*, High-resolution cryo-EM structures of actin-bound myosin states reveal the mechanism of myosin force sensing. *Proc Natl Acad Sci U S A* **115**, 1292-1297 (2018).
29. J. von der Ecken, S. M. Heissler, S. Pathan-Chhatbar, D. J. Manstein, S. Raunser, Cryo-EM structure of a human cytoplasmic actomyosin complex at near-atomic resolution. *Nature* **534**, 724-728 (2016).
30. F. Merino *et al.*, Structural transitions of F-actin upon ATP hydrolysis at near-atomic resolution revealed by cryo-EM. *Nat Struct Mol Biol* **25**, 528-537 (2018).
31. J. von der Ecken *et al.*, Structure of the F-actin-tropomyosin complex. *Nature* **519**, 114-117 (2015).
32. P. Luther, J. Squire, Three-dimensional structure of the vertebrate muscle M-region. *J Mol Biol* **125**, 313-324 (1978).
33. J. Robert-Paganin, O. Pylypenko, C. Kikuti, H. L. Sweeney, A. Houdusse, Force Generation by Myosin Motors: A Structural Perspective. *Chem Rev* **120**, 5-35 (2020).
34. C. Mueller, A. Graindorge, D. Soldati-Favre, Functions of myosin motors tailored for parasitism. *Curr Opin Microbiol* **40**, 113-122 (2017).
35. C. J. Powell *et al.*, Structural and mechanistic insights into the function of the unconventional class XIV myosin MyoA from Toxoplasma gondii. *Proc Natl Acad Sci U S A* **115**, E10548-E10555 (2018).
36. M. A. Rould, Q. Wan, P. B. Joel, S. Lowey, K. M. Trybus, Crystal structures of expressed non-polymerizable monomeric actin in the ADP and ATP states. *J Biol Chem* **281**, 31909-31919 (2006).
37. W. Wriggers, K. Schulten, Stability and dynamics of G-actin: back-door water diffusion and behavior of a subdomain 3/4 loop. *Biophys J* **73**, 624-639 (1997).
38. S. Z. Chou, T. D. Pollard, Mechanism of actin polymerization revealed by cryo-EM structures of actin filaments with three different bound nucleotides. *Proc Natl Acad Sci U S A* **116**, 4265-4274 (2019).
39. C. F. Costa *et al.*, Myopathy mutations in alpha-skeletal-muscle actin cause a range of molecular defects. *J Cell Sci* **117**, 3367-3377 (2004).
40. J. C. Sparrow *et al.*, Muscle disease caused by mutations in the skeletal muscle alpha-actin gene (ACTA1). *Neuromuscul Disord* **13**, 519-531 (2003).
41. S. E. Bergeron *et al.*, Allele-specific effects of thoracic aortic aneurysm and dissection alpha-smooth muscle actin mutations on actin function. *J Biol Chem* **286**, 11356-11369 (2011).
42. S. Q. Zheng *et al.*, MotionCor2: anisotropic correction of beam-induced motion for improved cryo-electron microscopy. *Nat Methods* **14**, 331-332 (2017).
43. J. Gomez-Blanco *et al.*, Using Scipion for stream image processing at Cryo-EM facilities. *J Struct Biol* 10.1016/j.jsb.2018.10.001 (2018).
44. A. Rohou, N. Grigorieff, CTFFIND4: Fast and accurate defocus estimation from electron micrographs. *J Struct Biol* **192**, 216-221 (2015).
45. S. H. Scheres, RELION: implementation of a Bayesian approach to cryo-EM structure determination. *J Struct Biol* **180**, 519-530 (2012).

46. P. B. Rosenthal, R. Henderson, Optimal determination of particle orientation, absolute hand, and contrast loss in single-particle electron cryomicroscopy. *J Mol Biol* **333**, 721-745 (2003).
47. S. Chen *et al.*, High-resolution noise substitution to measure overfitting and validate resolution in 3D structure determination by single particle electron cryomicroscopy. *Ultramicroscopy* **135**, 24-35 (2013).
48. G. Cardone, J. B. Heymann, A. C. Steven, One number does not fit all: mapping local variations in resolution in cryo-EM reconstructions. *J Struct Biol* **184**, 226-236 (2013).
49. J. B. Heymann, D. M. Belnap, Bsoft: image processing and molecular modeling for electron microscopy. *J Struct Biol* **157**, 3-18 (2007).
50. E. F. Pettersen *et al.*, UCSF Chimera--a visualization system for exploratory research and analysis. *J Comput Chem* **25**, 1605-1612 (2004).
51. T. I. Croll, ISOLDE: a physically realistic environment for model building into low-resolution electron-density maps. *Acta Crystallogr D Struct Biol* **74**, 519-530 (2018).
52. P. Emsley, B. Lohkamp, W. G. Scott, K. Cowtan, Features and development of Coot. *Acta Crystallogr D Biol Crystallogr* **66**, 486-501 (2010).
53. P. D. Adams *et al.*, PHENIX: a comprehensive Python-based system for macromolecular structure solution. *Acta Crystallogr D Biol Crystallogr* **66**, 213-221 (2010).
54. R. T. Kidmose *et al.*, Namdinator - automatic molecular dynamics flexible fitting of structural models into cryo-EM and crystallography experimental maps. *IUCrJ* **6**, 526-531 (2018).
55. L. G. Trabuco, E. Villa, E. Schreiner, C. B. Harrison, K. Schulten, Molecular dynamics flexible fitting: a practical guide to combine cryo-electron microscopy and X-ray crystallography. *Methods* **49**, 174-180 (2009).
56. T. D. Goddard *et al.*, UCSF ChimeraX: Meeting modern challenges in visualization and analysis. *Protein Sci* **27**, 14-25 (2018).
57. A. Houdusse, A. G. Szent-Gyorgyi, C. Cohen, Three conformational states of scallop myosin S1. *Proc Natl Acad Sci U S A* **97**, 11238-11243 (2000).
58. J. Yang *et al.*, The I-TASSER Suite: protein structure and function prediction. *Nat Methods* **12**, 7-8 (2015).
59. J. Bosch *et al.*, The closed MTIP-myosin A-tail complex from the malaria parasite invasion machinery. *J Mol Biol* **372**, 77-88 (2007).
60. W. Tian, C. Chen, X. Lei, J. Zhao, J. Liang, CASTp 3.0: computed atlas of surface topography of proteins. *Nucleic Acids Res* **46**, W363-W367 (2018).
61. A. M. Waterhouse, J. B. Procter, D. M. Martin, M. Clamp, G. J. Barton, Jalview Version 2--a multiple sequence alignment editor and analysis workbench. *Bioinformatics* **25**, 1189-1191 (2009).
62. X. Robert, P. Gouet, Deciphering key features in protein structures with the new ENDscript server. *Nucleic Acids Res* **42**, W320-324 (2014).

Figure legends

Figure 1. High-resolution reconstructions of filamentous Act1 (left) and MyoA-decorated Act1 (right). In the density maps, the central individual actin protomers and myosins are depicted in different colors. Jasplakinolide (JAS) and ADP are shown in red and yellow, respectively. The top middle part shows density maps around individual protein molecules and small molecule ligands. The bottom row shows density maps of selected motifs, as labeled, within the interfaces in the complexes. Additionally, density around phosphorylated Ser19 (S19-P) is shown.

Figure 2. A model of the light chains ELC and MTIP bound to MyoA. (A) An unsharpened map (gray) shows the location of the MyoA motor (blue) and the light chains ELC (magenta) and MTIP (cyan). (B) The Act1:MyoA:ELC:MTIP model in the rigor state shown in the context of the membrane-delimited sub-pellicular compartment.

Figure 3. Molecular interactions of MyoA with Act1. (A) MyoA is shown as blue cartoon and ActI as gray surface representation. The two adjacent actin protomers are colored with different shades of gray. The MyoA motifs contributing to the interface as well as the N-terminal helix and SH3 domain are highlighted and labeled. (B) The HCM-loop lies on one actin protomer, contacting SD1. The basic loop 2 (Lys632 and Lys634) interacts with the acidic N-terminus of Act1 (C) The HTH motif in the lower 50K domain contributes the majority of specific hydrogen bonds in the interface, interacting with the D-loop (SD2) and the C-terminal patch of Act1 between SD1 and SD3 in close vicinity of the D-loop in the adjacent actin subunit. (D) Loop 3 and the HTH motif visualized approximately 180° rotated with respect to panel C. Loop 3 (576-577) interacts with the adjacent actin monomer on SD1. The activation loop in the lower 50K domain protrudes towards the next SD1, Lys534 interacting with actin N-terminus.

598 **Figure 4. Internal cavities in filamentous and monomeric actin structures.** The
599 internal cavities were calculated using the CASTp server (60) and visualized as
600 transparent surfaces using Chimera (50). (A) The internal cavity in the PfAct1
601 filament and (B) the corresponding cavity rotated about 180° with the water hydrogen
602 bonding network depicted. (C) The corresponding channel in monomeric PfAct1
603 (4cbu; (11)). (D) The channel in the PfAct1 filament becomes solvent accessible
604 upon rotation of Trp80 and Asn166 side chains to alternative rotamers. (E) The
605 corresponding cavity in muscle actin (6djm; (38)) is shorter due to a conservative
606 amino acid change from Ile76 to V77 in PfAct1.

607

Table 1. Data collection and refinement statistics.

Data collection	**Act1-MyoA**	**Act1**
Magnification	75000 x	75000 x
Defocus range (μm)	0.8-2.6	0.8-2.6
Voltage (kV)	300	300
Microscope	Titan Krios	Titan Krios
Detector	Falcon 3	Falcon 3
No. of frames	46	46
Pixel size (Å/pixel)	1.09	1.09
Electron dose (e^-/Å^2)	49.22	52.4
No. of micrographs	2786	3953
Reconstruction (Relion)		
Software	Relion 2.1/3beta	Relion 3.0.7
Segments	239225	305480
Box size (px)	512	328
Rise (Å)	28.34	28.37
Azimuthal rotation (°)	-168.48	-167.65
Average resolution (Å) (FSC=0.143)	3.1	2.57
Model resolution (Å) (FSC=0.5)	3.2	2.7
Map sharpening B-factor (Å^2)	104	67
Model building (Phenix)		
No. of atoms	24052	15690
No. of amino acid residues	3020	1860
No. of water atoms		140
No. of ligand atoms (Mg^{2+}, ADP, JAS)	12	15
Average B-factor (Å^2)	62	37
Average B-factor for ligand atoms (Å^2)	42	36
Average B-factor for water (Å^2)		31
R.m.s.d. bond lengths (Å)	0	0.003
R.m.s.d. bond angles (°)	0.587	0.661
CC volume	0.84	0.83
CC masked	0.88	0.87
Molprobity score	1.60	1.52
Clash score	6.08	3.51
Ramachandran plot favoured/allowed/outliers (%)	96.7/3.3/0	98.5/1.5/0
Deposition codes		
PDB	6TU7	6TU4
EMDB	EMDB-10590	EMDB-10587

Movie captions

Movie 1. The Act1:MyoA map colored by local resolution. First, the malaria parasite actomyosin complex is rotated around the helical axis to present the overall quality of the map used to build the actomyosin model. The latter part of the movie shows the maps for a longitudinal Act1 dimer and MyoA separately. The slider on the right indicates the color code for the resolution in different parts of the map from 2.5 (blue) to 4.5 Å (red). The Fourier shell correlation threshold was 0.3.

Movie 2. Quality of the Act1:MyoA map. First, the MyoA-decorated filament is rotated around the helical axis, demonstrating high-resolution electron density, in which the majority of side chains are visible, sufficient for *de novo* atomic model building. In the latter part of the movie, each of the central protein subunits (4 actins and 2 myosins) is depicted with a different color. Jasplakinolide, located between actin subunits, is shown in red and ADP in the cleft between the actin subdomains is shown in yellow.

Movie 3. High-resolution map of the Act1 filament colored by local resolution. First, the filament is rotated around the helical axis, demonstrating high-resolution features. The latter part of the movie shows a single actin protomer. The slider on the right indicates the color code for the resolution in different parts of the map from 2.1 (magenta) to 2.5 Å (cyan). The Fourier shell correlation threshold was 0.143.

Movie 4. A cross-section of Act1 showing the internal channel extending from the nucleotide binding pocket towards Asn116 and Trp80 on the surface. The Act1 model is shown as surface representation, and the plane of view sections through the internal void revealing putative waters (red spheres) and ADP (sticks).

668 **Figures**

669

670 **Figure 1**

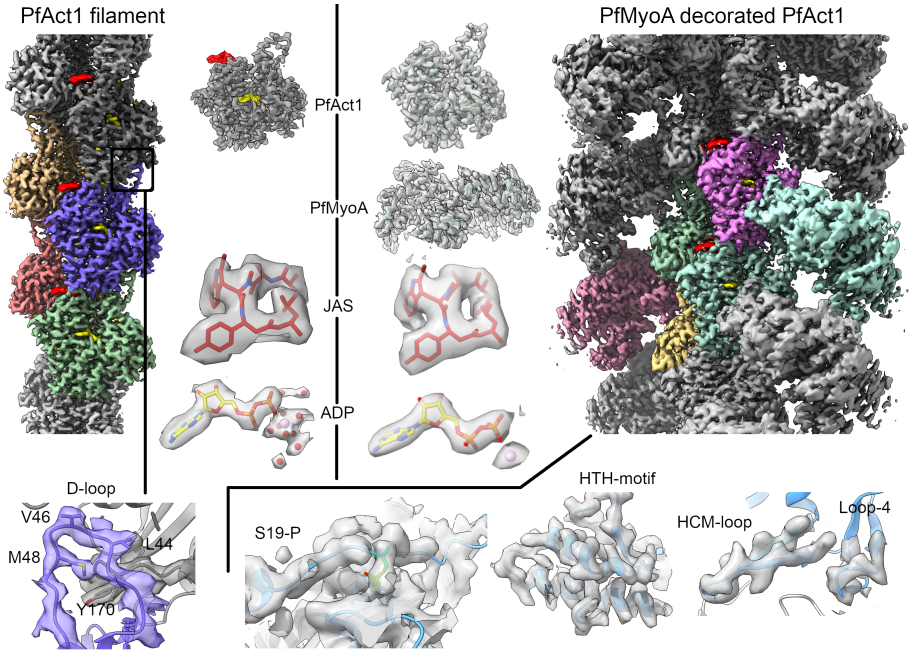

671

672

672 **Figure 2**

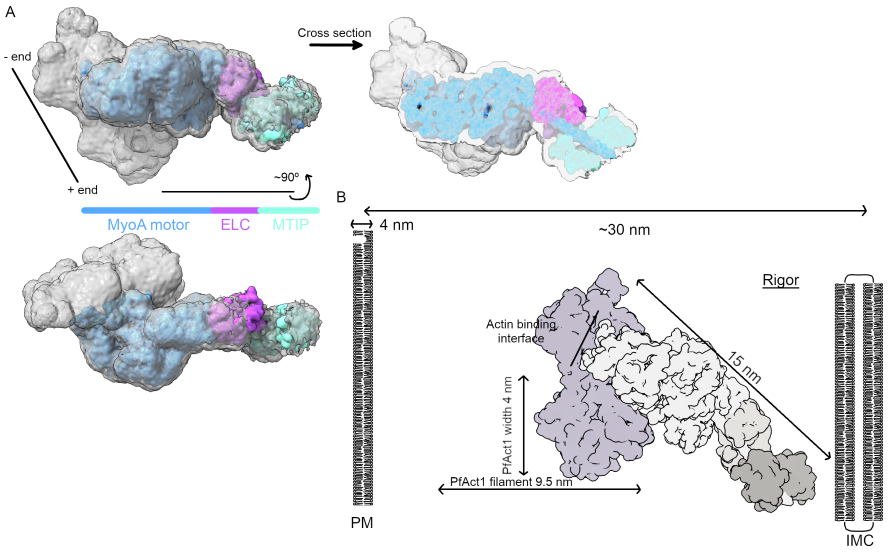

673

674

674 **Figure 3**

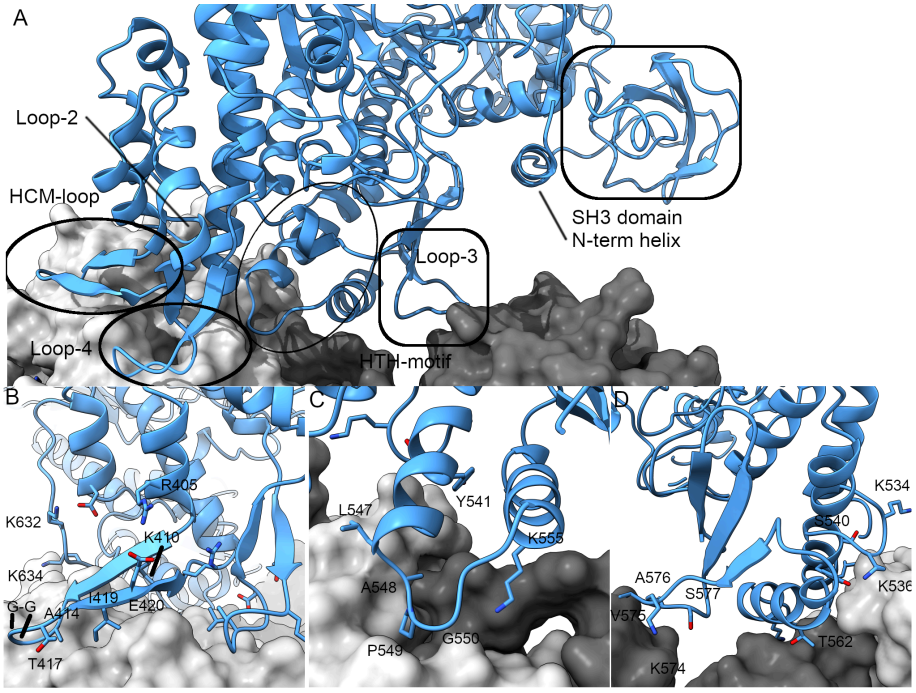

675

676

676 **Figure 4**

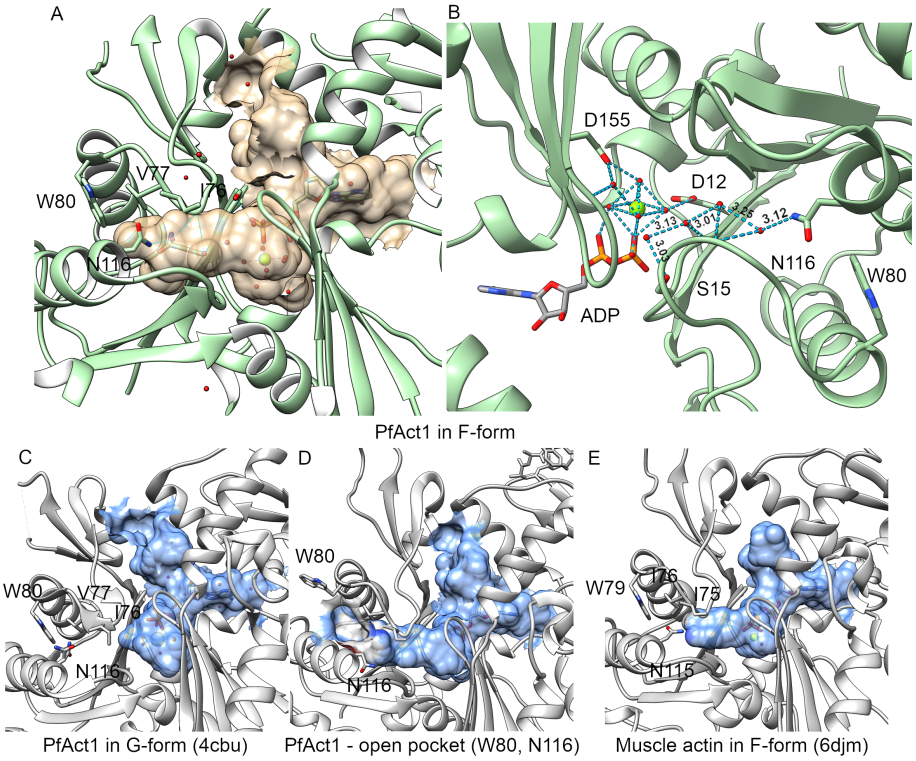

677

High-resolution structures of malaria parasite actomyosin and actin filaments

Juha Vahokoski, Lesley J. Calder, Andrea J. Lopez, Justin E. Molloy, Peter B. Rosenthal & Inari Kursula

Supplementary figures and legends

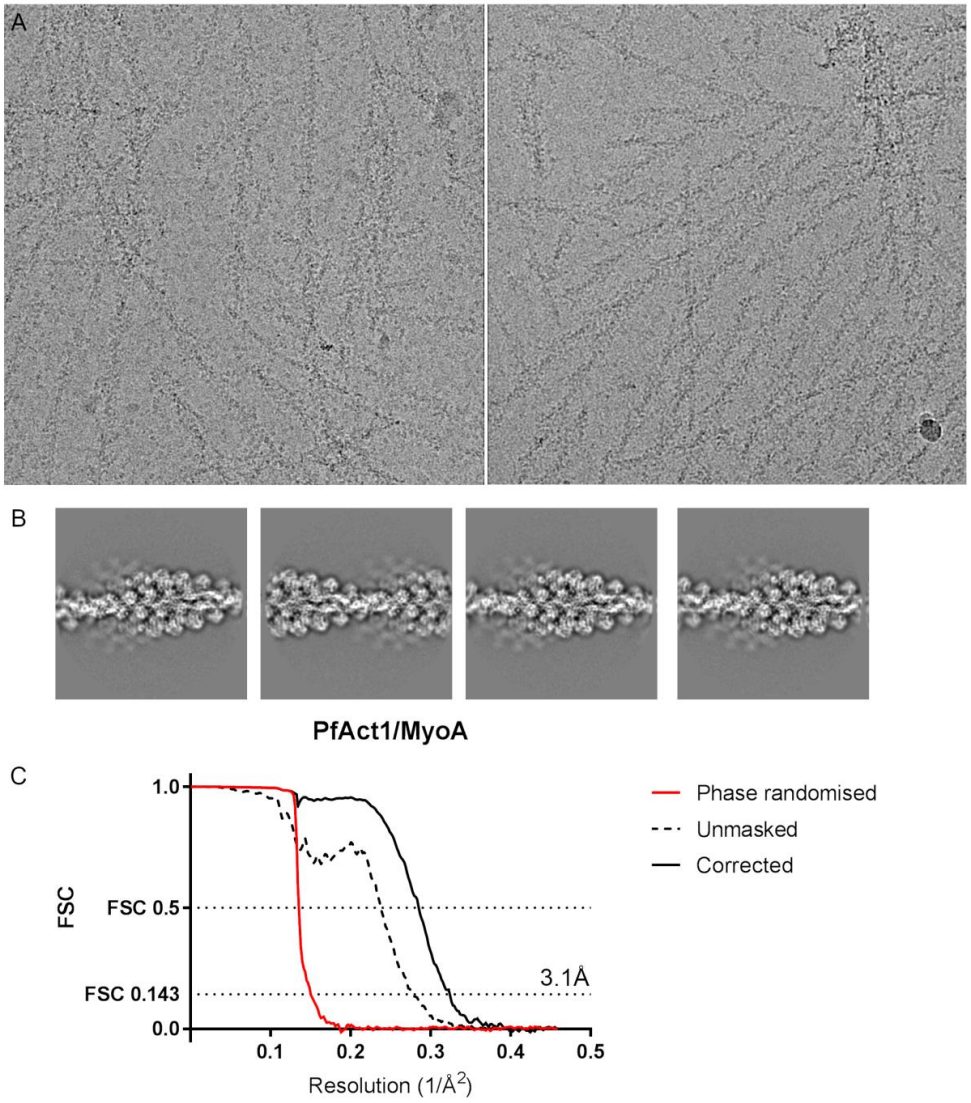

Figure S1. ActI:MyoA filaments and resolution reconstruction. (A) Representative micrographs of MyoA-decorated ActI filaments, (B) reference free classes derived from them, and (C) Fourier shell correlation of the ActI:MyoA complex. The masked curve was calculated from independently refined half-datasets with a soft-mask filtered to 15 Å.

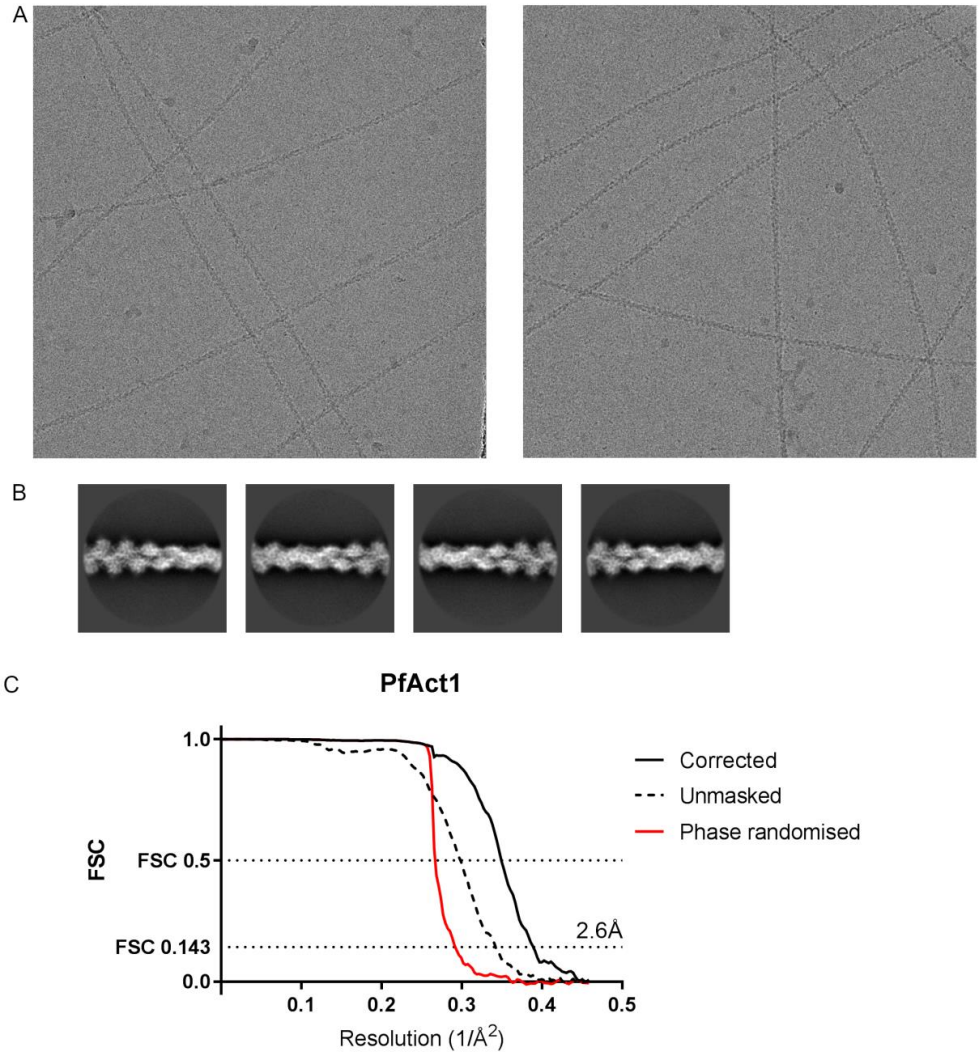

Figure S2. Examples of the Act1 filaments and resolution reconstruction. (A) Representative micrographs of ActI filaments low-pass filtered at absolute frequency 0.15, (B) reference free classes derived from them, and (C) Fourier shell correlation of the PfActI filament. The corrected curve was calculated from independently refined half-datasets with a soft-mask filtered to 15 Å in Relion.

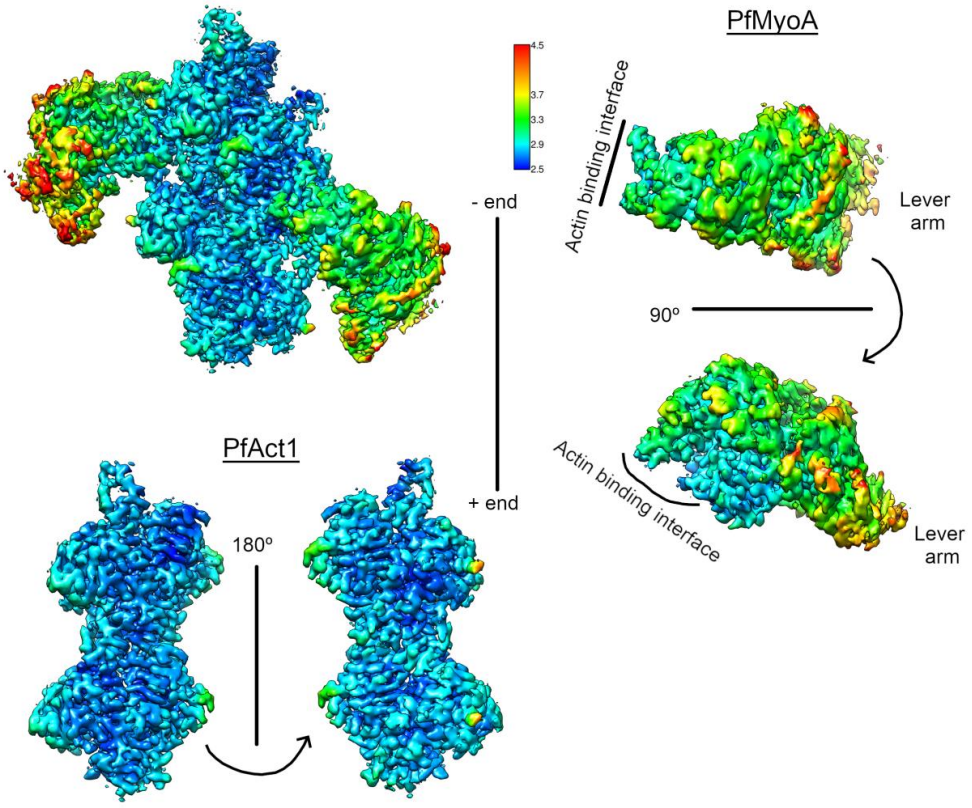

Figure S3. Local resolution of the MyoA-decorated Act1 filament. The local resolution estimation is based on the Fourier shell correlation threshold 0.3 calculated with Blocres in the Bsoft software package, which was applied to the final sharpened map.

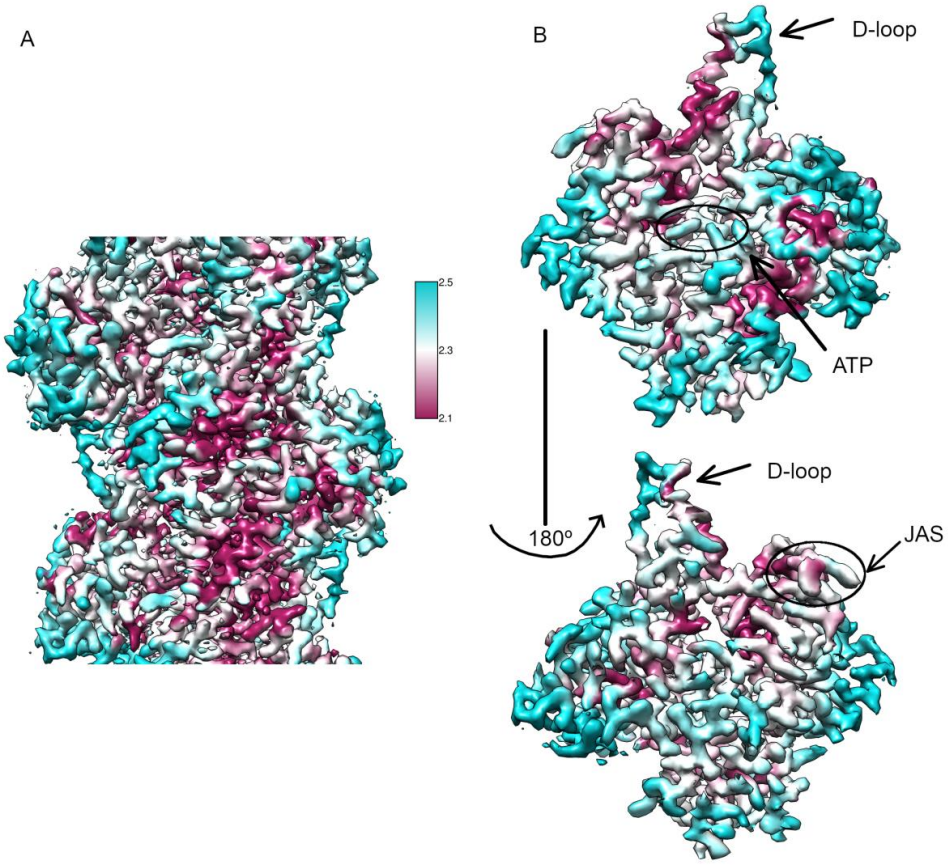

Figure S4. Local resolution of the Act1 filament. The local resolution estimation is based on Fourier shell correlation threshold 0.143 calculated with Blocres in the Bsoft software package, applied on the final sharpened map. The left panel shows a central section of the filament, and right panel show an individual actin protomer with the ligand densities highlighted.

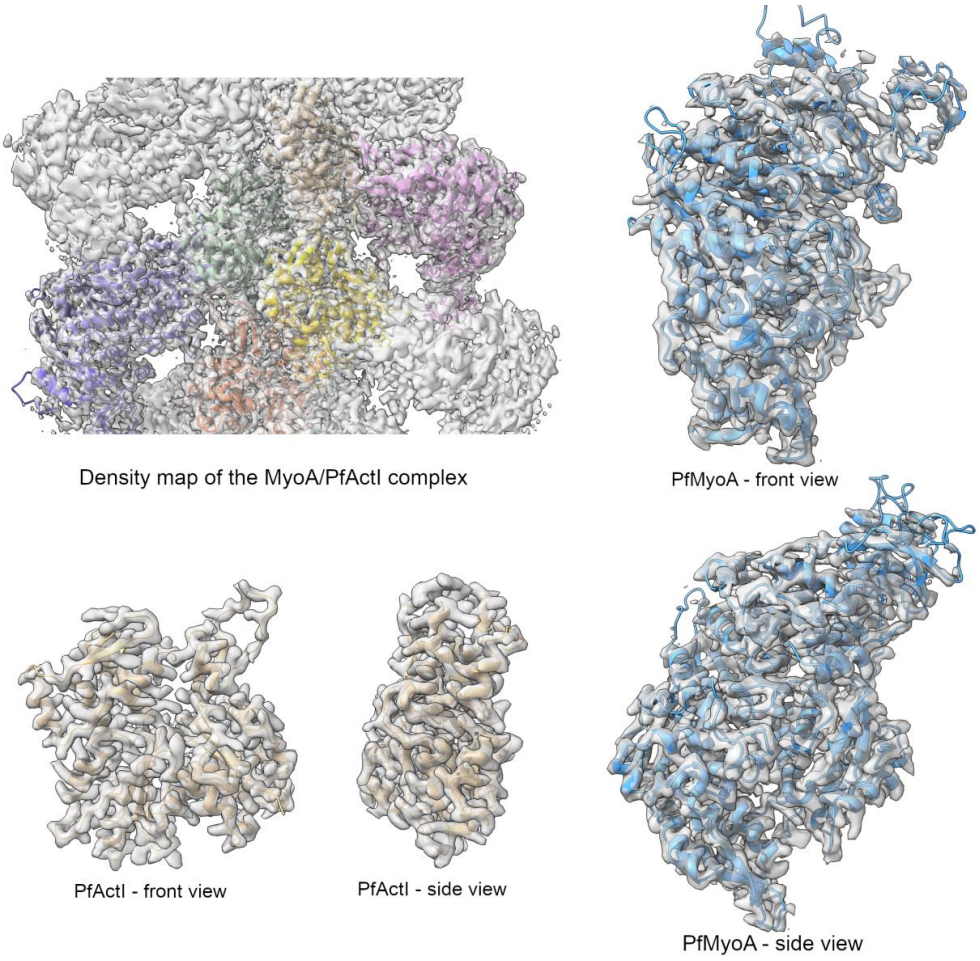

37

38

39 **Figure S5.** Density maps of the Act1:MyoA complex and individual sub-units.

40

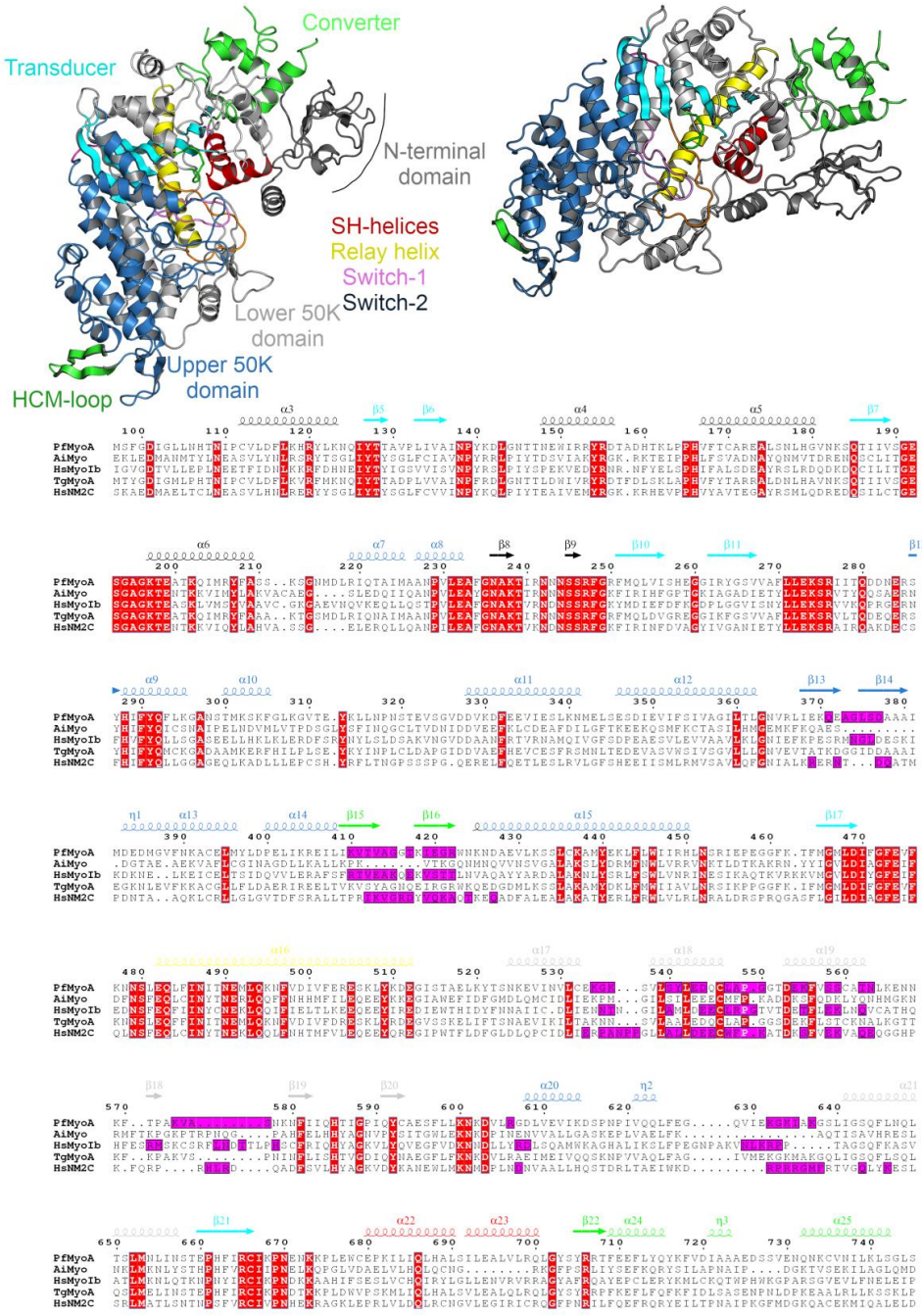
Converter
Transducer
N-terminal domain
SH-helices
Relay helix
Switch-1
Switch-2
Lower 50K domain
Upper 50K domain
HCM-loop
PfMyoA
AiMyo
HsMyoIb
TgMyoA
HsNM2C

41

42

Figure S6. Structure of the MyoA motor domain. The MyoA motor domain is depicted as cartoon representation in two different orientations, and the different motifs are shown in different colors and labeled. The coloring of the secondary structure elements above the sequence alignment corresponds to that of the myosin structure above. Strictly conserved residues are boxed with red and interface residues are indicated with purple boxes. The sequence alignment was performed in JalView (61) using default settings and visualized using the ESPript web interface (62). Pf: *Plasmodium falciparum*, Ai: *Argopecten irradians*, Hs: *Homo sapiens*, Tg: *Toxoplasma gondii*.

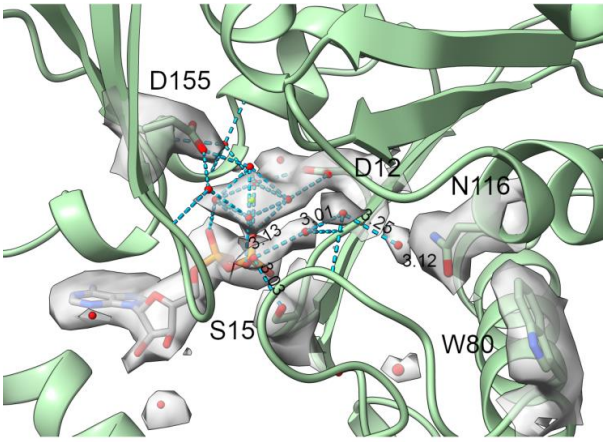

Figure S7. Active site in the Act1 filament. The figure shows the density map around the nucleotide-binding site, including ADP (sticks), Mg^{2+} (green sphere) with coordinating water molecules (red spheres), and putative water molecules (red spheres) in the internal cavity.

Errata for
Structural and biochemical characterization of Malaria parasites

Andrea Johana Lopez Moreno

Thesis for the degree philosophiae doctor (PhD)
at the University of Bergen

17.08.2021 Andrea López M.
(date and sign. of candidate)

17/8·21
(date and sign. of faculty)

Errata

Page 59 Misspelling: “promotes” – corrected to “promote”

Page 60 Incorrect words: “In contrast, the K270M mutant could form few long filaments at pH 6” – corrected to “In contrast, the K270M mutant formed long filaments at pH 6”

Page 60 Full stop missing: “Polymerized wild-type *Pf*ActI and K270M samples at different pHs, after ultracentrifugation pellets and supernatants, were collected.” – corrected to “Polymerized wild-type *Pf*ActI and K270M samples at different pHs. After ultracentrifugation pellets and supernatants, were collected.”

Page 62 Missing word: “a sedimentation assay was performed applying” – corrected to “a sedimentation assay was performed by applying”

Page 60 Incorrect word: “maintain apparently as” – corrected to “maintain as”

Page 63 Incorrect sentence: “At 100,000 *g,* 42.1% of the protein in the supernatant appears to be monomeric and extremely weak dimer (2.1%) and trimer (2.3%) band”– corrected to “At 100,000 *g,* 42.1% of the protein in the supernatant appears to be monomeric, 2.1% dimeric and 2.3% trimeric (extremely weak bands).”

Page 63 Incorrect symbol: 1,9% – corrected to 1.9%

Page 65 Missing words: “Contrary to the C_c curve in F-Buffer had a linear behavior.” – corrected to “Contrary to the C_c curve in F-Buffer, this plot had a linear behavior.”

Page 66 Misspelling: “GF Buffer” and “a. Samples after 1 h and 20 h in (d)” – corrected to “G Buffer” and “c. Samples after 1 h and 20 h in (d)”

Page 66 Full stop missing: “Moreover, *Pf*ActII presented an overshoot which is an unusual peak likely during the elongation phase.” – corrected to “Moreover, *Pf*ActII presented an overshoot which is an unusual peak, likely during the elongation phase.”

Page 67 Incorrect word: “variated”– corrected to “changed”

Page 67 Misspelling: “correspond” and “seconds”– corrected to “corresponds” and “second”

Page 72 Misspelling: “Fragmin”– corrected to “fragmin”

Page 73 Misspelling: “surfaced”– corrected to “surface”

Page 73 Missing word: “whereas in *Plasmodium* actins is ~0.3 Å larger” – corrected “whereas in *Plasmodium* actins it is ~0.3 Å larger”

Page 63 Incorrect punctuation sign: “the phosphate release, is blocked” – corrected to “the phosphate release is blocked”

Page 77 Misspelling: “F4”– corrected to “K4”

Page 78 Missing words: *Pf*Myosin constructs were cloned into the pFASTBacI vector (acceptor vector) with Strep-tag II, used for expression” – corrected to “*Pf*Myosin constructs were cloned into the pFASTBacI vector (acceptor vector) with Strep-tag II, and these were used for expression”

Page 79 Incorrect order of the words: “These myosins likely are” – corrected to “These myosins are likely”

Page 83 Missing word: “Actins are very conserved among the organisms” – corrected “Actins are very conserved among the eukaryotic organisms”

Page 83 Incorrect words: “Even though the amino acid sequence identity of *Pf*ActII is the lowest, compared with α-actins in terms of protein structure, *Pf*ActII is more similar to α-actins than *Pf*ActI”. – corrected to “Even though the amino acid sequence identity of *Pf*ActII is the lowest compared with α-actins, the protein structure of *Pf*ActII is more similar to α-actins than *Pf*ActI”.

Page 83 Misspelling: “on”. – corrected to “of”.

Page 84 Misspelling: “GF-Buffer”– corrected to “G-Buffer”

Page 84 Incorrect words: “it is likely that the time to set up the polymerization experiment has to be as faster (less than 10s between the 1 F-buffer is added to the samples and the first measurement)” – corrected to “it is likely that the time to set up the polymerization experiment has to be faster (less than 10s between the F-buffer is added to the samples and the first measurement)”

Page 85 Misspelling: “pick” and “This”– corrected to “peak” and “Thus”.

Page 86 Missing a punctuation sign: “Possibly it is the case also for *Pf*ActII,” – corrected “Possibly, it is the case also for *Pf*ActII”

Page 88 Incorrect words: “observe”. – corrected to “have”.

Page 89 Misspelling: “It”– corrected to “it”

Page 90 Incorrect word: “as fast as like sporozoites” – corrected to “as fast as sporozoites”

Page 91 Incorrect words: “Actin undergoes to major conformational changes from a monomeric to filamentous form”. – corrected to “Actin undergoes significant conformational changes from a monomeric to filamentous form”.

Page 91 Incorrect words: “neither MyoA or *Pf*ActI does not induce considerable conformational changes”. – corrected to “neither MyoA or *Pf*ActI induce considerable conformational changes”.

Page 91 Incorrect words: “CaM”. – corrected to “calmodulin”.

Page 92 Incorrect words: “available in”. – corrected to “available at”.

Page 92 Misspelling: “Motift”, “*Pf*MyoD” and, “*Pf*MyoF”– corrected to “Motif”, “*Pf*MyoK” and, “*Pf*MyoJ”

Page 94 Incorrect words: “Since *Pf*ActII is the most diverse actin and exclusive for the insect cell stages”. – corrected to “Since *Pf*ActII is the most diverse actin and exclusive to the insect cell stages”.

Page 94 Incorrect words: “On the other hand” , “with” and giving a molecular details of the actin”. – corrected to “Furthermore”, “to” and “giving molecular details of the actin”

Page 96 Incorrect sentence: “This work provided a first overview on the kinetics of *Pf*ActII polymerization. ” – corrected to “This work provided the first overview of the *Pf*ActII polymerization kinetics.”

Page 96 Misspelling and missing words: “Understanding the differences of force generation by the different myosins in *Pf*ActII or *Pf*ActII will give as information…” – corrected to “Understanding the differences of force generation by the different myosins in complex with *Pf*ActII or *Pf*ActII will give us information…”

Page 8 Misspelling in figure 2, paper II: “mM” – corrected to “µM”

Page 9 Incorrect words, paper II: “The overshoot” – corrected to “It”

Page 10 Misspelling in figure 3, paper II: “mM” – corrected to “µM”

Page 20 Incorrect words, paper II: “Although F-*Pf*ActII has a closed D-loop conformation (P41 and E48)” – corrected to “Although F-*Pf*ActII has a closed D-loop conformation”

Page 31 Issue with the PDF conversion, Figure S1, paper II: the letters are not aligned with the red columns – corrected to - the letters are aligned with the columns.

Graphic design: Communication Division, UiB / Print: Skipnes Kommunikasjon AS

uib.no

ISBN: 9788230841501 (print)
9788230855195 (PDF)